Transcranial Therapy for Intracerebral Hemorrhage and Other Brain Pathologies using Histotripsy

by

Tyler Gerhardson

A dissertation submitted in partial fulfillment
of the requirements for the degree of
Doctor of Philosophy
(Biomedical Engineering)
in the University of Michigan
2020

Doctoral Committee:

Associate Professor Zhen Xu, Chair
Professor J. Brian Fowlkes
Associate Professor Aditya S. Pandey
Associate Research Scientist Timothy L. Hall
Assistant Research Scientist Jonathan R. Sukovich

The struggle itself towards the heights is enough to fill a man’s heart.

- Albert Camus

Tyler Gerhardson

tgerhard@umich.edu

ORCID iD: 0000-0002-4548-5588

DEDICATION

For the anatomical donors and research animals.

ACKNOWLEDGEMENTS

I would like to begin by highlighting my sincere gratitude for my advisor Dr. Zhen Xu. Since beginning my graduate school career, Zhen has provided very direct and strong guidance in helping me achieve my goals as a graduate student and beyond. Her support and encouragement have helped me attain a great variety of success during my time at Michigan and I am constantly inspired by her capacity to lead. It is a great honor to have had the opportunity to work with Zhen over the past 5 years. I hold the other members of my dissertation committee in a similarly high regard: Drs. Timothy Hall, Jonathan Sukovich, Aditya Pandey and Brian Fowlkes. Tim Hall is an inspirational research scientist, engineer and teacher. Tim has taught me much about dissecting scientific questions and practical ways to approach answering them. His capacity to develop new technology in our lab is inspiring and I have learned a tremendous amount working with him during my graduate school process. Jonathan Sukovich has been another indispensable resource during my time as a graduate student and has played a significant role in developing the contents of this dissertation. Jonathan has great knowledge of basic physics, is extremely resourceful and has been easy to approach with nearly any question I had during grad school. Dr. Aditya Pandey has been critical in providing a clinical perspective to my research. His deep understanding of intracerebral hemorrhage and neurosurgical methods have significantly shaped the development of histotripsy as a therapy for brain pathologies. Brian Fowlkes has been another outstanding resource during my time as a graduate student. Brian has a huge depth of knowledge on physical acoustics and clinical applications of ultrasound. His input into my project has been extremely insightful. Finally, I would like to recognize Charles Cain for his thoughtful input into my research. Charles laid the foundation for histotripsy and although not a member of my dissertation committee, he helped shaped many parts of this dissertation.

In addition to my committee members I would also like to acknowledge the former and current members (undergraduate students, PhD students and post-docs) of the histotripsy group who I have been fortunate to overlap with during my time at Michigan: Eli Vlaisavljevich, Alex Duryea, Steven Allen, Xi Zhang, Thai-Son Nguyen, Aiwei Shi, Youhan Sunny, Jonathan Lundt, Jonathan Macoskey, Yige Li, Hedieh Tamaddoni, Tejaswi Worlikar, Sang Won Choi, Ryan Hubbard, Ning Lu, Greyson Stocker, Ellen Yeats, Scott Haskell, Christina Hendren, Dinank Gupta, Jeremy Deniega, Sarah Duclos, Varsha Kuma, Yuning Zhao and Reliza Mcginnis. This is a great group of individuals and I feel sincerely grateful to know and have worked with each one of them. I would like to draw specific attention to Eli Vlaisavljevich, I am extremely grateful for my interaction with Eli early in my PhD career. Eli helped me get started in lab and conversations with him helped me to understand and focus on the important components of my PhD. I would also like to draw attention to Jonathan Macoskey, Jonathan Lundt, Yige Li, Hedieh Tamadonni, and Tejaswi Worlikar who I have had the most overlap with during my time in lab. I enjoyed having each of them around as we moved through the PhD process together. I think the most meaningful and gratifying part of my PhD has been as a senior student where I have been able to pass my knowledge to the new students entering lab. It gives me much joy and satisfaction to see each new student eventually find success with their project and grow as a researcher.

I would also like to highlight and recognize the staff in our lab: Kim Ives, Dave Choi, Adam Fox. Kim has been extremely helpful and fun to work with. I have enjoyed spending time with and learning from her during the pig and mice studies I performed. Dave and Adam are great colleagues and have helped significantly in getting the cadaver study off the ground. I would also like to recognize the staff in the Department of Biomedical Engineering: Kathleen McCrumb, Rebecca Green, Dana Jackson, Chuck Nicholas and Erik Keup. Kathy and Becky were excellent in ensuring that important orders were placed and received on time. Both Chuck and Erik helped facilitate any issues I had with computer equipment or other technical problems.

Faculty and staff from departments external to Biomedical Engineering also deserve recognition. Badih Junior Daou, a resident in Neurosurgery was instrumental in getting the initial cadaver experiments off the ground. The faculty and staff in the Lurie Nanofabrication Facility helped much with various aspects of transducer and hydrophone design. Professor Richard Hughes in Industrial and Operations Engineering helped with the formulation of an optimization model presented in Chapter 6. Brian Eby and others at the University of Michigan Transportation Research Institute helped with various machining endeavors and provided insight into working with human cadavers. Glenn Fox, Kathleen Alsup and Kenneth Thompson with Anatomical Donations provide valuable insight into the initial cadaver experiments. Tom Chenevert, Suzan Lowe and James O'connor in Radiology were instrumental in working out logistics on transporting cadavers to and from the MRI system. Anupama Pal in Cancer Oncology and Lindsey Sheetz in Pharmaceutical Sciences were essential to the glioblastoma study presented in this dissertation.

Next, I would like to draw attention to a few professors from my undergraduate career who inspired and encouraged me to pursue my PhD: Drs. Anthony English (Tony), Bart Lipkens and Michael Rust. If it was not for my interaction with Dr. Lipkens, I would have never headed down a career path in acoustics. His work with acoustic standing waves and macro-scale acoustophoresis, got me excited with and interested in the application of acoustics to biomedical problems. Tony and Dr. Rust were both incredibly encouraging and supported me in my graduate school applications. I also want to recognize all my fellow interns from my time at FloDesign

Sonics. It was an exciting time to be an intern at FDSonics and I have great memories from that time in my life. I would like to also highlight my colleagues at Canon Medical Research, Xiaohui Zhan. I am grateful to have had the opportunity to work on Canon's next generation photon counting CT system and I learned a lot working with Xiaohui.

Finally, I would like to highlight my family and friends who provide my life with all its meaning and have encouraged and supported me through all my endeavors. My uncle, Dr. Kevin Walter has been a great source of advice during my time in graduate school and I am thankful for that. All of my longtime friends from Western MA are like family, they shaped and continue to shape me into the person I am today. I am grateful for our time together. In addition, the friends I have made between MA and MI have provided significant joy and meaning to my life. My best friend and partner Michelle Karker has been incredibly supportive, encouraging and relatable in all aspects of my life. I am very happy she is and continues to be a part of my life. I also want to highlight my two brothers and one sister: Jonathan, Maxwell and Chloe. I can always count on them being able to relate to my feelings and perspective of the world and life and I am grateful to have them around. I want to end by acknowledging the most important people in my life, my mom and dad, Jennifer and Bradly Gerhardson. They are humble and kind and their perspective of the world is refreshing and grounding. They are supportive without constraints and I know that they will always be supportive of the life I lead, regardless of the form it takes.

Table of Contents

LIST OF TABLES

LIST OF FIGURES

ABSTRACT

Brain pathologies including stroke and cancer are a major cause of death and disability. Intracerebral hemorrhage (ICH) accounts for roughly 12% of all strokes in the US with approximately 200,000 new cases per year. ICH is characterized by the rupture of vessels resulting in bleeding and clotting inside the brain. The presence of the clot causes immediate damage to surrounding brain tissue via mass effect with delayed toxic effects developing in the days following the hemorrhage. This leads ICH patients to high mortality with a 40% chance of death within 30 days of diagnosis and motivates the need to quickly evacuate the clot from the brain. Craniotomy surgery and other minimally invasive methods using thrombolytic drugs are common procedures to remove the clot but are limited by factors such as morbidity and high susceptibility to rebleeding, which ultimately result in poor clinical outcomes.

Histotripsy is a non-thermal ultrasound ablation technique that uses short duration, high amplitude rarefactional pulses (>26 MPa) delivered via an extracorporeal transducer to generate targeted cavitation using the intrinsic gas nuclei existing in the target tissue. The rapid and energetic bubble expansion and collapse of cavitation create high stress and strain in tissue at the focus that fractionate it into an acellular homogenate. This dissertation presents the role of histotripsy as a novel ultrasound technology with potential to address the need for an effective transcranial therapy for ICH and other brain pathologies.

The first part of this work investigates the effects of ultrasound frequency and focal spacing on transcranial clot liquefaction using histotripsy. Histotripsy pulses were delivered using two 256-

element hemispherical transducers of different frequency (250 and 500 kHz) with 30-cm aperture diameters. Treatment durations ranged from 0.9 – 42.4 min, following which liquefied clot volumes ranging from 6-59 mL were drained via catheter and syringe; treatment rates of up to 16.6 mL/min were achieved. The ultrasound-induced temperature rise within the skull bones remained below 4 °C for treatments delivered through all three skullcaps.

The second part addresses initial safety concerns for histotripsy ICH treatment through investigation in a porcine ICH model. 1.75-mL clots were formed in the frontal lobe of the brain. The centers of the clots were liquefied with histotripsy 48 h after formation, and the liquefied contents were either evacuated or left within the brain. A control group was left untreated. Histotripsy was able to liquefy the core of clots without direct damage to the perihematomal brain tissue. An average volume of 0.9 ± 0.5 mL (~50%) was drained after histotripsy treatment. All groups showed mild ischemia and gliosis in the perihematomal region; however, there were no deaths or signs of neurological dysfunction in any groups.

The third part presents the development of a novel catheter hydrophone method for transcranial phase aberration correction and drainage of the clot liquefied with histotripsy. A prototype hydrophone was fabricated to fit within a ventriculostomy catheter. Aberration correction based on measurements from the catheter hydrophone resulted in improvements in focal pressure of up to 60% were achieved at the geometric focus and 27%-62% across a range of electronic steering locations. The sagittal and axial -6-dB beam widths decreased from 4.6 to 2.2 mm in the sagittal direction and 8 to 4.4 mm in the axial direction, compared to 1.5 and 3 mm in the absence of aberration. The cores of clots liquefied with histotripsy were readily drained via the catheter.

The fourth part focuses on the development of a preclinical system for translation to human cadaver ICH models. A 360-element, 700 kHz hemispherical array with a 30 cm aperture was designed and integrated with an optical tracker surgical navigation system. Calibrated simulations of the transducer suggest an effective therapeutic target volume between 48 – 105 mL through the human skull with the ability to apply therapy pulses at pulse-repetition-frequencies up to 200 Hz. The navigation system allows real-time targeting and placement of the catheter hydrophone via a pre-operative CT or MRI.

The fifth and final part of this work extends transcranial histotripsy therapy beyond ICH to the treatment of glioblastoma. This section presents results from an initial investigation into cancer immunomodulation using histotripsy in a mouse glioblastoma model. The results suggest histotripsy has some immunomodulatory capacity as evidenced by a 2-fold reduction in myeloid derived suppressor cells and large increases in interferon-γ concentrations (3500 pg/mL) within the brain tumors of mice treated with histotripsy.

CHAPTER 1 Introduction

This dissertation is focused on the investigation and development of pulsed cavitational ultrasound therapy (histotripsy) as a noninvasive or minimally invasive transcranial ultrasound ablation therapy with primary emphasis on the treatment of intracerebral hemorrhage (ICH). This dissertation also contains the first-pass investigation into histotripsy mediated immunomodulatory effects in brain cancer (glioblastoma). Although focused primarily on ICH, the insights and technical developments specific to transcranial treatment of ICH will likely translate to the treatment of other brain pathologies through the skull (e.g., brain tumors). The dissertation is presented in four main parts: 1) The in-vitro feasibility for transcranial clot liquefaction using histotripsy with electronic focal steering is investigated through excised human skulls. 2) Initial safety concerns with histotripsy clot liquefaction within the brain are investigated in-vivo in a well-established porcine ICH model. 3) Technical innovations including the development of a catheter hydrophone aberration correction method and the development of a new pre-clinical array prototype for the treatment of ICH in human cadaver and porcine models. 4) The first-pass investigation into histotripsy mediated immunomodulation within a mouse glioblastoma model. This chapter will first introduce ICH, its mechanisms of injury and current clinical treatment options. This will be followed by an overview of some pre-clinical treatment methods under investigation. The underlying mechanism of the histotripsy technology will be introduced and its potential advantages for ICH treatment will be discussed. The translation of transcranial histotripsy to other brain pathologies (e.g., brain tumor) will also be discussed. A brief introduction to immune therapy and context for the immunomodulation study contained within this dissertation will be presented. The current chapter will conclude with an outline for the dissertation providing some overview for the following chapters.

1.1 Intracerebral Hemorrhage

Intracerebral hemorrhage (ICH) is a devastating form of stroke, leading to a 30-day survival rate of 40-50% and significant disability for those that survive [1], [2]. Large clots (> 60 mL) are even more detrimental to patient outcome with a 30-day mortality rate > 75%. Each year there are approximately 80,000 new ICH cases within the US and 4 million cases worldwide [3], [4]. The primary neurologic injury induced by ICH occurs immediately and is characterized by the mechanical distortion (i.e., mass effect) of neurons by the bleed, reduced cerebral blood flow and the influx of thrombin at the location of the bleed [5], [6]. The secondary injury to the brain occurs in the days and weeks following the hemorrhage and is characterized by the toxic effects associated with clot metabolism and processes associated with the inflammatory and complement systems' response to the presence of the clot [5].

1.2 Clinical Treatment Options

Standard treatment for ICH consists of either medical management or craniotomy surgery. Medical management uses monitoring and drugs to sustain and monitor blood flow and perfusion without removing the clot. However, this technique does not provide much relief and is not possible for large clots. Surgically removing the clot is necessary for most ICH cases that are not able to be managed. The primary goals of surgery are to reduce the mass effect, block toxic effects associated with hematoma metabolism and limit the inflammatory and complement responses to the clot [6]. However, these goals are not necessarily met if the surgery is highly invasive. For example, surgeries involving the removal of a portion of the skullcap and traversal of healthy brain tissue to remove the clot have not been shown to improve the functional outcome of patients or reduce the morbidity [7]. This is thought to be largely due to the neural damage and recurrence of bleeding associated with craniotomy surgery [6]. Due to these concerns, a minimally invasive intracranial catheter method has been gaining clinical momentum. A needle or catheter is placed into the clot via a small burr hole in the skullcap to inject thrombolytic drug (e.g., tissue plasminogen activator) and to drain the lysed clot over several (3-7) days. A recent small randomized clinical trial in the US (MISTIE) and data on thousands of patients from China have shown improved clinical outcome, including shorter hospital stays, an improvement in mobility, and independence in daily activities at follow-up [1], [8], [9]. Most recently, a large multicenter randomized trial (MISTIE III) showed that this method improved functional outcomes and survival when greater than 70% of the ICH was removed [10]. However, the intracranial catheter method has two major limitations. 1) Due to the slow perfusion of the drug, the catheter must remain continuously inserted in the clot for 3-7 days to achieve adequate liquefaction and evacuation of the clot creating the potential for secondary injury associated with the residual clot. This is especially true for larger clots. 2) The recurrence of bleeding due to the thrombolytic irrigation is a significant risk with the potential for inducing hematoma enlargement [11].

1.3 Treatment Options Under Investigation

A low-profile, aspiration-irrigation system recently approved by the US Food and Drug Administration (FDA) has recently been adopted for use in treating ICH (Apollo™ System). The system uses a combination of vibrational energy, irrigation and suction to remove the ICH. This system has an advantage over the intracranial catheter technique in that it avoids prolonged irrigation with thrombolytic drugs, reducing treatment times and adverse side-effects associated with thromolytics (e.g., re-bleeds). However, although this device claims “immediate” treatment, only about 50% of the clot volume is removed with patients remaining in the hospital an average of 15 days after symptom onset and no significant improvement in patient outcome [11]. Thus, the outcomes for patients with large clots (> 60 mL) and effects associated with secondary injury remain a concern.

Magnetic resonance guided focused ultrasound (MRgFUS) is a FUS technique that uses a thermal mechanism to deliberately kill tissue at a precise focal point and MR imaging to correct for skull- or tissue-induced acoustic aberration and monitor the efficacy of the treatment. MRgFUS has also been investigated as a potential ICH treatment technique and has shown the ability to liquefy clots through the skull in animal and human cadaver studies by increasing the temperature of the target clot by approximately 6 °C which is thought to cause mechanical breakdown of the clot via inertial cavitation [12], [13]. The resulting liquid can then be aspirated out with a drainage catheter inserted through a bur hole in the skull. This provides a minimally invasive alternative for ICH treatment that does not use thrombolytic drugs and provides much faster liquefaction than the current clinical treatments (~40 mL in 3 hours). However, due to the mechanism of liquefaction, skull overheating results from the applied ultrasound pulses owing to their relative long duration (100 µs) and high duty cycle (10%). As a result, MRgFUS has not been able to treat clots greater than 40 mL or regions within 2 cm of the skull, thus excluding the large volumes most detrimental to patient outcome (> 60 mL) and ~80% of the brain cortex region where clots can form [12]–[16]. Theoretically, MRgFUS systems should be capable of reducing the pulse length and moderately increasing the amplitude to achieve boiling histotripsy, a FUS regime that allows cavitation clouds to be generated at much lower pressures than intrinsic threshold histotripsy. Such a parameter change may be better suited to clot liquefaction and reduced skull heating. However, such studies have not yet been performed. Regardless of the parameters used, the requirement for MR guidance adds significant cost and complexity to the process of treating ICH via MRgFUS and hinders its potential for widespread clinical use.

1.4 Mechanism of Histotripsy Therapy

Histotripsy uses short (≤ 2 cycles or ≤ 4µs at 500kHz), high energy pulses at a very low duty cycle (< 0.1%) to generate cavitation microbubble clouds and corresponding lesions using the intrinsic threshold cavitation nucleation method (Fig. 1A & B). In this method, cavitation is generated when the peak-negative pressure directly exceeding the threshold intrinsic to the target media to excite the pre-existing nuclei in the target tissue (26 MPa) [17]–[20]. The rapid and energetic expansion and collapse of the generated cavitation bubbles create high stress and strain in the clot at the therapy focus that fractionates it into an acellular homogenate [21] (Fig. 1C). Histotripsy clot liquefaction has been demonstrated in deep vein thrombosis models both *in-vitro* and *in-vivo* [22], [23]. Histotripsy and boiling histotripsy have been used for treatment in an *in-vitro* large extravascular blood clot model [24]. Additionally, the *in-vitro* feasibility of histotripsy as a transcranial therapy has been investigated [25], [26].

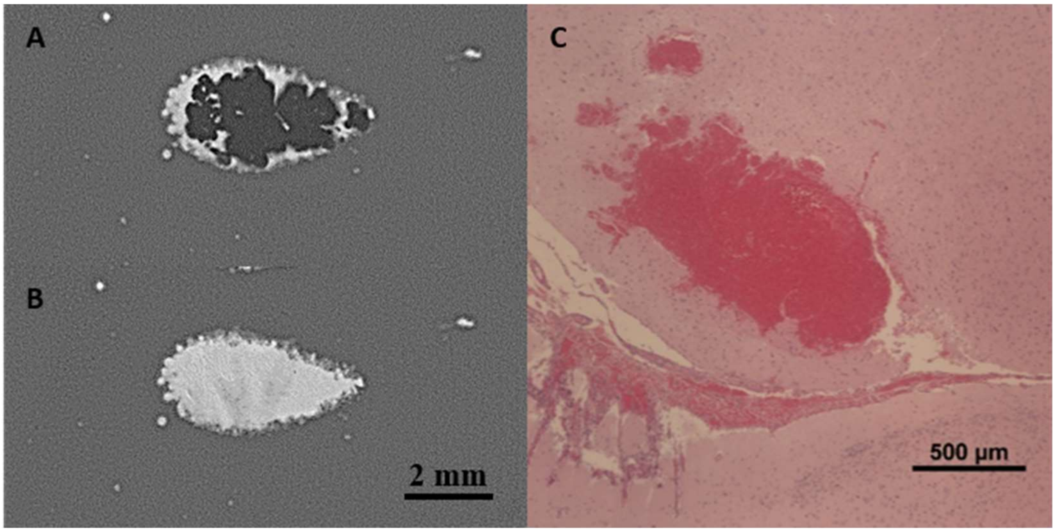

Figure 1.1. (A) A cavitation “bubble cloud” generated with a 500 kHz histotripsy pulse in a red blood cell (RBC) tissue mimicking phantom and (B) the lesion corresponding to the mechanical

disruption of the “bubble cloud”. (C) A lesion generated with histotripsy in an *in vivo* mouse brain.

1.5 Transcranial Histotripsy for the Treatment of ICH and Other Brain Pathologies

FUS techniques are currently the most promising concepts proposed for ICH treatment in that they a) avoid craniotomy (and thus any associated damage to healthy brain tissue), b) provide fast treatment and c) avoid the use of thrombolytic drugs that can induce re-bleeding. However, the only FUS technique proposed for ICH treatment up to this point, MRgFUS, is limited in that it is unable to treat large volumes (> 40 mL) and regions outside the center of the brain (≤ 2 cm from the skull surface) due to skull overheating, and requires continuous MRI monitoring, thus hindering its adoption for widespread clinical use. Histotripsy has potential advantage over MRgFUS in treating ICH as it has potential to overcome these limitations. By using extremely short pulses (microsecond duration) and a low duty cycle (≤ 0.1%) to minimize skull heating, we hypothesize that histotripsy can improve the treatment speed, expand the spatial treatment range to regions closer to the skull surface (≤ 2 cm) and liquefy large clot volumes (> 40 mL).

The ICH liquefied with histotripsy can be drained via catheter inserted through a small hole in the skull. This allows removal of liquefied clot with minimal collateral damage. Thus it is hypothesized that the catheter can be integrated with a miniature acoustic hydrophone (catheter hydrophone) that can be used to simultaneously correct the ultrasound distortion through the skull and precisely localize the ultrasound focus to the tip of the catheter. With the development of the catheter hydrophone and the use of already existing neuronavigation techniques (e.g., Medtronic Stealth Station) to co-register the physical location of the skull in the histotripsy array transducer with the pretreatment CT scan used to diagnose the ICH, the need for MRI can be overcome, with only the insertion of a catheter necessary to target, treat and drain the liquefied volume. This allows the potential for histotripsy to be applied in a standalone system and thus increases the potential for adoption of histotripsy into widespread clinical use.

1.6 Transcranial Histotripsy Ablation for Other Brain Pathologies

The transcranial volume ablation capabilities of histotripsy can likely be translated to minimally invasive or noninvasive ablation of other brain pathologies like cancer (solid tumors). For certain brain tumors with clearly demarcated boundaries (e.g., meningioma), transcranial ablation with histotripsy may be able to aid neurosurgeons in their ability to de-bulk the tumor and surgically resect it with minimal damage to surrounding healthy brain tissue. For other brain tumors with a more diffuse structure (e.g., glioblastoma), transcranial ablation using histotripsy may be able to be combined with immunotherapy methods to stimulate an anti-tumor immune response via the body's own immune system.

1.7 The Potential for Cancer Immunotherapy Combined with Histotripsy Ablation

The intention of cancer immunotherapy is to stimulate the body's own immune system to recognize the cancer and mount an anti-cancer response against it [27]. This is done via the activation of specific immunity. A primary challenge in stimulating specific immunity is the innate inability to differentiate the cancerous tumor from normal, healthy tissue. Recent scientific studies have revealed that the detection of tumor specific neoantigens plays an important role in immune therapy [28]. Under normal physiological conditions, such neoantigens are "hidden" from immune surveillance.

Both ultrasound and radiofrequency ablation modalities have been combined with cancer immunotherapy [29], [30]. The intention with ablating tumors while administering immunotherapy methods is that ablation of the solid tumor can disrupt and destroy the cell membranes and expose tumor debris and antigens to the host immune system *in vivo*. This is thought to boost the immunogenicity of the tumor and enhance the effect of immunotherapy techniques. However, traditional ultrasound ablation and radiofrequency ablation rely on thermal necrosis of the tumor via targeted deposition of energy via thermal absorption. Although thermal necrosis eventually breaks down the cell membrane, its ability to preserve the true nature of tumor debris and antigens may be limited. This is because the heat deposited may denature important immunologically relevant proteins. In contrast to such heat-based ablation methods, cryoablation is a method of ablating tissue that applies low temperatures to freeze tissue. This has shown evidence of immune modulation with the ability to preserve the nature of important intracellular proteins.

Due to its non-thermal, mechanically based mechanism for cell destruction, histotripsy may be better suited to generate tumor debris and expose the viable intracellular contents of tumor cells to the host immune system. Thus, it is hypothesized that histotripsy ablation of the tumor can significantly increase the tumor immunogenicity and enhance the potency of immunotherapy methods to stimulate an immune response against the tumor.

1.5 Outline of this Dissertation

This dissertation is comprised of eight chapters that document the details of the work done on the investigation and development of histotripsy therapy for the treatment of intracerebral hemorrhage and other transcranial applications.

Chapter 2 demonstrates the initial feasibility of liquefying blood clots through the human skull. Histotripsy pulses were delivered using two 256-element hemispherical transducers of different frequency (250 and 500 kHz) with 30 cm aperture diameters. A 4 cm diameter spherical volume of *in-vitro* blood clot was treated through three excised human skullcaps by electronically steering the focus through the target volume. Individual foci in the steering volume were spaced in intervals proportional to the acoustic wavelength (λ/2, 2λ/3 and λ) and 50 therapy pulses were delivered at ach steering location. Histotripsy pulses were delivered at a pulse repetition frequency (PRF) of 200 Hz, corresponding to a duty cycle of 0.08% (250 kHz) and 0.04% (500 kHz) for each focal location. Skull heating during treatment was monitored via thermocouples embedded into the skull bone. Treatment durations ranged from 0.9 – 42.4 minutes, after which the resulting liquefied clot volumes (which ranged from 6 – 59 mL, depending on treatment) could be drained via catheter and syringe. The fastest rate was 16.6 mL/min. The best parameter combination was λ spacing at 500 kHz which produced large liquefaction volumes through three skullcaps (23.1 ± 4.0, 37.1 ± 16.9 and 25.4 ± 16.9 mL) with the fast rates (3.2 ± 0.6, 5.1 ± 2.3 and 3.5 ± 0.4 mL/min). The therapy-induced temperature rise in the skull bones remained below 4 °C during all treatments.

Chapter 3 investigates the initial safety concerns of histotripsy mediated clot liquefaction and aspiration in a porcine ICH model. 1.75 mL clots were formed in the frontal lobe of the brain (N=18). Animals were divided into 3 treatment groups (n=6/group); in groups 2) and 3) clots were liquefied with histotripsy 48 hours after formation – following treatment the liquefied clot was either aspirated (group 2) or left in place (group 3); no treatment was delivered to the clots in group 1, which served as the control group. The centers of clots were liquefied with histotripsy 48 hours after formation and the content was either evacuated or left within the brain. A control group was left untreated. Pigs underwent MRI 7-8 days post clot formation and were subsequently euthanized. Neurological behavior was assessed throughout the survival period. Histological analysis was performed on harvested brains. A separate subset of pigs was euthanized ≤6 hr after treatment to investigate the acute effects of treatment. Histotripsy was able to liquefy the center of clots without direct damage to the perihematomal brain tissue. An average volume of 0.9±0.5 mL was drained after histotripsy treatment. All groups showed mild ischemia and gliosis in the perihematomal region, however, there were no deaths or signs of neurological dysfunction in any groups.

Chapter 4 demonstrates the proof-of-concept for using a novel catheter hydrophone device to both perform aberration correction through a human skull and drain the clot liquefied with histotripsy following treatment. A custom hydrophone was fabricated using a 0.5 x 0.5 x 0.3 mm PZT-5h crystal interfaced to a coaxial cable and integrated into a drainage catheter. An aberration correction algorithm was developed to correct the aberrations introduced between histotripsy pulses from each array element. Increases in focal pressure of up to 60% were achieved at the geometric focus and 27 – 62% across a range of electronic steering locations.

Chapter 5 investigates a strategy to allow the catheter hydrophone insertion through a burr hole in the skull and to experimentally evaluate the performance of the aberration correction using the catheter hydrophone after insertion. The insertion was done by designing and building a catheter holder that replaced one of the modular array elements in the histotripsy transducer and allowed the catheter hydrophone to be guided through the transducer and a burr hole in the skull to the transducer focus. Using the catheter hydrophone with this insertion strategy, measurements of the phase aberrations made using the device, and ensuing corrections of them, allowed pressures to be recovered up to 85.6% of those achieved following ideal aberration correction using a commercial hydrophone. This corresponded increases in the peak-negative pressure (compared to the no-aberration correction case) of up to 56.2% which correspondingly resulted in increases of the achievable liquefaction volume (for a fixed input power to the array) of up to 312%.

Chapter 6 provides details on the development of a pre-clinical histotripsy array prototype for the treatment of ICH in human cadaver models. A 360-element, 700 kHz hemispherical array with a 30 cm aperture was designed and integrated with an optical tracker surgical navigation system. Calibrated simulations of the transducer suggest an effective therapeutic target volume of between 48 – 105 mL through the human skull with the ability to apply therapy pulses at pulse-repetition-frequencies up to 200 Hz. The navigation system allows targeting real-time targeting and placement of the catheter hydrophone via a pre-operative CT or MRI.

Chapter 7 investigates the immune response of a mouse GL261 intracranial glioma model after histotripsy ablation of a fraction of an intracranial GBM. A total of 27 male mice were inoculated with GBM according to a GL261-luc2 C57 BL/6 albino mouse model protocol. Tumor monitoring was performed using T2-weighted MRI and bioluminescence imaging. Histotripsy treatment was applied to a portion of the tumor in 15 of the 27 mice. The remaining 12 were left untreated as controls. Directly following euthanasia in both treatment and control mice, brain tumors, spleens and lymph nodes were harvested for flow cytometry. In addition, for both groups, immunohistochemistry staining was performed on the primary tumor. Flow cytometry results yielded a two-fold decrease ($\alpha = 0.05$) in the number of myeloid derived suppressor cells (MDSCs) in the brain tissue of mice treated with histotripsy relative to that of the control mice. Additionally, a large increase in interferon gamma (IFN-γ) was observed in mice treated with histotripsy. Giemsa staining of sections of brain tumors from treated mice, sampled from regions away from the histotripsy lesion, showed shrunken cells with shrunken and pyknotic nuclei separated by edema with insufficient cells to assess the mitotic index. This contrasted with the sections of brain tumors from control mice where intact tumor cells and a high mitotic index were observed.

Chapter 8 summarizes the findings and contributions of this dissertation and provides a discussion on the future work needed in developing histotripsy therapy for ICH and other transcranial applications.

1.6 References

[1] J. P. Broderick, T. G. Brott, J. E. Duldner, T. Tomsick, and G. Huster, “Volume of intracerebral hemorrhage. A powerful and easy-to-use predictor of 30-day mortality,” *Stroke*, vol. 24, no. 7, pp. 987–993, 1993.

[2] M. L. Flaherty *et al.*, “Long-term mortality after intracerebral hemorrhage,” *Neurology*, vol. 66, no. 8, pp. 1182–1186, 2006.

[3] D. Mozaffarian *et al.*, “Executive summary: Heart disease and stroke statistics-2016 update: A Report from the American Heart Association,” *Circulation*, vol. 133, no. 4. pp. 447–454, 2016.

[4] E. V. Kuklina, X. Tong, M. G. George, and P. Bansil, “Epidemiology and prevention of stroke: A worldwide perspective,” *Expert Review of Neurotherapeutics*, vol. 12, no. 2. pp. 199–208, 2012.

[5] G. Xi, R. F. Keep, and J. T. Hoff, “Mechanisms of brain injury after intracerebral haemorrhage.,” *Lancet. Neurol.*, vol. 5, no. 1, pp. 53–63, 2006.

[6] A. I. Qureshi, S. Tuhrim, J. P. Broderick, H. H. Batjer, H. Hondo, and D. F. Hanley, “Spontaneous Intracerebral Hemorrhage,” *N. Engl. J. Med.*, vol. 344, no. 19, pp. 1450–1460, 2001.

[7] L. B. Morgenstern, A. M. Demchuk, D. H. Kim, R. F. Frankowski, and J. C. Grotta, “Rebleeding leads to poor outcome in ultra-early craniotomy for intracerebral hemorrhage,” *Neurology*, vol. 56, no. 10, pp. 1294–1299, 2001.

[8] T. Morgan, M. Zuccarello, R. Narayan, P. Keyl, K. Lane, and D. Hanley, “Preliminary findings of the minimally-invasive surgery plus rtPA for intracerebral hemorrhage evacuation (MISTIE) clinical trial,” *Acta Neurochir. Suppl.*, no. 105, pp. 147–151, 2008.

[9] D. F. Hanley *et al.*, “Safety and efficacy of minimally invasive surgery plus alteplase in intracerebral haemorrhage evacuation (MISTIE): a randomised, controlled, open-label, phase 2 trial,” *Lancet Neurol.*, vol. 15, no. 12, pp. 1228–1237, 2016.

[10] D. F. Hanley *et al.*, “Efficacy and safety of minimally invasive surgery with thrombolysis in intracerebral haemorrhage evacuation (MISTIE III): a randomised, controlled, open-label, blinded endpoint phase 3 trial,” *Lancet*, Feb. 2019.

[11] A. M. Spiotta *et al.*, “Initial multicenter technical experience with the apollo device for minimally invasive intracerebral hematoma evacuation,” *Oper. Neurosurg.*, vol. 11, no. 2, pp. 243–251, 2015.

[12] S. J. Monteith *et al.*, “Minimally invasive treatment of intracerebral hemorrhage with magnetic resonance–guided focused ultrasound,” *J. Neurosurg.*, vol. 118, no. 5, pp. 1035–1045, 2013.

[13] S. J. Monteith, N. F. Kassell, O. Goren, and S. Harnof, “Transcranial MR-guided focused ultrasound sonothrombolysis in the treatment of intracerebral hemorrhage,” *Neurosurg. Focus*, vol. 34, no. 5, p. E14, 2013.

[14] S. Monteith *et al.*, “Potential intracranial applications of magnetic resonance–guided focused ultrasound surgery,” *J. Neurosurg.*, vol. 118, no. 2, pp. 215–221, 2013.

[15] C. Wright, K. Hynynen, and D. Goertz, “In vitro and in vivo high intensity focused ultrasound thrombolysis,” *Invest. Radiol.*, vol. 47, no. 4, pp. 217–225, 2012.

[16] M. Ramanan and a Shankar, “Minimally invasive surgery for primary supratentorial intracerebral haemorrhage,” *J. Clin. Neurosci.*, vol. 20, no. 12, pp. 1650–1658, 2013.

[17] Z. Xu *et al.*, “Controlled ultrasound tissue erosion,” *IEEE Trans. Ultrason. Ferroelectr. Freq. Control*, vol. 51, no. 6, pp. 726–736, 2004.

[18] Z. Xu, J. B. Fowlkes, E. D. Rothman, A. M. Levin, and C. A. Cain, “Controlled ultrasound tissue erosion: The role of dynamic interaction between insonation and microbubble activity,” *J. Acoust. Soc. Am.*, vol. 117, no. 1, pp. 424–435, 2005.

[19] W. W. Roberts, T. L. Hall, K. Ives, J. S. Wolf, J. B. Fowlkes, and C. A. Cain, “Pulsed cavitational ultrasound: A noninvasive technology for controlled tissue ablation (histotripsy) in the rabbit kidney,” *J. Urol.*, vol. 175, no. 2, pp. 734–738, 2006.

[20] Z. Xu, G. Owens, D. Gordon, C. Cain, and A. Ludomirsky, “Noninvasive creation of an atrial septal defect by histotripsy in a canine model,” *Circulation*, vol. 121, no. 6, pp. 742–749, 2010.

[21] K. W. Lin *et al.*, “Histotripsy beyond the intrinsic cavitation threshold using very short ultrasound pulses: Microtripsy,” *IEEE Trans. Ultrason. Ferroelectr. Freq. Control*, vol. 61, no. 2, pp. 251–265, 2014.

[22] A. D. Maxwell, G. Owens, H. S. Gurm, K. Ives, D. D. Myers, and Z. Xu, “Noninvasive treatment of deep venous thrombosis using pulsed ultrasound cavitation therapy (histotripsy) in a porcine model,” *J. Vasc. Interv. Radiol.*, vol. 22, no. 3, pp. 369–377, 2011.

[23] A. D. Maxwell, C. A. Cain, A. P. Duryea, L. Yuan, H. S. Gurm, and Z. Xu, “Noninvasive Thrombolysis Using Pulsed Ultrasound Cavitation Therapy - Histotripsy,” *Ultrasound Med. Biol.*, vol. 35, no. 12, pp. 1982–1994, 2009.

[24] T. D. Khokhlova, W. L. Monsky, Y. A. Haider, A. D. Maxwell, Y. N. Wang, and T. J. Matula, “Histotripsy liquefaction of large hematomas,” *Ultrasound Med. Biol.*, vol. 42, no. 7, pp. 1491–1498, 2016.

[25] Y. Kim, T. Hall, Z. Xu, and C. Cain, “Transcranial histotripsy therapy: A feasibility study,” *IEEE Trans. Ultrason. Ferroelectr. Freq. Control*, vol. 61, no. 4, pp. 582–593, 2014.

[26] J. R. Sukovich *et al.*, “Targeted Lesion Generation Through the Skull Without Aberration Correction Using Histotripsy,” *IEEE Trans. Ultrason. Ferroelectr. Freq. Control*, vol. 63, no. 5, pp. 671–682, 2016.

[27] J. N. Blattman and P. D. Greenberg, “Cancer immunotherapy: A treatment for the masses,” *Science*, vol. 305, no. 5681. pp. 200–205, 2004.

[28] T. N. Schumacher and R. D. Schreiber, “Neoantigens in cancer immunotherapy,” *Science*, vol. 348, no. 6230. pp. 69–74, 2015.

[29] J. Unga and M. Hashida, “Ultrasound induced cancer immunotherapy,” *Advanced Drug Delivery Reviews*, vol. 72. pp. 144–153, 2014.

[30] F. F. Fagnoni, A. Zerbini, G. Pelosi, and G. Missale, “Combination of radiofrequency ablation and immunotherapy.,” *Front. Biosci.*, vol. 13, pp. 369–81, 2008.

CHAPTER 2 Effect of Frequency and Focal Spacing on Transcranial Histotripsy Clot Liquefaction using Electronic Focal Steering

This chapter has been published in *Ultrasound in Medicine and Biology*. 2017; 43(10): 2302-2317.

2.1 Introduction

Intracerebral hemorrhage (ICH) accounts for 10-15% of all strokes and affects approximately two million people worldwide [2]–[4]. ICH is characterized by blood vessel rupture within the brain that leads to the formation of a blood clot therein. Due to its encasement by the skull, the formation of a blood clot within the brain causes an increase in intracranial pressure that can cause immediate injury to neurons and axons via mechanical distortion. In addition, the rise in intracranial pressures (ICP) and brain swelling leads to secondary injuries that can occur as the cerebral perfusion pressure (CCP) decreases. The extent of the ICP increase is dependent on the size of the ICH and is a significant factor in patient outcome. Further, delayed cerebral toxicity is caused by the degradation of remaining blood products. In general, patients diagnosed with ICH have a 30-day mortality rate of approximately 40% [5]. Large clots (30 to 60 mL) are even more detrimental to patient outcome [5]–[8]. This necessitates a fast and effective evacuation procedure for blood clots formed within the brain. The mainstay treatment for ICH is surgical evacuation via a craniotomy. Craniotomy provides a quick access to evacuate clots; however, the procedure remains highly invasive as normal brain tissue may need to be traversed to remove the clots. In fact, craniotomy surgery leading to removal of ICH has not been shown to improve the functional outcome or reduce the morbidity and this lack of effectiveness may be related to the injury caused to surrounding cerebral tissue [9]–[12].

Minimally invasive clot evacuation techniques have been developed to overcome the issues associated with craniotomy-based surgeries. Specifically, techniques using a catheter inserted through a small hole in the skull to deliver thrombolytic drugs, such as recombinant tissue plasminogen activator (rt-PA), to liquefy clots and aspirate the liquefied volume have been investigated. However, due to the slow perfusion of the thrombolytic drugs into the clot, the treatment typically takes 3-7 days with the catheter within the ICH for the entire duration thus requiring a lengthy intensive care unit (ICU) stay. These techniques are currently undergoing clinical investigation with early results revealing an ability to reduce clot size as well as ICH related edema [13]–[15]. However, the functional outcome of ICH survivors has not improved, likely due to the long treatment time required to liquefy and aspirate the volume. Additionally, although such techniques have reported up to a 50% reduction in clot size, this may not be sufficient for large clots, where a greater reduction may be necessary and cause treatment times to exceed what is clinically feasible (i.e., > 7 days). For smaller clots typical of ischemic stroke, thrombolytic drugs, such as rt-PA, have been administered with and without contrast agent microbubbles and clots have been insonated with low-amplitude ultrasound pulses to increase the efficacy and rate of clot liquefaction [16]–[20]. The combination of microbubbles and ultrasound has shown improved penetration of thrombolytic drugs into clots [21]. Although such increased penetration may be sufficient for treating smaller clots found with ischemic stroke, the penetration depth may still be a limiting factor for larger clots typical of ICH.

High intensity focused ultrasound (HIFU) techniques have been investigated for various brain applications. Magnetic resonance guided focused ultrasound (MRgFUS) is one particular technique that uses a thermal mechanism to deliberately kill tissue at a precise focal point and MR imaging to correct for the acoustic aberration and monitor the efficacy of the treatment. MRgFUS has established itself as a transcranial therapy and has had success in treating single spots in the brain for movement disorders such as essential tremor [22], [23]. MRgFUS has also been used to enhance drug delivery through blood brain barrier for treatment of brain tumors [24]–[26]. In addition, MRgFUS has been shown to thermally lyse clots through the skull in animal and human cadaver studies by increasing the temperature of the target clot by approximately 6 °C which is thought to cause mechanical breakdown of the clot via inertial cavitation [27], [28]. The resulting liquid can then be aspirated out with a drainage catheter inserted through a bur hole in the skull. This provides a minimally invasive alternative for ICH treatment that does not use thrombolytic drugs and provides much faster liquefaction than the current clinical treatments. However, due to skull overheating caused by the applied ultrasound ($\geq$100 μs at 10% duty cycle), MRgFUS has not been able to treat clots greater than 40 mL or regions within 2 cm of the skull, thus excluding ~80% of the brain cortex region where clots can form [27], [29]–[31]. Additionally, although MRgFUS has shown the capacity to accelerate clot reduction time (3 hours to liquefy up to 40 mL), the treatment time is still long relative to that needed for critical cases (i.e., patients with clots greater than 60 mL).

Histotripsy is another FUS technology currently being developed for ICH treatment. Histotripsy uses short ($\leq$ 2 cycles or $\leq$ 4μs at 500kHz), high energy pulses at a very low duty cycle (< 0.1%) to generate cavitation microbubble clouds transcranially using the intrinsic threshold method. In this method, cavitation is generated with the peak-negative pressure directly exceeding the threshold intrinsic to the target media to excite the pre-existing nuclei in the target tissue [32]–[35]. In water based tissues such as clots this threshold is about 27 MPa with little change expected at different frequencies [36]. The rapid and energetic bubble expansion and collapse of cavitation create high stress and strain in the clot at the focus that fractionates it into an acellular homogenate [37]. In contrast to other FUS techniques, the tissue destruction caused by histotripsy has been shown to be purely mechanical, with negligible thermal effects [38]. Histotripsy clot liquefaction has been demonstrated in deep vein thrombosis model both *in-vitro* and *in-vivo* [39], [40]. Recently, histotripsy and boiling histotripsy have been used for treatment in an *in-vitro* large extravascular hematoma model [41]. Additionally, the *in-vitro* feasibility of histotripsy as a transcranial therapy for brain tissue has been investigated [42], [43].

Similar to MRgFUS, histotripsy can be used to liquefy clot through the skull, and the liquefied clot volume can be drained via a catheter inserted into the clot through a small burr hole. By using extremely short pulses (microsecond duration) and a low duty cycle ($\leq 0.1\%$) to minimize skull heating, we hypothesize that histotripsy can overcome the limitations of MRgFUS to accelerate the treatment speed, widen the treatment location range to regions closer to the skull surface, and liquefy clots larger than 40 mL.

In this paper, the use of histotripsy with electronic focal steering for fast transcranial clot liquefaction is demonstrated. The specific emphasis was to analyze the effects of transducer frequency and focal spacing on treatment efficacy and speed. Frequency is an important treatment parameter as attenuation through the skull, lesion size and electronic focal steering range are all factors affected by the frequency of the applied treatment. Likewise, the focal spacing is another significant treatment parameter as the spacing between individual points in a given treatment region affects the overall lesion, the number of treatment points and thus treatment speed. Frequency and focal spacing were chosen as the studied variables as it was expected that these variables had the largest potential to significantly reduce treatment time for the treatment of a given volume of clot. By making the focal spacing proportional to frequency and studying the effects of frequency and focal spacing we were able analyze treatment across a large range of treatment times. In addition, because the skull is highly absorbing and skull heating is a major issue limiting transcranial ultrasound therapy, the temperature rise in the skull during histotripsy treatment was measured.

2.2 Materials and Methods

2.2.1 Phased Array Histotripsy Transducers

Two different 256-element hemispherical ultrasound transducer arrays both with 15 cm focal distance were used in this study. The center frequencies were 250 kHz and 500 kHz. The arrays were built in-house according to methods similar to those described in [42]. The transducer elements populating the array were comprised of two 20 mm diameter flat, stacked piezo ceramic (PZ36) disc elements. The 256 transducer elements were used to populate a hemispherical scaffold, filling the entirety of the scaffold except for the most central region of the scaffold, in which there were no elements. Each transducer array was positioned into a tank of degassed water at room temperature. A 256-channel high voltage pulser capable of delivering short bursts was used to drive the elements of each array. The timing of the pulsers was controlled by a custom digital signal generator programmed through MATLAB (MathWorks, Natick, MA, USA) allowing independent control of each element of the array and the generation of complex synchronized pulsing patterns. The transducer was calibrated using a fiber optic hydrophone (FOPH) built in-house [44]. For measurements above the intrinsic threshold, cavitation exists 100% of the time and peak-negative pressures near or beyond 27 MPa cannot be measured. However, as the calibrations were performed in degassed water, there is a low probability of the occurrence of “incidental cavitation bubbles” in this media at pressures above 20 MPa [36]. Therefore, peak-negative pressure measurements beyond 20 MPa reported throughout this paper are estimated by linear summation of the peak-negative pressure amplitudes output by subsets of the individual transducer elements. This linear summation pressure extrapolation technique is only intended to serve as an indication of the probability of cavitation activity in the focal region and the *potential* pressure overhead available during treatment and not an accurate estimate of pressure *in situ*.

2.2.2 Sample Preparation

Skullcap Preparation: In all experiments, histotripsy was applied to the target blood clot through an excised human skullcap in a degassed water tank. To analyze the variation in clot liquefaction across skullcaps, three excised human skullcaps obtained through the University of Michigan Anatomical Donations Program were used for each transducer frequency and focal spacing combination. The skullcaps were defleshed and cleaned after extraction and continuously kept in either water or a bleach-water solution of up to a 5% concentration thereafter. The bleach was added to keep algae or bacteria from growing on the surface of the skullcap and the walls of the storage container. This accumulation of algae was noticed during storage of skulls during the duration of the 500 kHz treatments and the water required frequent replacement. The bleach-water storage solution was implemented around the time which the 250 kHz experiments began. Prior to experiments, the skullcaps were degassed inside a vacuum chamber for a minimum of one week. The measured dimensions and acoustic properties of the three skullcaps used in these experiments can be found in Table 2.1. The thickness, long and short axis and depth dimensions of the skullcaps were measured using 3D laser scans (Ultra HD 2020i, NextEngine, Santa Monica, California) of each skullcap. Attenuation and sound speed measurements were obtained by using a PVDF capsule hydrophone (HGL200, Onda, Sunnyvale, CA, USA) to measure the pressure and time of flight from individual elements of each array with and without the skullcap concentrically placed within the array. Using the 3D laser scans of each skullcap, the skullcap was mapped into 256 discrete thickness values that corresponded to the region of skull centered around the ray from each element. The attenuation was calculated using the decrease in peak negative pressure due to the presence of the skullcap. The speed of sound was calculated from the change in arrival time due to the presence of the skullcap.

Red Blood Cell (RBC) Phantom Preparation: RBC phantoms were used to analyze the lesion generation with electronic focal steering through excised human skullcaps. Phantoms were prepared from an agarose-saline mixture and RBCs according protocols previously established by our lab [45]. These phantoms consisted of three layers: a thin (~500 µm) RBC-agarose gel layer between two thicker (~10 mm) transparent agarose gel layers. As the RBC-agarose gel layer changed from translucent and red to transparent and colorless following the destruction of the RBC layer that resulted from cavitation, the phantom provided good contrast for visualizing cavitation damage.

Blood Clot Preparation: In vitro blood clots of 5 cm in diameter were made with bovine blood harvested from a local abattoir. Upon harvesting, the blood mixed with citrate phosphate dextrose (CPD) (Boston Bioproducts, Ashland, MA, USA) with a CPD-to-blood ratio of 1:9 (v:v) to prevent it from clotting. The blood was stored at 4 °C prior to use. All blood was used within two weeks of harvesting. 78 mL clots were prepared by mixing 75 mL of degassed bovine blood and 3 mL of calcium chloride (#21107, Sigma-Aldrich Co., St. Louis MO, USA) for a final concentration of 20 mM/L. The 78 mL blood/$CaCl_2$ mixture was poured into a latex condom and tied off to form a ~5 cm diameter spheroidal volume. Once sealed, the condoms were placed into a water bath kept at 38.6 °C for 6 hours to solidify. Solidified clots were transferred to a refrigerator at 4 °C for 12 hours prior to treatment. Before treatment, clots were allowed to warm to room temperature (i.e., 23 °C).

Table 2.1. The measured dimensions and acoustic properties of the three skullcaps.

	Major Dimensions (mm)			Thickness (mm)			Acoustic Properties		
Skull #	Long Axis	Short Axis	Depth	Min	Max	Mean	250 kHz Attenuation (dB/cm)	500 kHz Attenuation (dB/cm)	Sound Speed (m/s)
1	161	139	58	2.1	8.5	5.1 ± 1.3	14.4 ± 5.2	20.4 ± 6.6	2063 ± 402
2	173	145	63	3.7	10.4	7.0 ± 1.5	11.4 ± 4.3	11.7 ± 3.4	1991 ± 210
3	183	143	64	2.6	11.1	6.5 ± 1.3	14.6 ± 7.7	14.5 ± 4.5	2340 ± 354

2.2.3 Aberration Correction

Aberration correction was performed to recover the pressure lost due to the temporal defocusing through each skullcap. There was less concern in correcting the attenuation induced amplitude variation across the skullcap as lesion formation with intrinsic threshold histotripsy relies primarily on the focal region over which the pressure is above the intrinsic threshold. In fact, precision lesion formation through the skull using histotripsy has been shown even without any aberration correction (Sukovich et al. 2016). The purpose of performing aberration correction here was primarily to increase the pressure overhead for treatment with electronic focal steering. The skullcaps were fixed concentrically within the array and aligned so that the anterior and posterior, and left and right edges were equidistant from the interior of the array. The skullcaps were positioned into the array such that the geometric origin of the array was 10 mm into the skullcap relative to the cut-plane of the skullcap. A PVDF capsule hydrophone was positioned at the geometric origin of the array. The 256 array elements were triggered sequentially and the respective waveforms delivered through the skullcap were measured by the hydrophone. Using the difference in the arrival time of the peak-negative pressure for each element waveform, the delays required to realign the arrival of the peak-negative pressure for all 256 element waveforms were calculated and uploaded to the FPGA boards. The delay measurement performed at the single point was applied as a constant temporal offset for all phased steering locations within the treatment volume. These single location aberration correction delays were used for all electronic steering locations because a similar approach is intended to be used in future *in-vivo* and clinical treatment.

2.2.4 Focal Characterization through the Skullcaps

Following aberration correction, the ultrasound field produced at each frequency through each skullcap was characterized. This was done by obtaining the one-dimensional (1D) pressure profile along the 3 axes of the skullcaps and measuring pressure as a function of electronic focal steering through each skullcap.

Beam Profiles: To characterize the extent of focusing through each skullcap at 250 and 500 kHz, 1D beam profiles around the geometric focus were obtained with the skullcap positioned in the array. Beam profiles were measured at low pressure (i.e., < 2 MPa) using a PVDF capsule hydrophone. The hydrophone was positioned to the focus and scanned ± 25 mm from the geometric origin in 0.25 mm steps along the sagittal, coronal and axial axes. As intrinsic threshold histotripsy is dependent on the peak-negative pressure, beam profiles were constructed in reference to the peak-negative pressure at each hydrophone position. For each skull and frequency, the -6 dB beam width along each axis was measured.

Pressure vs. Electronic Focal Steering: To understand electronic focal steering through each skullcap at each frequency, the focal pressure as a function of electronic focal steering location was measured across a ± 20 mm range of locations centered at the geometric origin. The array was steered in 1 mm steps in the sagittal, coronal and axial dimension. For each steering location a PVDF capsule hydrophone was positioned to the location and used to measure the peak-negative pressure. To ensure the hydrophone was not damaged, the array was run at a low pressure amplitude for these measurements (i.e., < 2 MPa).

Lesion Generation with Electronic Focal Steering: To show the ability of histotripsy to precisely generate lesions through the skullcap, a 9 × 9 grid of lesions was generated transcranially in an RBC phantom. The RBC-agarose gel layer of the phantom was positioned in plane with the sagittal-coronal plane of the array. The grid was designed such that greatest steering distance was ± 10 mm from the geometric origin and individual focal points were separated by 2.5 mm steps in both the sagittal and coronal direction. Using the 500 kHz array and electronic focal steering, 81 steering locations were targeted. Lesions were generated by applying 200 histotripsy pulses to each focal point at an extrapolated peak-negative pressure of 36 MPa as measured through the skullcap at the geometric origin of the array. Pulses were applied at a pulse repetition frequency (PRF) of 0.5 Hz. After generating lesions within the RBC phantom, the phantom was placed on a light table and imaged with a DSLR camera (Canon, Tokyo, Japan).

2.2.5 Histotripsy Treatment

To evaluate histotripsy for clot liquefaction through the skullcap, clots were mounted within the skullcap and the center of the clot volume was aligned with the geometric origin of the array (Fig. 2.1). This positioning of the clot within the skullcap aligned with the findings that the majority of ICH cases occur in the central region of the brain [46], [47]. Using electronic focal steering, the focus of the array was steered through a 4 cm diameter spherical volume. The volume was filled with individual focal points according to a standard hexagonal-closed-packed (HCP) lattice pattern. Although low in f-number, the focus of these transducer arrays was not spherical.

Instead it was cigar shaped, with a longer axial dimension than transverse dimensions, although generated based on spherical foci, the HCP lattice pattern provided the most efficient focal point packing for volume treatment using histotripsy. This produced to a treatment volume of 33.5 mL, which corresponded well with the average clot volume for various clinical ICH studies and marked a volumetric tipping at which patient outcomes begin to correspond to a 50% or greater probability of death within 30 days of diagnosis [6], [48], [49]. For each frequency, the lattice focal point spacing was set to different fractions of a wavelength, specifically: λ/2, 2λ/3 and λ. Each treatment was applied at an overall pulse repetition frequency (PRF) of 200 Hz with 50 histotripsy pulses applied to each treatment location, corresponding to a duty cycle of 0.08% for 250kHz and 0.04% for 500kHz. To ensure intrinsic threshold histotripsy the pulse length was kept short (≤ 2 acoustic cycles or $\leq 4\mu$s at 500 kHz and ≤ 8 μs at 250 kHz). The intrinsic threshold within the clots was expected to be consistent between frequencies (i.e., about 27 MPa) [36]. The number of pulses per point was chosen to minimize the number of total pulses while providing effective lesion generation. Based on previous studies, using 50 pulses per point provides well-defined lesion formation at pressures in excess of the intrinsic threshold [37]. In choosing the PRF, we wanted to choose the fastest overall repetition rate that kept the PRF for a single location less than 1 Hz to avoid the cavitation memory effect described previously [50]. Since the minimum number of points to fill the treatment volume across parameter combinations was 217 points, an overall PRF of 200 Hz satisfied this requirement. Estimated linear extrapolated peak-negative pressures applied through the skullcaps of 35 and 70 MPa were used for the 250 and 500 kHz array, respectively. These different pressures were used to achieve approximately equivalent pressures at the periphery of the treatment region (i.e., furthest steering location from the geometric focus) at the two different frequencies. The peak-negative pressure at the periphery of the treatment region was in the range of 50-83% and 20-64% of the focal peak-negative pressure (i.e., geometric focus) for the 250 and 500 kHz treatment, respectively. The total clot volume liquefied with histotripsy was measured posttreatment by inserting the catheter into the clot and drawing off the liquefied volume using a 10 mL syringe. To ensure the reported drainage volumes corresponded to that resulting from histotripsy treatment only, 12 control clots, unexposed to histotripsy were drained using the same technique (control volume). The effective clot volume liquefied by histotripsy (liquefaction volume) with each frequency and focal spacing combination was calculated as the volume aspirated via the catheter minus the control volume. For each frequency and focal spacing combination, 6 clots were treated.

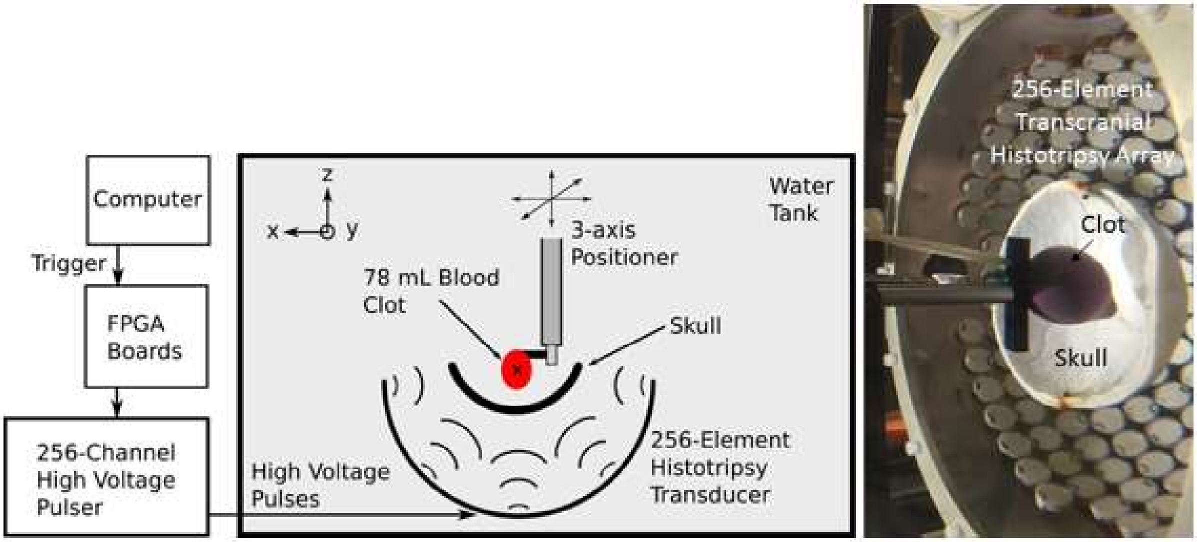

Figure 2.1. The experimental schematic of the setup used to perform the transcranial histotripsy clot treatments through the excised human skullcaps (left) and a photograph of the actual experimental setup (right). The blood clots were mounted within the skullcap and the center of the clot volume was aligned with the geometric origin of the array.

2.2.6 Gross Morphology and MRI

The gross morphology of blood clots was analyzed pre and post treatment by cutting a control, treated undrained and treated drained clot in half. The clots were imaged using a DSLR camera. T2-weighted MR images of the clots pre and post treatment were also obtained using a 7T

MRI scanner (Varian, Inc., Palo Alto, CA, USA). The clot images were captured using a fast spin-echo (FSE) sequence.

2.2.7 Skullcap Temperature Monitoring

To measure the temperature-rise of each skullcap during histotripsy treatment, four thermocouples (K-094, Physitemp Instruments Inc, Clifton, NJ, USA) were embedded directly into bone via holes slightly smaller than the thermocouple diameter such that bone made direct contact with the thermocouples. Thermocouples were positioned throughout each skullcap such that the locations were of varying thickness and gave a reasonable temperature distribution across each skullcap. Thermocouples were not positioned at the most superior portion of the skullcap as there were no elements within the central region of the array scaffold. Using the 500 kHz array, histotripsy was applied at an equivalent pressure and PRF as that used during the clot treatment experiments (i.e., 70 MPa and 200 Hz). Prior to treatment the skullcaps and surrounding water were at room temperature (23 °C). The temperature of the skullcap at each thermocouple location was measured and recorded for a total of 60 minutes. For each skullcap, histotripsy treatment was initiated approximately one minute after temperature monitoring started. Only the 500 kHz array and a 60-minute timespan were used as this was expected to show the most significant skull heating induced by histotripsy for the experiments in this paper. To approximate whether the temperature rise in the skullcaps was something capable of causing thermal damage to the skull and surrounding tissues, the average cumulative equivalent minutes at 43 °C (CEM_{43}) for each skullcap was calculated and compared with those CEM_{43} values reported to cause tissue damage. Since temperature monitoring was performed at room temperature (~ 20 °C) and not body temperature, the CEM_{43} values were calculated by adding a constant 37 °C offset to the average temperature change through each skullcap and using the equation provided in [51].

2.2.8 Post Hoc B-Mode Analysis of External Skull Surface during Treatment

To examine how histotripsy affected the external surface of a bleached skullcap during treatment with both the 250 and 500 kHz array, b-mode imaging of the surface of a bleached skull during treatment was performed following the initial set of experiments. A linear ultrasound probe (L-14, Ultrasonix, BK Ultrasound, Peabody, MA, USA) was inserted coaxially through the opening in the back of each array such that it was outside the sound field but sufficiently close to image the external surface of the skull. B-mode images were captured with the array off and on. This was done for both the 250 and 500 kHz array.

2.2.9 Statistical Analysis

In order to understand the relationship between the histotripsy clot liquefaction results obtained from the different treatment parameters and skullcaps used in this study, statistical analysis was performed. Three sets of independent, two-tailed, two-sample Student’s t-tests ($\alpha = 0.05$) were performed on the two main sets of data: volume drained due to histotripsy and the histotripsy clot liquefaction rate. The first set of t-tests analyzed the variation in results obtained between different focal spacing, holding the skullcap and frequency constant. The second set analyzed results obtained between different skullcaps holding focal spacing and frequency constant. The third set of t-tests analyzed the variation in results between different frequencies holding focal spacing and skullcap constant. By performing this set of multiple t-tests, we were able to analyze the volume liquefaction and rate effects of focal spacing for a given frequency, frequency for a given focal spacing and the variation across different skullcaps. Although comparisons between other parameter combinations was possible, the preceding analysis exhausted those comparisons pertaining to the design of the study. Any other comparisons made were post-hoc and performed after looking at the data. All comparisons made throughout this paper were considered statistically significant for p-value < 0.05.

2.3 Results

2.3.1 Focal Characterization through the Skullcaps

Beam Profiles: To characterize the extent of focusing through each skullcap using the 250 and 500 kHz arrays, 3-axis 1D beam profiles around the geometric focus were obtained with the skullcaps positioned in the array. Figure 2.2 shows the beam profiles at 250 and 500 kHz through skull 1. For a given frequency, the general shape of the profile was consistent through each skullcap. Along each axis, profiles at 250 kHz were more spatially spread than those at 500 kHz. The -6-dB beam widths along each axis for each skullcap and frequency are shown in Table 2.2.

Pressure vs. Electronic Focal Steering: To understand electronic focal steering through each skullcap with the 250 and 500 kHz array, the focal pressure as a function of electronic focal steering location was measured. Figure 2.3 shows the normalized peak-negative pressure as a function of electronic steering location for each skullcap at each frequency. For a given frequency the steering pressure profiles were similar for each skullcap. Along each axis, the pressure for the 500 kHz frequency decreased more rapidly than at 250 kHz, with the greatest differences in pressure occurring at the furthest steering locations from the geometric focus (i.e., ± 20 mm). The percentages for the average pressure decrease, across the three skullcaps, at -20 and +20 mm for each axis relative to the geometric focal pressure are show in Table 2.3. In general, at 500 kHz, the pressure decrease at the steering locations furthest from the geometric focus was approximately double that at 250 kHz.

Lesion Generation with Electronic Focal Steering: To show the ability of histotripsy to precisely generate lesions through the skullcap with electronic focal steering, lesions were generated transcranially in an RBC phantom at a range of steering locations. Figure 2.4 shows a 9 × 9 grid of lesions generated through a skullcap using electronic focal steering with the 500 kHz array. The distance between the center of each lesion was approximately 2.5 mm, which matched that specified with the applied electronic focal steering. Larger and distinct lesions were generated closer to the geometric origin while smaller, indistinct lesions were generated toward the corners of the grid beyond 10 mm from the geometric focus.

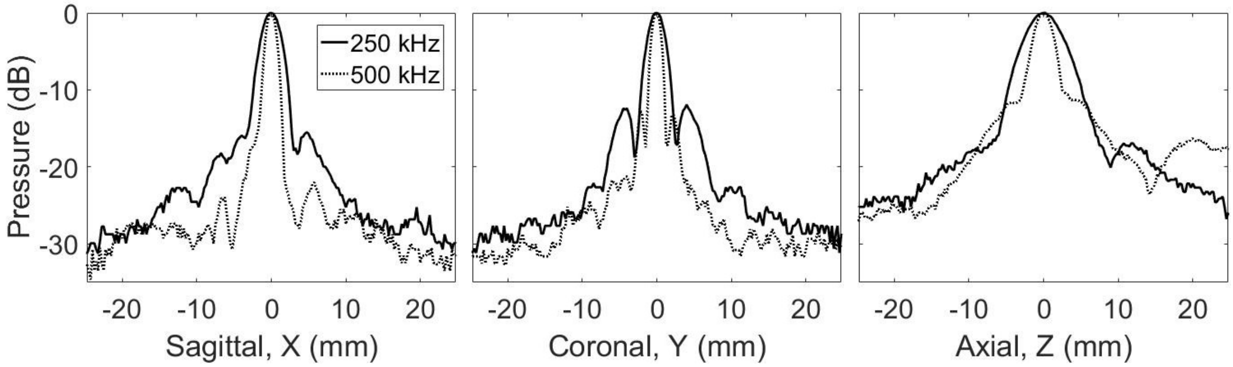

Figure 2.2. The 3-axis 1D beam profiles around the geometric focus through skull 1 positioned into the array obtained at 250 and 500 kHz.

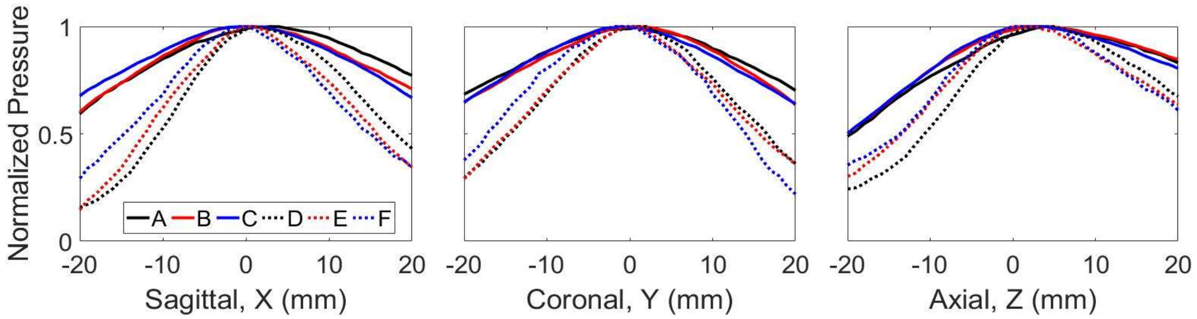

Figure 2.3. The peak-negative focal pressure as a function of electronic focal steering location was measured across a ± 20 mm range of locations centered at the geometric origin. Pressure steering profiles were obtained along the sagittal, coronal and axial dimension. Profile A – C correspond to the normalized pressure profile through skull 1 – 3, respectively, at 250 kHz. Profile D – F correspond to the normalized pressure through skulls 1 – 3, respectively, at 500 kHz.

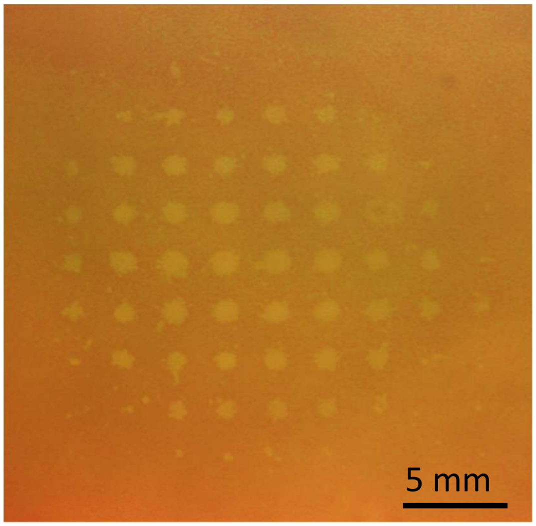

Figure 2.4. A 9 × 9 grid of lesions generated through a skullcap with electronic focal steering at 500 kHz. The distance between the center of each lesion was approximately 2.5 mm, which matched that specified with the applied electronic focal steering.

Table 2.2. The percentages for the average pressure decrease, across the three skullcaps, at -20 and +20 mm for each axis relative to the geometric focal pressure.

Frequency	Sagittal		Coronal		Axial	
	-20 mm	+ 20 mm	-20 mm	+20 mm	-20 mm	+20 mm
250 kHz	38±4%	28±4%	34±2%	34±3%	50±1%	17±2%
500 kHz	80±7%	63±4%	68±4%	69±7%	70±5%	36±3%

Table 2.3. The -6-dB widths of the 1D pressure profiles measured through the three skullcaps.

Skull #	Sagittal (mm)		Coronal (mm)		Axial (mm)	
	250 kHz	500 kHz	250 kHz	500 kHz	250 kHz	500 kHz
1	3.7	2.0	3.2	1.8	7.6	3.8
2	3.7	2.0	3.2	1.7	7.0	3.6
3	3.4	1.9	3.2	1.8	6.9	3.5

2.3.2 Histotripsy Treatment

For each frequency, the focus of the array was steered through a 4 cm diameter sphere corresponding to 33.5 mL. The gross morphology and MRI (Fig. 2.5 and 2.6) of a clot treated through a skullcap at 500 kHz with λ/2 focal spacing show the region of the clot liquefied with histotripsy. For each parameter combination, a total of 6 clots was treated through each skullcap. The liquefaction volume was reported as the average volume drained from treatment clots after subtracting the average volume drained from 12 control clots. In all experiments, effective clot liquefaction was achieved and drained with a catheter, in range of 6 – 59 mL in 0.9 – 42.4 minutes. The average liquefaction volume and rate with standard deviation for each combination of treatment parameters are shown in Figure 2.7 and Figure 2.8, respectively. The fastest liquefaction rate was 16.6 mL/min (15 mL in 0.9 min). The average control volume subtracted from the liquefaction volume of treated clots was 2.9 ± 1.8 mL (n = 12). The p-values for the multiple t-tests performed between the parameter combinations are shown in Tables 2.4 and 2.5.

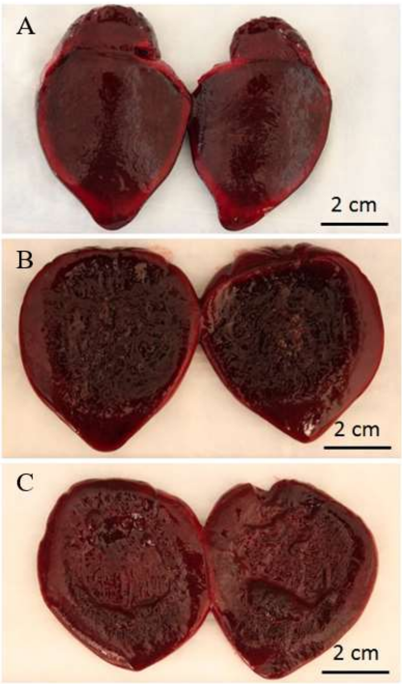

Figure 2.5. The gross morphology of a (A) control clot, (B) treated, undrained clot and (C) treated, drained clot. For the treated, undrained clot, the majority of the liquefied clot spilled out after removing it from the condom and cutting it in half, leaving a broken down slurry region approximately 4 cm in diameter. The treated, drained clot showed a 4 cm diameter cavity indicating the region left after removing the broken down slurry.

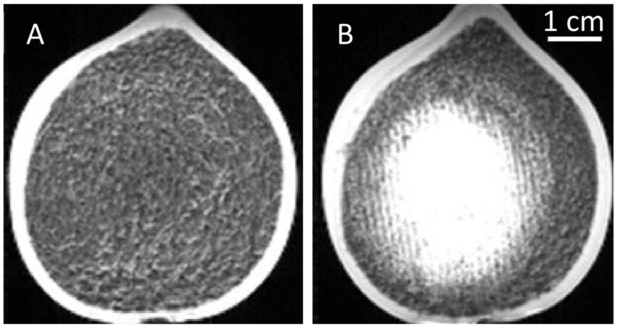

Figure 2.6. T2-weighted MR images of pre- and posttreatment clots for treatment with the 500 kHz array with lattice focal point spacing of λ/2. In the pretreatment images, the clot appeared uniformly dark. The posttreatment image showed a bright region approximately 4 cm in diameter that corresponded to the lysed blood cells in the liquefied clot. The bright region was densest in the center portion and became less so toward the periphery of the clot.

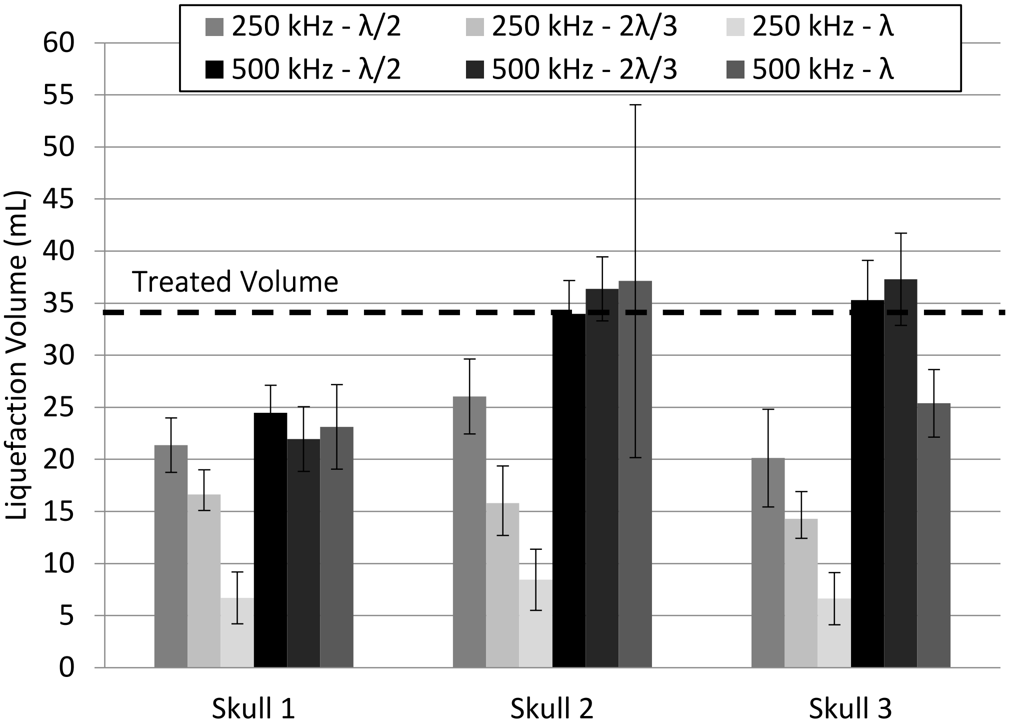

Figure 2.7. The average clot volume liquefied with histotripsy through each skullcap (n = 6) after subtracting the average control volume (n =12). Transcranial histotripsy treatment was applied using 250 and 500 kHz arrays with lattice focal point spacing of λ/2, 2λ/3 and λ.

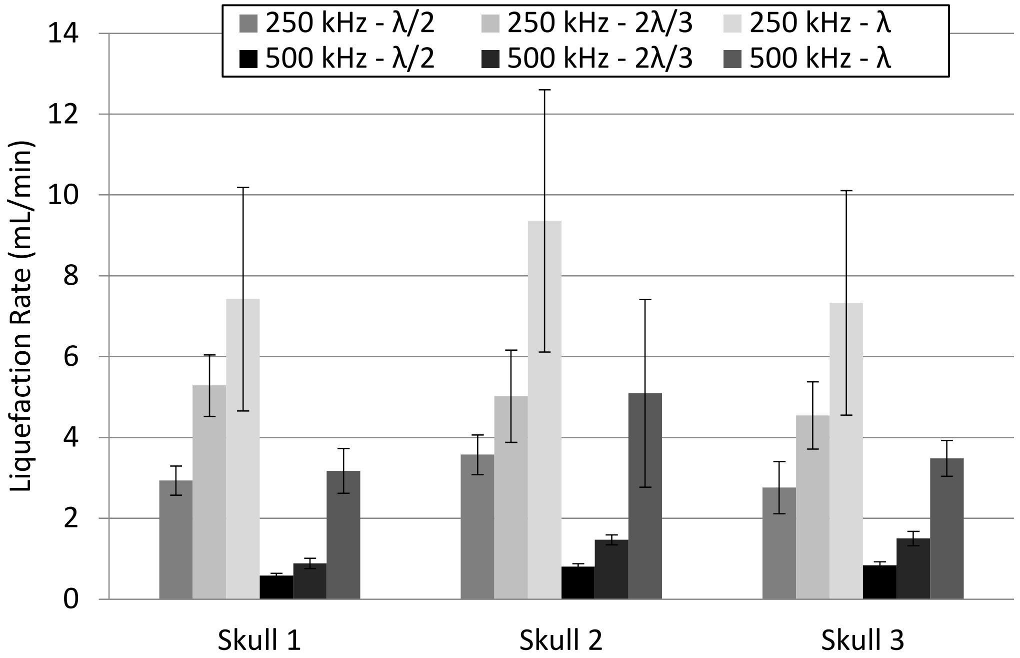

Figure 2.8. The average liquefaction rate for each frequency and focal spacing achieved through each skullcap.

Table 2.4. The p-values from the two-sample, two-tailed t-tests ($\alpha = 0.05$) performed on the liquefaction volumes (L.V.) and liquefaction rates (L.R.) between the focal spacing for each skullcap and between the skullcaps for each focal spacing treated at 250 kHz and 500 kHz.

250 kHz									
Spacing:		λ/2 v. 2λ/3	λ/2 v. λ	2λ/3 v. λ	Skull:		1 v. 2	1 v. 3	2 v. 3
Skull 1	L.V.	1.3E-03	1.4E-07	2.1E-06	λ/2	L.V.	2.4E-04	1.9E-04	0.53
	L.R.	4.4E-05	2.8E-03	9.8E-02		L.R.	2.8E-02	0.58	3.4E-02
Skull 2	L.V.	3.8E-04	1.3E-06	1.7E-03	2λ/3	L.V.	1.1E-05	4.0E-05	0.69
	L.R.	1.7E-02	1.5E-03	1.1E-02		L.R.	0.65	0.14	0.43
Skull 3	L.V.	2.8E-02	3.3E-04	4.8E-05	λ	L.V.	7.7E-02	0.31	0.13
	L.R.	1.9E-03	2.8E-03	4.0E-02		L.R.	0.29	0.95	0.27
500 kHz									
Spacing:		λ/2 v. 2λ/3	λ/2 v. λ	2λ/3 v. λ	Skull:		1 v. 2	1 v. 3	2 v. 3
Skull 1	L.V.	0.48	0.48	0.57	λ/2	L.V.	7.0E-05	9.0E-05	0.50
	L.R.	3.1E-04	4.8E-07	1.8E-06		L.R.	2.4E-03	1.9E-03	0.53
Skull 2	L.V.	0.17	0.7	0.93	2λ/3	L.V.	4.0E-06	3.0E-05	0.67
	L.R.	5.6E-07	1.1E-03	3.40E-03		L.R.	1.1E-05	4.0E-05	0.69
Skull 3	L.V.	0.41	4.1E-04	2.6E-04	λ	L.V.	0.13	0.29	0.18
	L.R.	9.3E-06	5.6E-08	1.4E-06		L.R.	7.7E-02	0.31	0.13

Table 2.5. The p-values from the two-sample, two-tailed t-tests ($\alpha = 0.05$) performed on the liquefaction volumes (L.V.) and liquefaction rates (L.R.) between 250 and 500 kHz for each focal spacing treated through each skullcap.

Spacing:		λ/2	2λ/3	λ
Skull 1	L.V.	2.7E-02	2.3E-03	3.4E-06
	L.R.	2.9E-08	6.8E-06	4.2E-03
Skull 2	L.V.	1.5E-03	3.9E-07	1.3E-02
	L.R.	8.9E-08	1.9E-05	2.6E-02
Skull 3	L.V.	1.0E-06	4.1E-07	1.2E-07
	L.R.	2.7E-05	5.3E-06	7.3E-03

2.3.3 Effects of Frequency

Across all skullcaps and focal spacing combinations, treatment with the 500 kHz array resulted in greater liquefaction volumes than the 250 kHz array. For example, after treatment through skull 2 at λ spacing, the average liquefaction volume was 37.1 ± 16.9 mL for 500 kHz and 8.5 ± 2.9 mL for 250 kHz. In contrast to the liquefaction volume, the 250 kHz array produced greater liquefaction rates than the 500 kHz array across all skullcap and focal spacing combinations. For example, treatment through skull 1 at λ/2 spacing had a liquefaction rate of 2.9 ± 0.4 mL/min for 250 kHz and 0.6 ± 0.1 mL/min for 500 kHz.

During the 250 kHz treatment, small white particulate was observed to fall off the back of the skullcaps during treatment. This was not observed during 500 kHz treatments. As skullcaps were stored in a bleach-water solution to prevent algae from growing and gassing up the skullcaps, the exterior surface of the skull eventually turned white and chalky from the bleach. During the 250 kHz treatments, this white particulate fell off the back of the skull, most likely because pre-focal cavitation eroded away the white, chalky layer caused by the bleach. Approximately halfway through treatments through skull 1, this effect seemed stopped. Analysis of the skull after treatment indicated that the white-chalky layer had been almost entirely removed with the true skull surface exposed. Skulls 1 – 3 after treatment with the 250 kHz array can be seen in Figure 2.9.

Figure 2.9. The external, superior portion of each skullcap after all treatments with the 250 kHz array. As skullcaps were stored in a bleach-water solution to prevent algae from growing and gassing up the skullcaps, the exterior surface of the skull eventually turned white and chalky. During the 250 kHz treatments, this white particulate fell off the back of the skull, most likely because the pre-focal cavitation eroded away the white, chalky layer caused by the bleach. Approximately halfway through treatments through skull 1, this effect stopped. Analysis of the skull after treatment indicated that the white-chalky layer had been almost entirely removed with the true skull surface exposed.

2.3.4 Effects of Focal Spacing

Three different focal spacing values, λ/2, 2λ/3 and λ, were used to apply identical treatment sets for a given frequency and skullcap. For the 250 kHz array, the liquefaction volume decreased as the focal spacing increased. In contrast, in all cases but one (2λ/3 vs. λ through skull 1), the liquefaction rate increased as the focal spacing increased. For treatment at 500 kHz through a given skullcap, focal spacing had no effect on the liquefaction volume aside from treatment through skull 3, where the λ focal spacing treatment drained significantly less volume than the λ/2 and 2λ/3 through the same skull. In contrast, the liquefaction rate increased with focal point spacing in all cases.

2.3.5 Variation across Skulls

250 kHz Array: For a given focal spacing, the 250 kHz array produced low variation in results across the three skullcaps. The only significant difference occurred in skull 2 at the λ/2 spacing. The volume liquefaction range for the 250 kHz array was 6 to 33 mL. The minimum liquefaction volume occurred through skull 3 with the λ focal spacing. The maximum occurred through skull 1 with the λ/2 focal spacing. The liquefaction rate range was 2.5 to 16.6 mL/min. The minimum rate occurred through skull 3 at a focal spacing of λ/2. The maximum occurred through skull 2 at a focal spacing of λ.

500 kHz Array: There was a greater variation in results across the three skullcaps for the 500 kHz treatment. Treatment through skull 1 with the 500 kHz array drained less volume for the λ/2 and 2λ/3 than the same treatments through skull 2 or 3. The volume liquefaction range for the 500 kHz array was 18 to 59 mL. Both the minimum and maximum liquefaction volume occurred through skull 2 with λ focal spacing. The liquefaction rate range was 0.6 to 8.1 mL/min. The minimum liquefaction rate occurred through skull 1 at the λ/2 focal spacing. The maximum occurred through skull 2 at the λ focal point spacing.

2.3.6 Skull Temperature Monitoring

Each skullcap showed a similar trend with respect to the temperature-rise over time (Fig. 2.10). That is, within the first 10 minutes, there was a steep increase in temperature followed by a more gradual increase in temperature for the remainder of the time. This gradual temperature increase is likely attributed to a gradual increase in temperature in the surrounding water, which was not accounted for. For each skullcap, the maximum temperature rise remained less than 4 °C. The temperature rise measured by different probes in the skullcaps showed a variation in temperature based on the location of the probe. For skullcaps 1 – 3, the probe measurements varied between 1.9 and 3.5, 2.5 and 3.6 and 2.1 and 2.8 °C, respectively. Average values for the CEM_{43} for skullcaps 1 – 3 calculated according to [51] were 0.32 ± 0.11, 0.66 ± 0.19 and 0.22 ± 0.08 minutes, respectively. These were roughly two orders of magnitude less than those thermal dose thresholds reported to cause damage to bone and bone marrow (CEM_{43} > 16 minutes) [51].

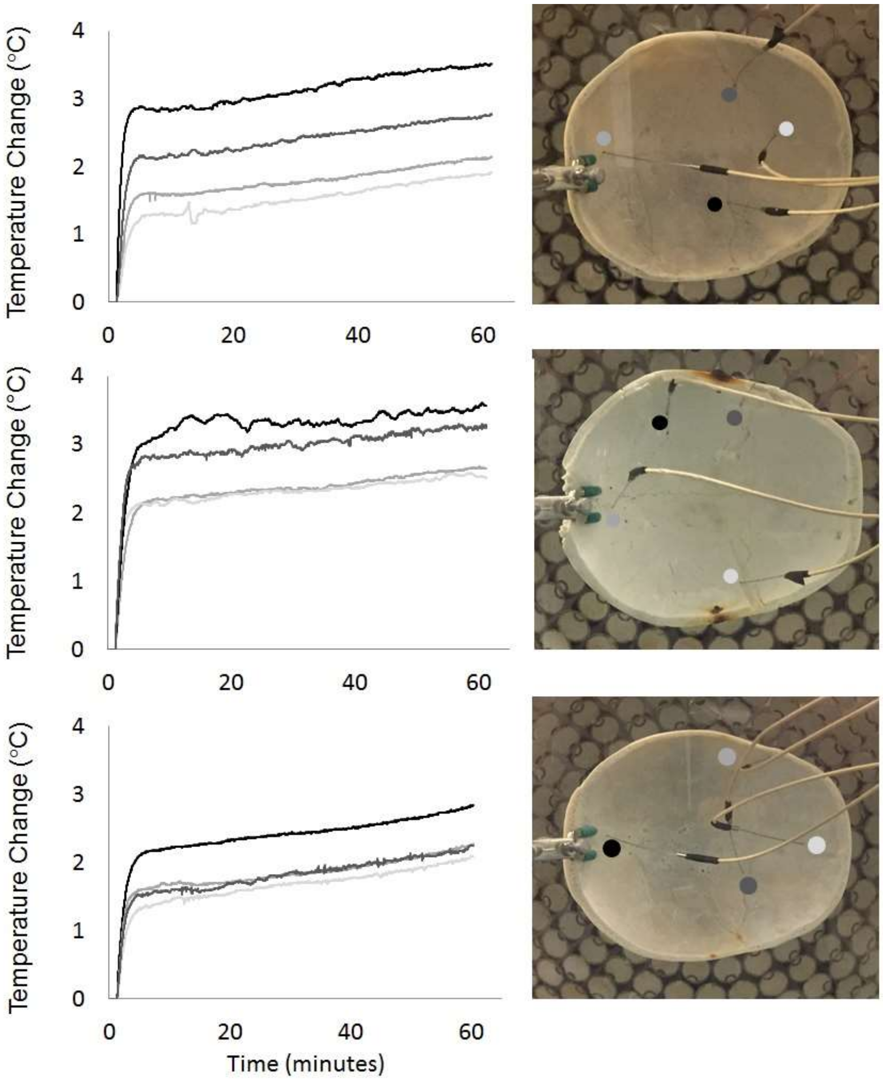

Figure 2.10. The change in temperature in each skullcap monitored at different locations while applying treatment with the 500 kHz array at a PRF of 200 Hz. For each skullcap, the maximum temperature rise remained less than 4 °C. The temperature rise measured by different probes in the skullcaps showed a variation in temperature based on the location of the probe. For skullcaps 1 – 3, the probe measurements varied between 1.9 and 3.5, 2.5 and 3.6 and 2.1 and 2.8 °C, respectively.

2.3.7 Post Hoc B-Mode Imaging of External Skull Surface during Treatment

To examine how histotripsy affected the external surface of a bleach skullcap during treatment, B-mode imaging of the surface of a bleached skull was performed following the initial set of experiments. **Figure 11** shows the B-mode images of the external skull surface with the array off, on at 250 kHz and on at 500 kHz. There was a noticeable cloud of particulate that formed with the 250 kHz array on that was not present with the array off. This was not observed with the 500 kHz array.

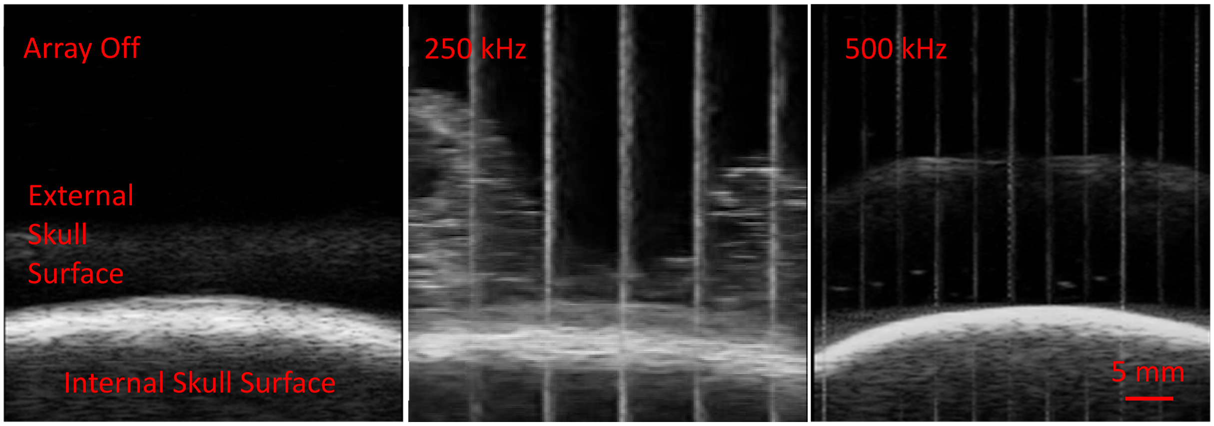

Figure 2.11. B-mode ultrasound images of external surface of a bleached skullcap during treatment with the 250 and 500 kHz array.

2.4 Discussion

The results demonstrate the use of histotripsy with electronic focal steering for fast transcranial clot liquefaction. Using electronic focal steering, it was possible to generate precise lesions through the excised human skullcaps and ultimately liquefy a 4 cm spherical volume within clots. By examining combinations of frequency and focal point spacing for electronically steered transcranial histotripsy treatment, volumes as large as 59 mL were liquefied within maximum treatment times (42.4 minutes) well below those of other minimally invasive techniques used to treat ICH. The concerns of skull heating associated with histotripsy were minimal with the average

CEM_{43} values through three different skullcaps approximately two orders of magnitude lower than those reported to cause damage to bone and bone marrow.

As the success of transcranial histotripsy ICH treatment is dependent upon removing the majority of the region of clot insonated in the minimum amount of time, the optimal parameter combination consists of a balance between the liquefaction volume and rate. Overall, the 250 kHz treatments produced much faster liquefaction rates than those at 500 kHz. However, the volumes drained at these large liquefaction rates produced with the 250 kHz array were much lower than those produced with the 500 kHz array (e.g., for skull 3, 250 kHz with λ spacing produced 6.63 mL while that at 500 kHz produced 25.38 mL). Based on the results shown here, the optimal treatment parameter combination among the ones tested was either the λ focal spacing applied at 500 kHz or the λ/2 focal spacing applied at 250 kHz. A post-hoc two-tailed t-test ($\alpha = 0.05$) showed no difference between the two parameter combinations with both producing large volume liquefaction at fast rates. However, the erosion of the external surface of the skullcap observed at 250 kHz was a significant concern. As this was not observed at 500 kHz, the λ focal spacing applied at 500 kHz is suggested as the optimal treatment parameter combination among the ones tested, as it was able to produce sufficiently large liquefaction volumes through skullcaps 1 – 3 (23.1 ± 4.0, 37.1 ± 16.9 and 25.4 ± 3.2 mL) with fast liquefaction rates (3.2 ± 0.6, 5.1 ± 2.3 and 3.5 ± 0.4 mL/min). Based on the bovine clot model used in this study, this presents an 11 – 33-fold increase in treatment rate when compared with current studies using MRgFUS, the fastest of the current minimally invasive ICH treatments under investigation [27]–[29], [31]. However, it should be noted that our clot model differed slightly from those used in the aforementioned MRgFUS studies which used either fresh porcine or human blood clotted at room temperature and could present discrepancies in the reported improvement. In regards to the current clinical minimally invasive treatments with rt-PA, the liquefaction volumes reported here are of a similar order as those shown in the literature [14]. However, the treatment time with rt-PA remains orders of magnitude greater than the treatment times reported in this study.

Overall, liquefaction volumes produced at 500 kHz were larger across all skullcap and focal point spacing combinations relative to those produced at 250 kHz. In addition, the 500 kHz liquefaction volumes were largely independent of focal spacing, something that was not observed at 250 kHz. An understanding of the reasons for this can be approached by considering the pressure steering profiles and the geometric focal pressure for the 250 and 500 kHz array. As the lesion size correlates well with the dimensions of the focus above the intrinsic threshold [52] and the 1D beam profiles (Fig. 2) show a much larger focal region at 250 kHz, the focal spacing was made proportional to the frequency of the array. This doubled the size of the absolute focal spacing at 250 kHz compared to that at 500 kHz. With identical peak-negative pressures across the entire treatment region, we would expect similar liquefaction results between the two frequencies for each focal spacing. However, due to the difference in the pressure steering profiles between the two frequencies (Fig. 3), there was an inherent challenge in comparing treatment between two different frequencies with electronic focal steering. To sustain either uniform pressure profiles or equivalent pressure profiles between frequencies, the pressure output from the array would need to be modulated across a large range quickly enough to keep up with the PRF of the applied treatment. Although this is a possibility with the current driving system, this technique of sustaining consistent pressures across an electronic focal steering volume has not yet been thoroughly investigated. However, by keeping pressures at the largest steering radii (± 20 mm from the geometric focus) approximately equal between the two frequencies (Table 3), we ensured some degree of comparability between the treatments. Nonetheless, the higher focal gain in the 500 kHz treatments resulted in a larger peak-negative pressures applied to regions close to the geometric focus than those for the 250 kHz treatments. The effects of these field property differences between the two frequencies were likely manifested in the differences observed between liquefaction volume for a given focal spacing at each frequency.

One effect that was observed during the 250 kHz and not during 500 kHz treatment was the small amount of micron-sized particulate falling off the back of the skullcaps. Literature shows that the primary component of household bleach, sodium hypochlorite, can deproteinize the surface layer of cortical bone without disrupting the mineral composition [53]–[56]. As skullcaps were stored in a bleach-water solution to prevent algae from growing prior to treatment with the 250 kHz array but not the 500 kHz array, the initial thought was that this particulate formation during the 250 kHz experiments was primarily due to the bleach-induced fragile, chalky mineral layer on the external surface of the skull that precipitated off during histotripsy treatment. However, post hoc B-mode imaging of the external surface of a bleached skullcap treated with 250 kHz and 500 kHz, showed particulate formation at 250 kHz but not 500 kHz. Therefore, the erosion of the skull surface was particular to treatment with the 250 kHz array. Based on the B-mode images alone, it is difficult to point directly to prefocal cavitation as the cause. However, this is likely the only mechanism that would cause such an effect. If prefocal cavitation, it is possible that this occurred due to the larger beam size at 250 kHz than at 500 kHz and an increased chance of the beam interfering with the skullcap. However, the portion of the beam interfering with the skull was likely well below the intrinsic threshold and preliminary studies show the 500 kHz focus can be positioned close (within 5 mm) to the skullcap without causing the effects seen here at 250 kHz, suggesting that something else is causing the prefocal cavitation at 250 kHz. One thought is that the likelihood of prefocal cavitation increases at lower frequency, which is based on the observation that the probability of producing "incidental cavitation bubbles" (occurring at pressures below intrinsic threshold) is greater at lower frequencies than at higher frequencies [36]. The increased likelihood of initiating incidental bubbles in combination with a high PRF to sustain the "incidental bubbles" might have resulted in the presence of prefocal cavitation at 250 kHz and not at 500 kHz. Future cavitation detection experiments with time windowing at the skull surface should be able to validate prefocal cavitation as the cause.

The concern for histotripsy induced skull heating was minimal in that the average CEM_{43} values for each skullcap were about two orders of magnitude lower than those reported to cause damage in bone and bone marrow [51]. Due to the in-vitro nature of these experiments, the heat sink effects into skin and brain tissue were not examined in this study and remain a concern requiring further analysis. However, based on the CEM_{43} values reported to cause damage in skin and brain tissue, these initial skull heating results are promising. Skin damage has not been reported for CEM_{43} values less than 20 minutes. Although the CEM_{43} threshold for brain damage is lower and a bit more complicated than that of skin and bone with a range of values depending on the region, any concerns of the skull heat sink effects overheating brain tissue could be mitigated by reducing PRF if necessary. Skull heating has been a major issue for MRgFUS, limiting the treatment location profile and treatment rate. In certain *in-vivo* and *in-vitro* MRgFUS studies, to reduce the heating, cool water was continuously circulated over the skull [57], [58]. The clot liquefaction and skull heating results presented in this study show the ability of histotripsy to perform rapid clot liquefaction while suggesting the potential of keeping the skull and surrounding tissue within a safe temperature range. However, although these experiments provided a good starting point to analyze the potential of unwanted heating effects caused by histotripsy, it is difficult to claim how they will translate to in-vivo or clinical cases where surrounding tissues and perfusion may contribute to histotripsy induced temperature changes.

As the majority of ICH cases occur in the central region of the brain [46], [47]. The central position of the clots within the skullcaps in this study was a reasonable starting point for analyzing the potential of histotripsy to liquefy clots representative of ICH. However, the remaining ICH cases occur in off center brain regions such as the cortical lobes, cerebellum and brainstem. In this study, we chose to limit our investigation to the liquefaction of a clot volume located in what would be the central region of the brain and the potential to treat volumes off-center was not examined. By mechanically repositioning the skull or the array, these regions can be reached. However, this mechanical repositioning may cause changes to skull heating and thus requires further investigation.

The results throughout this paper have been reported as “liquefaction volumes” drained from treated clots with a catheter and 10 mL syringe. This drainage technique was used as it is expected that a similar technique will be used to remove the volume of clot liquefied with histotripsy in a clinical setting and one we are currently working to integrate with a miniature acoustic hydrophone to enable aberration correction. Histotripsy treatments targeting other organs have often attempted to completely liquefy the entire treatment region into an acellular homogenate (e.g., tumor ablation). However, in the context of ICH treatment and this study, complete liquefaction of the clot is not necessary and liquefaction needs only to be performed to the extent where the treated volume can be drained from the clot using the catheter and syringe. This can be observed in the gross morphology of the treated clot (Fig. 7), where the broken down slurry remains after treatment and is removed after drainage with the catheter. This is likely the reason it was possible to generate consistent liquefaction volumes across different focal spacing at

500 kHz. Therefore, to optimize histotripsy for ICH treatment, the goal should be to fractionate the clot sufficiently to drain from the catheter for clot removal, and small clot pieces remaining may be acceptable as long as they are small enough to drain via catheter.

2.5 Conclusion

This study investigated the effects of ultrasound frequency and focal spacing on the treatment efficacy and treatment speed alongside the temperature rise in the skull during transcranial histotripsy clot liquefaction. The specific emphasis of the study was to analyze the effects of transducer frequency and focal spacing on treatment efficacy and speed and show histotripsy's feasibility for rapid, minimally invasive ICH treatment. The fastest liquefaction rate across all clot treatments was 16.6 mL/min (15 mL in 0.9 min). The λ focal spacing applied at 500 kHz is suggested as the best treatment parameter combination among those tested, as it was able to produce large liquefaction volumes through skullcaps 1 – 3 (23.1 ± 4.0, 37.1 ± 16.9 and 25.4 ± 16.9 mL) with the fast liquefaction rates (3.2 ± 0.6, 5.1 ± 2.3 and 3.5 ± 0.4 mL/min), presenting an 11 – 33-fold increase in treatment rate when compared with treatments using MRgFUS and orders of magnitude faster than clinical minimally invasive techniques using rt-PA. In addition, the skull heating effects of transcranial histotripsy at the parameter combinations examined in this study indicated minimal concern with average CEM_{43} values about two orders of magnitude lower than those reported to cause thermal damage in bone and bone marrow. Future work will focus on applying the results of this study to *in-vivo* clot treatment in a porcine model.

2.6 Appendix

2.6.1 Simulation of the Amplitude Field at the External Surface of the Skull

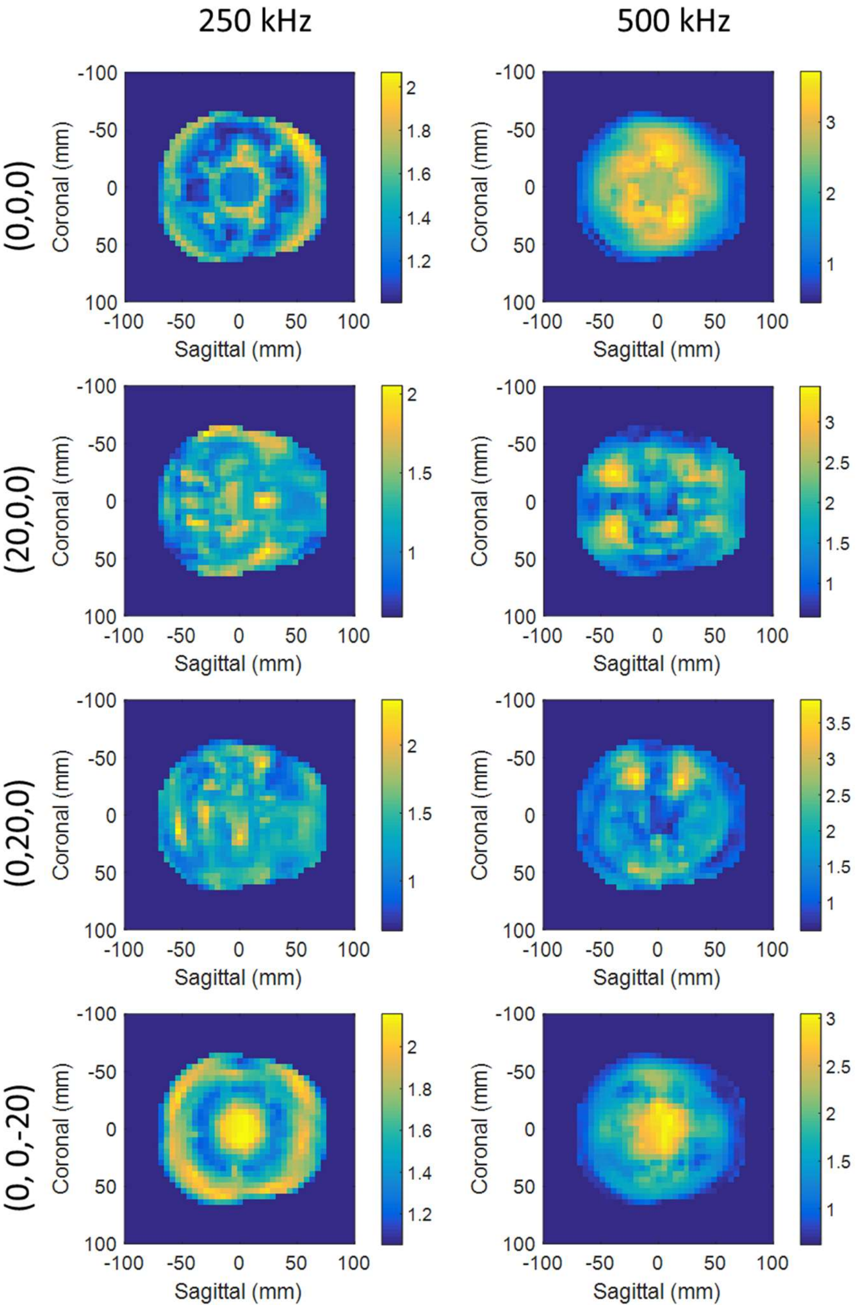

Figure 2.12. Field maps of the peak-negative pressure at the external surface of an excised human skullcap placed in the field of the 250 and 500 kHz, 256-element hemispherical array. Field maps were generated via a calibrated linear simulation (FOCUS, Michigan State University, East Lansing, MI). A CT scan of a human skullcap was converted into a point cloud and sampled at points that intersected with the rays of the 256 elements. The peak-negative pressure at each point

in the field was simulated, projected and interpolated onto a 2D plane. Field maps were generated for discrete electronic steering locations that described the extent of the steering range used in the study described in this chapter. The units of the color bar are MPa.

2.7 References

[1] T. Gerhardson, J. R. Sukovich, A. S. Pandey, T. L. Hall, C. A. Cain, and Z. Xu, “Effect of Frequency and Focal Spacing on Transcranial Histotripsy Clot Liquefaction, Using Electronic Focal Steering,” *Ultrasound Med. Biol.*, vol. 43, no. 10, pp. 2302–2317, 2017.

[2] A. I. Qureshi, A. D. Mendelow, and D. F. Hanley, “Intracerebral haemorrhage,” *The Lancet*, vol. 373, no. 9675. pp. 1632–1644, 2009.

[3] E. V. Kuklina, X. Tong, M. G. George, and P. Bansil, “Epidemiology and prevention of stroke: A worldwide perspective,” *Expert Review of Neurotherapeutics*, vol. 12, no. 2. pp. 199–208, 2012.

[4] D. Mozaffarian *et al.*, “Executive summary: Heart disease and stroke statistics-2016 update: A Report from the American Heart Association,” *Circulation*, vol. 133, no. 4. pp. 447–454, 2016.

[5] M. L. Flaherty *et al.*, “Long-term mortality after intracerebral hemorrhage,” *Neurology*, vol. 66, no. 8, pp. 1182–1186, 2006.

[6] J. P. Broderick, T. G. Brott, J. E. Duldner, T. Tomsick, and G. Huster, “Volume of intracerebral hemorrhage: A powerful and easy-to-use predictor of 30-day mortality,” *Stroke*, 1993.

[7] J. Broderick, T. Brott, T. Tomsick, J. Tew, J. Duldner, and G. Huster, “Management of intracerebral hemorrhage in a large metropolitan population,” *Neurosurgery*, vol. 34, no. 5, pp. 882–887, 1994.

[8] M. S. Dennis, “Outcome after brain haemorrhage,” *Cerebrovascular Diseases*, vol. 16, no. SUPPL. 1. pp. 9–13, 2003.

[9] G. J. Hankey and C. Hon, “Surgery for primary intracerebral hemorrhage: is it safe and effective? A systematic review of case series and randomized trials.,” *Stroke; a journal of cerebral circulation*, vol. 28, no. 11. pp. 2126–32, 1997.

[10] H. M. Fernandes, B. Gregson, S. Siddique, and A. D. Mendelow, “Surgery in intracerebral hemorrhage: The uncertainty continues,” *Stroke*, vol. 31, no. 10. pp. 2511–2516, 2000.

[11] A. D. Mendelow *et al.*, “Early surgery versus initial conservative treatment in patients with spontaneous supratentorial intracerebral haematomas in the International Surgical Trial in Intracerebral Haemorrhage (STICH): A randomised trial,” *Lancet*, vol. 365, no. 9457, pp.

387–397, 2005.

[12] A. D. Mendelow *et al.*, “Early surgery versus initial conservative treatment in patients with spontaneous supratentorial lobar intracerebral haematomas (STICH II): A randomised trial,” *Lancet*, vol. 382, no. 9890, pp. 397–408, 2013.

[13] N. Hattori, Y. Katayama, Y. Maya, and A. Gatherer, “Impact of stereotactic hematoma evacuation on medical costs during the chronic period in patients with spontaneous putaminal hemorrhage: a randomized study,” *Surg. Neurol.*, vol. 65, no. 5, pp. 429–435, 2006.

[14] T. Morgan, M. Zuccarello, R. Narayan, P. Keyl, K. Lane, and D. Hanley, “Preliminary findings of the minimally-invasive surgery plus rtPA for intracerebral hemorrhage evacuation (MISTIE) clinical trial,” *Acta Neurochir. Suppl.*, no. 105, pp. 147–151, 2008.

[15] W. Z. Wang *et al.*, “Minimally invasive craniopuncture therapy vs. conservative treatment for spontaneous intracerebral hemorrhage: Results from a randomized clinical trial in China,” *Int. J. Stroke*, vol. 4, no. 1, pp. 11–16, 2009.

[16] A. V. Alexandrov, A. M. Demchuk, W. S. Burgin, D. J. Robinson, and J. C. Grotta, “Ultrasound-Enhanced Thrombolysis for Acute Ischemic Stroke: Phase I. Findings of the CLOTBUST Trial,” *J. Neuroimaging*, vol. 14, no. 2, pp. 113–117, 2004.

[17] S. Datta *et al.*, “Correlation of cavitation with ultrasound enhancement of thrombolysis,” *Ultrasound Med. Biol.*, vol. 32, no. 8, pp. 1257–1267, 2006.

[18] C. K. Holland, S. S. Vaidya, S. Datta, C. C. Coussios, and G. J. Shaw, “Ultrasound-enhanced tissue plasminogen activator thrombolysis in an in vitro porcine clot model,” *Thromb. Res.*, vol. 121, no. 5, pp. 663–673, 2008.

[19] K. E. Hitchcock and C. K. Holland, “Ultrasound-assisted thrombolysis for stroke therapy: Better thrombus break-up with bubbles,” in *Stroke*, 2010, vol. 41, no. 10 SUPPL. 1.

[20] S. Meairs, A. Alonso, and M. G. Hennerici, “Progress in sonothrombolysis for the treatment of stroke,” *Stroke*, vol. 43, no. 6, pp. 1706–1710, 2012.

[21] S. Datta, C. C. Coussios, A. Y. Ammi, T. D. Mast, G. M. de Courten-Myers, and C. K. Holland, “Ultrasound-Enhanced Thrombolysis Using Definity?? as a Cavitation Nucleation Agent,” *Ultrasound Med. Biol.*, vol. 34, no. 9, pp. 1421–1433, 2008.

[22] W. J. Elias *et al.*, “The use of magnetic resonance-guided high intensity focused ultrasound to treat essential tremor,” *J. Acoust. Soc. Am.*, vol. 134, no. 5, pp. 4090–4090, 2013.

[23] W. J. Elias *et al.*, “A Pilot Study of Focused Ultrasound Thalamotomy for Essential Tremor,” *http://dx.doi.org/10.1056/NEJMoa1300962*, 2013.

[24] K. Hynynen *et al.*, “Focal disruption of the blood-brain barrier due to 260-kHz ultrasound bursts: A method for molecular imaging and targeted drug delivery,” *J. Neurosurg.*, vol.

105, no. 3, pp. 445–454, 2006.

[25] M. A. O'Reilly and K. Hynynen, "Ultrasound enhanced drug delivery to the brain and central nervous system," *International Journal of Hyperthermia*, vol. 28, no. 4. pp. 386–396, 2012.

[26] E. Nance *et al.*, "Non-invasive delivery of stealth, brain-penetrating nanoparticles across the blood - Brain barrier using MRI-guided focused ultrasound," *J. Control. Release*, vol. 189, pp. 123–132, 2014.

[27] S. J. Monteith *et al.*, "Minimally invasive treatment of intracerebral hemorrhage with magnetic resonance–guided focused ultrasound," *J. Neurosurg.*, vol. 118, no. 5, pp. 1035–1045, 2013.

[28] S. J. Monteith, N. F. Kassell, O. Goren, and S. Harnof, "Transcranial MR-guided focused ultrasound sonothrombolysis in the treatment of intracerebral hemorrhage," *Neurosurg. Focus*, vol. 34, no. 5, p. E14, 2013.

[29] S. Monteith *et al.*, "Potential intracranial applications of magnetic resonance–guided focused ultrasound surgery," *J. Neurosurg.*, vol. 118, no. 2, pp. 215–221, 2013.

[30] C. Wright, K. Hynynen, and D. Goertz, "In vitro and in vivo high intensity focused ultrasound thrombolysis," *Invest. Radiol.*, vol. 47, no. 4, pp. 217–225, 2012.

[31] M. Ramanan and a Shankar, "Minimally invasive surgery for primary supratentorial intracerebral haemorrhage," *J. Clin. Neurosci.*, vol. 20, no. 12, pp. 1650–1658, 2013.

[32] Z. Xu *et al.*, "Controlled ultrasound tissue erosion," *IEEE Trans. Ultrason. Ferroelectr. Freq. Control*, vol. 51, no. 6, pp. 726–736, 2004.

[33] Z. Xu, J. B. Fowlkes, E. D. Rothman, A. M. Levin, and C. A. Cain, "Controlled ultrasound tissue erosion: The role of dynamic interaction between insonation and microbubble activity," *J. Acoust. Soc. Am.*, vol. 117, no. 1, pp. 424–435, 2005.

[34] W. W. Roberts, T. L. Hall, K. Ives, J. S. Wolf, J. B. Fowlkes, and C. A. Cain, "Pulsed cavitational ultrasound: A noninvasive technology for controlled tissue ablation (histotripsy) in the rabbit kidney," *J. Urol.*, vol. 175, no. 2, pp. 734–738, 2006.

[35] Z. Xu, G. Owens, D. Gordon, C. Cain, and A. Ludomirsky, "Noninvasive creation of an atrial septal defect by histotripsy in a canine model," *Circulation*, vol. 121, no. 6, pp. 742–749, 2010.

[36] E. Vlaisavljevich *et al.*, "Effects of Ultrasound Frequency and Tissue Stiffness on the Histotripsy Intrinsic Threshold for Cavitation," *Ultrasound Med. Biol.*, vol. 41, no. 6, pp. 1651–1667, 2015.

[37] K. W. Lin *et al.*, "Histotripsy beyond the intrinsic cavitation threshold using very short ultrasound pulses: Microtripsy," *IEEE Trans. Ultrason. Ferroelectr. Freq. Control*, vol. 61,

no. 2, pp. 251–265, 2014.

[38] K. Kieran *et al.*, “Refining Histotripsy: Defining the Parameter Space for the Creation of Nonthermal Lesions With High Intensity, Pulsed Focused Ultrasound of the In Vitro Kidney,” *J. Urol.*, 2007.

[39] A. D. Maxwell, C. A. Cain, A. P. Duryea, L. Yuan, H. S. Gurm, and Z. Xu, “Noninvasive Thrombolysis Using Pulsed Ultrasound Cavitation Therapy - Histotripsy,” *Ultrasound Med. Biol.*, vol. 35, no. 12, pp. 1982–1994, 2009.

[40] A. D. Maxwell, G. Owens, H. S. Gurm, K. Ives, D. D. Myers, and Z. Xu, “Noninvasive treatment of deep venous thrombosis using pulsed ultrasound cavitation therapy (histotripsy) in a porcine model,” *J. Vasc. Interv. Radiol.*, vol. 22, no. 3, pp. 369–377, 2011.

[41] T. D. Khokhlova, W. L. Monsky, Y. A. Haider, A. D. Maxwell, Y. N. Wang, and T. J. Matula, “Histotripsy liquefaction of large hematomas,” *Ultrasound Med. Biol.*, vol. 42, no. 7, pp. 1491–1498, 2016.

[42] Y. Kim, T. Hall, Z. Xu, and C. Cain, “Transcranial histotripsy therapy: A feasibility study,” *IEEE Trans. Ultrason. Ferroelectr. Freq. Control*, vol. 61, no. 4, pp. 582–593, 2014.

[43] J. R. Sukovich *et al.*, “Targeted Lesion Generation Through the Skull Without Aberration Correction Using Histotripsy,” *IEEE Trans. Ultrason. Ferroelectr. Freq. Control*, vol. 63, no. 5, pp. 671–682, 2016.

[44] J. E. Parsons, C. A. Cain, and J. B. Fowlkes, “Cost-effective assembly of a basic fiber-optic hydrophone for measurement of high-amplitude therapeutic ultrasound fields,” *J. Acoust. Soc. Am.*, vol. 119, no. 3, pp. 1432–1440, 2006.

[45] A. D. Maxwell, T. Y. Wang, L. Yuan, A. P. Duryea, Z. Xu, and C. A. Cain, “A tissue phantom for visualization and measurement of ultrasound-induced cavitation damage,” *Ultrasound Med. Biol.*, vol. 36, no. 12, pp. 2132–2143, 2010.

[46] M. I. Aguilar and T. G. Brott, “Update in Intracerebral Hemorrhage,” *The Neurohospitalist*. 2011.

[47] R. D. Zimmerman, J. A. Maldjian, N. C. Brun, B. Horvath, and B. E. Skolnick, “Radiologic estimation of hematoma volume in intracerebral hemorrhage trial by CT scan,” *Am. J. Neuroradiol.*, 2006.

[48] M. Zuccarello *et al.*, “Early surgical treatment for supratentorial intracerebral hemorrhage: A randomized feasibility study,” *Stroke*, 1999.

[49] T. Brott *et al.*, “Early hemorrhage growth in patients with intracerebral hemorrhage,” *Stroke*, 1997.

[50] T.-Y. Wang, Z. Xu, T. L. Hall, J. B. Fowlkes, and C. A. Cain, “An efficient treatment strategy for histotripsy by removing cavitation memory.,” *Ultrasound Med. Biol.*, vol. 38,

no. 5, pp. 153–766, 2012.

[51] P. S. Yarmolenko *et al.*, “Thresholds for thermal damage to normal tissues: An update,” *International Journal of Hyperthermia*, vol. 27, no. 4. pp. 320–343, 2011.

[52] E. Vlaisavljevich, T. Gerhardson, T. Hall, and Z. Xu, “Effects of f-number on the histotripsy intrinsic threshold and cavitation bubble cloud behavior,” *Phys. Med. Biol.*, vol. 62, no. 4, pp. 1269–1290, 2017.

[53] A. Boyde and M. H. Hobdell, “Scanning electron microscopy of primary membrane bone,” *Zeitschrift für Zellforsch. und Mikroskopische Anat.*, vol. 99, no. 1, pp. 98–108, 1969.

[54] J. J. Broz, S. J. Simske, W. D. Corley, and A. R. Greenberg, “Effects of deproteinization and ashing on site-specific properties of cortical bone,” *J. Mater. Sci. Mater. Med.*, vol. 8, no. 6, pp. 395–401, 1997.

[55] F. M. Kerbl, P. Devilliers, M. Litaker, and P. D. Eleazer, “Physical effects of sodium hypochlorite on bone: An ex vivo study,” *J. Endod.*, vol. 38, no. 3, pp. 357–359, 2012.

[56] M. Otter, S. Goheen, and W. S. Williams, “Streaming potentials in chemically modified bone,” *J. Orthop. Res.*, vol. 6, no. 3, pp. 346–359, 1988.

[57] N. McDannold, E. J. Park, C. S. Mei, E. Zadicario, and F. Jolesz, “Evaluation of three-dimensional temperature distributions produced by a low-frequency transcranial focused ultrasound system within ex vivo human skulls,” *IEEE Trans. Ultrason. Ferroelectr. Freq. Control*, vol. 57, no. 9, pp. 1967–1976, 2010.

[58] K. Hynynen *et al.*, “Pre-clinical testing of a phased array ultrasound system for MRI-guided noninvasive surgery of the brain-A primate study,” *Eur. J. Radiol.*, vol. 59, no. 2, pp. 149–156, 2006.

CHAPTER 3 Histotripsy Clot Liquefaction in a Porcine Intracerebral Hemorrhage Model

This chapter has been published in *Neurosurgery*. 2017; 43(10): 2302-2317. © Neurosurgery. Reprinted with permission, from [1].

3.1 Introduction

Intracerebral hemorrhage (ICH) is a devastating form of hemorrhagic stroke, leading to a 30-day mortality of 40% and significant disability for those who survive [2], [3]. The primary neurologic injury induced by ICH occurs immediately and is characterized by the mass effect and increased intracranial pressure (ICP) which in turn leads to a reduction in cerebral perfusion pressure (CPP) causing further ischemic injuries [4], [5]. The secondary injury to the brain develops in the days following the hemorrhage and is characterized by the toxic effects associated with clot metabolism and processes associated with the inflammatory and complement systems' response to erythrolysis [4]. In particular, the infusion of hemolysates into the brain has shown damaging effects in rats and pigs with the primary injury mechanism attributed to iron overload and the generation of reactive oxygen species [4]. Thus, the immediate removal of intracranial blood products reduces brain pressure and removes products responsible for secondary cerebral injuries.

Many techniques have been developed to remove ICH with the goal of removing the maximal amount of clot in the most minimally-invasive manner. Currently, surgeons utilize craniotomy, endoscopic, and lytic approaches in evacuating the hematoma. The craniotomy-based approach is maximally-invasive while the endoscopic approach is less invasive but still requires traversing normal tissue with a large port. The intraclot lytic method is being tested in the MISTIE III trial, however, this approach relies on an evacuation process that takes days and cannot be initiated immediately. There is an unmet need for a minimally-invasive method that can be applied immediately following ICH and allow evacuation of clot within minutes.

Histotripsy is a novel noninvasive focused ultrasound (FUS) technique that differs from magnetic resonance guided FUS (MRgFUS) in its therapeutic mechanism and possesses advantages for rapid liquefaction and removal of ICH. Instead of using long ultrasound pulses at moderate amplitude to heat and thermally necrose tissue, histotripsy uses very short (<0.1%), high amplitude ultrasound pulses (>27 MPa) applied from outside the body to generate a cluster of targeted, focused cavitation microbubbles (bubble cloud) without the use of extrinsically administered microbubbles [6]–[9]. The rapid bubble expansion and collapse create significant stress and strain in tissue that mechanically fractionate it into an acellular liquid[10]. Recent studies have shown the ability for transcranial clot liquefaction through humans skulls *in-vitro*, with liquefaction rates in the range of 2-5 mL/min [11], [12]. The liquefied volume can be drained through a burr hole in the skull via catheter. It should be noted that in this study, craniotomy is performed, because the geometry of the pig skull is not amenable for ultrasound propagation. In human, craniotomy will not be needed, as in vitro studies already shows that histotripsy can be applied from outside the intact human skull to liquefy the clot.

With the current study we present the first analysis of histotripsy-based liquefaction of ICH *in-vivo.* There is significant concern that the lysed blood products generated by histotripsy treatment will cause severe neurological injury[4], [13]–[17]. A previous study reported that lysed blood directly injected into the pig brain with the similar volume (~2mL) as used in this study lead to significant cerebral injury and even death[17]. Thus, we have set to investigate the safety of histotripsy clot liquefaction in a well-established porcine ICH model[18]. The primary goals of this study were: (1) to evaluate initial safety concerns of histotripsy in liquefying ICH utilizing MR imaging, histopathology, and porcine neurological functioning and (2) to determine ability to evacuate the histotripsy-treated ICH utilizing a simple drainage technique.

3.2 Materials and Methods

3.2.1 Animals

The protocols involved in this study were approved by the pertinent group at our university. Male and female pigs (30-35 kg) were obtained from an authorized dealer.

3.2.2 Experimental Groups and Study Overview

Pigs were divided into three groups: two treatment groups and one control group (n=6/group). In one treatment group, the clot was liquefied with histotripsy and the liquefied contents were evacuated with a needle and syringe immediately following treatment (treatment-drained). In the second treatment group, the clot was liquefied and the contents were left within the brain (treatment-undrained). The timeline of the study can be seen in Figure 3.1. In a randomized order, craniotomies were performed, and hematomas were formed within the brain on day 1. For treatment groups, clots were liquefied with histotripsy 48 hours after they were formed (day 3). Ideally a 24-hour treatment window would have been used but due to the significant surgical burden of the craniotomy and clot injection, pigs were given 48 hours to recover. To assess degree to which pigs tolerated the clots that underwent histotripsy liquefaction (drained and undrained) relative to those that did not receive histotripsy treatment, pigs were survived 5 to 6 days following treatment. Magnetic resonance imaging (MRI) was performed on a subset (n=4-

6/group) of each group on day 8 or 9. Pigs were euthanized directly following MRI and brains were fixed and sectioned for histology.

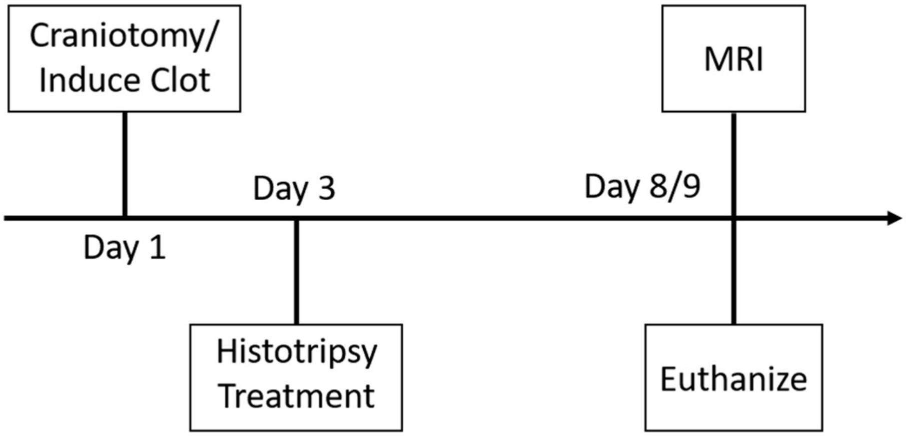

Figure 3.1. The timeline of the study. For the treatment-drained pigs, the volume was drained directly following histotripsy treatment on day 3.

3.2.3 Porcine ICH Model

All surgical procedures during the clot formation were performed using aseptic techniques. Pigs were intubated and maintained on isoflurane gas. A transcutaneous intra-arterial catheter was placed into the common femoral artery of the pig to allow for removal of arterial blood for ICH formation. Following the placement of a longitudinal incision in the scalp, the skin and periosteum were separated and a 5 cm craniotomy was performed. The craniotomy was necessary to provide an acoustic window for histotripsy therapy, as the geometry of the pig skull is not conducive to ultrasound transmission.

Immediately following the craniotomy, clots were formed in the cerebral white matter using the porcine lobar intracerebral hemorrhage model described by Wagner et al. [18]. A 20-guage needle was connected to the arterial line via extension tubing, and fed through an infusion pump (Baxter, Deerfield, IL, USA). The needle was inserted to a depth of 2-5 mm into the white matter of the left frontal lobe, approximately 2 mm laterally from the longitudinal fissure and 1 cm anterior of the ventricles. 1.75 mL of blood was infused over 13 minutes. This relatively small volume was chosen with consideration to the size of the pig brain and has been established as a standard volume for this ICH model [18]. Although slightly larger volumes have been reported using this model [17], we observed an increased likelihood of pig death when the volume was increased much beyond 1.75 mL. Following clot formation, the incision was sutured closed.

3.2.4 Neurological Evaluation

The neurological status of each pig was evaluated according to a grading scale similar to that used by Tanaka et al. and Yamaguchi et al. [19], [20]. To assess neurological status of the pigs, scores were generated from a 25-point scale; 0 (no deficit) and 25 (severe deficit). Neurological signs for the grading scale included appetite (4 points), standing position (5), head position (2), utterance (2), gait (3) and motor function (fore and hind limbs: 4 each) and facial paralysis (1). Neurological behavior was evaluated daily starting with a preoperative evaluation on the clot formation date.

3.2.5 Histotripsy Treatment

Histotripsy treatment was applied to anesthetized pigs through the scalp using a 1 MHz, 8-element, hand-held transducer (Fig. 3.2). A phased-array B-mode ultrasound probe was inserted coaxially into the transducer to allow treatment targeting and monitoring. The histotripsy transducer was coupled to the pig brain via degassed saline placed on top of the pig head. The transducer was guided by hand using B-mode guidance during all treatments. The cavitation activity generated by histotripsy appears intensely hyperechoic with time-varying brightness on B-mode, allowing it to be easily identified and monitored during treatment.

Histotripsy treatments were delivered using ultrasound pulses with peak-negative pressures of 30-40 MPa, at pulse-repetition frequencies (PRF) of 40-60 Hz. Prior to treatment, the bulk clot volume appeared hyperechoic on B-mode ultrasound. The central portion of the clot was treated until the targeted region went from hyperechoic (intact clot) to hypoechoic (liquefied clot) as observed via B-mode. A 1-2 mm rim of untreated clot was left intentionally left at the clot boundary as a safety margin. In the treatment-drained group the hypoechoic liquefied content was drained via an 18-gauge needle and 3 mL syringe following treatment. In the treatment-undrained group the liquefied content was left within the brain for the duration of the porcine survival.

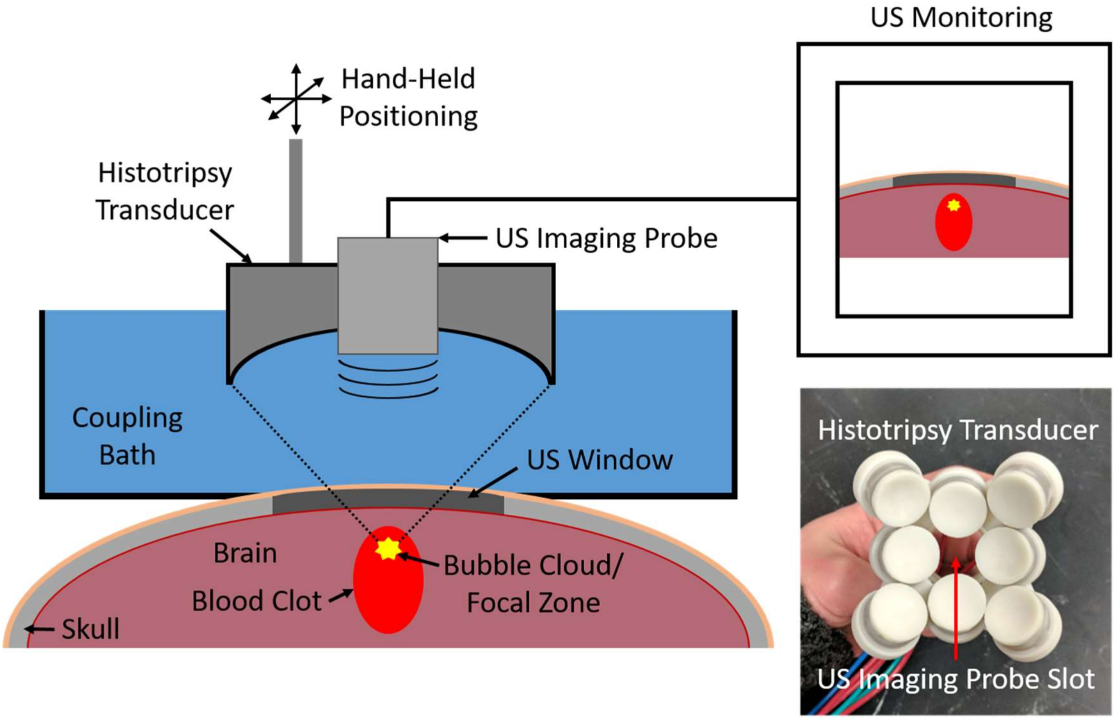

Figure 3.2. An experimental schematic of the histotripsy treatment.

3.2.6 In Vivo Magnetic Resonance Imaging (MRI) Protocol

Samples from each group (n=4-6/group) were evaluated on a 3T MR scanner (MR750, General Electric, Waukesha, WI) 7 to 8 days after the hematoma was formed. The imaging protocol included axial T2 Fast Spin Echo (FSE), T2 Fluid Attenuated Inversion Recovery (FLAIR), T2*-weighted Multi Echo Recombined Gradient Echo (MERGE) and T1 sequences. To examine perihematomal edema, ring shaped regions of interest (ROIs) on the FLAIR images in the periphery of the hematoma were compared to similar shaped ROIs made on the contralateral side of the brain in an identical anatomical site. MRI evaluations were performed by a board certified neuroradiologist who was blinded to the treatment and control groups.

3.2.7 Histological Analysis

Following MR scans, pigs were euthanized. Following euthanasia, the heads were removed fixed whole in 10% phosphate buffered formalin (Fisher Chemical, Pittsburgh, PA, USA). Following fixation, the brains were removed and sectioned around the location of the ICH and stained with hematoxylin and eosin (H&E), Perls' Prussian blue, CD45, and neurofilament 200.

3.2.8 Acute Treatment

A subset of acute treatments was performed to more effectively highlight the immediate effects of histotripsy on the clot and surrounding brain tissue. For the acute subset, treatment was applied directly after the infused blood had coagulated. The liquefied contents were left undrained and the pigs were euthanized within 1 hour following the completion of treatment. Fixation followed the same procedures described above. The fixed brains were imaged using a T2-weighted FSE sequence on a 7T MRI (Varian, Inc., Palo Alto, CA, USA) and sectioned around the location of the ICH.

3.2.9 Statistical Methods

Within each group, pair-wise, independent 2-tailed t-tests ($\alpha=0.05$) were used to compare the signal intensity in ROIs made in the perihematomal region on FLAIR images to that in ROIs made on the contralateral side of the brain. Pair-wise comparisons of the signal intensity in the perihematomal ROI normalized by the mean signal intensity in the contralateral side of the brain were made between each group using independent 2-tailed t-tests ($\alpha=0.05$).

3.3 Results

3.3.1 Acute Treatment

In acute pigs, the untreated clot was fully hypointense on MRI (Fig. 3.3a) which suggested a coagulated acute clot [21]. This contrasted with the hyperintense core and hypointense rim of the clot treated with histotripsy (Fig. 3.3b) which indicated the region of lysed red blood cells (RBCs) surrounded by a rim of un-lysed, intact clot [21]. The H&E stained sections of the brain from the untreated and treated pig showed a fully coagulated acute clot (Fig. 3.3c) and a homogenized, acellular core surrounded by an intact rim (Fig. 3.3d), respectively. There was no evident damage to the surrounding perihematomal region based on the H&E stained sections.

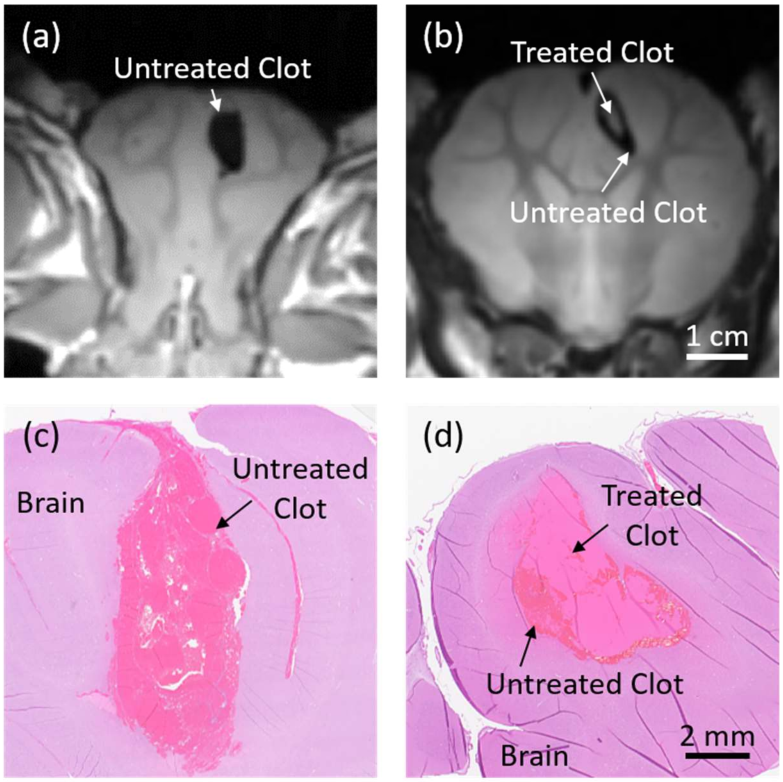

Figure 3.3. The T2-weighted FSE MRI of *ex-vivo*, formalin-fixed acute clot and brain for the (a) untreated pig and (b) treated pig. H&E stained sections of the acute clot and brain for the (c) untreated pig and (d) treated pig. Sections from the untreated pigs showed fully intact coagulated clots whereas the clots treated with histotripsy were characterized by an acellular, homogenized core surrounded by an intact rim of untreated clot.

3.3.2 Neurological Evaluation

There were no significant neurological differences between any of the groups. For each category other than appetite, all pigs received a net score of 0. Appetite scores fluctuated between 0 and 3 but the fluctuations appeared random and showed no relation to a specific group.

3.3.3 Evacuation of the Liquefied Clot after Histotripsy

Directly following histotripsy treatment, the liquefied core of clot was evacuated using a simple drainage technique (Fig. 3.4). Prior to histotripsy treatment, the clots were fully hyperechoic on B-mode (Fig. 3.4a). As histotripsy was applied, the core of the clot transformed from a hyperechoic to hypoechoic appearance, indicating liquefaction (Fig. 3.4b). Inserting the needle to the center and pulling back on the plunger of the syringe easily evacuated the liquid core of the clot. It was not possible to remove the intact hyperechoic regions of the clot. After evacuating the core, a hyperechoic strip corresponding to the intact rim of the clot was left behind (Fig. 3.4c). On average the volume drained after treatment was 0.9±0.5 mL (Tab. 3.1). For pig 6, the reported volume drained was slightly greater than that of the initial clot formed, which was caused by the accidental suction of some of the fluid filling the space between the brain and scalp. Excluding this data point, the average volume drained was 0.7±0. 2 mL.

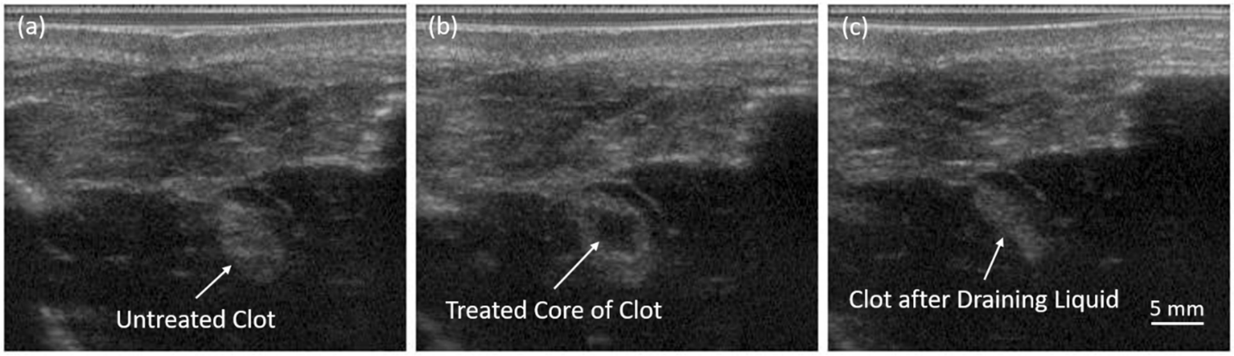

Figure 3.4. B-mode ultrasound images of the clot from a treatment-drained pig (a) before treatment, (b) after treatment and (c) after drainage. Histotripsy treatment produced a hypoechoic core of liquefied clot that was able to be evacuated through a simple drainage technique using a needle and syringe.

Table 3.1. The volume of clot drained from each treatment-drained pig following histotripsy.

	Pig 1	Pig 2	Pig 3	Pig 4	Pig 5	Pig 6*	Mean	Std. Dev.
Volume Drained (mL)	0.5	0.7	0.7	1	0.7	1.8	0.9	0.5

* The slightly greater volume drained was caused by suction of some of the fluid filling the space between the brain and scalp on withdrawal of the needle from the brain.

3.3.4 MRI

All pigs from each group survived 7-8 days post clot formation, at which point MRI was performed (Fig. 3.5). Clots in the control and treatment-undrained groups had a T2 signature typical of a chronic stage ICH with a central hyperintense region surrounded by a hypointense boundary [21]. Similar image characteristics were observed in T2*-weighted images while the T1-weighted images were characterized primarily with a hyperintense region across the entire clot. The T2 FLAIR images showed a hyperintense ring surrounding the clot, indicating the presence of edema. In contrast to the control and treatment-undrained group, the treatment-drained group showed sections where the central region of the clot was successfully evacuated after histotripsy treatment. In these sections, the signal from the hematoma region was more isointense on T2 and T1-weighted images with hypointense spots.

Edema in the perihematomal region was quantified via the T2 FLAIR images. For each group the perihematomal region showed higher T2 FLAIR signal intensity as compared to the contralateral side (Table 2) (p-value<0.05), which was expected due to the presence of the hematoma [22]. Normalized pair-wise comparisons of T2 FLAIR signal in the perihematomal region showed no significant changes between groups (p-value>0.05).

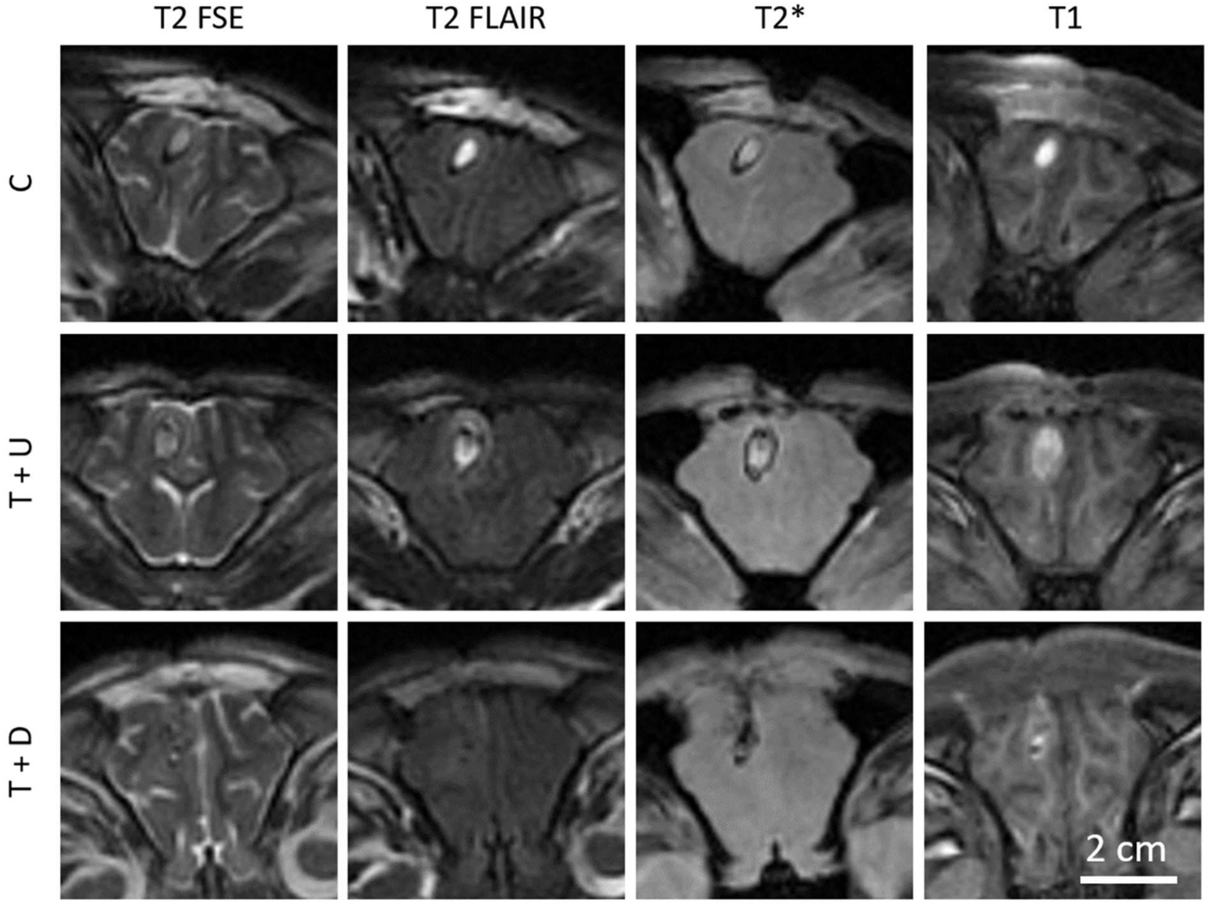

Figure 3.5. MRI of the brain sections with clot from a control (C), treatment-undrained (T-U) and treatment-drained (T-D) pig.

Table 3.2. Measurements made from the ROIs drawn on T2-weighted FLAIR images.

	FLAIR		
	Ipsilateral	Contralateral	(Ipsilateral/Contralateral$_{ave}$)
C (n = 5)	718 ± 168	478 ± 54	1.50 ± 0.35
T/U (n = 6)	722 ± 130	513 ± 60	1.40 ± 0.25
T/D (n = 5)	620 ± 103	402 ± 45	1.54 ± 0.26

3.3.5 Histology

Brains were sectioned around the location of the ICH and stained. In the control group (Fig. 3.6 top), the histology showed well-formed organizing clots with overall normal brain parenchyma surrounding the clot. There was some evidence of cortical ischemia and gliosis, as normally seen in ICH. There was mild lymphocyte and macrophage infiltration at the periphery of the clot with minimal extension into the cortex. Axonal spheroids, indicative of axonal disruption were concentrated around the periphery with a high concentration at the distal end of the clot. The Perls' stain highlighted a circumferential ring of hemosiderin at the clot periphery. The treatment-undrained group (Fig. 3.6 middle) showed ischemia and gliosis surrounding the clot with hemosiderin deposits at the periphery. The portion of clot remaining in the treatment-drained group (Fig. 3.6 bottom) showed similar characteristics to that of the other groups. In one pig from both treatment groups, there was evidence of mild subarachnoid inflammation and hemorrhage, likely from prefocal cavitation, which can occur when the transducer focus is moved close to the boundary of the brain.

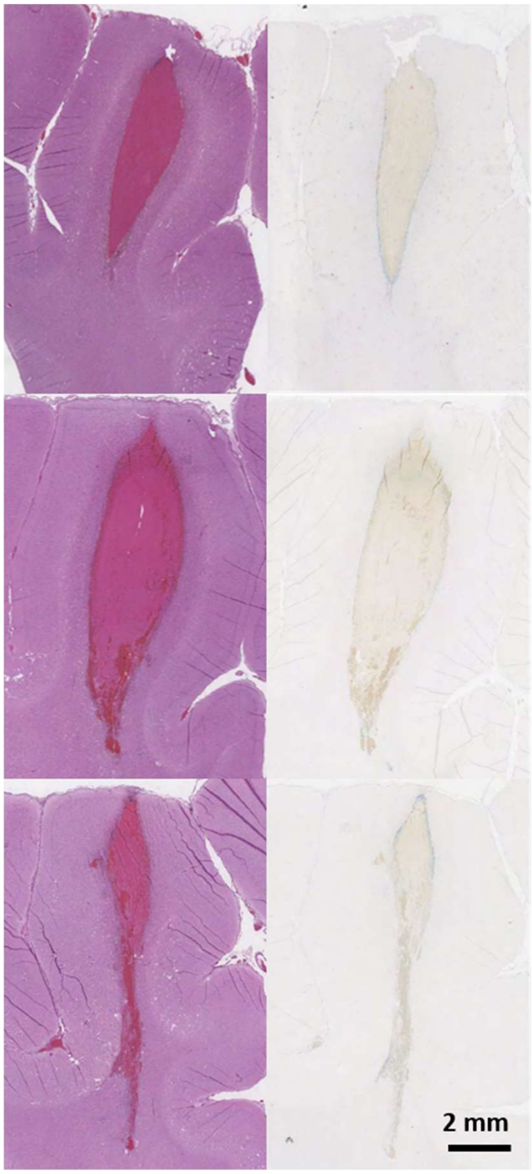

Figure 3.6. H&E (left) and Perls' prussian blue (right) stains of brain sections with clot from a control (top), treatment-undrained (middle) and treatment-drained (bottom) pig. The blue color in the Perls' Prussian blue indicated hemosiderin deposition.

3.4 Discussion

This study presents the first analysis of histotripsy-based liquefaction of ICH *in-vivo*. Clot cores were accurately targeted and successfully liquefied using histotripsy without significant damage to overlying or surrounding perihematomal cerebral tissue as evident on histology and

MRI. The liquefied content of the treated cores was easily evacuated with a simple drainage technique and when left undrained had no effect on pig survival and no measured effect on neurological behavior. This study addresses the initial the safety concerns of using histotripsy for ICH treatment.

The precision of histotripsy treatment was exemplified by the fact that we were able to intentionally leave a 1-2 mm rim of clot intact which minimized the possibility of causing immediate, direct damage to the perihematomal region via the cavitation activity of the bubble cloud. In a clinical case, it is hypothesized that this would prevent rebleed as the vessel responsible for a rebeleeed should be at the periphery. While there was evidence of mild subarachnoid damage in two of the treatment pigs, likely from prefocal cavitation, it was small in extent and confined to small regions at the periphery of the brain, with no evidence of neurological compromise. However, the presence of this raises some safety concerns and further studies may be needed to understand its long term effects and its effect on rebleed. This could be done using a bacterial collagenase porcine ICH model [23]. The liquefied core was easily drained using a simple drainage technique. Given the small initial volume of the clots (1.75 mL) and the fact that we intentionally left a rim of clot intact, only about half of the initial clot volume was liquefied and subsequently drained. Consequently, a significant portion of the initial clot remained within the brain after evacuation of the treated portion. The small clot volume is a limitation of the porcine model due to the small size of the pig brain. With larger clots typical of human ICH where early intervention is likely a necessity (≥30 mL) [2], a larger proportion of the clot can be targeted while leaving the same size rim intact and thus a larger percentage of the clot can be liquefied and evacuated.

Previous studies injecting 2.5 mL of lysed blood into the porcine brain have revealed significant cerebral injury with erythrolysis including poor neurological functioning and death [4],

[17]. The adverse outcome is thought to be caused by the toxic effect of the hemolysates. In this study, the lysed blood contents generated with histotripsy showed some cerebral swelling and gliosis but no effect on survival or neurological function. The hemosiderin was confined mostly to the rim of the clot and there was no observed difference in edema. As other studies report much more striking effects due to the introduction of lysed blood into the brain [13]–[17], the minimal effect observed here could be related to the rim of intact clot left untreated which may have served as a barrier between the liquefied clot and surrounding brain tissue.

Given prior studie s[11], [12] as well as the current *in-vivo* study, histotripsy may prove to be a unique approach to rapid liquefaction and evacuation of ICH in a minimally-invasive manner. In comparison to MRgFUS, which uses longer pulses and requires MRI, histotripsy can treat large[11] and superficial regions [24] in shorter durations of time. As MRgFUS relies on thermal absorption to necrose tissue in the targeted region, the therapy must be delivered slowly, typically on the order of ≤0.2 mL/min, to avoid perilesional and skull heating. Overall, to achieve safe liquefaction at clinically relevant timescales, MRgFUS therapy is restricted to small, central volumes within the brain. In a previous *in-vitro* histotripsy ICH study, 40 mL clots were liquefied in 20 minutes (2 mL/min) by applying histotripsy transcranially through human skulls while the skull heating remained within a clinically safe range [11]. The goal is to develop this minimally invasive technology without reliance on MRI. Patients with primary ICH who do not have a vascular lesion as evident on CT will be candidates for histotripsy treatment of ICH. Localization can be done by utilizing a preoperative CT and neuro-navigation to place the transducer focus at the center of the ICH. Real-time treatment monitoring will be done via cavitation mapping through the skull using the histotripsy transducer itself [25]. Post treatment, the ICH will be immediately evacuated utilizing a previously placed catheter hydrophone [12] and the drain will be left in place for further drainage.

The current study has limitations and additional work is necessary to further demonstrate the clinical efficacy and safety of histotripsy for use in ICH treatment. Although this model is well-established, the small ICH volume limits the clinical relevance for therapeutic effects. Large ICH models (human cadavers or skull phantoms) with ICH at different anatomical locations are needed to capture human ICH experience. Further, longer term survival studies (up to 3 months) are needed to understand the long term safety of histotripsy treatment. Additionally, as the pig skull is not conducive to the transmission of focus ultrasound, a craniotomy was necessary and effects of skull heating and associated safety implications at the skull-brain interface could not be addressed. In human, the craniotomy will not be needed. The effect to the skull and the brain close to the skull will be investigated using the human cadaver model.

3.5 Conclusion

This study presents the first analysis of histotripsy-based liquefaction of ICH *in-vivo.* We aimed to investigate the initial safety concerns of histotripsy clot liquefaction in a well-established porcine ICH model. The liquefied content of the treated cores was easily evacuated with a simple drainage technique and when left undrained had no effect on pig survival and no measured effect on neurological behavior. Further safety studies are needed to understand the long term safety (up to 3 months) associated with using this technology as well as to understand prefocal cavitation and address the risk of rebleeds.

3.6 References

[1] T. Gerhardson *et al.*, “Histotripsy Clot Liquefaction in a Porcine Intracerebral Hemorrhage Model,” *Neurosurgery*, 2019.

[2] J. P. Broderick, T. G. Brott, J. E. Duldner, T. Tomsick, and G. Huster, “Volume of intracerebral hemorrhage. A powerful and easy-to-use predictor of 30-day mortality,” *Stroke*, vol. 24, no. 7, pp. 987–993, 1993.

[3] M. L. Flaherty *et al.*, “Long-term mortality after intracerebral hemorrhage,” *Neurology*, vol. 66, no. 8, pp. 1182–1186, 2006.

[4] G. Xi, R. F. Keep, and J. T. Hoff, “Mechanisms of brain injury after intracerebral haemorrhage.,” *Lancet. Neurol.*, vol. 5, no. 1, pp. 53–63, 2006.

[5] A. I. Qureshi, S. Tuhrim, J. P. Broderick, H. H. Batjer, H. Hondo, and D. F. Hanley, “Spontaneous Intracerebral Hemorrhage,” *N. Engl. J. Med.*, vol. 344, no. 19, pp. 1450–1460, 2001.

[6] Z. Xu *et al.*, “Controlled ultrasound tissue erosion,” *IEEE Trans. Ultrason. Ferroelectr. Freq. Control*, vol. 51, no. 6, pp. 726–736, 2004.

[7] Z. Xu, J. B. Fowlkes, E. D. Rothman, A. M. Levin, and C. A. Cain, “Controlled ultrasound tissue erosion: The role of dynamic interaction between insonation and microbubble activity,” *J. Acoust. Soc. Am.*, vol. 117, no. 1, pp. 424–435, 2005.

[8] W. W. Roberts, T. L. Hall, K. Ives, J. S. Wolf, J. B. Fowlkes, and C. A. Cain, “Pulsed cavitational ultrasound: A noninvasive technology for controlled tissue ablation (histotripsy) in the rabbit kidney,” *J. Urol.*, vol. 175, no. 2, pp. 734–738, 2006.

[9] Z. Xu, G. Owens, D. Gordon, C. Cain, and A. Ludomirsky, “Noninvasive creation of an atrial septal defect by histotripsy in a canine model,” *Circulation*, vol. 121, no. 6, pp. 742–749, 2010.

[10] K. W. Lin *et al.*, “Histotripsy beyond the intrinsic cavitation threshold using very short ultrasound pulses: Microtripsy,” *IEEE Trans. Ultrason. Ferroelectr. Freq. Control*, vol. 61, no. 2, pp. 251–265, 2014.

[11] T. Gerhardson, J. R. Sukovich, A. S. Pandey, T. L. Hall, C. A. Cain, and Z. Xu, “Effect of Frequency and Focal Spacing on Transcranial Histotripsy Clot Liquefaction, Using Electronic Focal Steering,” *Ultrasound Med. Biol.*, vol. 43, no. 10, pp. 2302–2317, 2017.

[12] T. Gerhardson, J. R. Sukovich, A. S. Pandey, T. L. Hall, C. A. Cain, and Z. Xu, “Catheter Hydrophone Aberration Correction for Transcranial Histotripsy Treatment of Intracerebral Hemorrhage: Proof-of-Concept,” *IEEE Trans. Ultrason. Ferroelectr. Freq. Control*, vol. 64, no. 11, 2017.

[13] G. Xi, Y. Hua, R. R. Bhasin, S. R. Ennis, R. F. Keep, and J. T. Hoff, “Mechanisms of edema formation after intracerebral hemorrhage: effects of extravasated red blood cells on blood flow and blood-brain barrier integrity.,” *Stroke.*, vol. 32, no. 12, pp. 2932–8, 2001.

[14] G. Xi, R. F. Keep, and J. T. Hoff, “Erythrocytes and delayed brain edema formation following intracerebral hemorrhage in rats.,” *J. Neurosurg.*, vol. 89, no. 6, pp. 991–996,

1998.

[15] J. Wu, Y. Hua, R. F. Keep, T. Schallert, J. T. Hoff, and G. Xi, "Oxidative brain injury from extravasated erythrocytes after intracerebral hemorrhage," *Brain Res.*, vol. 953, no. 1–2, pp. 45–52, 2002.

[16] P. G. Matz, P. R. Weinstein, and F. R. Sharp, "Heme oxygenase-1 and heat shock protein 70 induction in glia and neurons throughout rat brain after experimental intracerebral hemorrhage," *Neurosurgery*, vol. 40, no. 1, pp. 152–162, 1997.

[17] K. R. Wagner, G. Xi, Y. Hua, G. M. de Courten-Myers, and J. P. Broderick, "Blood components and acute white matter edema development following intracerebral hemorrhage: are hemolysates edemogenic?," in *Stroke*, 2000, p. 345.

[18] K. R. Wagner *et al.*, "Lobar intracerebral hemorrhage model in pigs: Rapid edema development in perihematomal white matter," *Stroke*, vol. 27, no. 3, pp. 490–497, 1996.

[19] Y. Tanaka *et al.*, "Experimental model of lacunar infarction in the gyrencephalic brain of the miniature pig: Neurological assessment and histological, immunohistochemical, and physiological evaluation of dynamic corticospinal tract deformation," *Stroke*, vol. 39, no. 1, pp. 205–212, 2008.

[20] M. Yamaguchi, C. Zhou, D. D. Heistad, Y. Watanabe, and J. H. Zhang, "Gene transfer of extracellular superoxide dismutase failed to prevent cerebral vasospasm after experimental subarachnoid hemorrhage.," *Stroke.*, vol. 35, no. 11, pp. 2512–7, 2004.

[21] T. A. G. M. Huisman, "Intracranial hemorrhage: Ultrasound, CT and MRI findings," *European Radiology*, vol. 15, no. 3. pp. 434–440, 2005.

[22] K. Dul and B. P. Drayer, "CT and MR imagining of intracerebral hemorrhage," in *Intracerebral hemorrhage*, C. S. Kase and L. R. Caplan, Eds. Boston: Butterworth-Heinemann, 1994, pp. 73–98.

[23] S. Mun-Bryce, A. C. Wilkerson, N. Papuashvili, and Y. C. Okada, "Recurring episodes of spreading depression are spontaneously elicited by an intracerebral hemorrhage in the swine," *Brain Res.*, vol. 888, no. 2, pp. 248–255, 2001.

[24] J. R. Sukovich, Z. Xu, T. L. Hall, S. P. Allen, and C. A. Cain, "Treatment envelope of transcranial histotripsy applied without aberration correction," in *The Journal of the Acoustical Society of America*, 2016.

[25] J. R. Sukovich, T. L. Hall, J. J. Macoskey, and Z. Xu, "Real-time transcranial histotripsy treatment monitoring and localization using acoustic cavitation emission feedback," in *6th International Symposium on Focused Ultrasound*, 2018.

CHAPTER 4 Catheter Hydrophone Aberration Correction for Transcranial Histotripsy Treatment of Intracerebral Hemorrhage: Proof-of-Concept

This chapter has been published in *IEEE Transactions on Ultrasonics, Ferroelectrics, and Frequency Control*. 2017; 64(11): 1684-1697. © IEEE. Reprinted with permission, from [1].

4.1 Introduction

Hemorrhagic stroke or intracerebral hemorrhage (ICH) accounts for about 15% of all strokes and affects roughly two million people worldwide [2]–[4]. ICH is caused by the rupture of blood vessels within the brain thus leading to the accumulation of blood products within the brain parenchyma. The initial injury post bleed leads to a mass-occupying lesion and thus mechanical injury of adjacent neurons, axons, and supporting cellular matrix. In addition, the presence of the ICH leads to a rise in intracranial pressure (ICP) which in turn leads to a decrease in cerebral perfusion pressure and related ischemia. The secondary injury to the brain occurs over days and weeks and is caused by the cytotoxicity related to metabolism of red blood cell (RBC) components, specifically hemoglobin. This combination of primary and secondary injuries associated with ICH leads to an approximate 30-day mortality rate of 40% [5], [6].

The standard clinical treatments for ICH consist of either medical management to optimize cerebral blood flow while decreasing ICP or a craniotomy surgery to remove the ICH [7]–[10]. Medical management may be sufficient for a small ICH volume but to normalize ICP as well as to prevent secondary injuries, it is essential to remove the clot burden. Craniotomy surgery provides quick access for clot evacuation, but it is highly invasive leading to additional damage as normal cerebral tissue must be traversed, and an evaluation on its effectiveness for a large number of cases remains inconclusive [11]–[14].

Minimally invasive clot evacuation techniques using thrombolytic drugs and catheters have been gaining clinical support and are currently undergoing clinical trials [15]–[17]. The most common approach utilizes a ventriculostomy catheter placed within the clot and the administration of thrombolytic drugs, such as recombinant tissue plasminogen activator, allowing liquefaction and drainage of the clot. Although early patient outcomes have shown promise in reducing clot size, the functional outcome of ICH survivors has not improved. While this is a minimally invasive technique, it takes days (3)–(7) to evacuate the ICH and there are hemorrhagic complications that are related to the administration of thrombolytic drugs. For small blood clots in ischemic stroke, these techniques have been combined with low-amplitude ultrasound pulses with and without contrast agents [18]–[24]. Although these techniques have shown an improved treatment rate relative to those used for ICH, such approaches remain limited for treating large clots characteristic of ICH by the lack of perfusion of microbubbles and drugs deep into the interior of the clot. In addition, the drugs used have a high risk of rebleed, adverse localized edema and swelling side effects.

Magnetic resonance guided focused ultrasound (MRgFUS) has recently been developed to assist minimally invasive clot evacuation techniques used to treat ICH; however, treatment times are long and the process leads to overheating the skull. Animal and human cadaver studies have shown that applying MRgFUS outside the skullcap can liquefy clots without the need for thrombolytic drugs [25]–[27].The resulting liquid can then be aspirated out with a needle. Although MRgFUS has shown the ability to shorten the clot reduction time, the use of pulses greater than100 μs at a relatively high duty cycle (10%) limit the treatment range within the skull and present an issue of the skull overheating [25], [28]–[30]. Furthermore, the need for costly MR imaging for the entire MRgFUS treatment is a roadblock for any future widespread clinical adoption.

Histotripsy is a focused ultrasound technology that controls cavitation to liquefy soft tissue such as clots. Histotripsy uses short, high-energy pulses to generate cavitation microbubble clouds using the intrinsic nuclei existing in the target tissue [31]–[34]. High stress and strain is generated in tissue at the focus due to the rapid bubble expansion and collapse that fractionates the tissue into an acellular homogenate [35]. The ability to liquefy clots using histotripsy has been demonstrated in leg vessels both in vitro and in vivo [36]–[42]. Histotripsy and boiling histotripsy were also reported to treat an in vitro model of large extravascular hematomas in the absence of aberration [43]. Recent work has shown the in vitro feasibility of histotripsy as a transcranial therapy [44], [45]. We have also shown the ability to liquefy clots through excised human skullcaps using histotripsy in an in vitro study [46]. Similar to MRgFUS, histotripsy can be used to liquefy clots through the skull. The liquefied volume can then be aspirated via a catheter inserted into the clot through a small bur hole. The purpose of this paper was to propose a solution to the problem of skull aberrations in developing histotripsy as a minimally invasive technology for treating ICH.

One significant barrier in developing focused ultrasound technologies for ICH and other transcranial therapies is the ultrasound distortion induced by the skull. Due to sound speed and thickness inhomogeneities inherent to the skull, both MRgFUS and histotripsy suffer from ultrasound defocusing caused by skull-induced acoustic aberration. This causes significant focal amplitude loss and beam widening, resulting in an overall decrease in treatment efficacy and precision [47], [48]. MRgFUS is capable of correcting for skull-induced acoustic aberrations using MRI guidance and computed tomography (CT) scans obtained prior to treatment. However, this technique requires a sophisticated algorithm, significant treatment planning and extensive MRI time required for MRgFUS treatment leading to a prohibitively high cost. Moreover, these aberration corrections (ACs) degrade if the skull moves with respect to the transducer. MR acoustic radiation force imaging techniques can outperform CT methods and overcome issues of degraded corrections associated with potential movements of the skull [49]. However, this technique still relies on MRI making it expensive and potentially difficult to adopt.

Many other approaches have been investigated to overcome the skull-induced acoustic aberration for transcranial applications of focused ultrasound with varying degrees of success. Simulation techniques are completely noninvasive and use CT images of the skull obtained prior to treatment to derive the thickness and acoustic properties of the skull to approximate the aberration through the skull and correct for it [50]–[54]. These techniques have shown good corrections [55]. However, they require significant treatment planning and time (i.e., 2 h to execute the simulation) [56]. Furthermore, the difference in position of a patient's head between prior scans and treatment can lead to error. Time-reversal techniques involve (1) acquiring a signal transmitted through the skull to or from a single point within the field (2) time reversing the signals and (3) re-emitting the signals by the elements of the array [57]–[64]. Variations of acoustic sources and reflectors placed at the focus have been examined in vitro including implanted hydrophones and acoustic stars [65]–[67]. Hydrophones allow measurement of the waveform timing information with a high degree of accuracy and are a consistent reference for various AC techniques, thus AC using a hydrophone as a receiver remains a near optimal correction technique.

A catheter hydrophone (CH) solution for AC in histotripsy treatment of ICH was devised based on two considerations. First, the mainstay minimally invasive approach to ICH treatment already requires inserting a catheter through a small bur hole in the skull to drain the liquefied clot.

Second, AC with a hydrophone is considered a near optimal AC technique. A miniature acoustic hydrophone integrated into a drainage catheter provides the ability to conduct the AC necessary for histotripsy treatment while simultaneously providing a means to drain the liquefied clot volume. Since commercial hydrophones are too large to fit within catheters used in minimally invasive brain surgery (I.D.~2 mm), we needed to fabricate our own miniature hydrophone that could fit inside a catheter. The primary goals of this initial study were (1) to fabricate a hydrophone small enough to fit within a catheter and (2) to show the proof-of-concept of using a CH AC technique for transcranial histotripsy ICH treatment.

4.2 Materials and Methods

4.2.1 Experimental Equipment

Transcranial Phased Array Transducer: A 500-kHz 256-element hemispherical transcranial histotripsy array with 15-cm focal distance was used in this paper. The array was built in our lab using similar methods as those described in [68]. The individual elements populating the array were comprised of two 1-MHz 20-mm diameter flat, stacked piezo ceramic discs (PZ36, Ferroperm, Kvistgaard, Denmark) that produced a combined center frequency of 500 kHz. The array was placed into a water tank with base dimensions of 60 × 60 cm and height of 40 cm. Degassed water was added to the tank such that the level was approximately 1 cm from the top of the tank. A 256-channel high voltage pulser, capable of delivering short (≤2 acoustic cycles) high-amplitude ultrasound pulses, was used to drive the elements of the array. The pulser was connected to a field programmable gated array (FPGA) board (Altera DE1, Terasic Technology, Dover, DE, USA) which was used to control the array. The clock speed of the FPGA was 100 MHz, giving the driver a temporal precision of 10 ns. Histotripsy pulse sequence parameters were defined through a custom MATLAB (MathWorks, Natick, MA, USA) program and uploaded to the FPGA board.

Catheter Hydrophone Fabrication: A custom, miniature hydrophone integrated with a silicone rubber drainage catheter capable of performing AC and draining liquefied clot was fabricated in our laboratory. The main challenge in fabricating this hydrophone was keeping the piezoelectric element of the hydrophone small enough to fit within the catheter (2-mm I.D.) while maintaining high enough sensitivity to measure acoustic waveforms through the skull. Due to its high coupling coefficient and high sensitivity, PZT-5h was used as the piezoelectric element. A 0.5 × 0.5 mm chip of PZT-5h (Steminc-Piezo, Miami, FL) was diced from a larger 0.3-mm-thick wafer using a razor blade. The dimensions of the crystal were made as small as possible with respect to the wavelength of the transducer's operating frequency in attempt to establish a point-receiver measurement technique. The PZT chip was interfaced to a coaxial cable by soldering the positive and ground leads of a 1.77-mm O.D. coaxial cable to the respective silver electrodes on the opposing 0.5 × 0.5 mm faces of the PZT-5h crystal (Fig. 4.1). The crystal and its point of attachment to the cable were coated with epoxy (Loctite E-00NS, Düsseldorf, Germany) such that the epoxy layer was flush with the casing of the coaxial cable and all electrically conductive components were sealed. Any visible bubbles surrounding the crystal-cable interface were removed prior to the epoxy curing. After the epoxy cured, the crystal cable assembly was inserted fully into the drainage catheter so that the tip of the assembly touched the end of the catheter. The coaxial cable acted as the guide wire to guide the assembly through the catheter. With the exception of those presented in the *Hydrophone Characterization—Time-of-flight Measurements and Directivity* section, all experiments using the CH were performed with the miniature hydrophone inserted into the catheter sheath. In that section, the measurements were done without the sheath because the CH could not accurately be rotated 180° given our current setup, which was necessary for characterizing the directivity of the hydrophone.

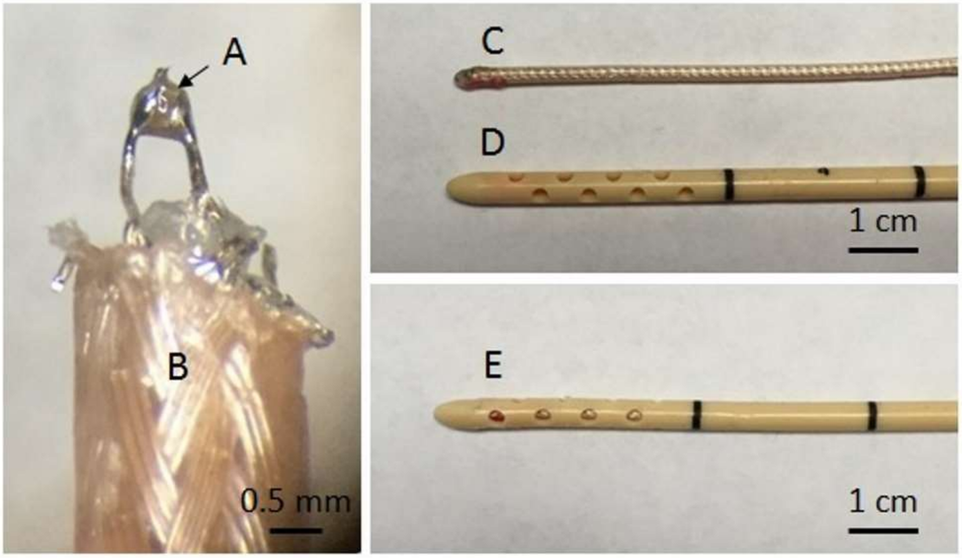

Figure 4.1. Images of the fabrication steps of a custom catheter hydrophone. (A) Indicates a 0.5 × 0.5 × 0.3 mm PZT-5 crystal soldered between the leads of a (B) 1.77 mm OD coaxial cable. (C) Shows the crystal-cable assembly after coating the tip with epoxy and (D) shows the clinical drainage catheter. (E) Displays the final assembly of the catheter hydrophone.

4.2.2 Hydrophone Characterization

Noise Characterization: To perform AC it was important that the CH had sufficient signal-to-noise ratio (SNR) as to distinguish characteristic features (e.g., peak-negative pressure) from the waveform of each individual element. Such features were used as reference points to obtain the corrective delays among the 256 individual element waveforms transmitted through the skull. An average SNR was obtained by averaging the SNR for each of the 256 single element waveforms measured with the CH. SNR calculations were performed by measuring the ultrasound pulse signal from each of 256 individual elements while operating the array at pressure conditions comparable to those used in transcranial treatment. A signal with the array powered off was obtained as the pure noise reference. To understand the attenuation effects of the catheter sheath, the average insertion loss (i.e., pressure decrease with the catheter sheath surrounding the miniature hydrophone relative to the miniature hydrophone without the sheath) from all 256 waveforms was measured.

Time-of-Flight Measurements and Directivity: Since intrinsic threshold histotripsy relies on the amplitude of the peak-negative pressure, the efficacy of AC using our CH was dependent on its ability to temporally align the peak negative pressure from the individual element waveforms. To understand our hydrophone's ability to align these signals, it was important to quantify any variation in the peak-negative pressure time-of-flight as a function of the angle of ultrasound propagation from the array with respect to the CH. Due to the hemispherical shape of the array, the angle of the pulse received by the hydrophone from the elements varied from 0°–360°. Time-of-flight measurements acquired with the CH (without the catheter sheath) were compared to those made with a PVDF capsule hydrophone (Cap. Hyd.) (HGL200, Onda, Sunnyvale, CA, USA), which has minimal variability in the time-of-flight as a function of angle of ultrasound propagation. The catheter sheath was excluded from these measurements, because the CH could not accurately be rotated 180° in the catheter sheath with our current setup. Any directivity shown in this measurement was therefore inherent to the custom hydrophone in the absence of the sheath. Each hydrophone was positioned to the geometric origin of the array by performing three-axis beam scans of the pressure field and moving the hydrophone to the location of the peak-negative pressure. The 256 individual elements of the array were then fired individually, one at a time, and the time-of-flight of each pulse from the array to the geometric focus was measured. This experiment was repeated using our CH. To ensure that the CH was "finding" the same focus as the Cap. Hyd. during the preliminary scans and those variations in the time-of-flight measurements were not a result of discrepancies in position between the hydrophones within the array, the CH was rotated 180° with respect to the array and measurements were repeated. A set of angular dependent delays were calculated by subtracting the CH measured peak-negative pressure time-of-flight from that of the Cap. Hyd.

4.2.3 Sample Preparation

Skullcap Preparation: As the presence of extracranial tissue (i.e., skin and brain) was expected to be a minor source of aberration relative to the skull, experiments were conducted using an excised human skullcap. The skullcap obtained through the University of Michigan Anatomical Donations Program. The skullcap was defleshed and cleaned after extraction and continuously kept in water thereafter. Prior to experiments the skullcap was degassed inside a vacuum chamber for a minimum of a week. A 3-D laser scan (Ultra HD 2020i, NextEngine, Santa Monica, California) of the skullcap was used to map the skullcap into 256discrete thickness values that corresponded to the region of skullcap centered around the ray from each element based on concentric positioning of the skullcap within the array.

Red Blood Cell Phantom Preparation: RBC phantoms were used to analyze the size of lesions generated through the skull using histotripsy pulses. RBC phantoms were prepared from an agarose-saline mixture and RBCs following previously established protocols [69]. These phantoms consisted of three layers: a very thin (∼500 μm) RBC-agarose gel layer sandwiched between two transparent agarose gel layers (∼10 mm thick). The RBC-agarose gel layer provided contrast for indicating cavitation damage. That is, the RBC-agarose gel layer changed from translucent and red to transparent and colorless following the RBC lysis that resulted from cavitation-induced lysis of RBCs.

Blood Clot Preparation: The capability of the CH AC for transcranial histotripsy clot liquefaction was evaluated through in vitro experiments using bovine blood clots. Bovine blood was harvested from a local abaittor and mixed with citrate phosphate dextrose (CPD) (Boston

Bioproducts, Ashland, MA, USA) with a CPD-to-blood ratio of 1:9 (v:v) to prevent it from clotting during transport and storage. The blood was stored at 4 °C prior to usage and used within two weeks of harvesting. Clots were prepared by mixing 75 mL of degassed bovine blood and 3 mL of calcium chloride (#21107, Sigma-Aldrich Co., St. Louis MO, USA) for a final concentration of 20 mm/l. The 78 mL blood/CaCl2 mixture was poured into a latex condom and tied off to form a 50-mm diameter sphere shaped volume. The clots were placed into a water bath kept at 38.6 °C for 6 h to solidify. Solidified clots were transferred to a refrigerator at 4 °C for 12 h prior to treatment. Before treatment clots were brought to room temperature (~23 °C).

4.2.4 Catheter Hydrophone Measurements and Aberration Correction

Catheter Hydrophone Measurements: The skullcap was positioned concentrically within the array and aligned such that the plane along which it was cut lie 10 mm beyond the plane of the outermost elements of the array. This positioning, with the geometric focus near the center of the skull, corresponds to one which will potentially be used to treat the majority of ICH cases in the future in vivo and clinical applications [70], [71]. The CH was then positioned to the geometric origin of the array by performing three-axis beam scans of the pressure field and moving the hydrophone to the location of the peak-negative pressure (Fig. 4.2). The 256 individual elements of the array were then triggered one at a time to emit histotripsy pulses which were measured with the CH. A total of 50 waveforms were acquired from each of the 256 elements of the array and averaged together to generate a single waveform for each element. The entire acquisition took about 10 min. The 256 waveforms were then loaded into the AC algorithm used to perform AC.

Aberration Correction: An AC algorithm was designed to calculate the delays required to align the peak-negative pressure of the 256 waveforms acquired through the skull to geometric origin of the array. The AC algorithm consisted of 4 steps: 1) a first-order bandpass filter with a passband between 100 and 850 kHz was used to reduce the noise in the waveforms; 2) the time points of the peak-negative values of the pressure were then found for each of the 256 elements of the array; 3) the requisite delays for AC (i.e., how long the firing times of each element must be delayed with respect to one another in order to ensure their concurrent arrival at the focus) were then calculated with respect to the time point at which the peak-negative value from an arbitrary reference element was recorded from step 2. This was done by subtracting each of the 256 measured delays from the reference value; and 4) to ensure that the calculated delays were within a reasonable time window given the known characteristics of the skullcap (thickness and sound speed) and histotripsy waveforms, a windowing function was used to exclude delays that fell outside of a 4 μs window centered about the mean of the calculated delays. This 4 μs window was based on a calculation of the largest expected delay based on the maximum and minimum thickness (11.1 and 2.6 mm, respectively) of the specific skullcap used and an average sound speed (2300 m/s) taken from the literature [72]. As the sound speed was not specific to the skullcap and also varied throughout the skullcap, we expected some degree of error in the exclusion of waveforms. Such errors were expected to arise from signals with low SNR where variability in noise peaks could alter the true delay calculation. Delays excluded by the windowing function were set equal to that of their nearest neighboring element. Due to restrictions on the minimum (0 μs) and maximum (68 μs) relative delays between the firing times of individual elements imposed by the FPGA, a fixed offset was then applied to the delay set such that the minimum delay was 0 μs. The final delay set was then uploaded to the FPGA boards and set as a fixed temporal offset to the triggering times of each element.

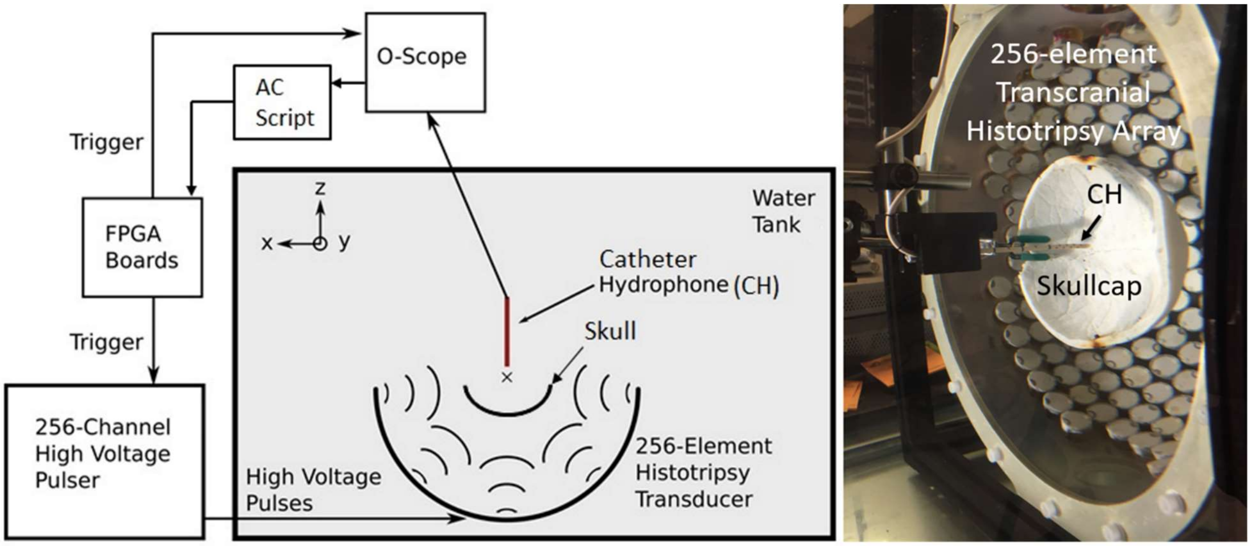

Figure 4.2. The experimental schematic of the setup used to perform the transcranial histotripsy clot treatments through the excised human skullcaps (left) and a photograph of the actual experimental setup (right). The 256 individual elements of the array were triggered one-at-a-time, to emit histotripsy pulses. Waveforms were measured by the catheter hydrophone (CH) and uploaded to an aberration correction algorithm. The 256 element delays were obtained and uploaded to the FPGA boards.

4.2.5 Evaluation of Catheter Hydrophone Aberration Correction

Focal Pressure Measurements: To characterize the alignment of the waveforms at the focus and ultimately the peak-negative pressure recovered due to AC, the transcranial focal pressure was measured under conditions where the array was operated with and without AC. For the transcranial case without AC, the 256 elements of the array were triggered in unison. For the transcranial case with AC, each element was delayed by its respective delay calculated using the AC algorithm and CH measurements. Focal pressure waveforms with AC were obtained using measurements made with both the CH and PVDF Cap. Hyd. To ensure cavitation did not disrupt measurements, pressure measurements were obtained below 20 MPa using a fiber optic hydrophone (FOPH) built in-house [73]. For measurements above the intrinsic threshold, cavitation exists 100% of the time, thus rarefactional pressures beyond 26–30 MPa are unlikely to be generated or measured. Due to this, precise measurements of peak-negative pressures nearing or beyond the intrinsic threshold cannot be made and as such, those peak-negative pressures beyond 20 MPa stated throughout this paper are estimated by linear summation of the measured peak-negative pressure amplitudes of the individual transducer elements. These pressure extrapolations are intended only as indications of the likelihood of cavitation in the focal region and the pressure overhead during treatment. For peak-negative pressures below 20 MPa, the focal pressure obtained from the linear summation method matches well with the direct FOPH measurements.

Beam Profiles: To further characterize the extent to which AC realigned the waveforms at the focus, 1-D beam profiles in the absence of aberration and through the skullcap with and without AC were obtained. Beam profiles were measured at low pressure (i.e., <2 MPa) using a PVDF Cap. Hyd. (HGL200, Onda, Sunnyvale, CA, USA). For the case where aberration was absent and transcranial case without AC, the 256 elements of the array were triggered in unison. For the transcranial case with AC, each element was delayed by its respective delay calculated using the AC algorithm and the CH measurements. The hydrophone was positioned to the focus and scanned ±25 mm from the geometric origin in 0.25-mm steps in the sagittal, coronal and axial directions. For each case, the −6-dB beamwidth was measured.

Pressure versus Electronic Focal Steering: To understand the extent to which AC performed at a single position (i.e., the geometric origin) improved the electronic focal steering of the array transcranially, the focal pressure as a function of electronic focal steering position was measured with and without AC across a range of steering locations. For the case without AC, the 256 elements of the array were triggered in unison. For the case with AC, the individual element delays calculated using the CH measurements performed only at the geometric origin of the array were added to the delays for each steered location. The array was steered ±20 mm from the geometric origin in 1-mm steps in the sagittal, coronal and axial dimension. For each driving condition at each steering position a PVDF Cap. Hyd. was positioned to the steering location and used to measure the peak-negative pressure.

Lesion Generation Using Electronic Focal Steering: To further evaluate single point AC with the CH, lesions were generated transcranially in an RBC phantom at a range of steering locations. The individual element delays calculated using the CH measurements performed only at the geometric origin of the array were again added to the steering delays for each steered location. An RBC phantom was positioned into the skullcap with the RBC-agarose gel layer in plane with the sagittal-coronal plane of the array. Using electronic focal steering, the focus was steered through a 9 × 9 grid of steering positions: ±10 mm from the geometric origin in 2.5-mm steps in the sagittal and coronal direction. 200 histotripsy pulses were applied to each point at a linearly extrapolated peak-negative pressure of 36 MPa as measured through the skullcap at the geometric origin of the array. Pulses were delivered to each point at a pulse repetition frequency (PRF) of 0.5 Hz. Following lesion generation, the RBC phantoms and corresponding lesions were placed on a light table and imaged. Post processing of optical images was done using MATLAB in a method similar to that described in previous papers [74], [75]. Images were gray-scaled and lesions were circled. The area and diameter of lesions was determined by calibrating the pixel size and counting the number of white pixels.

In Vitro Clot Treatment Using Electronic Focal Steering: To show the effects of transcranial histotripsy with CH AC in treating ICH an in vitro bovine clot ICH model was developed and treated using transcranial histotripsy. Following AC with the CH, clots were mounted centrally within the skullcap such that geometric focus was approximately within the center of the clot. Using phased steering, the focus of the array was steered through a 20-mm diameter spherical, hexagonal-closed-packed lattice pattern. The lattice focal point spacing was set to 1.5 mm (λ/2). This corresponded to 1749 discrete treatment points. A total of 200 pulses at a peak-negative pressure of 36 MPa were applied to each focal point at an overall PRF of 200 Hz and local PRF of ~0.5 Hz. The total clot volume liquefied with histotripsy was drained by inserting the CH into the clot, removing the hydrophone and aspirating the liquefied volume using a 10-mL syringe. To ensure the reported drainage volumes corresponded to that resulting from histotripsy treatment, three control clots, unexposed to histotripsy were drained using the same technique. The lesions of undrained clots treated with histotripsy were analyzed using B-mode ultrasound and T2-weighted MRI. Drained clots were fixed in 10% phosphate buffered formalin (Sigma-Aldrich, St. Louis, MO, USA) and imaged using a DSLR camera (Canon, Tokyo, Japan).

4.3 Results

4.3.1 Hydrophone Characterization

Noise Characterization: An average SNR was obtained by averaging the SNR for each of the 256 single element waveforms measured with the CH. The mean SNR was 36.9 ± 12.7 dB. Fig. 4.3 shows the noise floor and an unfiltered single element waveform measured using the CH. The key features of the waveform, including the peak-negative signal, were well above the noise floor and able to be distinguished. The average insertion loss of the catheter across all 256 waveforms was −14 ± 4.2 dB.

Time-of-Flight Measurements and Directivity: To understand how the time-of-flight of the peak-negative pressure measured by our CH varied with the direction of ultrasound propagation from the array, the peak-negative pressure time-of-flight measured by the CH (without the catheter sheath) was compared to that measured with a PVDF Cap. Hyd. (Fig. 4.4). The catheter sheath was excluded from these measurements because the CH could not accurately be rotated 180° in the catheter sheath with our current setup. The reported angular dependent delays were inherent to the custom hydrophone in the absence of the sheath. The Cap. Hyd. measured a flat time-of-flight around 110.5 μs across all angular positions of ultrasound propagation from the array. In contrast, the CH showed a deviation from this in that the time-of-flight varied with the angular position. The time-of-flight between 100° and 300° gradually increased from 110.5 μs at 100°, peaked around 112.5 μs at 200° and gradually decreased back to 110.5 μs at 300°. A set of angular dependent delays were calculated by subtracting the CH measured peak-negative pressure time-of-flight from that of the Cap. Hyd. [Fig. 4.4(c)]. To ensure this variation in time-of-flight was not a result of a discrepancy in position relative to the Cap. Hyd. but rather a characteristic inherent to the CH, the CH was rotated 180° with respect to the array and measurements were repeated. The result was an approximate 180° shift in the angular position at which the peak offset occurred [Fig. 4.4(d)].

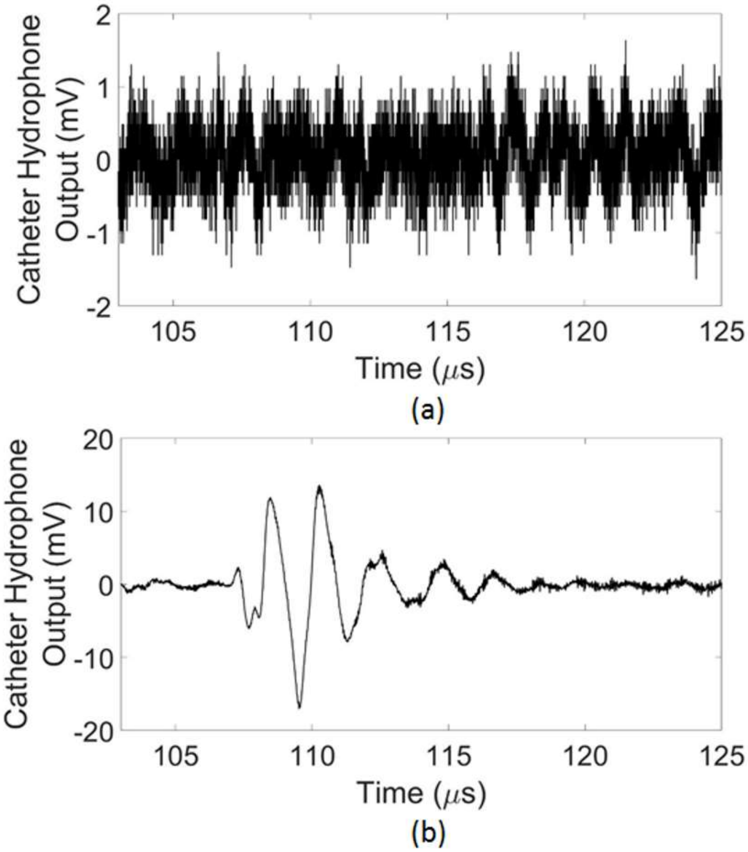

Figure 4.3. (a) The catheter hydrophone noise floor and (b) an unfiltered single element waveform measured using the catheter hydrophone.

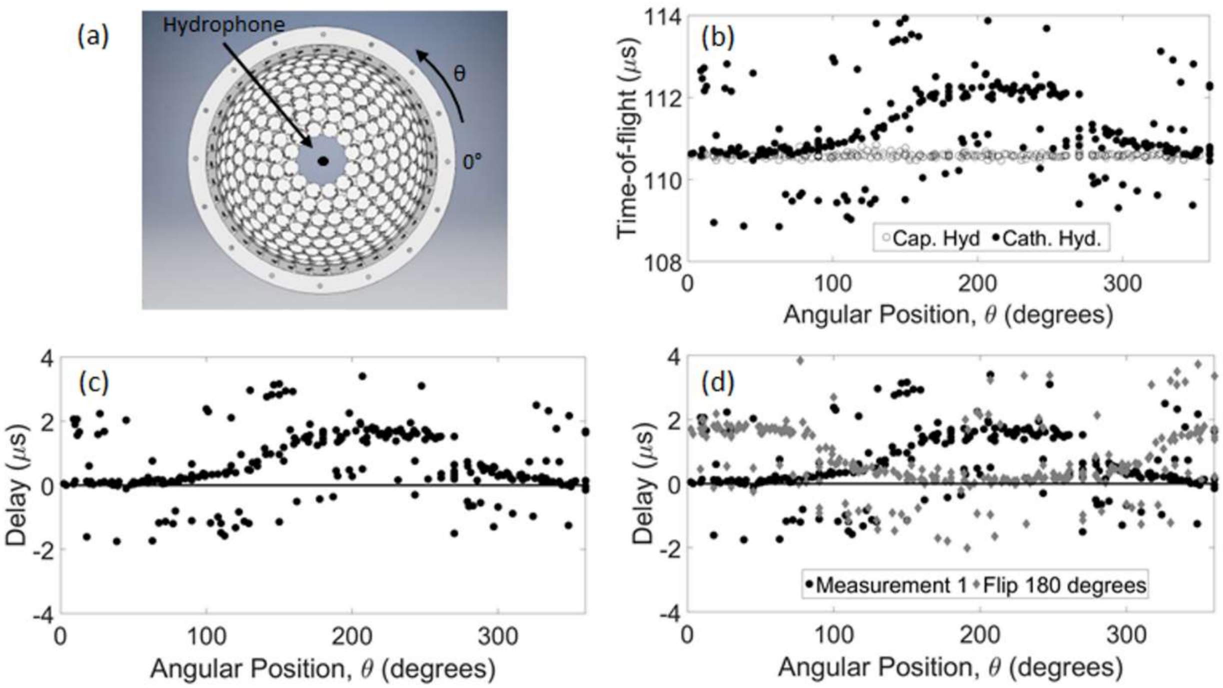

Figure 4.4. The peak-negative pressure time-of-flight measured by the catheter hydrophone (Cath. Hyd.) compared to that measured with a PVDF capsule hydrophone (Cap. Hyd.). (a) Shows the position of each hydrophone within the array used to measure the (b) time-of-flight of each waveform. (c) Delays in the catheter hydrophone measurement relative to the capsule hydrophone were calculated by subtracting those measured with the capsule hydrophone. (d) The measurement was repeated after flipping the catheter hydrophone 180° with respect to the array.

4.3.2 Aberration Correction

An AC algorithm was designed to calculate the delays necessary to realign the peak-negative pressure of the 256 waveforms delivered through the skull. Fig. 4.5 shows three waveforms delivered through the skullcap measured with the CH. There was a noticeable variation in the peak-negative signal time-of-flight among the elements. The waveform delivered from element A had a peak-negative signal that arrived 0.5 μs earlier than that of the reference element. Whereas, the waveform delivered from element B arrived 1.2 μs later than that of the reference element. 10% of the waveforms fell outside the 4 μs window and were readjusted. The relative differences in the time-of-flight among the 256 elements were extracted as the AC delays and uploaded to the FPGA boards.

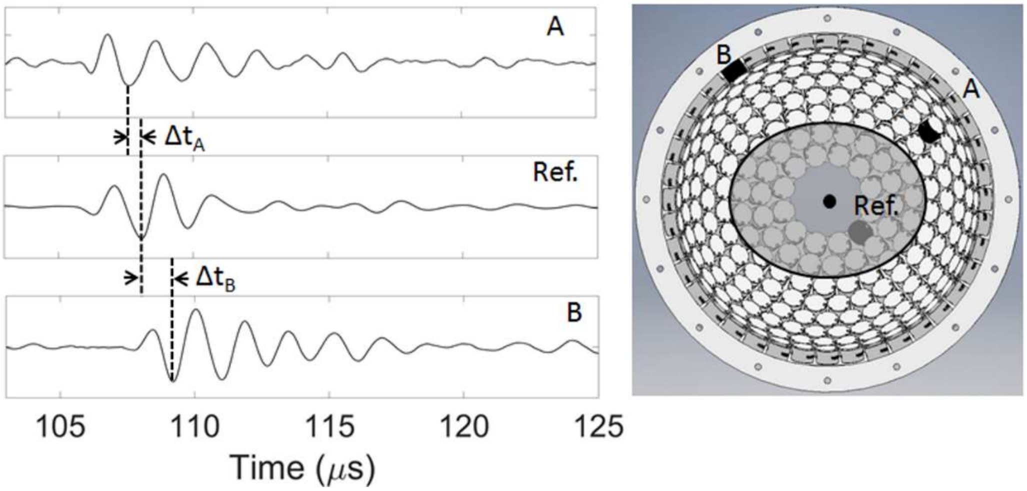

Figure 4.5. Three single element waveforms delivered through the skullcap measured with the catheter hydrophone.

4.3.3 Evaluation of Catheter Hydrophone Aberration Correction

Focal Pressure Measurements: There was a noticeable similarity in plotting the delays calculated with the AC algorithm versus those expected based on the thickness and sound speed of the specific skullcap used in this paper [Fig. 4.6(a)]. Uploading the delays obtained with the CH corresponded to a 60% increase in the peak-negative pressure at the point where AC was performed relative to the no AC case [Fig. 4.6(b)]. A comparison between focal waveforms after AC performed with a commercial PVDF Cap. Hyd. and CH (Fig. 4.7) showed a 95% increase in the peak-negative pressure by the commercial hydrophone over the case without AC and a 35% increase over the case with the CH AC.

Beam Profiles: To characterize the refocusing effects of CH AC, sagittal, coronal and axial beam profiles were obtained in the absence of aberration and through the skullcap with and without AC (Fig. 4.8). For all three axes, CH AC sharpened the main lobe of the beam profiles relative to those obtained without AC. AC also reduced the amplitude of the largest side lobes present without

AC. This lead to a reduction in the −6-dB beamwidth along the sagittal and axial axes to values closer to that obtained with the absence of aberration (Table 4.I). After AC, the −6-dB beam widths in each dimension were within 1.5 mm of their respective width with the absence of aberration compared to 5 mm without AC.

Pressure versus Electronic Focal Steering: After performing AC at only the geometric origin of the array, the focus was steered to a range of positions along the sagittal, coronal and axial axes within the skullcap using phased steering. The peak-negative pressure at each steering location was measured. The normalized peak-negative pressure as a function of transcranial steering position with no aberration and with and without AC is shown in Fig. 4.9. The increase at the point where AC was performed (i.e., geometric focus) was 60%. Table II shows percentage change in the peak-negative pressure for each steering direction. For the coronal and axial axes, the peak-negative pressure measured with AC remained greater than or equal to that measured without AC across the entire steering range examined. In the coronal direction the largest peak-negative pressure increase (62%) was observed +1 mm from the point where AC was performed. For the sagittal axis, the peak-negative pressure measured with AC remained greater than or equal to that measured without AC across a range from −18 to 14 mm. Beyond this range (−19 to −20 mm and 15 to 20 mm), the peak-negative pressure measured with AC was less than that measured without AC. The no aberration case showed pressure losses to a lesser degree at far steering radii than either case with aberration.

Lesion Generation Using Electronic Focal Steering: CH AC was performed at a single point and lesions were generated at discrete electronic steering locations in an RBC phantom positioned within the skullcap. Fig. 4.10(a) shows a 10×10 mm grid of transcranial lesions generated after single point AC. Lesions were generated at nearly each point within the 9 × 9 grid with larger and distinct lesions closer to the center and smaller, indistinct lesions toward the corners of the grid beyond 10 mm from the geometric focus. The legion diameter was largest at the geometric origin of the array, where AC was performed, and decreased as the steering distance increased. The diameter of the lesion generated at the AC point (geometric focus) was 1.3 mm. Along the sagittal axis, the lesion diameter decreased to 0.84 and 0.74 mm at the respective negative and positive extremes of the grid (−10 and 10 mm) [Fig. 4.10(b)]. Along the coronal axis, the lesion diameter decreased to 0.40 and 0.24 mm at the respective positive and negative extremes of the grid (−10 and 10 mm) [Fig. 4.10(c)].

In Vitro Clot Treatment Using Electronic Focal Steering: CH AC was performed at a single point and transcranial histotripsy was applied with electronic focal steering. Posttreatment B-mode ultrasound and T2-weighted MR images of the sagittal-coronal plane showed a well-defined lesion in the center of the clot (Fig. 4.11). The ultrasound image showed a dark, circular contiguous lesion that measured approximately 12 mm in diameter. Similarly, the MR image showed a dense bright contiguous core lesion that was similar in diameter. However, the MR image also showed bright, partially treated blotches of lysed clot beyond this dense core that filled the entirety of the treatment region (i.e., 20-mm diameter). Following treatment, the miniature hydrophone was removed from the catheter and used to drain the liquefied volume. Fig. 4.12 shows the gross morphology of a treated clot after draining the liquefied volume. A total of six clots were treated and drained within about 30 min. The average volume drained from six clots after histotripsy treatment was 4.07± 0.91 mL. This corresponded well to the 20-mm diameter scanned volume of 4.19 mL. The treatment rate was 0.13 mL/min.

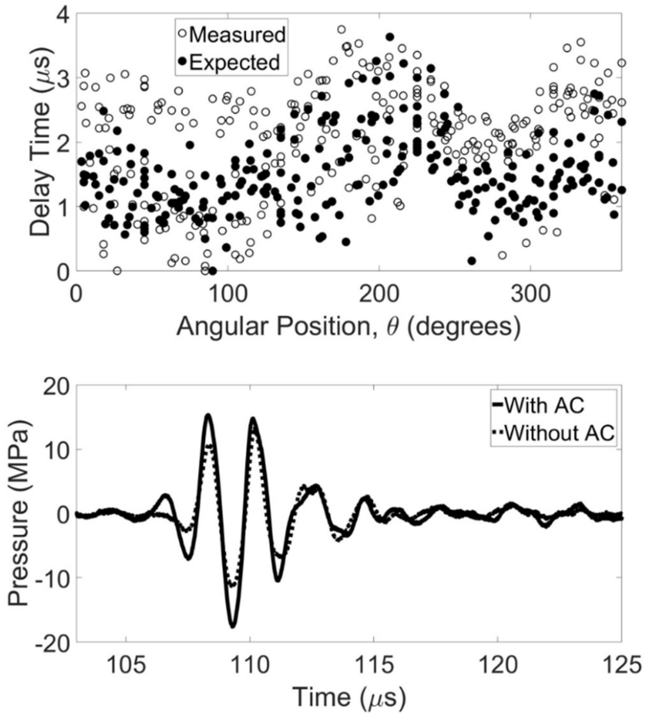

Figure 4.6. (a) Delays obtained via catheter hydrophone aberration correction plotted with those delays expected based on the sound speed and thickness of the skullcap used in this study. (b) The focal waveform obtained after implementing aberration correction compared to that without.

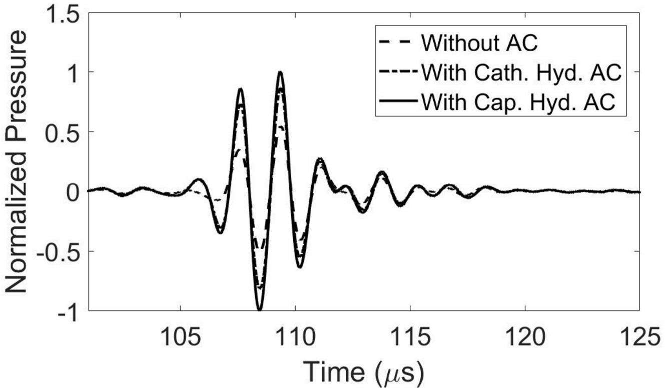

Figure 4.7. Focal waveforms after aberration correction performed with catheter hydrophone (Cath. Hyd.) and PVDF capsule hydrophone (Cap. Hyd.) measurements compared to that with no aberration correction.

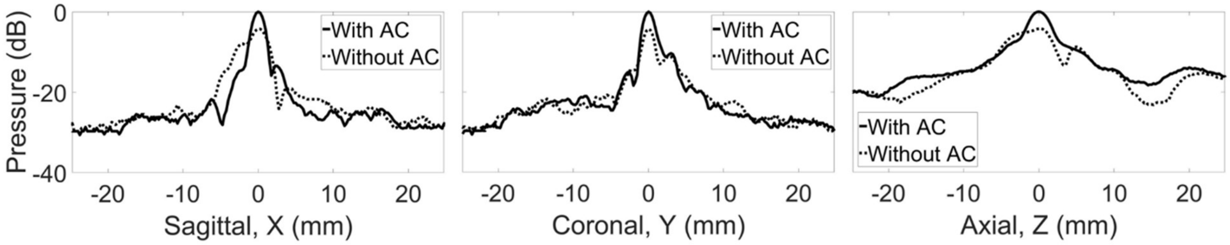

Figure 4.8. The (a) sagittal, (b) coronal and (c) axial beam profile measured through the skull with and without catheter hydrophone aberration correction (AC).

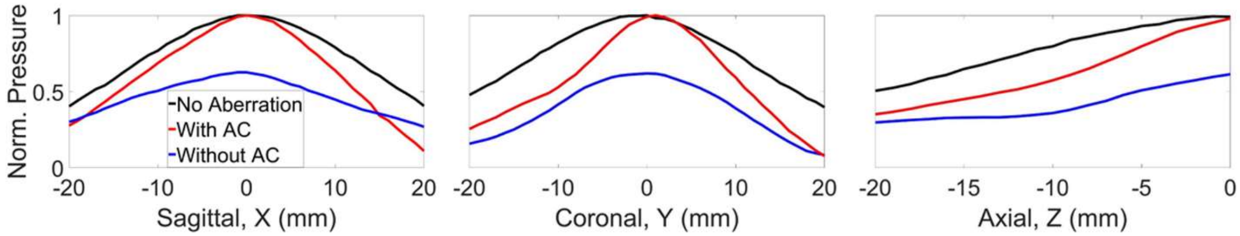

Figure 4.9. The normalized pressure as a function of steering position with no aberration and with and without aberration correction measured along the (a) sagittal, (b) coronal and (c) axial axis.

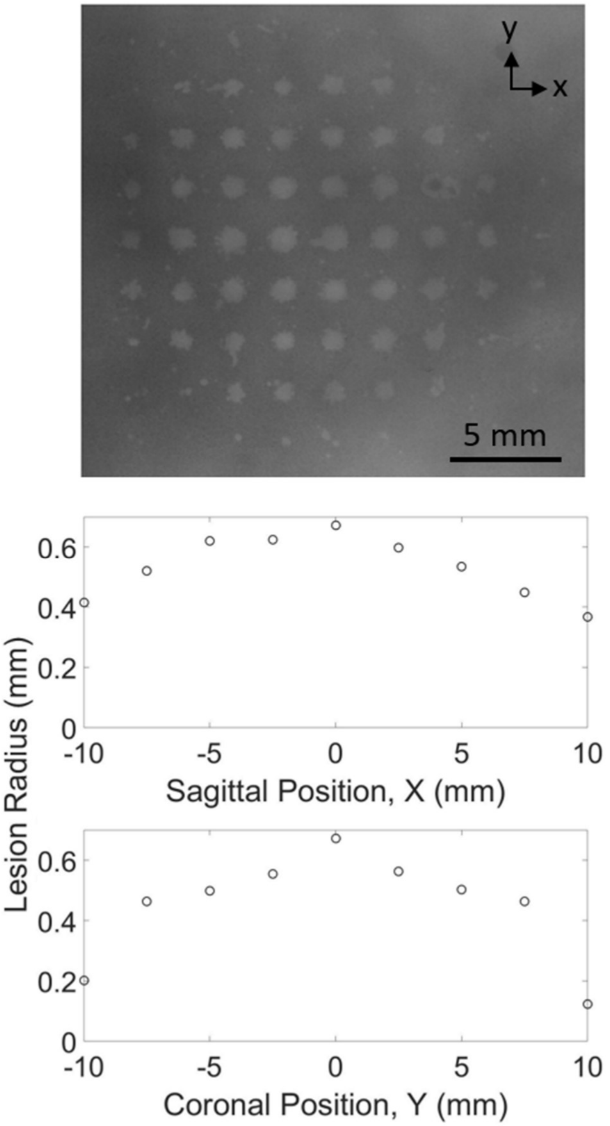

Figure 4.10. (a) Discrete lesions generated in an RBC phantom with electronically steered transcranial histotripsy after single point catheter hydrophone aberration correction. The lesion diameter plotted as a function of position along the (b) sagittal axis and coronal axis.

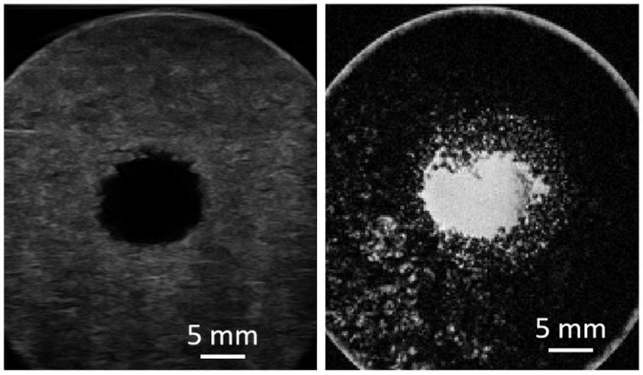

Figure 4.11. Posttreatment (a) ultrasound and (b) T2-weighted MR images of the sagittal-coronal plane a clot after electronically steered histotripsy treatment with catheter hydrophone aberration correction.

Figure 4.12.The gross morphology of posttreatment clot after draining liquefied volume.

Table 4.1. -6 dB beam widths obtained by operating the array without catheter hydrophone AC, with AC and in the absence of aberration.

	Sagittal	Coronal	Axial
Without AC	4.6 mm	2.2 mm	8 mm
With AC	2.2 mm	2.2 mm	4.4 mm
No Aberration	1.5 mm	1.5 mm	3 mm

Table 4.2. The percentage change in the peak-negative pressure between measurements with and without catheter hydrophone aberration correction for each steering direction.

	-20 mm	-10 mm	-5 mm	5 mm	10 mm	20 mm
Sagittal	-8%	36%	50%	61%	43%	-59%
Coronal	61%	27%	37%	61%	52%	0%
Axial	18%	60%	57%	--	--	--

4.4 Discussion

The CH used to correct the skull-induced aberration for transcranial histotripsy represents a fast (~10-min correction time) and minimally invasive mechanism of correcting aberrations for future in vivo application. Particularly for ICH treatment, a drainage catheter is needed to drain the liquefied clot. A miniature hydrophone incorporated within the catheter can overcome the need for MRI-based AC, which MRgFUS currently relies on, and has the potential to significantly simplify the process of AC for transcranial histotripsy treatment of ICH. The results in this paper demonstrate the proof-of-concept and feasibility of CH AC for transcranial histotripsy treatment of ICH. Using the CH, AC was performed at a single point to increase the peak-negative pressure by 60% and sharpen main lobe of the beam. The feasibility for precise histotripsy treatment after single point AC with the CH was demonstrated by the increased peak-negative pressure and discrete lesion formation across a range of electronic steering locations, with no significant damage outside the focal zone. The in-vitro clot experiments performed in this paper showed the ability to perform CH AC, apply transcranial histotripsy treatment to a volume of clot, and then drain the liquefied volume with the catheter. This can be achieved an order magnitude faster than the current minimally invasive catheter techniques using thrombolytic drugs [16]. However, it is slightly less than the treatment rate reported with MRgFUS (~0.2 mL/min) [25]–[27]. This is primarily because the array was driven with a low-pressure overhead (i.e., 36MPa, 10 MPa over the intrinsic threshold) and enough pulses to completely liquefy the treatment region. This is not entirely necessary in order to drain the treated region with a catheter. In a study recently accepted for publication, we show liquefaction rates of about 3.5 mL/min using greater pressure (70 MPa) and fewer pulses (50) [46].

Low SNR was an issue with early iterations of the CH prototypes that made distinguishing the ultrasound waveforms measured through the skull difficult. This caused calculation errors when using the peak-negative signal of the measurements to deduce the relative delays among the 256 single element waveforms. However, this issue was significantly improved by incorporating a shielded coaxial cable. The version of the custom hydrophone used in this paper had sufficient SNR to distinguish the peak-negative pressure from the waveform of each individual element and thus provided a reference point by which to calculate the relative delays. One concern is that using a full human skull will cause a multiplicity of echoes and may disrupt AC. However, proper windowing of the acquisition time will allow such echoes to be excluded from consideration. Assuming the hydrophone tip is sufficiently far from any portion of the skull surface, the time of arrival versus the echo time should be sufficiently far apart for minimal measurement issues.

As the range of clot sizes for ICH varies, histotripsy volume treatment is an important aspect of successful ICH treatment. By performing CH AC at a single point, it was possible to increase the peak-negative pressure across a range of steered locations away from the point at which the AC measurements were acquired, allowing treatment using electronic focal steering. The overall pressure loss as the focus is steered-to greater distances is an inherent quality of electronic focal steering and was observed even in the case with no aberration. However, the absence of the skullcap showed losses to a lesser degree. Single point AC may be sufficient for treating ICH cases where the clot boundaries are within the steering range at which pressures are above the intrinsic threshold. This range is a function of the pressure applied to the geometric focus. Still, while AC with the CH at a single point led to increased pressures in the bulk of the steered-through volume compared to the no AC case, at steering locations far from the AC point, there was a decreased peak-negative pressure compared to the no AC case. Similar effects to these were seen by Vignon et al. [76] where the improvement in corrective delays acquired from a single point became worse than the uncorrected case at steering angles greater than 30°. However, these effects were attributed to a conversion to shear waves at incidence angles greater than 30°, which the correction did not account for [77]. Due to the hemispherical shape of the array used here, the max incidence angle was on the order of about 8° and shear wave conversion at larger steering angles was likely not a factor. Instead, two factors likely accounted for this: 1) refractive effects and 2) the change in skull thickness through which each pulse propagates en route to the steered-to location. In regards to the first, while refractive deviations to the pulse trajectories are not expected to significantly contribute to aberration of pulses steered near the origin, this may not be the case at larger steering radii. This is because as the steering radius is increased, the incidence angles of the pulses with the skull's surface can change significantly enough to affect their post-skull trajectories and thus the potential for misalignment at large steering radii. It should be noted, however, that due to the short pulse duration and the necessity of constructive interference to reach the intrinsic threshold, this effect is unlikely to generate off target damage as the tendency toward deconstructive interference would drop the pressure below the intrinsic threshold. We are currently developing an AC algorithm that uses measurements at multiple points along the axis of insertion (i.e., the axis along which the catheter is inserted) to account for refraction effects, which may increase the pressure at a farther steering locations.

In regards to the second factor, as the trajectories of the pulses within the skull change, the path lengths through bone which each pulse must travel also change, which causes additional misalignment between the pulses as the steering angle increases away from the measurement location. As pulses are aligned at the geometric origin after initial AC, such misalignment can only result in deconstructive interference between the pulses as the focus is steered, and thus lower the pressure. However, in the no AC case, the innate, uncorrected aberration can reduce the magnitude of the losses generated by the additional misalignment due to steering and result in higher pressure amplitudes than with AC. A similar discussion regarding differing propagation paths is proposed by Lindsey and Smith, where steering a 2-D imaging probe 15° through skull bone showed decreased correlation of the steered wave front arrival between adjacent elements on the imaging array [78]. We are currently investigating: 1) how much this effect contributes to the observed results; 2) the farthest limit of steering locations beyond which AC reduces the pressure even with multilocation measurements; and 3) methods of correcting for potential losses due to it.

Although the CH used in this paper was sufficient to measure the waveforms through the skull, fit within a catheter, and improve the focusing through the skull, there was some deviation in its performance when compared to the PVDF Cap. Hyd. Using the Cap. Hyd. with the same correction algorithm showed a 95% increase in the peak-negative pressure at the geometric origin through the skullcap used in this paper (a 35% greater increase over the CH). Since this measurement is a metric on how well the individual waveforms were temporally aligned using time-of-flight measurements made with each hydrophone, it is likely that the deviation in performance in relation to the Cap. Hyd. was due to the angular dependent delay in the time-of-flight measurements of individual waveforms made with the CH. One additional comment is that as this paper used an excised human skullcap instead of a full human skull, it was possible to insert the CH into the open end of the skullcap. Although this orientation sufficed for showing the proof-of-concept, this insertion trajectory is not likely in a clinical setting where catheters are often inserted through small holes drilled through the skullcap. An ideal CH insertion strategy would involve removing an element from the array overlying the hole drilled for access to the clot and guiding the CH through the hole in the array into the skull. This flipped insertion strategy is likely to affect the quality of signal acquisition as it the flips the orientation of the device such that the coaxial cable and catheter interfere with the propagation path from a number of elements. However, any amplitude or phase distortion can likely be overcome using an edge detection correction technique. As our histotripsy array is made with each element as a removable module, we plan to build a catheter holder that can easily be fit through each element module opening. This would allow a large range of possible entrance points into the skull for a large range of clot locations. Future in vitro experiments will use full human skulls with a small hole drilled into the skullcap for inserting the CH.

4.5 Conclusion

The purpose of this paper was to establish the proof-of-concept for using CH AC as an AC technique in the development of histotripsy as a minimally invasive technology for treating ICH. A custom miniature hydrophone was integrated with a drainage catheter. A time delay-based AC algorithm was developed to allow AC using the CH measurements at a single location. The CH was characterized and the functionality of using CH measurements to perform AC was measured. Finally, an in vitro study was conducted to demonstrate the proof-of-concept of using the CH for clot liquefaction and drainage through an excised human skullcap. This paper exemplified the potential of such a device to be used for future in vivo studies and clinical applications of minimally invasive treatment for ICH using transcranial histotripsy. Future work includes examining the potential for angular dependence in time-of-flight measurements, establishing a catheter insertion strategy, and developing a catheter array with associated AC algorithm that uses measurements at multiple points to potentially increase the electronic focal steering range.

4.6 Appendix

4.6.1 IEEE TUFFC Cover Photo

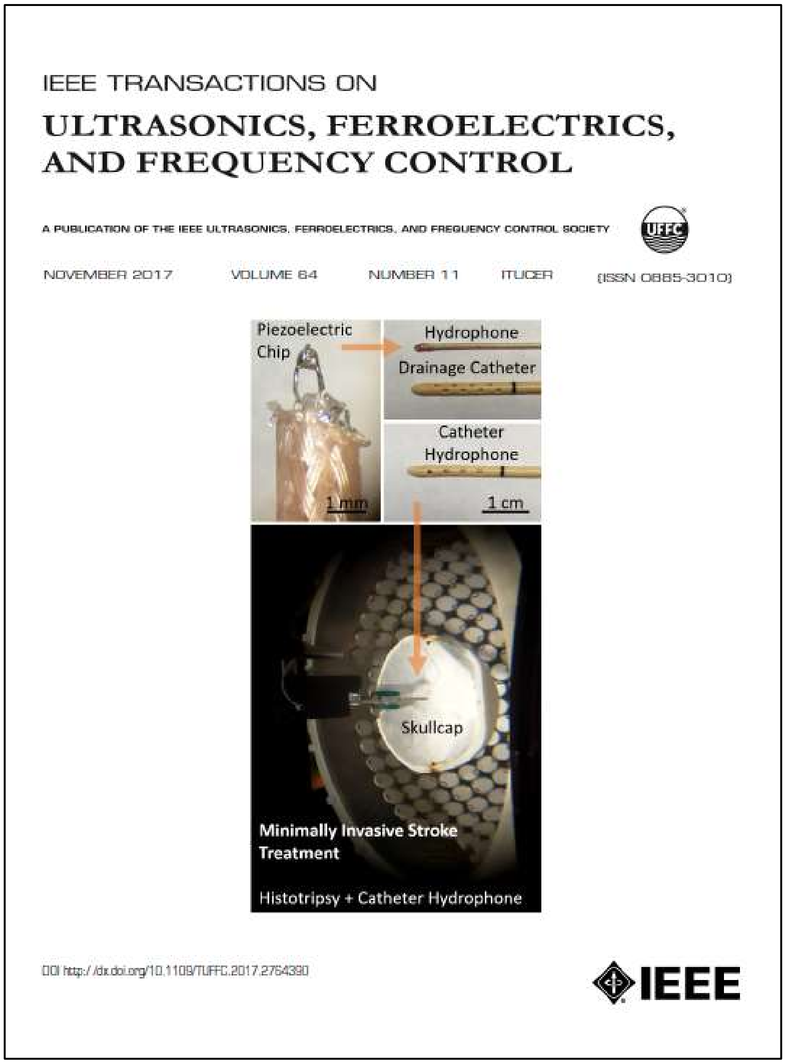

IEEE TRANSACTIONS ON

ULTRASONICS, FERROELECTRICS, AND FREQUENCY CONTROL

A PUBLICATION OF THE IEEE ULTRASONICS, FERROELECTRICS, AND FREQUENCY CONTROL SOCIETY

NOVEMBER 2017 VOLUME 64 NUMBER 11 ITUCER (ISSN 0885-3010)

Minimally Invasive Stroke Treatment

Histotripsy + Catheter Hydrophone

DOI http://dx.doi.org/10.1109/TUFFC.2017.2764390

4.7 References

[1] T. Gerhardson, J. R. Sukovich, A. S. Pandey, T. L. Hall, C. A. Cain, and Z. Xu, "Catheter Hydrophone Aberration Correction for Transcranial Histotripsy Treatment of Intracerebral Hemorrhage: Proof-of-Concept," *IEEE Trans. Ultrason. Ferroelectr. Freq. Control*, vol. 64, no. 11, pp. 1684 - 1697, 2017.

[2] A. I. Qureshi, A. D. Mendelow, and D. F. Hanley, "Intracerebral haemorrhage," *The Lancet*, vol. 373, no. 9675. pp. 1632–1644, 2009.

[3] D. Mozaffarian *et al.*, "Executive summary: Heart disease and stroke statistics-2016 update: A Report from the American Heart Association," *Circulation*, vol. 133, no. 4. pp. 447–454, 2016.

[4] E. V. Kuklina, X. Tong, M. G. George, and P. Bansil, "Epidemiology and prevention of stroke: A worldwide perspective," *Expert Review of Neurotherapeutics*, vol. 12, no. 2. pp. 199–208, 2012.

[5] M. L. Flaherty *et al.*, "Long-term mortality after intracerebral hemorrhage," *Neurology*, vol. 66, no. 8, pp. 1182–1186, 2006.

[6] J. P. Broderick, T. G. Brott, J. E. Duldner, T. Tomsick, and G. Huster, "Volume of intracerebral hemorrhage: A powerful and easy-to-use predictor of 30-day mortality," *Stroke*, 1993.

[7] F. Rincon and S. A. Mayer, "Clinical review: Critical care management of spontaneous intracerebral hemorrhage," *Crit. Care*, vol. 12, no. 6, pp. 237–251, 2008.

[8] C. T. Skidmore and J. Andrefsky, "Spontaneous intracerebral hemorrhage: Epidemiology, pathophysiology, and medical management," *Neurosurgery Clinics of North America*, vol. 13, no. 3. pp. 281–288, 2002.

[9] A. R. Gujjar, E. Deibert, E. M. Manno, S. Duff, and M. N. Diringer, "Mechanical ventilation for ischemic stroke and intracerebral hemorrhage: Indications, timing, and outcome," *Neurology*, vol. 51, no. 2, pp. 447–451, 1998.

[10] M. N. Diringer, "Intracerebral hemorrhage: pathophysiology and management.," *Crit. Care Med.*, vol. 21, no. 10, pp. 1591–1603, 1993.

[11] G. J. Hankey and C. Hon, "Surgery for primary intracerebral hemorrhage: is it safe and effective? A systematic review of case series and randomized trials.," *Stroke; a journal of cerebral circulation*, vol. 28, no. 11. pp. 2126–32, 1997.

[12] H. M. Fernandes, B. Gregson, S. Siddique, and A. D. Mendelow, "Surgery in intracerebral hemorrhage: The uncertainty continues," *Stroke*, vol. 31, no. 10. pp. 2511–2516, 2000.

[13] A. D. Mendelow *et al.*, "Early surgery versus initial conservative treatment in patients with spontaneous supratentorial intracerebral haematomas in the International Surgical Trial in

Intracerebral Haemorrhage (STICH): A randomised trial," *Lancet*, vol. 365, no. 9457, pp. 387–397, 2005.

[14] A. D. Mendelow *et al.*, "Early surgery versus initial conservative treatment in patients with spontaneous supratentorial lobar intracerebral haematomas (STICH II): A randomised trial," *Lancet*, vol. 382, no. 9890, pp. 397–408, 2013.

[15] N. Hattori, Y. Katayama, Y. Maya, and A. Gatherer, "Impact of stereotactic hematoma evacuation on medical costs during the chronic period in patients with spontaneous putaminal hemorrhage: a randomized study," *Surg. Neurol.*, vol. 65, no. 5, pp. 429–435, 2006.

[16] T. Morgan, M. Zuccarello, R. Narayan, P. Keyl, K. Lane, and D. Hanley, "Preliminary findings of the minimally-invasive surgery plus rtPA for intracerebral hemorrhage evacuation (MISTIE) clinical trial," *Acta Neurochir. Suppl.*, no. 105, pp. 147–151, 2008.

[17] W. Z. Wang *et al.*, "Minimally invasive craniopuncture therapy vs. conservative treatment for spontaneous intracerebral hemorrhage: Results from a randomized clinical trial in China," *Int. J. Stroke*, vol. 4, no. 1, pp. 11–16, 2009.

[18] A. V. Alexandrov, A. M. Demchuk, W. S. Burgin, D. J. Robinson, and J. C. Grotta, "Ultrasound-Enhanced Thrombolysis for Acute Ischemic Stroke: Phase I. Findings of the CLOTBUST Trial," *J. Neuroimaging*, vol. 14, no. 2, pp. 113–117, 2004.

[19] S. Datta *et al.*, "Correlation of cavitation with ultrasound enhancement of thrombolysis," *Ultrasound Med. Biol.*, vol. 32, no. 8, pp. 1257–1267, 2006.

[20] S. Datta, C. C. Coussios, A. Y. Ammi, T. D. Mast, G. M. de Courten-Myers, and C. K. Holland, "Ultrasound-Enhanced Thrombolysis Using Definity?? as a Cavitation Nucleation Agent," *Ultrasound Med. Biol.*, vol. 34, no. 9, pp. 1421–1433, 2008.

[21] A. V. Alexandrov *et al.*, "A pilot randomized clinical safety study of sonothrombolysis augmentation with ultrasound-activated perflutren-lipid microspheres for acute ischemic stroke," *Stroke*, vol. 39, no. 5, pp. 1464–1469, 2008.

[22] C. K. Holland, S. S. Vaidya, S. Datta, C. C. Coussios, and G. J. Shaw, "Ultrasound-enhanced tissue plasminogen activator thrombolysis in an in vitro porcine clot model," *Thromb. Res.*, vol. 121, no. 5, pp. 663–673, 2008.

[23] K. E. Hitchcock and C. K. Holland, "Ultrasound-assisted thrombolysis for stroke therapy: Better thrombus break-up with bubbles," in *Stroke*, 2010, vol. 41, no. 10 SUPPL. 1.

[24] S. Meairs, A. Alonso, and M. G. Hennerici, "Progress in sonothrombolysis for the treatment of stroke," *Stroke*, vol. 43, no. 6, pp. 1706–1710, 2012.

[25] S. J. Monteith *et al.*, "Minimally invasive treatment of intracerebral hemorrhage with magnetic resonance-guided focused ultrasound: Laboratory investigation," *J. Neurosurg.*, vol. 118, no. 5, pp. 1035–1045, 2013.

[26] S. J. Monteith, N. F. Kassell, O. Goren, and S. Harnof, “Transcranial MR-guided focused ultrasound sonothrombolysis in the treatment of intracerebral hemorrhage,” *Neurosurg. Focus*, vol. 34, no. 5, p. E14, 2013.

[27] M. Ramanan and a Shankar, “Minimally invasive surgery for primary supratentorial intracerebral haemorrhage,” *J. Clin. Neurosci.*, vol. 20, no. 12, pp. 1650–1658, 2013.

[28] S. Monteith *et al.*, “Potential intracranial applications of magnetic resonance–guided focused ultrasound surgery,” *J. Neurosurg.*, vol. 118, no. 2, pp. 215–221, 2013.

[29] C. Wright, K. Hynynen, and D. Goertz, “In vitro and in vivo high intensity focused ultrasound thrombolysis,” *Invest. Radiol.*, vol. 47, no. 4, pp. 217–225, 2012.

[30] W. J. Elias *et al.*, “The use of magnetic resonance-guided high intensity focused ultrasound to treat essential tremor,” *J. Acoust. Soc. Am.*, vol. 134, no. 5, pp. 4090–4090, 2013.

[31] Z. Xu *et al.*, “Controlled ultrasound tissue erosion,” *IEEE Trans. Ultrason. Ferroelectr. Freq. Control*, vol. 51, no. 6, pp. 726–736, 2004.

[32] Z. Xu, J. B. Fowlkes, E. D. Rothman, A. M. Levin, and C. A. Cain, “Controlled ultrasound tissue erosion: The role of dynamic interaction between insonation and microbubble activity,” *J. Acoust. Soc. Am.*, vol. 117, no. 1, pp. 424–435, 2005.

[33] W. W. Roberts, T. L. Hall, K. Ives, J. S. Wolf, J. B. Fowlkes, and C. A. Cain, “Pulsed cavitational ultrasound: A noninvasive technology for controlled tissue ablation (histotripsy) in the rabbit kidney,” *J. Urol.*, vol. 175, no. 2, pp. 734–738, 2006.

[34] Z. Xu, G. Owens, D. Gordon, C. Cain, and A. Ludomirsky, “Noninvasive creation of an atrial septal defect by histotripsy in a canine model,” *Circulation*, vol. 121, no. 6, pp. 742–749, 2010.

[35] K. W. Lin *et al.*, “Histotripsy beyond the intrinsic cavitation threshold using very short ultrasound pulses: Microtripsy,” *IEEE Trans. Ultrason. Ferroelectr. Freq. Control*, vol. 61, no. 2, pp. 251–265, 2014.

[36] A. D. Maxwell, G. Owens, H. S. Gurm, K. Ives, D. D. Myers, and Z. Xu, “Noninvasive treatment of deep venous thrombosis using pulsed ultrasound cavitation therapy (histotripsy) in a porcine model,” *J. Vasc. Interv. Radiol.*, vol. 22, no. 3, pp. 369–377, 2011.

[37] A. D. Maxwell, C. A. Cain, A. P. Duryea, L. Yuan, H. S. Gurm, and Z. Xu, “Noninvasive Thrombolysis Using Pulsed Ultrasound Cavitation Therapy - Histotripsy,” *Ultrasound Med. Biol.*, vol. 35, no. 12, pp. 1982–1994, 2009.

[38] X. Zhang, G. E. Owens, H. S. Gurm, Y. Ding, C. A. Cain, and Z. Xu, “Noninvasive thrombolysis using histotripsy beyond the intrinsic threshold (microtripsy),” *IEEE Trans. Ultrason. Ferroelectr. Freq. Control*, vol. 62, no. 7, pp. 1342–1355, 2015.

[39] X. Zhang *et al.*, “Noninvasive thrombolysis using microtripsy: A parameter study,” *IEEE*

Trans. Ultrason. Ferroelectr. Freq. Control, vol. 62, no. 12, pp. 2092–2105, 2015.

[40] X. Zhang, G. E. Owens, C. A. Cain, H. S. Gurm, J. Macoskey, and Z. Xu, “Histotripsy Thrombolysis on Retracted Clots,” *Ultrasound Med. Biol.*, vol. 42, no. 8, pp. 1903–1918, 2016.

[41] X. Zhang *et al.*, “Non-Invasive Thrombolysis Using Microtripsy in a Porcine Deep Vein Thrombosis Model,” *Ultrasound Med. Biol.*, vol. 43, no. 7, pp. 1378–1390, 2017.

[42] R. Devanagondi *et al.*, “Hemodynamic and Hematologic Effects of Histotripsy of Free-Flowing Blood: Implications for Ultrasound-Mediated Thrombolysis,” *J. Vasc. Interv. Radiol.*, vol. 26, no. 10, pp. 1559–1565, 2015.

[43] T. D. Khokhlova, W. L. Monsky, Y. A. Haider, A. D. Maxwell, Y. N. Wang, and T. J. Matula, “Histotripsy liquefaction of large hematomas,” *Ultrasound Med. Biol.*, vol. 42, no. 7, pp. 1491–1498, 2016.

[44] Y. Kim, T. Hall, Z. Xu, and C. Cain, “Transcranial histotripsy therapy: A feasibility study,” *IEEE Trans. Ultrason. Ferroelectr. Freq. Control*, vol. 61, no. 4, pp. 582–593, 2014.

[45] J. R. Sukovich *et al.*, “Targeted Lesion Generation Through the Skull Without Aberration Correction Using Histotripsy,” *IEEE Trans. Ultrason. Ferroelectr. Freq. Control*, vol. 63, no. 5, pp. 671–682, 2016.

[46] T. Gerhardson, J. R. Sukovich, A. S. Pandey, T. L. Hall, C. A. Cain, and Z. Xu, “Effect of Frequency and Focal Spacing on Transcranial Histotripsy Clot Liquefaction, Using Electronic Focal Steering,” *Ultrasound Med. Biol.*, vol. 43, no. 10, pp. 2302–2317, 2017.

[47] G. T. Clement and K. Hynynen, “Correlation of ultrasound phase with physical skull properties,” *Ultrasound Med. Biol.*, vol. 28, no. 5, pp. 617–624, 2002.

[48] J.-F. Aubry, M. Tanter, M. Pernot, J.-L. Thomas, and M. Fink, “Experimental demonstration of noninvasive transskull adaptive focusing based on prior computed tomography scans,” *J. Acoust. Soc. Am.*, vol. 113, no. 1, pp. 84–93, 2003.

[49] Y. Hertzberg, A. Volovick, Y. Zur, Y. Medan, S. Vitek, and G. Navon, “Ultrasound focusing using magnetic resonance acoustic radiation force imaging: Application to ultrasound transcranial therapy,” *Med. Phys.*, vol. 37, no. 6, pp. 2934–2942, 2010.

[50] X. Zeng and R. J. McGough, “Evaluation of the angular spectrum approach for simulations of near-field pressures,” *J. Acoust. Soc. Am.*, vol. 123, no. 1, pp. 68–76, 2008.

[51] G. T. Clement, P. J. White, and K. Hynynen, “Enhanced ultrasound transmission through the human skull using shear mode conversion,” *J. Acoust. Soc. Am.*, vol. 115, no. 3, pp. 1356–1364, 2004.

[52] G. T. Clement and K. Hynynen, “A non-invasive method for focusing ultrasound through the human skull,” *Physics in Medicine and Biology*, vol. 47, no. 8. pp. 1219–1236, 2002.

[53] K. Hynynen *et al.*, “500-Element ultrasound phased array system for noninvasive focal surgery of the brain: A preliminary rabbit study with ex vivo human skulls,” *Magn. Reson. Med.*, vol. 52, no. 1, pp. 100–107, 2004.

[54] L. Marsac *et al.*, “Ex vivo optimisation of a heterogeneous speed of sound model of the human skull for non-invasive transcranial focused ultrasound at 1 MHz,” *Int. J. Hyperth.*, vol. 33, no. 6, pp. 635–645, 2017.

[55] F. Marquet *et al.*, “Non-invasive transcranial ultrasound therapy based on a 3D CT scan: protocol validation and in vitro results,” *Phys. Med. Biol.*, vol. 54, no. 9, pp. 2597–2613, 2009.

[56] D. Chauvet *et al.*, “Targeting accuracy of transcranial magnetic resonance–guided high-intensity focused ultrasound brain therapy: a fresh cadaver model,” *J. Neurosurg.*, vol. 118, no. 5, pp. 1046–1052, 2013.

[57] J. Gâteau, L. Marsac, M. Pernot, J. F. Aubry, M. Tanter, and M. Fink, “Transcranial ultrasonic therapy based on time reversal of acoustically induced cavitation bubble signature,” *IEEE Trans. Biomed. Eng.*, vol. 57, no. 1, pp. 134–144, 2010.

[58] M. Pernot *et al.*, “In vivo transcranial brain surgery with an ultrasonic time reversal mirror,” *J. Neurosurg.*, vol. 106, no. 6, pp. 1061–1066, 2007.

[59] D. J. Phillips, S. W. Smith, O. T. von Ramm, and F. L. Thurstone, “SAMPLED APERTURE TECHNIQUES APPLIED TO B-MODE ECHOENCEPHALOGRAPHY.,” *Acoust Hologr*, vol. 6, pp. 103–120, 1975.

[60] S. W. Flax and M. O’Donnell, “Phase-Aberration Correction Using Signals From Point Reflectors and Diffuse Scatterers: Basic Principles,” *IEEE Trans. Ultrason. Ferroelectr. Freq. Control*, vol. 35, no. 6, pp. 758–767, 1988.

[61] M. Fink, “Time Reversal of Ultrasonic Fields—Part I: Basic Principles,” *IEEE Trans. Ultrason. Ferroelectr. Freq. Control*, vol. 39, no. 5, pp. 555–566, 1992.

[62] J. L. Thomas and M. A. Fink, “Ultrasonic beam focusing through tissue inhomogeneities with a time reversal mirror: application to transskull therapy,” *IEEE Trans. Ultrason. Ferroelectr. Freq. Control*, vol. 43, no. 6, pp. 1122–1129, 1996.

[63] M. Fink, G. Montaldo, and M. Tanter, “Time-Reversal Acoustics in Biomedical Engineering,” *Annu. Rev. Biomed. Eng.*, vol. 5, no. 1, pp. 465–497, 2003.

[64] F. Vignon, J. F. Aubry, M. Tanter, A. Margoum, and M. Fink, “Adaptive focusing for transcranial ultrasound imaging using dual arrays,” *J. Acoust. Soc. Am.*, vol. 120, no. 5, pp. 2737–2745, 2006.

[65] R. Seip, P. Van Baren, and E. S. Ebbini, “Dynamic Focusing in Ultrasound Hyperthermia Treatments Using Implantable Hydrophone Arrays,” *IEEE Trans. Ultrason. Ferroelectr. Freq. Control*, vol. 41, no. 5, pp. 706–713, 1994.

[66] M. Pernot, G. Montaldo, M. Tanter, and M. Fink, "'Ultrasonic stars' for time-reversal focusing using induced cavitation bubbles," *Appl. Phys. Lett.*, vol. 88, no. 3, pp. 1–3, 2006.

[67] K. J. Haworth, J. B. Fowlkes, P. L. Carson, and O. D. Kripfgans, "Towards Aberration Correction of Transcranial Ultrasound Using Acoustic Droplet Vaporization," *Ultrasound Med. Biol.*, vol. 34, no. 3, pp. 435–445, 2008.

[68] Y. Kim, A. D. Maxwell, T. L. Hall, Z. Xu, K. W. Lin, and C. A. Cain, "Rapid prototyping fabrication of focused ultrasound transducers," *IEEE Trans. Ultrason. Ferroelectr. Freq. Control*, 2014.

[69] A. D. Maxwell, T. Y. Wang, L. Yuan, A. P. Duryea, Z. Xu, and C. A. Cain, "A tissue phantom for visualization and measurement of ultrasound-induced cavitation damage," *Ultrasound Med. Biol.*, vol. 36, no. 12, pp. 2132–2143, 2010.

[70] M. I. Aguilar and T. G. Brott, "Update in Intracerebral Hemorrhage," *The Neurohospitalist*. 2011.

[71] R. D. Zimmerman, J. A. Maldjian, N. C. Brun, B. Horvath, and B. E. Skolnick, "Radiologic estimation of hematoma volume in intracerebral hemorrhage trial by CT scan," *Am. J. Neuroradiol.*, 2006.

[72] R. M. Jones and K. Hynynen, "Comparison of analytical and numerical approaches for CT-based aberration correction in transcranial passive acoustic imaging," *Phys. Med. Biol.*, vol. 61, no. 1, pp. 23–36, 2015.

[73] J. E. Parsons, C. A. Cain, and J. B. Fowlkes, "Cost-effective assembly of a basic fiber-optic hydrophone for measurement of high-amplitude therapeutic ultrasound fields," *J. Acoust. Soc. Am.*, vol. 119, no. 3, pp. 1432–1440, 2006.

[74] A. D. Maxwell, C. A. Cain, T. L. Hall, J. B. Fowlkes, and Z. Xu, "Probability of Cavitation for Single Ultrasound Pulses Applied to Tissues and Tissue-Mimicking Materials," *Ultrasound Med. Biol.*, vol. 39, no. 3, pp. 449–465, 2013.

[75] T.-Y. Wang, Z. Xu, T. L. Hall, J. B. Fowlkes, and C. A. Cain, "An efficient treatment strategy for histotripsy by removing cavitation memory.," *Ultrasound Med. Biol.*, vol. 38, no. 5, pp. 153–766, 2012.

[76] F. Vignon, W. T. Shi, M. R. Burcher, and J. E. Powers, "Determination of temporal bone isoplanatic patch sizes for transcranial phase aberration correction," in *Proceedings - IEEE Ultrasonics Symposium*, 2008, pp. 1286–1289.

[77] S. Pichardo and K. Hynynen, "Treatment of near-skull brain tissue with a focused device using shear-mode conversion: A numerical study," *Phys. Med. Biol.*, vol. 52, no. 24, pp. 7313–7332, 2007.

[78] B. D. Lindsey and S. W. Smith, "Pitch-catch phase aberration correction of multiple isoplanatic patches for 3-D transcranial ultrasound imaging," *IEEE Trans. Ultrason.*

Ferroelectr. Freq. Control, vol. 60, no. 3, pp. 463–480, 2013.

CHAPTER 5 Performance Evaluation of Practical Catheter Hydrophones for Aberration Correction to Aid Histotripsy Treatment of Intracerebral Hemorrhage

5.1 Introduction

The use of focused ultrasound (FUS) applied transcranially for noninvasive or minimally invasive treatment of various brain pathologies has been extensively explored and developed [1]–[13]. Histotripsy is a relatively new FUS technology being developed for transcranial applications. In contrast to other FUS techniques that rely on the deposition of heat applied from outside the skull to induce thermal necrosis of the targeted brain tissue, histotripsy uses microsecond duration, low duty cycle (<0.1%), high amplitude acoustic pulses to generate cavitation microbubble clouds from the endogenous gas nuclei within the target tissue [14]–[17]. The rapid bubble expansion and collapse generated with histotripsy produces a localized environment of high stress and strain. These conditions fractionate and eventually liquefy the tissue into an acellular homogenate [18]. By using a very low duty cycle, the heating to the skull is significantly reduced compared to the transcranial FUS thermal ablation, allowing potential treatment of a wider range of locations in the brain without overheating the skull.

In applying FUS transcranially, phase aberration is induced by sound speed and thickness inhomogeneities inherent to the skull and overlying tissue. This phase aberration can result in significant amplitude loss and beam widening, resulting in an overall decrease in treatment efficacy and precision [19], [20]. Many different approaches to correct for this aberration have been explored with different levels of success. Such approaches include simulations [20]–[25], acoustic lenses [26], magnetic resonance acoustic radiation force imaging (MR-ARFI) [27], [28]and time-reversal techniques using implanted acoustic sources, receivers or reflectors [29]–[34]. Recently we have proposed the use of a catheter hydrophone for aberration correction in minimally invasive treatment of intracerebral hemorrhage (ICH) with histotripsy where the insertion of a drainage catheter into the clot is necessary to remove the clot [35]. The proof-of-concept of aberration correction with a catheter hydrophone was shown previously by Clement *et al* [36].

Our initial proof-of-concept study [35] was performed to show that 1) a miniature hydrophone integrated to the catheter tip can be used for aberration correction through the skull, 2) transcranial histotripsy can be used to liquefy the clot, and 3) the liquefied clot can be drained via a catheter. Accurate insertion of the catheter hydrophone through the skull to the therapy focus requires an insertion strategy and the insertion angle may impact the accuracy of the hydrophone measurement. The goal of this study was to develop a strategy to allow the catheter hydrophone insertion through a burr hole in the skull and to experimentally evaluate the performance of the aberration correction using the catheter hydrophone after insertion. A forward-facing chip hydrophone and a side-facing cylinder hydrophone were investigated. A catheter holder was specially designed and built with 3D printing to enable the accurate placement of the catheter hydrophone through the histotripsy transducer and a burr hole in the skull. The performance of the catheter hydrophone for aberration correction was evaluated using an excised human skullcap.

5.2 Materials and Methods

5.2.1 Experimental Equipment

Transcranial Histotripsy Phased Array Transducer: A 500 kHz hemispherical transcranial histotripsy array with 256 removable element modules was designed and built in-house using 3D rapid prototyping methods similar to those previously described [37]. All elements populating the array were modular and were mounted in an aluminum scaffold. A 256-channel high voltage pulser, capable of delivering short (≤ 2 acoustic cycles) high amplitude electrical pulses, was used to drive the elements of the array. The pulser was controlled by a set of custom microcontrollers implemented on field-programmable gate array (FPGA) boards (DE0-nano, Terasic Technology, Taiwan) which were used to independently control each element of the array. Histotripsy pulse sequence parameters were defined through a custom MATLAB (MathWorks, Natick, MA, USA) program and uploaded to the FPGAs.

Catheter Hydrophone: The catheter hydrophone was comprised of a hydrophone inserted into a ventriculostomy catheter (EDM Ventricular Catheter, Medtronic, Minneapolis, MN, USA). To investigate how the insertion angle impacts the aberration correction, two different hydrophones with orthogonal acoustic apertures orientations were explored: A forward facing piezoelectric chip (detailed in *Forward Facing Hydrophone* section) and a side-facing piezoelectric cylinder hydrophone (detailed in *Side Facing Hydrophone* section).

Forward-Facing Hydrophone: The forward-facing hydrophone consisted of a piezoelectric chip with its poled direction aligned with the direction of insertion of the catheter hydrophone (Fig. 5.1a). The hydrophone was fabricated in-house. The piezoelectric chip was interfaced to a coax cable via conductive epoxy (8331S, MG Chemicals, Surrey, B.C., Canada) and insulated with a non-conductive epoxy (EA E-00CL, Loctite, Düsseldorf, Germany). The chip was 500 × 500 μm with a thickness of 300 μm.

Side-Facing Hydrophone: The side-facing hydrophone consisted of a piezoelectric cylinder with its poled direction orthogonal to the direction of insertion of the catheter hydrophone (Fig. 5.1b). A hydrophone with a cylindrical piezoelectric element was purchased from a commercial vendor (Y-138, Sonic Concepts Inc., Bothell, WA, USA). The cylinder had a diameter of 0.8 mm and height of 0.9 mm.

Catheter Hydrophone Holder: To accurately insert the catheter hydrophone through the histotripsy array and the skull to the array focus, a catheter holder was specially designed and fabricated with 3D printing. The catheter holder consisted of a 3D printed solid body with a central guide hole for the catheter and was designed to fit in place of any of the 256 modular elements within the array (Fig. 5.2). The catheter was marked with scale markings and a shaft collar was placed around the shaft of the catheter to control the depth of insertion into the array. To place the hydrophone at the geometric focus, the tip of the catheter was inserted approximately 15.2 cm from the face of the catheter holder (15 cm for the focal distance plus 0.2 cm for the thickness of the catheter).

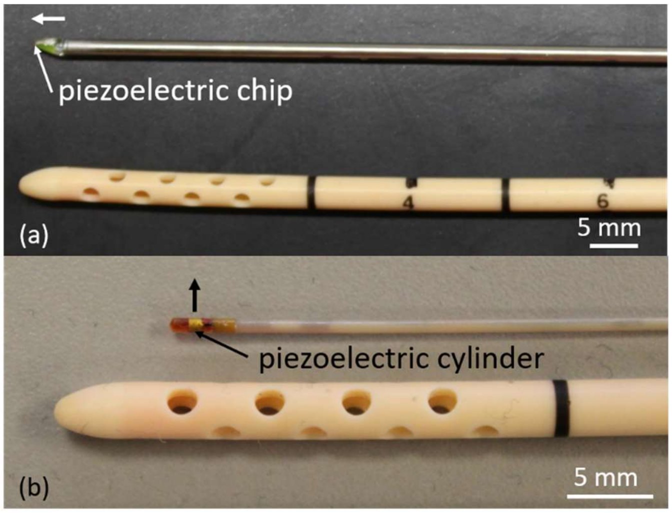

Figure 5.1. (a) The forward-facing hydrophone had its acoustic aperture pointed in the direction of insertion of the catheter hydrophone. (b) The side-facing hydrophone had its acoustic aperture pointed orthogonal to the direction of insertion of the catheter hydrophone. The arrows indicate the forward and side-facing direction of the hydrophones. The hydrophones were inserted into the ventriculostomy catheter (shown in the below the forward and side-facing hydrophone).

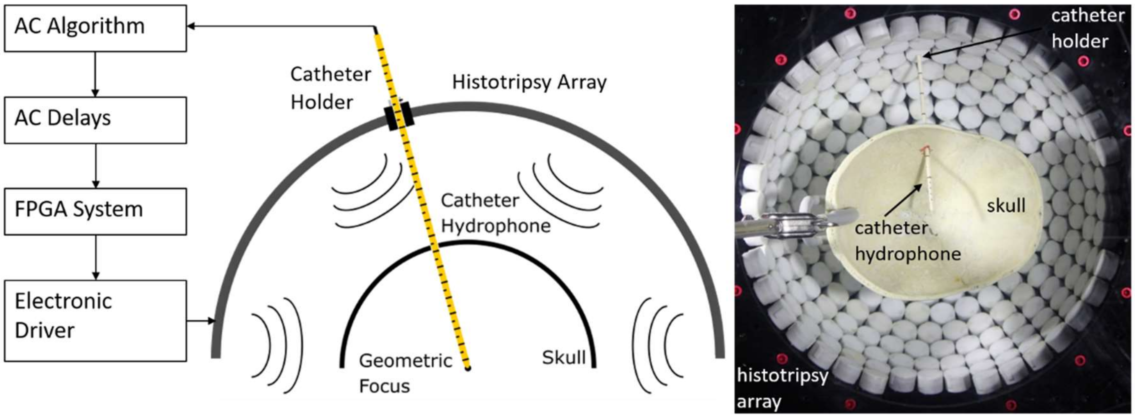

Figure 5.2. A schematic of the catheter hydrophone aberration correction (AC) experiments (left) and the physical experimental setup for the aberration correction experiments (right).

5.2.2 Hydrophone Characterization

Electrical Impedance and Sensitivity Measurements: The electrical impedance curves for each hydrophone were obtained via a network analyzer (VNA 2180, Array Solutions, Sunnyvale, TX, USA). The impedance was analyzed between 0.1 – 5 MHz with a step size of 10 kHz.

The sensitivity of each hydrophone (within the catheter) to a single calibrated 500 kHz transducer module was estimated. Measurements were made by placing each hydrophone 15 cm from the face of the transducer module. For the forward-facing hydrophone, the transducer module was oriented such that its normal ray was in-line with the shaft of the hydrophone. For the side-facing hydrophone, it was oriented such that its normal ray was orthogonal with the shaft of the hydrophone. The pressure output of the transducer was increased in roughly 500 kPa increments and the peak-to-peak amplitude of the signal produced by the hydrophone was recorded.

Impact of Insertion Angle: Experiments were performed to characterize the temporal precision of measurements made with each hydrophone (forward and side-facing) when inserted to the geometric focus via the catheter holder. This was done by guiding the hydrophones (within the catheter) to the geometric focus of the array via the catheter holder (without the skull) and pinging each element of the array one-at-a-time. The time-of-flight (TOF) was calculated for each measurement. The TOF captured by each hydrophone inserted into the array were compared to the TOF captured by a PVDF capsule hydrophone (HGL200, Onda, Sunnyvale, CA, USA) placed at the geometric focus of the array in a standard orientation (tip pointing directly at the back of the hemisphere array).

5.2.3 Transcranial Aberration Correction with the Catheter Hydrophone and Insertion Strategy

Aberration Correction Setup: Aberration correction experiments using the catheter hydrophone and the insertion strategy were performed through an excised human skullcap. The skullcap was fixed with respect to the array such that the cut plane of the skullcaps was 1 cm in front of the geometric focus. The catheter hydrophone was inserted through a burr hole in the skullcap to the geometric focus using the catheter holder as previously described. Waveforms from each of the 255 modular elements (256 minus the removed module for the catheter holder) were measured and uploaded to an algorithm to calculate relative delays among the 255 elements. These were uploaded to the FPGAs to trigger the electronic diving system of the array accordingly.

Aberration Correction Algorithm: An aberration correction algorithm was implemented to calculate the time needed to delay the pulse emitted from each element with respect to one another to ensure their concurrent arrival at the measurement point. The algorithm consisted of three steps: (1) a band pass filter with a lower and upper cutoff frequency of 50 kHz and 1.5 MHz was used to reduce the noise in the waveforms; (2) the TOF of the waveforms incident on the hydrophone was calculated for all 255 elements; (3) the relative delays (i.e., how long the emission time of each element must be delayed to ensure their concurrent arrival at the focus) were calculated. This was done by subtracting the 255 TOF values from that of an arbitrary reference element. These delays were uploaded to the FPGAs to trigger the electronic diving system of the array accordingly. As a “gold-standard” reference, aberration correction was also performed using a capsule hydrophone in a standard orientation.

5.2.4 Evaluation of Catheter Hydrophone Aberration Correction

To assess the potential clinical value of this correction strategy for ICH treatment we assessed the focusing through an excised human skullcap. Beam profiles in the sagittal, coronal and axial directions were measured at a relatively low pressure (< 2 MPa) using a capsule hydrophone with and without aberration correction. The peak pressure values were also measured at the same acoustic power input with and without aberration correction.

In-vitro clot was treated through the skull with and without catheter hydrophone aberration correction at a fixed acoustic power to show the potential clinical value of this method for ICH treatment. Clots were prepared with whole bovine blood according to methods described in [38]. The focus was electronically steered through a 10 mm radius spherical volume using a hexagonal close packed (HCP) steering pattern, with lattice point spacing of 1.5 mm.

5.3 Results

5.3.1 Hydrophone Characterization

Electrical Impedance and Sensitivity Measurements: The electrical impedance curves for the hydrophones are shown in Figure 5.3. The curves indicated a resonant frequency for the forward and side-facing hydrophone at about 3.3 and 2.2 MHz, respectively.

The response of the hydrophones (within the catheter) to a single 500 kHz element was measured. The estimated sensitivities of the forward and side-facing were 480 and 692 mV/MPa, respectively (Fig. 5.4a). The frequency response of each hydrophone to the waveform produced by the 500 kHz element showed a response centered around 500 kHz (Fig. 5.4b).

Impact of the Insertion Angle: Experiments were performed to characterize the temporal precision of measurements made with each hydrophone (forward and side-facing) when inserted to the geometric focus via the catheter holder. Figure 5.5a shows the peak-negative TOF measured with each hydrophone. The TOF measured in the free field without the skull was plotted as a function of the ascending angle of incidence between the element and hydrophone, with respect to the catheter insertion axis. The TOF for the forward and side-facing hydrophones showed some flat portions but had significant variation. The standard deviation of the TOF measured by the peak negative signal for the capsule, forward and side-facing hydrophone was 0.15 μs, 2.70 μs and 1.52 μs, respectively.

As the peak-negative TOF from forward and side-facing hydrophone measurements showed significant variation, we evaluated the front edge of the waveform envelope as a more robust feature for obtaining precise timing information across all angles. The edge was defined as 15% of the maximum of the normalized envelope the waveform. Figure 5.5b shows the TOF measured by the front edge with each hydrophone. The forward and side-facing hydrophones showed relatively flat TOFs across all angles with evident offsets at a fraction of angles about 90° from the intended measurement face. The standard deviation of the edge TOF for the capsule, forward and side-facing hydrophone was 0.13 μs, 0.36 μs and 0.53 μs, respectively.

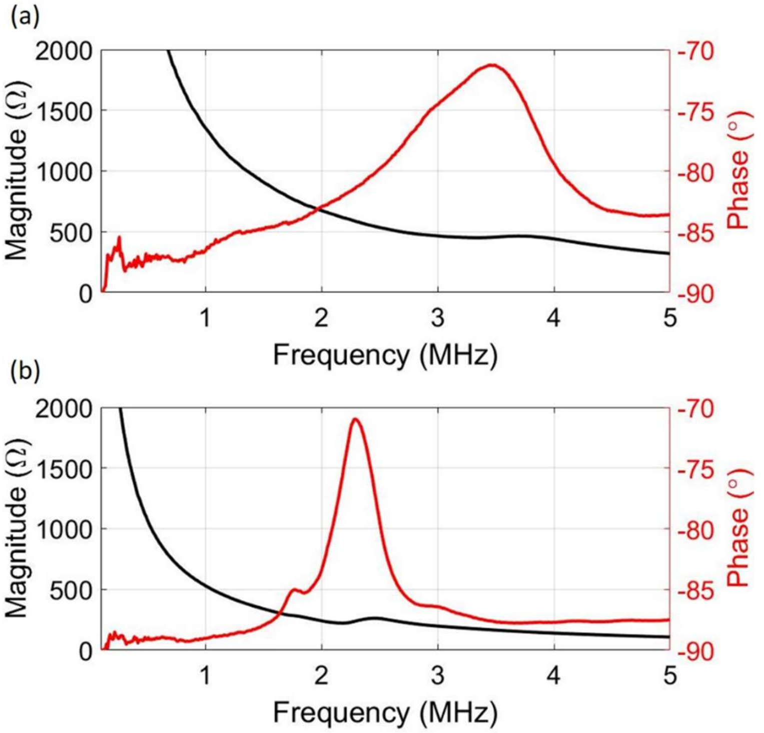

Figure 5.3. The electrical impedance curves for the (a) forward and (b) side-facing hydrophones.

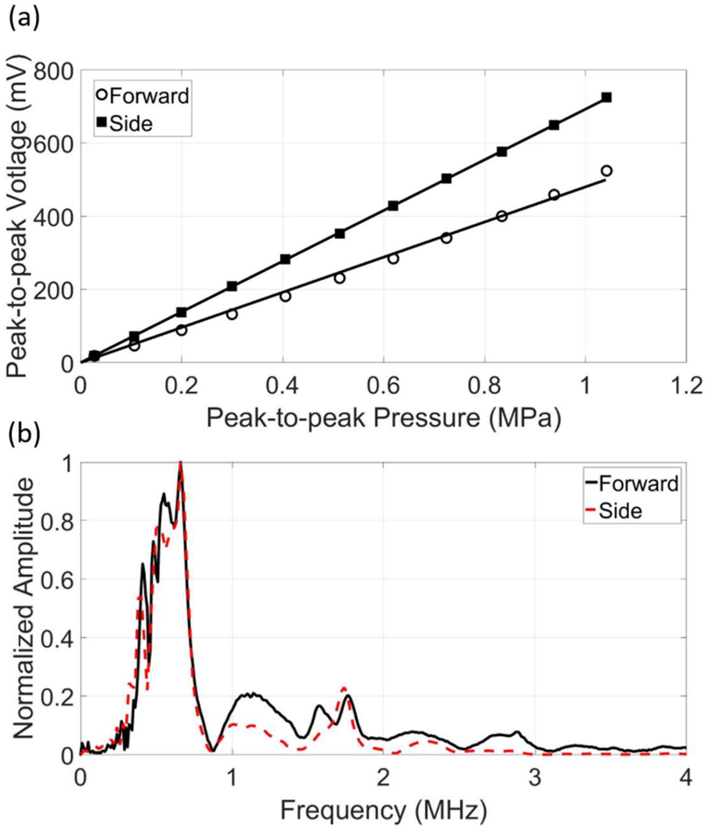

Figure 5.4. (a) The peak-to-peak voltage output by the forward and side-facing hydrophone as a function of the peak-to-peak pressure output by a single 500 kHz element measured at 15 cm. The estimated sensitivity for the forward and side-facing hydrophone was 480 and 692 mV/MPa, respectively. (b) The frequency response of each hydrophone to the waveform produced by a single 500 kHz element.

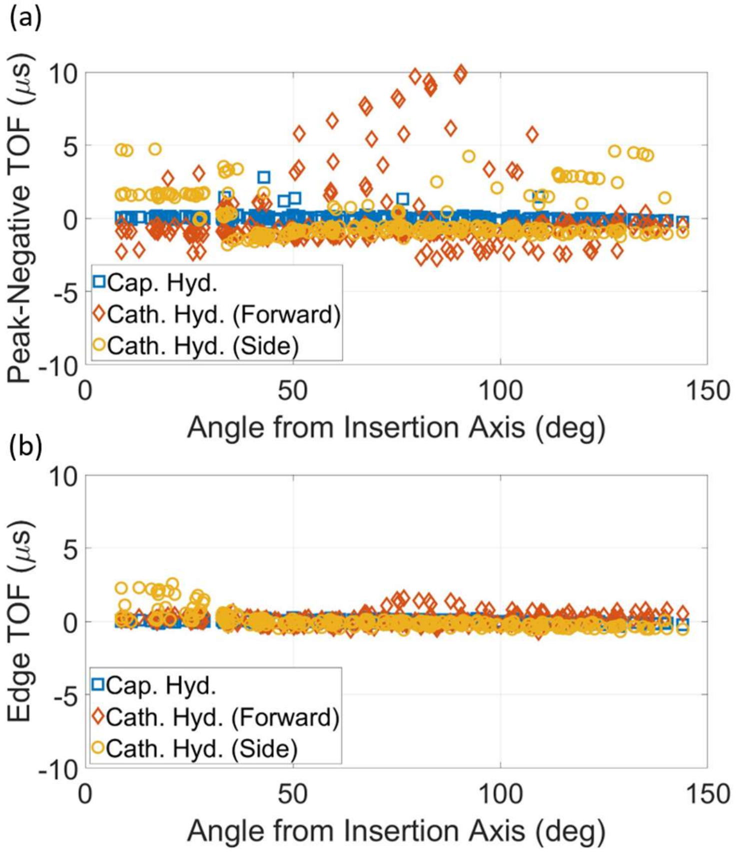

Figure 5.5. The (a) peak-negative and (b) edge TOF. TOFs were subtracted by the mean TOF for each data set to center the variations in the TOF about zero.

5.3.2 Evaluation of Catheter Hydrophone Aberration Correction with the Insertion Strategy

Using the insertion strategy with the custom-built catheter holder, the catheter hydrophone was inserted through a burr hole in the skull to the histotripsy transducer focus. Figure 5.6 shows the 3-axis beam profile through the skull with no correction and with aberration correction using the forward and side-facing catheter hydrophones, where the catheter hydrophone was placed at a central location of the skull (Fig. 5.2). The beam profile using the commercial capsule hydrophone correction placed at the focus in a standard orientation was used as a reference. Capsule and catheter hydrophone correction showed improved focusing as seen with the reduced side lobes and increased beam amplitude. The -3 dB beam width of the focus for each case is shown in Table 5.1.

The beam width for catheter hydrophone aberration correction was within 0.4 mm of that for capsule hydrophone aberration correction. Using the catheter hydrophone, the peak-negative pressure was increased by 56.2% and 47.8% with the forward and side-facing hydrophone, respectively. This corresponded to 86.5% and 81.9% of the pressure produced with the capsule hydrophone correction.

To understand the implications of catheter hydrophone aberration correction on clot treatment, volumes of *in-vitro* clots were targeted and treated with and without aberration correction at a fixed acoustic power. In this case, the forward-facing catheter hydrophone was used. The MR images of the clots after treatment are shown in Figure 5.7. Due to the increased focal pressure, the lysed region of the clot was extended closer to the boundary of the targeted treatment region with aberration correction than with no correction. This resulted in a larger liquefied volume (5.23 mL) than with no correction (1.27 mL).

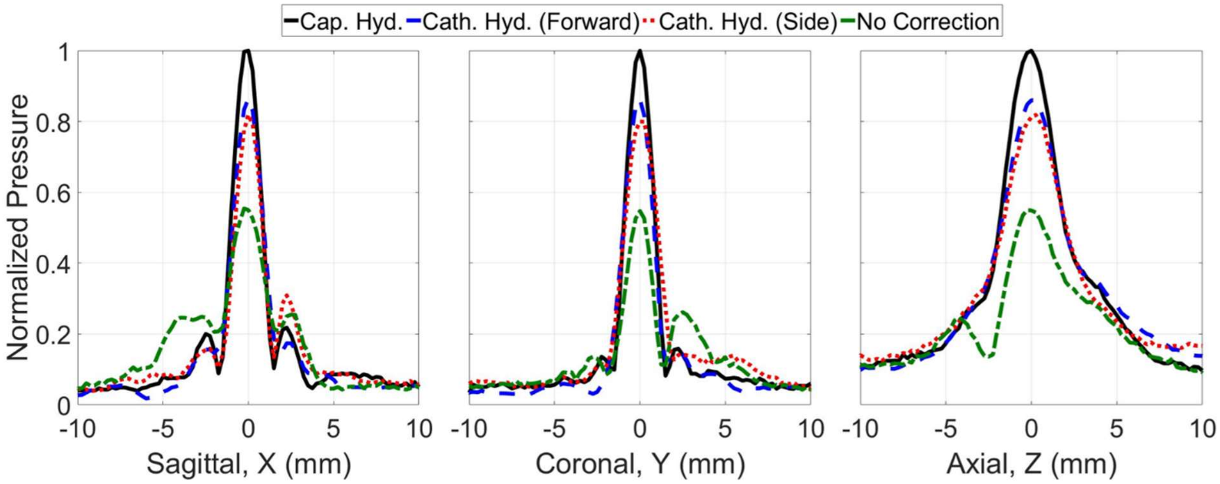

Figure 5.6. The 3-axis beam profiles measured through the excised human skullcap with (Cap. Hyd.) correction, catheter hydrophone (Cath. Hyd.) correction and no correction.

Table 5.1. A summary of the performance for each hydrophone used for aberration correction.

	Percent of pressure achieved with ideal aberration correction	Pressure increase after aberration correction compared to no correction
Capsule Hyd.*	100%	80.0%
Catheter Hyd. (Forward)	86.5%	56.2%
Catheter Hyd. (Side)	81.9%	47.8%

*Capsule hydrophone measurement was used as the ideal case for aberration correction (100%) to compare with the aberration correction cases using the catheter hydrophones.

Table 5.2. The -3 dB beam widths measured for each case.

	Sagittal, X (mm)	Coronal, Y (mm)	Axial, Z (mm)
Capsule Hyd.	1.30	1.25	2.47
Catheter Hyd. (Forward)	1.37	1.34	2.76
Catheter Hyd. (Side)	1.27	1.57	2.83
No Correction	1.75	1.08	2.64

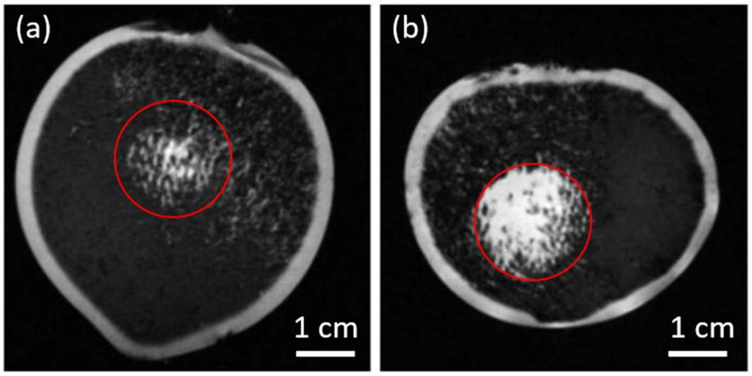

Figure 5.7. MR images of clots after treatment with (a) no correction and with (b) catheter hydrophone aberration correction. The red circles indicate the perimeter of the targeted region for each case. The slices shown are taken from the center of the targeted region.

5.4 Discussion

The goal of this study was to develop a strategy to allow the catheter hydrophone insertion through a burr hole in the skull and to experimentally evaluate the performance of the aberration correction using the catheter hydrophone after insertion. Both hydrophones showed performance within 80% of that achieved with a commercial capsule hydrophone, which is taken to be a "gold-standard" aberration correction. The capsule hydrophone has a large diameter (> 1 cm), thus cannot be used for the ICH treatment where a small diameter catheter is used (~2 mm). This is within range of the performance presented by other transcranial aberration correction methods. Simulation methods using 3D image sets have reported corrections around 80-83% that of a standard hydrophone correction [24], [29]. Methods using MR-ARFI have reported a slight advantage to simulation methods [27]. Minimally invasive, time-reversal corrections have shown even greater performance with corrections greater than 90% of that obtained with a standard hydrophone [29]. The increased pressure achieved with catheter hydrophone aberration correction was able to increase the volume liquefied with electronic focal steering at a fixed acoustic power.

The strategy investigated here required the insertion of the catheter hydrophone through the back of the array. This orientation created a large range of angles beyond normal incidence with the hydrophone aperture. In attempt to understand the impact of this circumstance on performance, we explored two piezoelectric hydrophones with orthogonal aperture orientations (forward and side-facing). While the peak-negative TOF for both hydrophones showed significant variation at incidence angles around 90° from the intended measurement face (for both hydrophones), using the edge of the waveform envelope significantly improved the measurement precision across angles. However, small offsets in the TOF remained for a fraction of incidence angles around 90° from the intended measurement face. The exact cause of the offsets is not known but we suspect that their presence had to do with issues maintaining signal fidelity for measurements at angles orthogonal to the intended measurement face due to inherent properties of the hydrophones (e.g., poling direction, fabrication procedures).

Future performance improvements for this aberration correction strategy will lie in developing a catheter hydrophone that is less prone to directional phase variability. We chose piezoelectric hydrophones because of their high sensitivity and ability to measure signals with a high signal-to-noise ratio (SNR) through the skull. However, the size, limited geometry of the acoustic aperture as well as the fabrication procedures for these hydrophones likely led to the phase variability seen across measurements at the large range of incidence angles in this application. For example, the largest dimension of these hydrophones was on the order of $\lambda/3 - \lambda/4$. Thus, the geometry of these piezoelectric hydrophones may be a limiting factor for improved performance in future development of this technique. One potential avenue with promise is the use of fiber optic hydrophones (FOHPs) which may provide a more refined solution to the problems presented here. This is due to their small apertures (100 µm, $\lambda/30$), consistent directional response and minimal fabrication procedures, making them potentially less susceptible to some of the phase variation affects seen with piezoelectric hydrophones in this and previous studies [35]. Although these hydrophones have low sensitivity and SNR, adding thin interference layers to the aperture can significantly improve the sensitivity and may be an approach to pursue in future development of this technique [39]–[42]. Future work for this study also includes testing catheter hydrophone aberration correction with this insertion strategy through different skulls and locations within the skull[1].

Although this insertion strategy provides a large range of possible entry points for insertion of the catheter hydrophone, it is limited in that it mechanically couples the array to the head. This coupling significantly confines the mechanical repositioning of the array around the patient's head. Such repositioning may be necessary if the electronic focal steering range is insufficient to treat the entirety of the clot volume (i.e., repositioning of the geometric focus of the array to the new

---

[1] Initial characterization on the performance of this method in different locations and skulls is presented in the Appendix at the end of this chapter under *Performance for Different Locations and Skulls*.

location in the clot may be necessary). A potential alternative to the strategy described in the current chapter is to embed the hydrophone within the tip of the catheter sheath, merging the catheter sheath and hydrophone into a single object. This contrasts with the catheter hydrophone presented in this chapter which consists of two objects (i.e., hydrophone and catheter sheath). This would allow the surgeon to insert the catheter sheath with the embedded hydrophone into the clot before the patient is placed into the array via a simple guidewire. After insertion of the catheter sheath with embedded hydrophone, the catheter guidewire could then be removed. Since the catheter sheath without the guidewire is flexible, the portion of the sheath remaining outside the brain could then be snaked out of the array without impacting the position of the hydrophone.

5.5 Conclusion

The goal of this study was to develop a strategy to allow the catheter hydrophone insertion through a burr hole in the skull and to experimentally evaluate the performance of the aberration correction using the catheter hydrophone after insertion. Using two piezoelectric hydrophones with orthogonal aperture orientations, performance within 80% of the “gold-standard” correction was achieved, this corresponded to pressure improvements up to 56.2% and an ability to increase the volume of clot liquefied with histotripsy at a fixed acoustic power by 312%. Future performance improvements for this correction strategy will lie in developing a catheter hydrophone that is less prone to directional phase variability (e.g., FOHPs).

5.6 Appendix

5.6.1 Performance for Different Locations and Skulls

Methods:

As ICH occurs in different regions of the brain the correction was evaluated at different anatomical positions through an excised human skullcap. Figure 5.8 shows the four anatomical positions examined: a central, posterior, anterior and lateral (left) position. Non-central positions were spaced approximately 20 mm from the central position. In addition, to evaluate the variability across skulls we assessed the correction through a second excised human skullcap. Skullcaps were prepared in a manner similar to that described in [35], [38]. The dimensions and acoustic properties of the skullcaps used are shown in Table 5.3. Dimensions and properties were measured according to methods described in [38].

To show the potential clinical value of using catheter hydrophone aberration correction with this insertion strategy for ICH treatment, volumes of *in-vitro* clots were targeted with and without catheter hydrophone aberration correction at each anatomical position through skull 1 and the central position through skull 2.

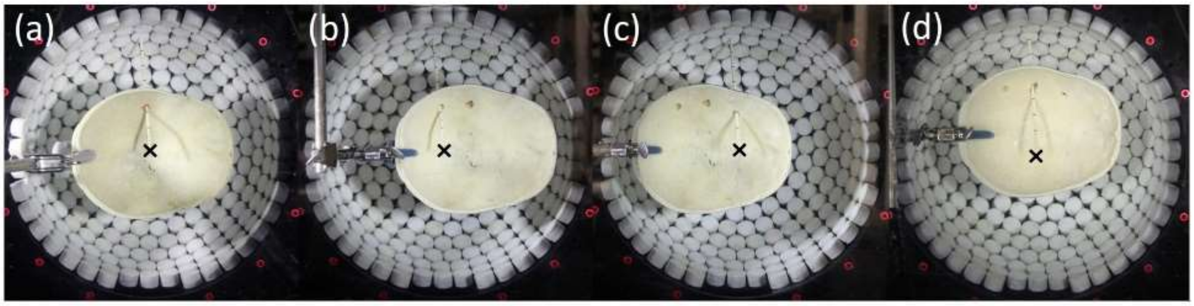

Figure 5.8. Catheter hydrophone aberration correction was applied in the (a) central, (b) posterior, (c) anterior and (d) lateral region of the skull.

Table 5.3. The dimensions and acoustic properties of the excised human skullcaps.

	Major dimensions (mm)			Thickness (mm)			Acoustic properties	
Skull#	Long axis	Short axis	Depth	Min	Max	Mean	500 kHz Attenuation (dB/cm)	Sound speed (m/s)
1	183	143	64	2.6	11.1	6.5 ± 1.3	14.5 ± 4.5	2340 ± 354
2	163	139	51	1.9	9.2	6.4 ± 1.0	10.7 ± 4.0	2649 ± 316

Results:

A summary of the performance of the correction with the catheter hydrophone with respect to the capsule hydrophone is shown in Table 5.4. The capsule hydrophone is considered as a baseline for the correction performance of the forward and side-facing hydrophones. The forward and side-facing hydrophone showed mostly consistent performance across the different skulls and anatomical positions examined (within 5%). The peak-negative pressure achieved relative to that achieved with the capsule hydrophone was between 82.2% – 86.0% for the forward-facing hydrophone and 81.9% – 86.0% for the side-facing hydrophone. The pressure recovered (relative to no correction) with the catheter hydrophone using either the forward or side-facing hydrophone was between 17.6% – 57.7%. The capsule hydrophone correction recovered pressures between 38.4% – 78.8%. The greatest pressure recovered with catheter hydrophone aberration correction was in the lateral position through skull 1. The least pressure recovered was in the central position through skull 2. This matched the greatest and least pressure recovered with capsule hydrophone correction.

To show the potential clinical value of using catheter hydrophone aberration correction with this insertion strategy for ICH treatment, volumes of *in-vitro* clots were targeted with and without catheter hydrophone aberration correction at each anatomical position through skull 1 and the central position through skull 2. The MR images of the clots after treatment are shown in Figure 5.9. In general, at a fixed driving pressure of the array, the lysed region of the clot was extended closer to the boundary of the targeted treatment region with aberration correction than without. Table 5.5 shows a summary of the increased lysed volume after histotripsy treatment through the skull with catheter hydrophone aberration correction relative to that without. The increase in the lysed volume ranged from 14% – 676%. The largest increase was for treatment in the lateral position through skull 1. The smallest increase was for treatment in the central position through skull 2.

Table 5.4. A summary of the performance for each hydrophone across locations and skulls.

	Percent of pressure achieved with ideal aberration correction					Pressure increase after aberration correction compared to no correction				
Skull/ Position	1/ Central	1/ Posterior	1/ Anterior	1/ Lateral	2/ Central	1/ Central	1/ Posterior	1/ Anterior	1/ Lateral	2/ Central
Cap. Hyd.	100%	100%	100%	100%	100%	80.0%	53.9%	68.2%	82.75	38.4%
Cath. H. (Forward)	86.5%	85.5%	82.2%	--	--	56.2%	33.5%	39.5%	--	--
Cath. H. (Side)	81.9%	85.4%	82.7%	86.0%	85.0%	47.8%	31.5%	38.3%	57.7%	17.6%

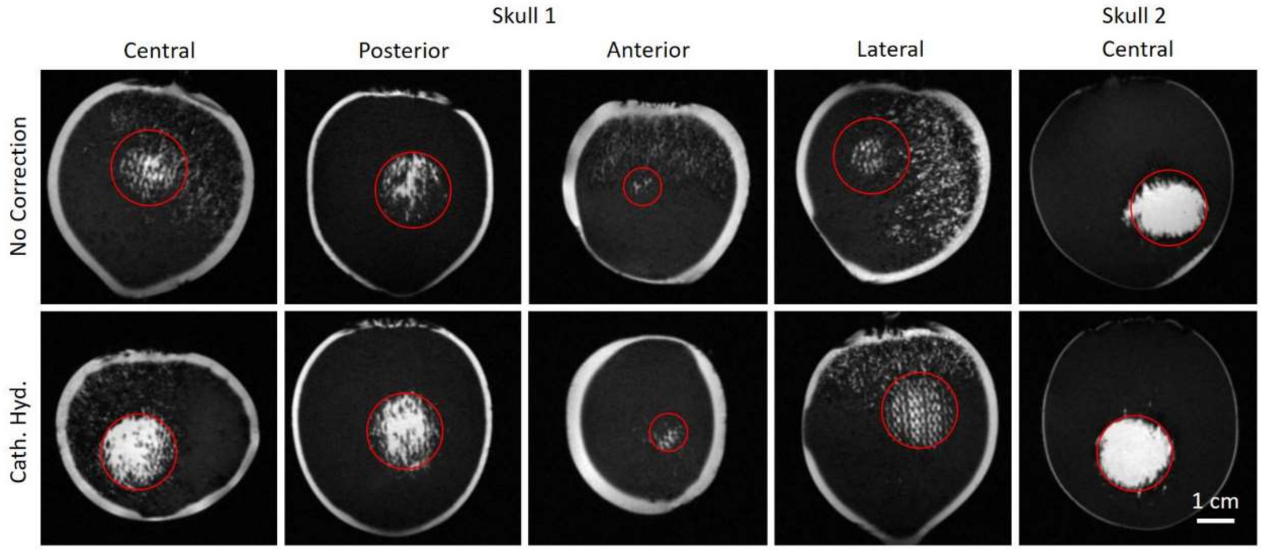

Figure 5.9. MR images of clots after treatment with no correction (top row) and with catheter hydrophone aberration correction (bottom row). The red circles indicate the perimeter of the targeted region for each case. The slices shown are taken from the center of the targeted region.

Table 5.5. A summary of the volumes of clot lysed after treatment with and without correction across different locations and skulls.

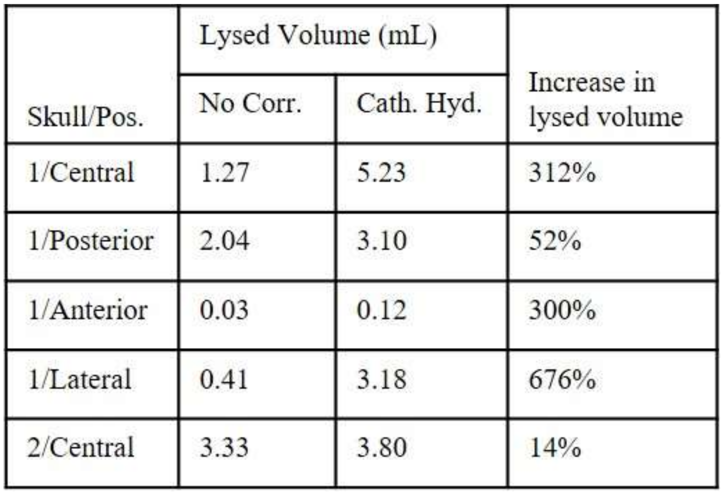

Skull/Pos.	Lysed Volume (mL)		Increase in lysed volume
	No Corr.	Cath. Hyd.	
1/Central	1.27	5.23	312%
1/Posterior	2.04	3.10	52%
1/Anterior	0.03	0.12	300%
1/Lateral	0.41	3.18	676%
2/Central	3.33	3.80	14%

Summary:

These results suggest that the performance of the catheter hydrophone in the described insertion strategy is largely consistent across different locations and skulls. The improvement in focusing through the skull corresponds to a measurable improvement in the treatment efficacy at a fixed driving pressure.

5.7 References

[1] M. Pernot, J. F. Aubry, M. Tanter, J. L. Thomas, and M. Fink, “High power transcranial beam steering for ultrasonic brain therapy,” *Phys. Med. Biol.*, vol. 48, no. 16, pp. 2577–2589, 2003.

[2] W. J. Elias *et al.*, “A Pilot Study of Focused Ultrasound Thalamotomy for Essential Tremor,” *http://dx.doi.org/10.1056/NEJMoa1300962*, 2013.

[3] N. McDannold, G. T. Clement, P. Black, F. Jolesz, and K. Hynynen, “Transcranial magnetic resonance imaging- guided focused ultrasound surgery of brain tumors: initial findings in 3 patients,” *Neurosurgery*, vol. 66, no. 2, pp. 323–332, 2010.

[4] E. Martin, D. Jeanmonod, A. Morel, E. Zadicario, and B. Werner, “High-intensity focused ultrasound for noninvasive functional neurosurgery,” *Ann. Neurol.*, vol. 66, no. 6, pp. 858–861, 2009.

[5] K. Hynynen, “MRI-guided focused ultrasound treatments,” *Ultrasonics*, vol. 50, no. 2. pp.

221–229, 2010.

[6] K. Hynynen and G. Clement, “Clinical applications of focused ultrasound—The brain,” *Int. J. Hyperth.*, vol. 23, no. 2, pp. 193–202, 2007.

[7] F. J. Fry, “Transkull transmission of an intense focused ultrasonic beam,” *Ultrasound Med. Biol.*, vol. 3, no. 2–3, 1977.

[8] E. S. Ebbini, S. I. Umemura, M. Ibbini, and C. A. Cain, “A Cylindrical-Section Ultrasound Phased-Array Applicator for Hyperthermia Cancer Therapy,” *IEEE Trans. Ultrason. Ferroelectr. Freq. Control*, vol. 35, no. 5, pp. 561–572, 1988.

[9] D. R. Daum and K. Hynynen, “A 256-element ultrasonic phased array system for the treatment of large volumes of deep seated tissue,” *IEEE Trans. Ultrason. Ferroelectr. Freq. Control*, vol. 46, no. 5, pp. 1254–1268, 1999.

[10] J. Sun and K. Hynynen, “The potential of transskull ultrasound therapy and surgery using the maximum available skull surface area.,” *J. Acoust. Soc. Am.*, vol. 105, no. 4, pp. 2519–2527, 1999.

[11] K. B. Ocheltree, P. J. Benkeser, L. A. Frizzell, and C. A. Cain, “An Ultrasonic Phased Array Applicator for Hyperthermia,” *IEEE Trans. Sonics Ultrason.*, vol. 31, no. 5, p. 526, 1984.

[12] F. J. Fry and S. A. Goss, “Further studies of the transkull transmission of an intense focused ultrasonic beam: Lesion production at 500 kHz,” *Ultrasound Med. Biol.*, vol. 6, no. 1, pp. 33–35, 1980.

[13] F. J. Fry, S. A. Goss, and J. T. Patrick, “Transkull focal lesions in cat brain produced by ultrasound,” *J. Neurosurg.*, vol. 54, no. 5, pp. 659–663, 1981.

[14] Z. Xu *et al.*, “Controlled ultrasound tissue erosion,” *IEEE Trans. Ultrason. Ferroelectr. Freq. Control*, vol. 51, no. 6, pp. 726–736, 2004.

[15] Z. Xu, J. B. Fowlkes, E. D. Rothman, A. M. Levin, and C. A. Cain, “Controlled ultrasound tissue erosion: The role of dynamic interaction between insonation and microbubble activity,” *J. Acoust. Soc. Am.*, vol. 117, no. 1, pp. 424–435, 2005.

[16] W. W. Roberts, T. L. Hall, K. Ives, J. S. Wolf, J. B. Fowlkes, and C. A. Cain, “Pulsed cavitational ultrasound: A noninvasive technology for controlled tissue ablation (histotripsy) in the rabbit kidney,” *J. Urol.*, vol. 175, no. 2, pp. 734–738, 2006.

[17] Z. Xu, G. Owens, D. Gordon, C. Cain, and A. Ludomirsky, “Noninvasive creation of an atrial septal defect by histotripsy in a canine model,” *Circulation*, vol. 121, no. 6, pp. 742–749, 2010.

[18] K. W. Lin *et al.*, “Histotripsy beyond the intrinsic cavitation threshold using very short ultrasound pulses: Microtripsy,” *IEEE Trans. Ultrason. Ferroelectr. Freq. Control*, vol. 61, no. 2, pp. 251–265, 2014.

[19] G. T. Clement and K. Hynynen, “Correlation of ultrasound phase with physical skull properties,” *Ultrasound Med. Biol.*, vol. 28, no. 5, pp. 617–624, 2002.

[20] J.-F. Aubry, M. Tanter, M. Pernot, J.-L. Thomas, and M. Fink, “Experimental demonstration of noninvasive transskull adaptive focusing based on prior computed tomography scans,” *J. Acoust. Soc. Am.*, vol. 113, no. 1, pp. 84–93, 2003.

[21] G. T. Clement and K. Hynynen, “A non-invasive method for focusing ultrasound through the human skull,” *Physics in Medicine and Biology*, vol. 47, no. 8. pp. 1219–1236, 2002.

[22] K. Hynynen *et al.*, “500-Element ultrasound phased array system for noninvasive focal surgery of the brain: A preliminary rabbit study with ex vivo human skulls,” *Magn. Reson. Med.*, vol. 52, no. 1, pp. 100–107, 2004.

[23] M. Wintermark *et al.*, “T1-weighted MRI as a substitute to CT for refocusing planning in MR-guided focused ultrasound,” *Phys. Med. Biol.*, vol. 59, no. 13, pp. 3599–3614, 2014.

[24] F. Marquet *et al.*, “Non-invasive transcranial ultrasound therapy based on a 3D CT scan: protocol validation and in vitro results,” *Phys. Med. Biol.*, vol. 54, no. 9, pp. 2597–2613, 2009.

[25] D. Chauvet *et al.*, “Targeting accuracy of transcranial magnetic resonance–guided high-intensity focused ultrasound brain therapy: a fresh cadaver model,” *J. Neurosurg.*, vol. 118, no. 5, pp. 1046–1052, 2013.

[26] G. Maimbourg, A. Houdouin, T. Deffieux, M. Tanter, and J. F. Aubry, “3D-printed adaptive acoustic lens as a disruptive technology for transcranial ultrasound therapy using single-element transducers,” *Phys. Med. Biol.*, vol. 63, no. 2, 2018.

[27] Y. Hertzberg, A. Volovick, Y. Zur, Y. Medan, S. Vitek, and G. Navon, “Ultrasound focusing using magnetic resonance acoustic radiation force imaging: Application to ultrasound transcranial therapy,” *Med. Phys.*, vol. 37, no. 6, pp. 2934–2942, 2010.

[28] L. Marsac *et al.*, “MR-guided adaptive focusing of therapeutic ultrasound beams in the human head,” *Med. Phys.*, vol. 39, no. 2, pp. 1141–1149, 2012.

[29] J. Gâteau, L. Marsac, M. Pernot, J. F. Aubry, M. Tanter, and M. Fink, “Transcranial ultrasonic therapy based on time reversal of acoustically induced cavitation bubble signature,” *IEEE Trans. Biomed. Eng.*, vol. 57, no. 1, pp. 134–144, 2010.

[30] M. Pernot *et al.*, “In vivo transcranial brain surgery with an ultrasonic time reversal mirror,” *J. Neurosurg.*, vol. 106, no. 6, pp. 1061–1066, 2007.

[31] M. Fink, “Time Reversal of Ultrasonic Fields—Part I: Basic Principles,” *IEEE Trans. Ultrason. Ferroelectr. Freq. Control*, vol. 39, no. 5, pp. 555–566, 1992.

[32] J. L. Thomas and M. A. Fink, “Ultrasonic beam focusing through tissue inhomogeneities with a time reversal mirror: application to transskull therapy,” *IEEE Trans. Ultrason.*

Ferroelectr. Freq. Control, vol. 43, no. 6, pp. 1122–1129, 1996.

[33] M. Pernot, G. Montaldo, M. Tanter, and M. Fink, "'Ultrasonic stars' for time-reversal focusing using induced cavitation bubbles," *Appl. Phys. Lett.*, vol. 88, no. 3, pp. 1–3, 2006.

[34] R. Seip, P. Van Baren, and E. S. Ebbini, "Dynamic Focusing in Ultrasound Hyperthermia Treatments Using Implantable Hydrophone Arrays," *IEEE Trans. Ultrason. Ferroelectr. Freq. Control*, vol. 41, no. 5, pp. 706–713, 1994.

[35] T. Gerhardson, J. R. Sukovich, A. S. Pandey, T. L. Hall, C. A. Cain, and Z. Xu, "Catheter Hydrophone Aberration Correction for Transcranial Histotripsy Treatment of Intracerebral Hemorrhage: Proof-of-Concept," *IEEE Trans. Ultrason. Ferroelectr. Freq. Control*, vol. 64, no. 11, pp. 1684 - 1697, 2017.

[36] G. T. Clement and K. Hynynen, "Micro-receiver guided transcranial beam steering," *IEEE Trans. Ultrason. Ferroelectr. Freq. Control*, vol. 49, no. 4, pp. 447–453, 2002.

[37] Y. Kim, A. D. Maxwell, T. L. Hall, Z. Xu, K. W. Lin, and C. A. Cain, "Rapid prototyping fabrication of focused ultrasound transducers," *IEEE Trans. Ultrason. Ferroelectr. Freq. Control*, vol. 61, no. 9, pp. 1559–1574, 2014.

[38] T. Gerhardson, J. R. Sukovich, A. S. Pandey, T. L. Hall, C. A. Cain, and Z. Xu, "Effect of Frequency and Focal Spacing on Transcranial Histotripsy Clot Liquefaction, Using Electronic Focal Steering," *Ultrasound Med. Biol.*, vol. 43, no. 10, pp. 2302–2317, 2017.

[39] C. Koch, "Coated fiber-optic hydrophone for ultrasonic measurement," *Ultrasonics*, vol. 34, no. 6, pp. 687–689, 1996.

[40] V. Wilkens and C. Koch, "Fiber-optic multilayer hydrophone for ultrasonic measurement," *Ultrasonics*, vol. 37, no. 1, pp. 45–49, 1999.

[41] P. C. Beard and T. N. Mills, "Extrinsic optical-fiber ultrasound sensor using a thin polymer film as a low-finesse Fabry–Perot interferometer," *Appl. Opt.*, vol. 35, no. 4, p. 663, 1996.

[42] P. Morris, A. Hurrell, A. Shaw, E. Zhang, and P. Beard, "A Fabry–Pérot fiber-optic ultrasonic hydrophone for the simultaneous measurement of temperature and acoustic pressure," *J. Acoust. Soc. Am.*, vol. 125, no. 6, pp. 3611–3622, 2009.

CHAPTER 6 Design, Fabrication and Initial Validation of a Histotripsy Transducer for the Treatment of Intracerebral Hemorrhage (ICH): An Integrated Pre-Clinical System

6.1 Introduction

The previous four chapters have laid a foundation for furthered development of histotripsy as a minimally invasive transcranial therapy for ICH. Chapter 2 showed the initial *in-vitro* feasibility of histotripsy clot liquefaction using excised human skullcaps. Chapter 3 addressed some initial *in-vivo* safety concerns within a porcine ICH model. Chapters 4 and 5, presented a novel method for aberration correction based on the clinical need to drain the liquefied clot. Although, the success of these studies has generated an initial body of evidence to demonstrate the potential of using histotripsy as a minimally invasive treatment for ICH, additional pre-clinical studies with *in-vitro* and *in-vivo* models that better capture the true human ICH experience and systems that better meet the clinical requirements are needed for further validation.

The challenge with validation on more relevant models is that few models truly capture the human ICH experience and remain relevant to characterizing both the efficacy and safety of transcranial focused ultrasound (FUS) therapy. Monteith *et al.* presents the use of human cadaver models and porcine models in combination with excised human skulls to investigate the use of magnetic resonance-guided focused ultrasound (MRgFUS) as a minimally invasive method to safely liquefy clot through the skull [1]. The use of human cadavers is ideal from an anatomical standpoint while the use of human skulls and porcine models allows investigation into the biological response in a live model. In addition, Eames *et al.* have developed full human head phantoms for validation of transcranial focused ultrasound [2]. These phantoms provide a more controllable surrogate to human cadavers but may be limited in their capacity to model the true ICH experience. It is likely that some combination of these different models will be necessary in further validating histotripsy as a safe and effective treatment for ICH.

In considering the need for additional preclinical studies, considerations for a system better tuned to the clinical requirements of an effective ICH treatment should also be made. The histotripsy transducers used in the previously discussed *in-vitro* transcranial studies consisted of 256 elements at 250 and 500 kHz. Although these transducers showed some initial success in liquefying clots through the human skull, there remains significant space to investigate design parameters that may improve the peak output, transmission and steer-ability though the human skull. Such parameters include the drive frequency, piezoelectric material, transducer module size and design, and module packing density. In addition, the previous transducers were designed as bench-top systems with little ability to be adapted to a more clinically relevant experimental setting. Thus, additional effort should be made in adapting the histotripsy array transducer to the clinical space.

The purpose of this chapter is five-fold: (1) to present an evaluation of parameters important to improving the design of a transcranial histotripsy array, (2) present the design of a new pre-clinical prototype histotripsy transducer intended for transcranial ICH treatment, (3) provide some initial performance metrics for the final design, (4) present the full pre-clinical system prototype intended for use in cadavers with ICH and (5) show initial investigation into the system performance on human cadaver models.

6.2 Materials and Methods

6.2.1 Evaluation of Design Parameters

Transmission Measurements through Excised Human Skulls: The transmission of acoustic pulses through excised human skullcaps (n = 7) at discrete frequencies (500 kHz, 700 kHz, 900 kHz, 1 MHz and 2 MHz) was measured. Lower frequencies were not considered in this experiment due to the observation of cavitation on the surface of the skull at 250 kHz [3]. A capsule hydrophone (HGL200, Onda, Sunnyvale, Ca) was placed 150 mm from a single element ultrasound transducers with noted frequencies, that were fabricated in-house. A degassed, excised human skullcap was placed approximately halfway between the hydrophone and the ultrasound transducer. This distance was similar to the anticipated distanced between the external skull surface and the surface of the array elements in a therapy setting. The skullcap was oriented such that its surface was approximately normal to the ray emitted from the ultrasound transducer. Transducers were electronically driven to produce ~1.5 cycle acoustic pulses at their center frequency. At each frequency, measurements of the peak-negative pressure were made with and without the skull in place via the capsule hydrophone.

Approximating Spatiotemporal Variation through Excised Human Skulls: Experiments were performed to approximate the spatiotemporal variation inherent to the skull and investigate how it impacted the peak-negative focal pressure achieved through the skull for array elements of different dimensions. The approximation has two main assumptions: (1) the skull can be considered as a series of point-source re-emitters of the ultrasound pulse that enters it and (2) that the therapy focal point is far enough away from the skull surface that the pathlength differences from the re-emitted pulses are negligible and those do not introduce additional phase variations, allowing the focal pressure to be approximated by simply summing the individual phase-shifted waveforms. A degassed, excised human skullcap was placed 300 mm from an ultrasound transducer that was fabricated in-house. This distance was used so that the section of wave propagating through the skull approximated a plane wave. A capsule hydrophone was placed on the other side of the skullcap, approximately 5 mm from the internal surface of the skull. The hydrophone was then scanned through a 40 × 40 mm grid in the lateral-elevational plane, with a step size of 2 mm. At each location, the acoustic waveform was captured and the time-of-flight (TOF) was measured. TOF measurements were made using the edge of the acquired waveform envelope, which was defined as 15% of the envelope peak. Identical measurements were made without the skullcap and used to calibrate out any temporal variations not caused by propagation through the skull.

The grid of spatially varying time values measured through sections of skullcaps (n = 7) was used to simulate the effects of aberration on ~1.5 cycle waveforms emitted through the skull. This was done by first windowing the 40×40 mm grid into a 40×40, 20×20, 16×16, 12×12, 8×8 and 4×4 mm grid. A Gaussian pulse was then generated in MATLAB to resemble a 700 kHz 1.5 cycle waveform, similar to pulses used in intrinsic threshold histotripsy. To simulate the aberrated waveform for hypothetical element sizes, this un-aberrated waveform was shifted according the relative delays of the pixels within each window size. The shifted waveforms were then summed. The peak-negative amplitude of the shifted, summed waveforms was then divided by the peak-negative amplitude of the un-shifted, summed waveforms. The fraction of the un-aberrated waveform at each hypothetical element size was compared to obtained from the 4×4 mm grid via pair-wise, independent 2-tailed t-tests (α=0.05).

Investigating Piezoelectric Materials for Array Elements: Different piezoelectric elements were constructed using a range of piezoelectric materials in order to identify that with the best combination of pressure-output and durability under high load/PRF driving conditions. The specific elements tested are listed in Table 6.1. Peak-negative pressure output measurements were performed at 150 mm (the planned focal distance of the hemispherical array) using a calibrated capsule hydrophone (HGL085, Onda, Sunnyvale, CA). All piezoelectric materials were acoustically tuned to the propagation medium (water) using two matching layers. The matching network for each material was identical and consisted of a copper mesh-epoxy composite as the first (or inner matching layer) and a 3D printed plastic as the second (or outer matching layer). Durability tests were performed by driving the transducers at high PRFs (200 Hz) and monitoring the pressure output over time.

Table 6.1. Piezoelectric materials tested.

Material	**Frequency**	**Manufacturer**	**Geometry**	**Surface Area**
PZ36	700 kHz	MEGGIT	20 mm disc (wrap)	314 mm^2
PZT 4	700 kHz	Steminc	20 mm disc	314 mm^2
PZT 4 50% Comp.	700 kHz	Del-Piezo	17×17 mm square	289 mm^2
PZT 5 50% Comp.	700 kHz	Del-Piezo	17×17 mm square	289 mm^2

6.3 Results

6.3.1 Evaluation of Design Parameters

Transmission Measurements through Excised Human Skulls: The transmission through excised human skullcaps at discrete frequencies was measured. Figure 6.1 shows the transmission at 500 kHz, 700 kHz, 900 kHz, 1 MHz and 2 MHz through sections of excised human skullcaps. The mean transmission remained relatively flat between 500 kHz and 1 MHz (roughly 30%). There was a clear decrease in the mean transmission between 1 MHz and 2 MHz.

Approximating Spatiotemporal Variation through Excised Human Skulls: Experiments were performed to approximate the spatiotemporal variation inherent to the skull and investigate how it impacted the peak-negative focal pressure achieved through the skull for array elements of different dimensions. Figure 6.2a shows the spatiotemporal variation through a section of an excised human skullcap highlighting the different "hypothetical element sizes" (i.e., window sizes) investigated. Figure 6.2b shows the simulated effects of aberration on a histotripsy waveform for a hypothetical 40×40 mm element. The simulated aberrated waveform had a reduced peak-negative pressure in comparison to the unaberrated waveform. The ratio of the peak-negative pressure of the aberrated waveform to the peak-negative pressure of an un-aberrated waveform was calculated to produce the fraction of the un-aberrated waveform. Figure 6.3 shows the average (n = 7) fraction of an unaberrated waveform as a function of hypothetical element sizes. The fraction of unaberrated waveform was small for large hypothetical element sizes (40×40 mm) and gradually increased close to unity for small hypothetical element sizes (4×4 mm). For 40×40 and 20×20 mm elements, the fraction of the unaberrated waveform was statistically different that of from 4×4 mm ($\alpha = 0.05$).

Investigating Piezoelectric Materials for Array Elements: The peak-negative pressure output as a function of peak drive voltage for all piezoelectric materials tested is shown Figure 6.4. Of the materials tested, PZ36 and the PZT5 50% composite were optimal performers producing nearly equal peak-negative pressures at maximal driving voltages, with peak-negative pressures exceeding 1.4 MPa. However, the PZT 5 composite failed within 1 hour when being driven above 1500 V at a clinically relevant PRF (200 Hz), whereas the PZ36 was able to sustain its pressure output at this PRF (Fig. 6.5).

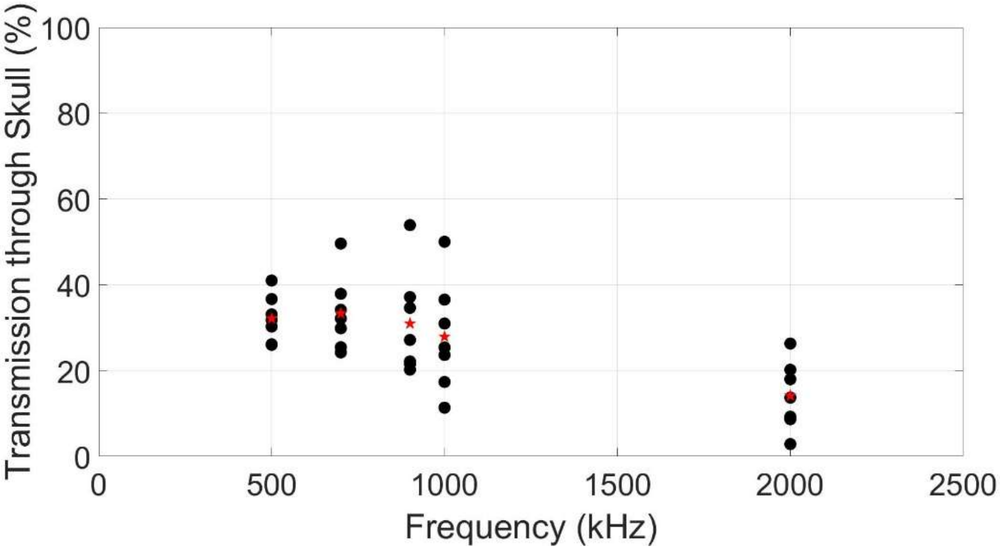

Figure 6.1. The peak-negative transmission through excised human skullcaps (n = 7) at discrete frequencies: 500 kHz, 700 kHz, 900 kHz, 1 MHz and 2 MHz. Red stars indicate the mean.

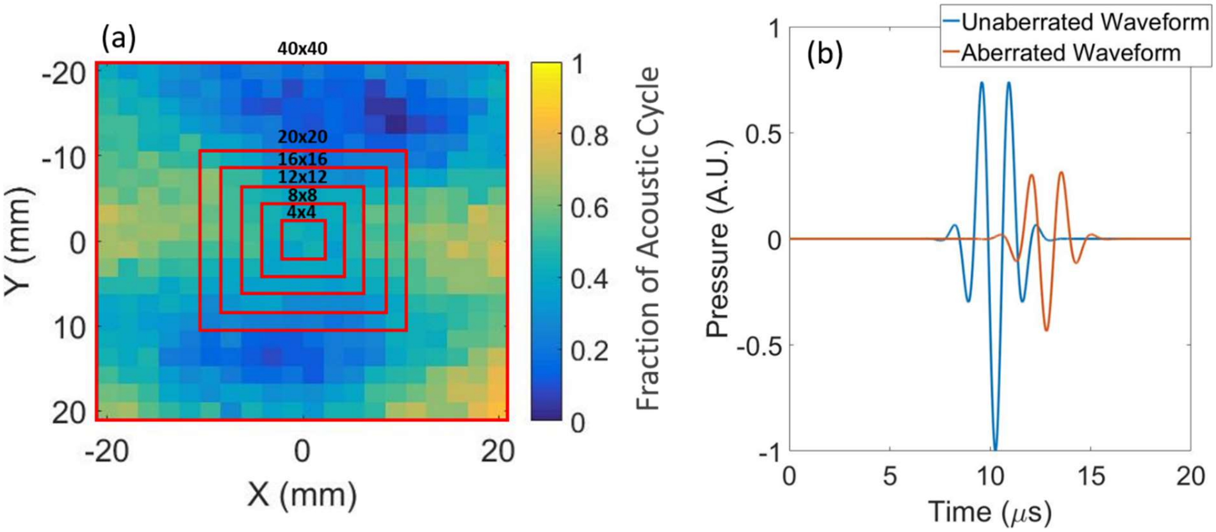

Figure 6.2. (a) The spatiotemporal variation through a section of an excised human skullcap highlighting the different hypothetical element sizes (i.e., window sizes). (b) The simulated effects of aberration on a histotripsy waveform for a hypothetical 40×40 mm element.

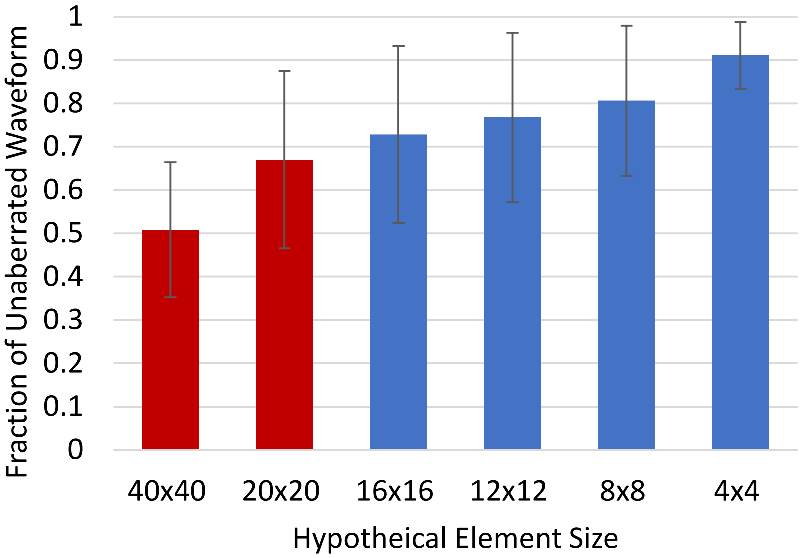

Figure 6.3. Approximated impact of spatiotemporal variation through the skull on peak-negative pressure transmission for array elements of different dimension. The ratio of the peak-negative pressure of a simulated aberrated waveform to the peak-negative pressure of a nonaberrated waveform was calculated to produce the fraction of the unaberrated waveform. The fraction of unaberrated waveform was small for large hypothetical element sizes (40×40 mm) and gradually increased close to unity for small hypothetical element sizes (4×4 mm). Note: red bars indicate statistically significant difference from 4×4 mm ($\alpha = 0.05$).

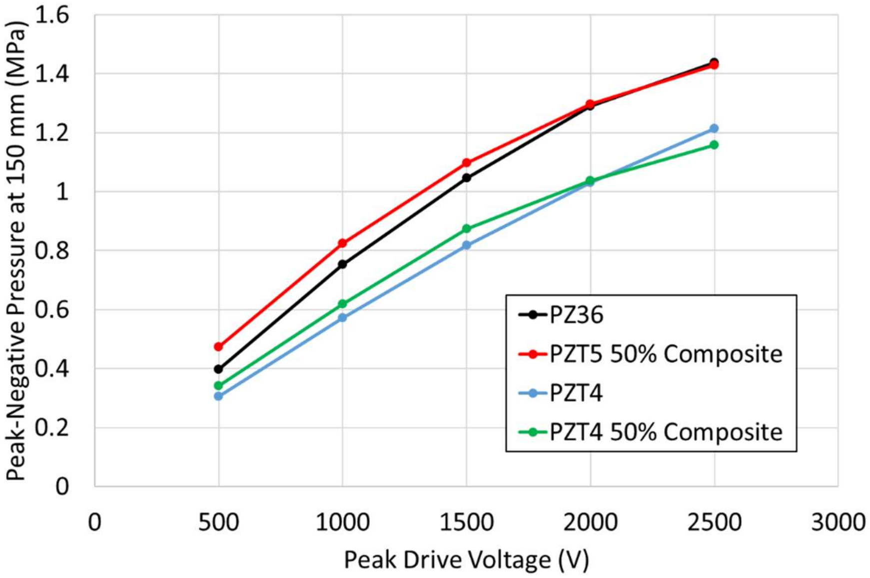

Figure 6.4. The peak-negative pressure output as a function of peak drive voltage for all piezoelectric materials tested.

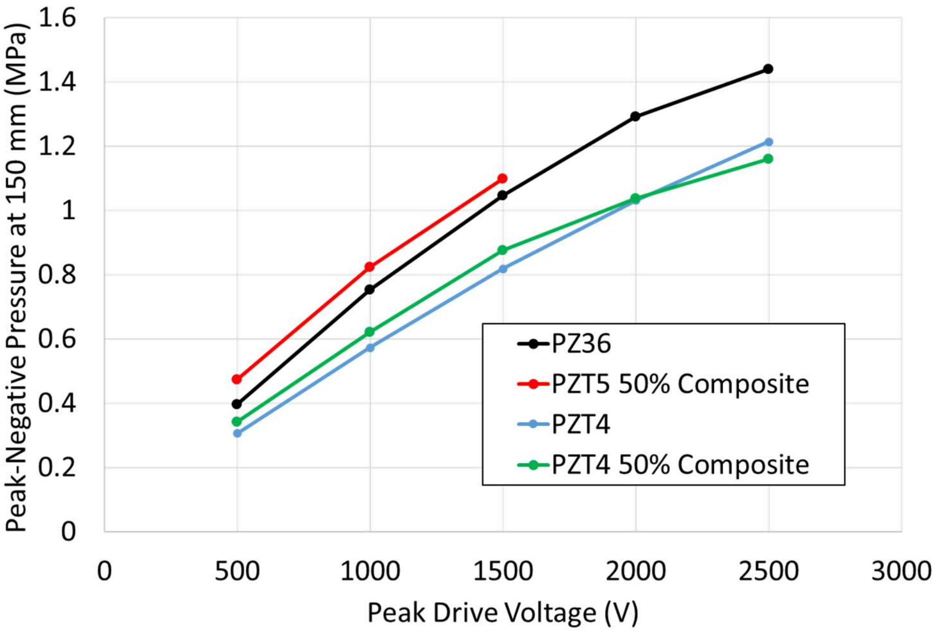

Figure 6.5. The initial durability tests for a subset of materials at a PRF of 200 Hz. For each piezoelectric material, the curves are extended to the maximum pressure at which the transducers could sustain for at least 1 hour when driven at a PRF of 200 Hz.

6.3.2 Final Transducer Design

Design Overview: The structural design of the new ICH transducer was based off of those developed previously and consisted of a hemispherical array with a focal distance of 150 mm. Based on the results obtained in the experiments investigating the design parameters described, PZ36 elements with a center frequency of 700 kHz were chosen to make the new elements of the array. The size of the individual array elements was chosen to be 17×17 mm which, based on the geometry of the array scaffold, allowed 360 of them to be populated into the array.

Individual Transducer Module Design: The housing of the individual transducer modules consisted of plastic printed with stereolithography (PerFORM, DSM Desotech Inc, Elgin, IL). The housing of a single element and its overall dimensions is shown in Figure 6.6a. The modules were designed with an O-ring retaining groove that allowed them to be secured to the array scaffold via an easily removable O-ring. This allowed modules to be easily replaced with a catheter holder with potential for the arbitrary placement of the catheter hydrophone (See Chapter 5). Additionally, the modules had a second O-ring groove intended to seal the hemisphere scaffold and allow it to be filled with an acoustic coupling fluid. The 17×17 mm, 700 kHz PZ36 square was potted into the plastic housing using a high-strength epoxy (EA E-120HP, Loctite, Düsseldorf, Germany) and backed marine-grade epoxy (Marine Grade Epoxy System, TAP Plastics, USA). The marine epoxy backing ensured a water-tight seal around the PZ36 element that allowed the module to be fully submersed. The transducers were fabricated with a dual matching layer to improve transmission into the water based propagating media (Fig. 6.6b). The matching design utilized the 3D printed plastic housing as the first matching layer (ML1) and a second plastic made with selective laser sintering (PA 650, Advanced Laser Materials LLC, Temple, TX) as the second matching layer (ML2). The acoustic properties of the PZ36 and matching layers used in the transducer design are shown in Table 6.2.

Hemispherical Array Design: The hemispherical array transducer consisted of 360 individual square elements with an aperture of 300 mm (Fig. 6.7a). The elements were patterned to optimize their packing within the 300 mm diameter hemisphere scaffold. The elements positioned toward the back of the hemisphere scaffold were circularly patterned around a lateral axis while the two rings of elements positioned near the edge of the hemisphere scaffold were circularly patterned around a central axis (Fig. 6.7b). This packing strategy was adopted to keep regions of densely packed elements in regions that were thought to follow the natural curvature of the skull. Overall, the packing strategy allowed the active area of individual transducer modules to occupy 73.6% of the total hemisphere surface area.

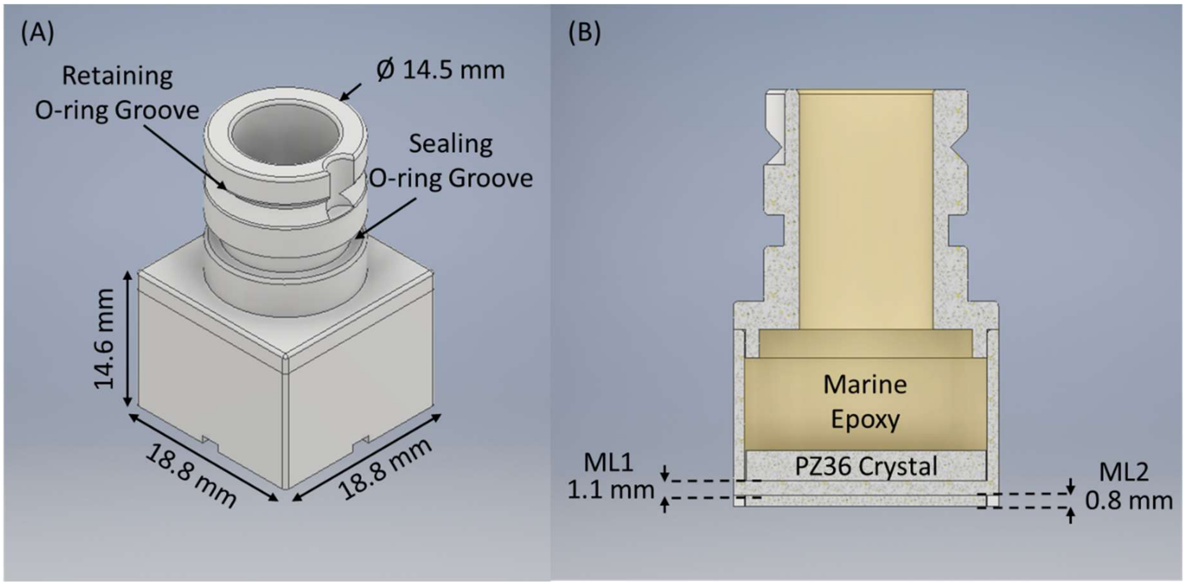

Figure 6.6. The (a) overall design and (b) cross-section indicating the acoustic matching for the single element transducers comprising the array. Matching layer is abbreviated as ML.

Table 6.2. The acoustic properties of the PZ36 and matching layers used in the transducer design.

Material	Acoustic Impedance (MRayl)	Sound Speed (m/s)
PZ36	17.6	2842
PerFORM (ML1)	5.3	3200
PA 650 (ML2)	2.2	2150

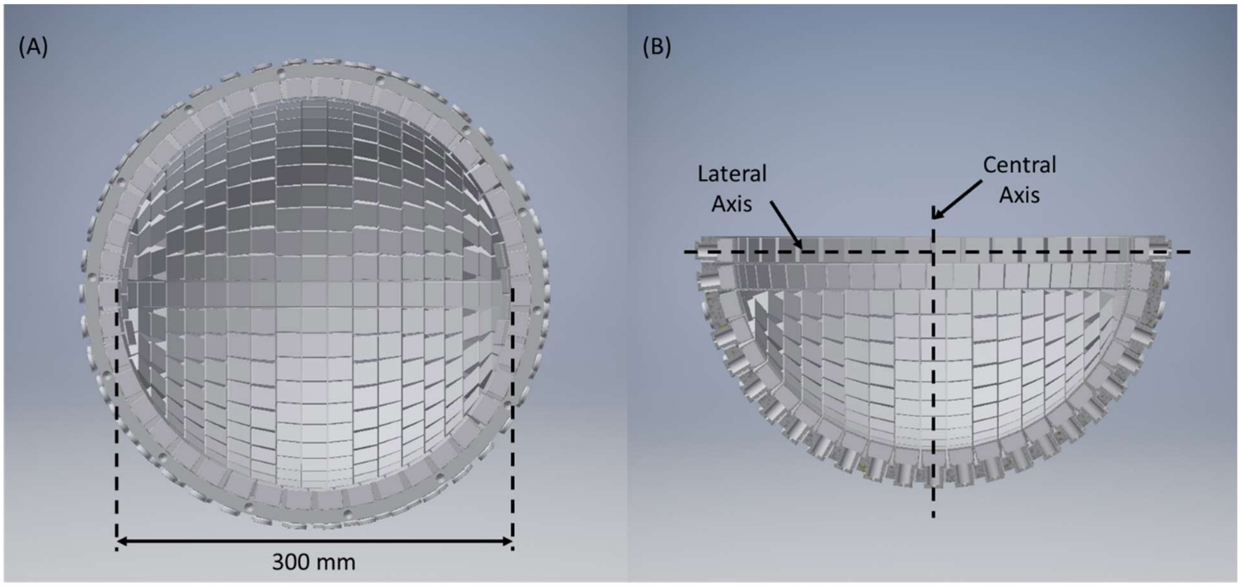

Figure 6.7. A (a) top-down view and (b) cross-sectional view of the overall design. The cross-sectional view highlights the axes around which the element patterning was done for the final hemisphere array transducer design.

6.3.3 Transducer Performance

Performance of the Transducer Modules: The pressure waveform produced from a single module at 150 mm for a peak drive voltage of 3 kV is shown in Figure 6.8. The acoustic waveform is a short (~1.5 cycle) pulse with a single large negative cycle[2]. The output of the modules at 150 mm (the focal distance of the array) as a function of drive voltage in the free field and through the human skull is shown in Figure 6.9 (left). At a peak drive voltage of 5 kV, a single module is capable of generating a peak-negative pressure of just over 1.6 MPa in the free field and just about 1 MPa through the skull. The trans-skull transmission of a single module through the skull was plotted as a function of the drive voltage (Fig. 6.9, right). The plot suggests, that as the transducer is driven harder, the trans-skull transmission increases. Driving the transducer at just 500 V results

---

[2] The drive waveform for the transducer modules consists of a 700 kHz half cycle pulse. A simplified circuit diagram for a single channel of the electronic drive system for the new transducer array and waveform it produced is shown in Figure 6.15 in Miscellaneous Figures and Tables in the Appendix at the end of this chapter.

in a trans-skull transmission of 35% while driving the transducer at 5 kV results in a trans-skull transmission of just about 60%. This change in transmission is likely due to a reduction of the non-linear effects of waveform propagation through the skull compared to that of the free-field and thus a reduction of the acoustic saturation effect associated with nonlinear propagation.

The long term durability of modules was assessed by driving modules (n = 8) continuously with a drive voltage of 3 kV at a PRF of 200 Hz for 7 consecutive days. This corresponded to roughly 120 million pulses. Table 6.3 shows the pre- and post-test output as well as the greatest decline in the transducer output. The pre-test output was 1.56 ± 0.04 MPa and the post-test output was 1.56 ± 0.05 MPa. The greatest decline in a single element was 5.3%.

Performance of the Hemispherical Array: The peak-negative pressure output of the 360 element hemisphere array transducer was simulated using a linear simulation program (FOCUS, Michigan State University, East Lansing, MI) across a ± 50 mm electronic focal steering range (Fig. 6.10). The simulation was calibrated using the output of a single module driven at 3 kV in the free field and through the skull. Phase aberration was simulated by applying a two-fold reduction to the steering profile through the skull. The maximum pressure achieved in the free field and through the skull without and with aberration was estimated to be 540, 288 and 144 MPa. The -3 dB steering range for each condition was 29 mm (Table 6.4). The steering range was also characterized by the range above the intrinsic threshold (>26 MPa). The smallest steering range (diameter) above intrinsic threshold achieved in the free field and through the skull without and with aberration was 65, 55 and 45 mm, respectively (Table 6.4). The above threshold steering ranges were used to calculate above threshold volumes (assuming ellipsoidal geometries). The above threshold volumes for the free field and through the skull without and with aberration were estimated to be 177, 105 and 48 mL, respectively.

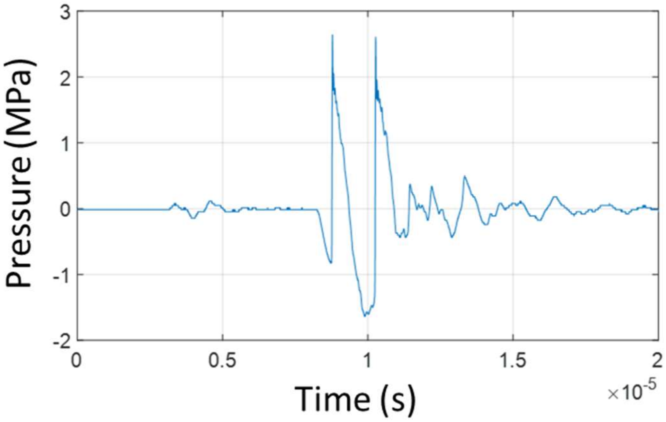

Figure 6.8. The pressure waveform produced from a single module at 150 mm for a drive voltage of 3 kV.

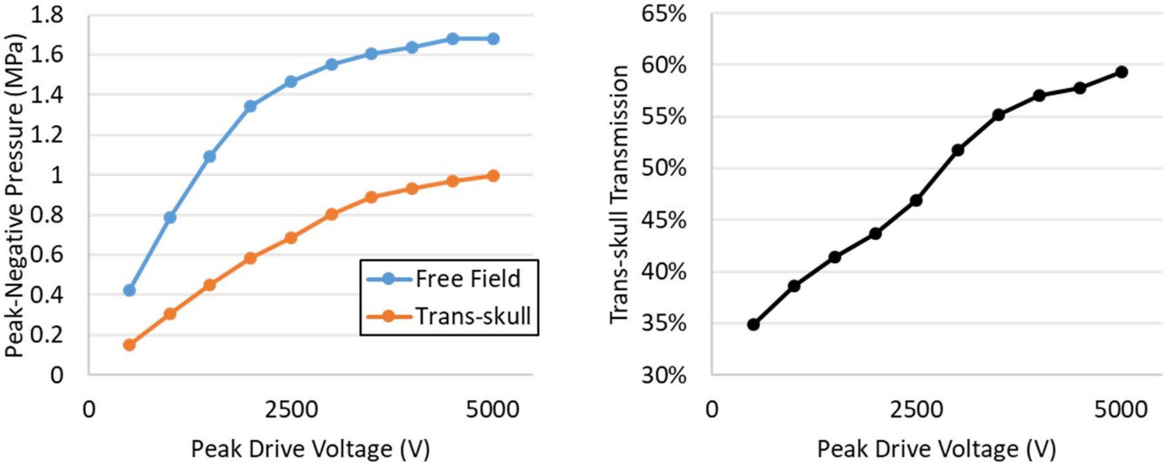

Figure 6.9. The output of the modules at 150 mm as a function of drive voltage in the free field and through the human skull (left) and the trans-skull transmission of a single module through the skull (right). The trans-skull transmission was calculated as ($P_{\text{-Trans-skull}}/P_{\text{-Free Field}}$)×100%.

Table 6.3. Results of the transducer module durability test.

Pre-test output	1.56 ± 0.04 MPa
Post-test output	1.56 ± 0.05 MPa
Greatest decline	5.3%

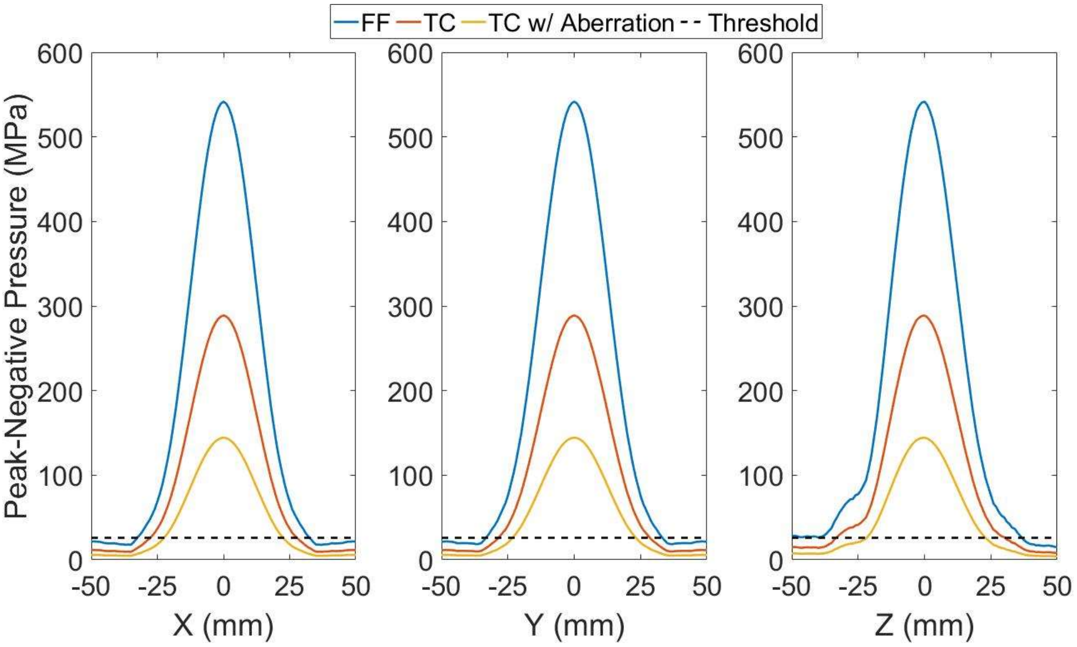

Figure 6.10. The peak-negative pressure output of the 360 element hemisphere array transducer was simulated across a ± 50 mm electronic focal steering range. The simulation was calibrated to the output of a single 17×17 mm element driven at 3 kV in the free field (FF) and through the skull (TC = transcranial). Aberration through the skull was simulated via a two-fold reduction in the TC steering profile. The dashed line indicates the histotripsy intrinsic threshold (26 MPa).

Table 6.4. The 3-axis steering range and above threshold volume for different simulation conditions.

		Steering Range			Volume
		X (mm)	Y (mm)	Z (mm)	(mL)
FF	-3 dB	29	29	29	-
	> 26 MPa	65	67	78	177
TC	-3 dB	29	29	29	-
	> 26 MPa	55	57	64	105
TC w/ Aberration	-3 dB	29	29	29	-
	> 26 MPa	45	46	45	48

6.3.4 Pre-clinical System Prototype for Human Cadaver Experiments

Experimental Setup for the Treatment of Human Cadavers: This array was designed for use in experiments involving cadaver models. Experiments were carried out with human cadaver specimens received from the Anatomical Donations Program (ADP) at the University Michigan and performed in lab space provided by ADP. The general experimental schematic of the setup for cadaver experiments is shown in Figure 6.11a. In order to get the cadaver head into the tank for treatment, the cadaver was placed on a hydraulic lift table with an inclinable bed. Once positioned over the array, the bed was tilted down to lower the cadaver into the water tank containing the array. To allow real-time tracking and surgical planning the setup was integrated with an optical tracker surgical navigation system (StealthStation S7, Medtronic, Dublin, Ireland). This device uses cameras and sets of geometrically unique optical trackers mounted to the surgical equipment and the patient head to track the 3-dimensional locations of these tools with respect to the patient head. By registering an MR or CT image to the patient head, the location of these tools can be virtually represented with respect to the MR or CT data set. Figure 6.11b shows a schematic of the camera-facing-view of the setup. Optical trackers were rigidly fixed onto the cadaver head, array structure and catheter hydrophone structure. Trackers attached to the array and catheter hydrophone were used to register each as a surgical tool within the treatment planning software. The tracker attached to the head was treated as the global reference frame of the system which the array and hydrophone trackers reference in the virtual planning space. A high-resolution 3D T1-weighted MRI dataset (e.g., MP RAGE) was registered to the cadaver and fixed within the within the coordinate system of the global tracker.

Positioning the Head and Insertion of the Catheter Hydrophone: A mechanical structure for holding the head at a fixed position within the array was designed (Figure 6.12, left). A glass composite ring (Resolve Halo, Össur, Iceland) was rigidly fixed to the head via pointed set screws. The superior face of the ring interfaced with a plastic plate that had a custom cutout to allow the head to be placed within the array. To allow repeatable placement within the array, a custom locking mechanism fixed the transverse position of the composite ring. A fixed angle guide was made using 3D printing methods to allow insertion and repeatable placement of the hydrophone aperture to the geometric focus of the array. To place the hydrophone within the brain, a bur hole was drilled in the skull and a rigid sheath (1.3 mm outer diameter) was then guided through it. The hydrophone was then inserted through the sheath and extended past the end of the sheath to the geometric focus of the array. An optical tracker was placed onto the end of the rigid sheath to allow the sheath tip to be virtually tracked within the MRI dataset. Trilateration methods using acoustic signals produced by the array elements and measured with the hydrophone suggest the hydrophone tip can be placed within ± 2 mm of the geometric focus of the array. Figure 6.12 (right) shows the location of the sheath tip (green crosshair) within the sagittal, axial and coronal view of the MRI dataset. The red dot indicates the geometric focus of the array within the MRI dataset. As visualized in the MRI, the crosshair of the sheath is setback a few mm from the red dot. This was intentionally designed into the setup to account for the distance between the hydrophone aperture and the sheath tip.

Ultrasound Transmission Measurements through the Cadaver Head: Ultrasound transmission measurements through the cadaveric head were made via the inserted hydrophone. Individual elements were driven with a short (~2 cycles), high voltage pulse (~1 kV_{pp}). The pressure output of approximately one of every 8 elements of the 360-element array was measured via the hydrophone (n = 44). Transmission measurements were calculated as the ratio of the peak-negative pressure measured through the head to that measured in the free field. Figure 6.13 shows the trans-skull transmission of discrete elements of the array. Measurements were made for an embalmed cadaver head (~3-week post-mortem) that had been removed from the torso about 1 week prior to the experiment and a unembalmed head (~66 h post-mortem) that remained attached to the torso. The average transmission through the embalmed cadaver head was 5% ± 4%. The average transmission through the unembalmed cadaver head was 19% ± 11%. Figure 6.14 shows the estimated pressure field through the 66 h post-mortem cadaver with the geometric focus of the array placed in the left thalamus of the brain. In this location of the brain, the above threshold steering range is estimated to be approximately 40 mm, allowing treatment of an approximate volume of 35 mL.

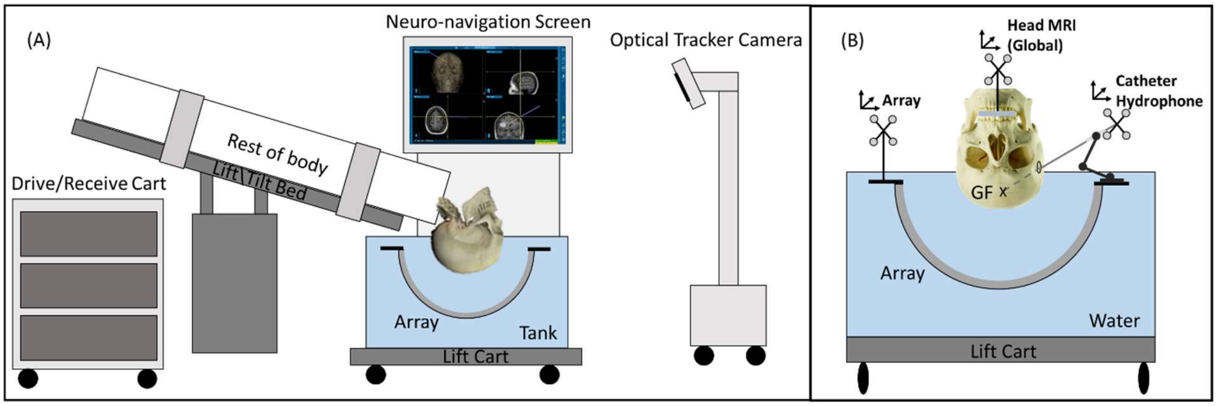

Figure 6.11. (A) The general experimental schematic of the setup for cadaver experiments. (B) A schematic of the camera-facing-view of the setup.

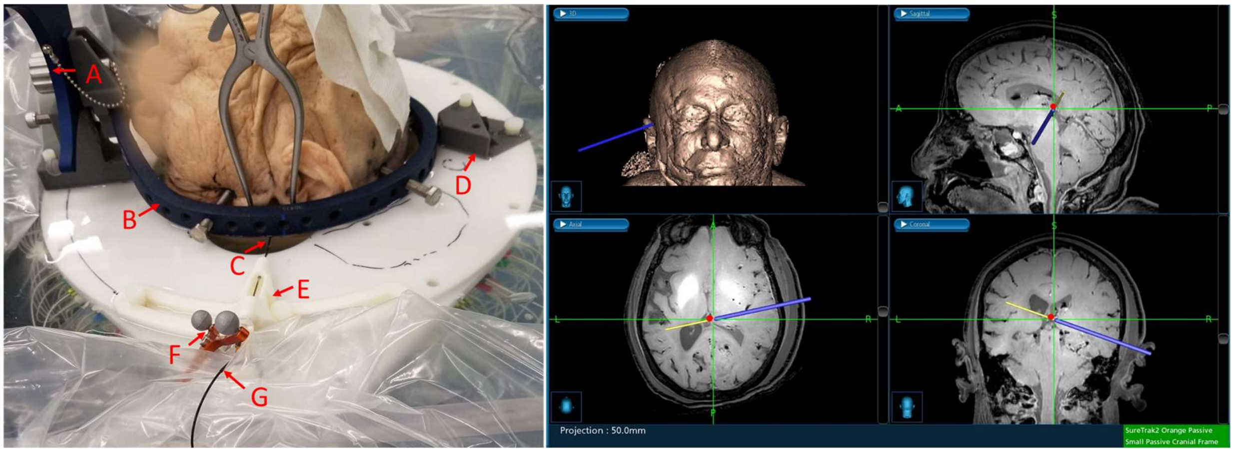

Figure 6.12. (Left) The mechanical structure for holding the head at a fixed position within the array. Red letter labels are defined as follows, A: Optical tracker rigidly attached to head, B: Glass composite ring for rigidly fixing head, C: Rigid sheath for hydrophone insertion, D: Head alignment jigs to rigidly fix position of head within array, E: Fixed angle guide for sheath insertion, F: Optical tracker rigidly attached to insertion sheath, G: hydrophone. (Right) The location of the sheath tip (green crosshair) within the sagittal, axial and coronal view of the MRI dataset. The red dot indicates the geometric of the focus of the array within the MRI dataset. The crosshair of the sheath is setback a few mm from the red dot. This was intentionally designed into the setup to account for the distance between the hydrophone aperture and the sheath tip.

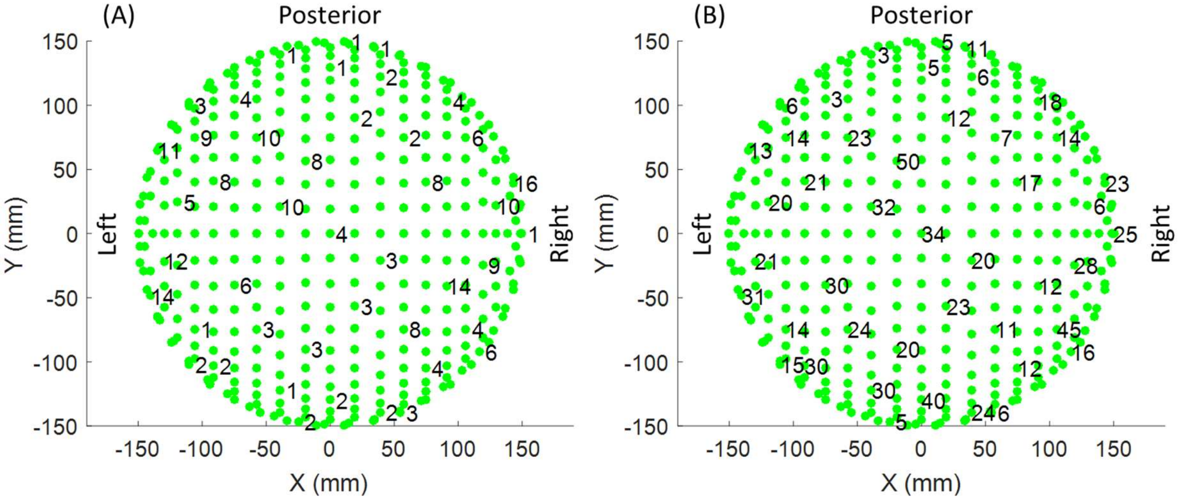

Figure 6.13. The trans-skull transmission of discrete elements of the array measured through the (A) embalmed cadaver ~3-week post-mortem and (B) unembalmed cadaver ~66 h post-mortem. The 3D array element coordinates are projected onto a 2D plane. Units: %.

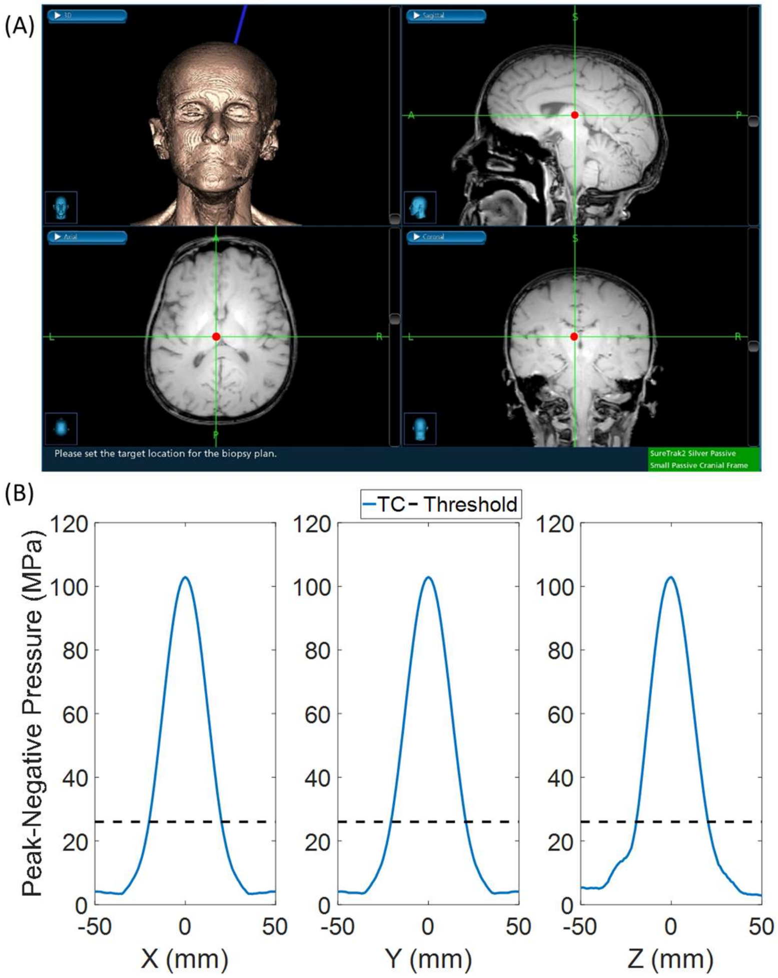

Figure 6.14. (A) The view from the neuro-navigation software showing the transducer focus within the left thalamus of the 66 h post-mortem cadaver brain. (B) The estimated pressure field at this location within the brain. The above threshold steering radius (> 26 MPa) was approximately 40 mm.

6.4 Discussion

The trans-skull transmission was mostly consistent between 500 kHz and 1 MHz (~30%). As acoustics absorption increases with frequency, the similarity in transmission across frequencies suggests the major component of transmission loss through the skull are reflections off the surface of the skull. Considering only trans-skull transmission, this suggests that frequencies within this range should achieve similar pressures through the skull. However, the drive frequency impacts other factors that are important in focused ultrasound transducer design. For a given focused transducer, focal gain increases with frequency and thus the peak geometric focal pressure is greater at higher frequencies. In fact, from a standpoint of peak geometric focal pressure output through the skull, an ideal combination of trans-skull transmission and focal gain is 1.5 MHz[3]. In addition, experimental data has shown that, for the same drive voltage, the surface pressure at a single element face scales with frequency[4], increasing the absolute focal pressure at higher frequencies even further. Given that the therapeutic mechanism of histotripsy relies on exceeding a rarefactional pressure threshold of 26 MPa, the increase in pressure with frequency suggests higher frequencies are better for histotripsy transducer design. However, other important therapeutic factors such as array steer-ability, focal volume and phase aberration are negatively impacted at higher frequencies. For a given focused transducer, higher frequencies result in reduced electronic focal steering ranges and tighter focal zones[5][6], which reduces the effective treatment range and treatment efficiency (i.e., more focal points for the same target volume) [3]. In addition, given a fixed aberrator such as the skull, the effects of phase aberration are more severe for higher frequencies (i.e., the coherence of the ultrasound is more greatly disturbed)[7]. Assuming these can be corrected and assuming a constant fraction of a cycle worth of precision is necessary for good aberration correction, the absolute temporal precision for "good" aberration correction

---

[3] Figure 6.16 in the Miscellaneous Figures and Tables section of the Appendix shows the product of focal gain and trans-skull transmission as a function of frequency.

[4] Figure 6.17 in the Miscellaneous Figures and Tables section of the Appendix shows the surface pressure of an identical 2 cm disc of PZ36 at 500 and 700 kHz.

[5] Figure 6.18 in the Miscellaneous Figures and Tables section of the Appendix shows the approximated focal volume as a function of frequency.

[6] Figure 6.19 in the Miscellaneous Figures and Tables section of the Appendix shows the full-width-half-max (FWHM) for the electronic focal steering profiles generated from a 968 element, 150 mm radius hemispherical transducer across different drive frequencies.

[7] Figure 6.20 in the Miscellaneous Figures and Tables section of the Appendix shows the ratio of the peak-negative pressure of a simulated aberrated waveform to the peak-negative pressure of a nonaberrated waveform across different frequencies. Simulations were performed using measurements from excised human skulls.

also increases, increasing requirements on correction methods[8]. These considerations of focal volume, steer-ability and phase aberration highlight the benefits of using lower drive frequencies for histotripsy therapy. However, there may also be undesired effects at frequencies below a certain cut-off. In past experiments, transcranial treatment with 250 kHz produced noticeable cavitation on the external surface of the skull [3]. One thought on the appearance of this phenomenon is that the likelihood of off-focus cavitation or even surface cavitation (i.e., cavitation at an interface between two materials) increases at lower frequency. This is attributed to the observation that the probability of producing *incidental cavitation bubbles* (cavitation that occurs below intrinsic threshold) is greater at lower frequencies than at higher frequencies [4]. Although treatment with an identical array at 500 kHz did not present this effect, due to the reduced focal gain lower frequency transducers may ultimately lack sufficient pressure overhead for a clinical system where volume treatment across a range of locations within the brain is necessary. The appendix provides an analysis of the impact of incidence angle on the trans-skull transmission at different locations within the brain[9]. A drive frequency of 700 kHz was chosen for the new transducer design as it allowed significant improvements in the absolute pressure achieved through the skull via focal gain and surface pressure effects without major reductions to the steer- ability and focal volume.

The spatiotemporal variation through the skull was assessed to understand the impact of element size on intra-element phase aberration through the skull. Given the spatial distribution of the phase aberrating properties of the human skulls examined here, the smaller the hypothetical element size (e.g., 4×4 mm), the less aberrated the waveform. From the perspective of designing

---

[8] Figure 6.21 in the Miscellaneous Figures and Tables section of the Appendix shows a plot of a fraction (1/8) of a cycle length at different frequencies.

[9] An analysis of the steer-ability of a 256-element 500 kHz array at a range of different focal locations within the brain is provided in the Impact of Incidence Angle on Trans-skull Transmission in the Appendix of this Chapter.

a transcranial phased array this indicates that the phase aberrating properties of the skull are predominantly manifested among individual elements of the array and thus can be accounted for by corrections (e.g., rephasing the elements) via the catheter hydrophone measurements [5] or other means [6]–[9]. However, from a statistical standpoint, the measured differences in aberration effects from that of a near optimal element size (4×4 mm) occurred only at element sizes of 20×20 mm or greater. Thus, from a standpoint of correcting for phase aberration, elements as small as 4×4 mm should not be necessary but rather need only to be smaller than 20×20 mm to achieve near optimal performance. This is an insightful piece of information as there are other design considerations that may favor larger elements. From a theoretical standpoint, for a fixed frequency piezoelectric crystal, there may be a point of diminishing return in decreasing the element size, at which point, the aspect ratio of the crystal will impact its transduction efficiency in the piston mode [10]. From a practical standpoint, there are other considerations. For example, reducing the element size increases the number of elements needed to efficiently pack the surface area of the hemisphere array. Assuming a 75% packing efficiency, it would take over 4000 5×5 mm elements to pack a 300 mm diameter hemisphere[10]. Although a larger element count improves other aspects like the steer-ability of the transducer, it also increases the number of channels needed in the driving electronic system, the amount of cable connecting the transducers to the drive system (the cable bundle for 360 1 mm O.D. coax cables is ~2 inches) and the overall footprint of the system. An element size of 17×17 mm was chosen for the final design as it kept the total number of elements reasonable (i.e., a few hundred elements can easily be made in-house) and from a standpoint of phase aberration, should provide performance consistent with smaller elements (4×4

---

[10] Figure 6.22 in the Miscellaneous Figures and Tables shows the number of square elements as a function element length for a 300 mm diameter hemisphere with a packing efficiency of 75%.

mm). It is worth reiterating that the method used to assess the impact of spatiotemporal variation through the skull on peak-negative focal pressure is an approximation intended to make a relative comparison across array elements of different dimensions. The approximation has two main assumptions: (1) the skull can be considered as a series of point-source re-emitters of the ultrasound pulse that enters it and (2) that the therapy focal point is far enough away from the skull surface that the pathlength differences from the re-emitted pulses are negligible and those do not introduce additional phase variations, allowing the focal pressure to be approximated by simply summing the individual phase-shifted waveforms. Although we do not anticipate deviation from these assumptions to largely impact the results presented, the validity of these assumptions should be further investigated.

The primary criteria for the piezoelectric material was (1) the ability to achieve a large pressure output and (2) the ability to withstand driving conditions needed for rapid clot liquefaction through the skull (i.e., a PRF of 200 Hz). In terms of the absolute peak-negative pressure produced, both the PZ36 and the PZT5 50% composite were optimal performers of the materials tested. However, when driven at a PRF of 200 Hz and a peak drive voltage above 1.5 kV, the PZT5 50% composite failed within 1 hour. In contrast, the PZ36 could be driven at high drive amplitudes (2.5 kV) and clinically relevant PRFs (200 Hz) for at least 1 hour without losses in performance. There are a few points to highlight regarding these experiments. The first is that the composites, due to the partial epoxy composition, had thin sputtered gold electrodes whereas the PZ36 and PZT4 had relatively thick silver fired electrodes. It is possible that the durability of PZ36 and PZT4 was partially due to the thicker, better adhered electrodes. The second point is that the surface area of the PZ36 disc was slightly larger (~8%) than that of the PZT composites. However, even if taking the difference in surface area into account, the pressures generated with the PZ36 were still beyond those generated with either PZT composite within their durable operating range. An additional note is that the PZ36 disc used in this study had a wraparound electrode which likely reduced the effective acoustic area. Despite these points, PZ36 still remains the optimum candidate in terms of peak-negative output and durability.

The final transducer design is tuned to meet clinical requirements of an effective ICH treatment. The individual transducer modules were capable of generating large peak-negative pressures in the free field (up to 1.6 MPa) that translated to large pressures through the skull (up to 1 MPa). One interesting observation was the behavior of the trans-skull transmission as the transducers were driven harder. The increase in transmission with drive voltage suggests that the attenuating presence of the skull reduces the nonlinear propagation effects that are present in the free field [11]. This observation may suggest that calibrations and simulations where linear methods are often utilized [12] may be more accurate when applied to trans-skull pressure fields. In addition to achieving large pressure outputs, the individual transducer modules were also durable at high drive conditions (1.5 MPa, 200 Hz PRF) which are necessary for rapid clot liquefaction through the skull [3]. The transducer modules were packed within the hemispherical scaffold in an arrangement to ensure densely populated regions match the natural curvature of the skull. This was done to keep the rays of elements in densely populated regions as close to normal incidence with the skull as possible, given the hemispherical geometry of the array, and thus provide optimal transmission through the skull in those densely populated sections. Simulations suggest that the full array is capable of generating pressures beyond the intrinsic threshold across a large electronic focal steering range through the skull (~ 45 – 55 mm)[11]. After calibrating the

---

[11] The steer-ability of the array can be greatly increased with minimal impact to the pressure overhead by using nearly 1000 10×10 mm elements (Figure. 6.23 and Table 6.5 in the section Miscellaneous Figures and Tables in Appendix of the chapter).

simulation with pressure measurements obtained through the skull, the pressures were reduced two-fold across the steering range to simulate phase aberration. A 2-fold reduction is similar to what has been observed experimentally within the moderate frequency (500 kHz) histotripsy regime [5], [13]. In practice, the transcranial pressure fields will be somewhere between those with no aberration correction and perfect aberration correction. This translates to an effective therapeutic volume range between 48 – 105 mL. The lower bound of this range is well beyond the average ICH volume reported in various clinical studies (~30 mL) [14]–[16]. In addition to the steering range, the peak pressure it can generate is nearly 3-fold greater than that of the transducers used in previous studies[12][3]. It is anticipated that a larger pressure overhead will be necessary in future pre-clinical studies where proof-of-concept for volume treatment at different locations in the brain will be necessary [17], [18]. Although histotripsy has shown the capacity to generate sparse lesions across a range of locations within the brain [19], preliminary studies have also shown significant pressure loss due to incidence angle effects when targeting additional locations through the skull[13]. Although it may be possible to minimize the pressure loss due to reflections by reorienting the transducer with respect to the skull[14], the net transmission through the skull is expected to vary across different treatment locations within the brain.

---

[12] A comparison of the peak output and steer-ability of the newly designed 360 element, 700 kHz array and the 256 element, 500 kHz array is shown in Figure 6.24 in the Miscellaneous Figures and Tables section in the Appendix.

[13] The effects of incidence angle on trans-skull transmission were evaluated to assess the worst-case-scenario pressure loss that occurs when targeting different locations through the skull. This analysis can be found in the Appendix of this chapter under Impact of Incidence Angle on Trans-skull Transmission.

[14] The array can likely be rotated to some optimal set of angles with respect to the skull. The initial work on an optimization model to strategically orient the array around the head is shown in the Appendix of this chapter under Development of a Ray-Tracing Optimization Model.

The integration of the transducer array with an optical neuro-navigation system is motivated by the ubiquitous clinical use of frameless navigation methods in neurosurgery [20]. Such navigation techniques are widely used in volume resection of both tumors and ICH [20]–[22]. The simple attachment of optical trackers to the array structure and catheter hydrophone allow relevant features of these tools (geometric focus of array and tip of catheter hydrophone tip) to be tracked in real-time within the optical field. By registering a patient's head placed within the optical field to its respective preoperative or diagnostic 3D image dataset (MRI or CT), the geometric focus and catheter hydrophone tip can be virtually tracked with respect to the image of the patient's brain, allowing targeted placement of these tools within the real brain. Independent studies on the accuracy of such optical navigation methods for the placement of similar tools suggest an accuracy of 2-3 mm [23]. For comparison, independent studies on the accuracy of frame-based stereotactic methods report accuracies of 1-2 mm [23]. Literature of the field and discussions with practicing neurosurgeons suggest that an accuracy of 2-3 mm is sufficient for volume resection of ICH [21]. The current setup is designed to place the geometric focus of the transducer to a predetermined location within the brain. Once this has been achieved, the catheter hydrophone can be aligned with a predefined insertion path and inserted through a small bur hole in the skull to the geometric focus of the transducer. Following placement, aberration correction can be performed [5], the catheter hydrophone can then be removed and treatment can be performed via electronic focal steering [24]. The mechanical setup of the integrated system is intentionally rudimentary, designed with just enough features to allow the capacity to assess the feasibility of histotripsy as a surgical method for ICH liquefaction and resection. Once the proof-of-concept of this surgical approach is established future iterations of this system can adopt more sophisticated positioning and coupling systems and systems that enhance the workflow for the surgeon. In addition, as the driving electronics are capable of receiving acoustic signals, real time cavitation mapping can be integrated into the system with the capacity to map the cavitation activity in real-time and the potential to track treatment progression [25], [26]. This can be integrated with the neuro-navigation system to allow treatment monitoring to be overlaid with the anatomical image used for neuro-navigation.

The placement of the hydrophone within the brain allows direct measurement of the acoustic field at the location of treatment. Not only does this allow aberration correction to be performed but it allows trans-skull transmission measurements to be obtained. This may be useful as the net sound loss through the skull can be used to provide insight to the peak drive amplitude needed for treatment. The transmission measurements made with the catheter hydrophone through the 66-hr post-mortem unembalmed cadaver head were reasonable and suggest sufficient head room for volume treatment deep in the brain (up to 35 mL). Based on discussions with the ultrasound community, it was anticipated that cadavers beyond 48 h post-mortem would exhibit enhanced attenuation due to the buildup of gas within the tissue that would impair treatment. Although this may be a factor in the transmission measurements presented here, volume treatment within the brain remains feasible. It is possible that the application of histotripsy pulses at a high PRF (e.g., 200 Hz) may be prone to initiating prefocal cavitation if gas concentrations in the tissue are high. Initial experiments are underway to assess the efficacy of treatment in different locations of the human cadaver brain. Future work involves understanding the safety and efficacy of transcranial clot liquefaction within the cadaveric brain.

6.5 Conclusion

The purpose of this chapter is five-fold: 1) to present an evaluation of parameters important to improving the design of a transcranial histotripsy array, (2) present the design of a new pre-clinical prototype histotripsy transducer intended for transcranial ICH treatment, (3) provide some initial performance metrics for the final design, (4) present the full pre-clinical system prototype intended for use in cadavers with ICH and (5) show initial investigation into the system performance on human cadaver models. The trans-skull transmission at different frequencies, spatiotemporal variation through the skull and performance of different piezoelectric materials provided insight into the design of a new transducer. The final design consisted of 360 individual transducer modules comprised of 17×17 mm PZ36 elements with a center frequency of 700 kHz arranged strategically into a 300 mm diameter hemispherical transducer. The transducer was durable through high drive conditions (1.5 MPa, 200 Hz) and when being driven under these conditions should allow an effective steering range beyond ± 20 mm (~30 mL spherical volume) with sufficient headroom to overcome transmission loss through the skull. The transducer was integrated into a pre-clinical treatment setup with neuro-navigation to allow targeting and treatment in ICH cadavers. Initial transmission measurements made through the unembalmed cadaver head suggest sufficient head room for volume treatment. Future work involves understanding the safety and efficacy of transcranial clot liquefaction within the cadaveric brain.

6.6 Appendix

6.6.1 Miscellaneous Figures and Tables

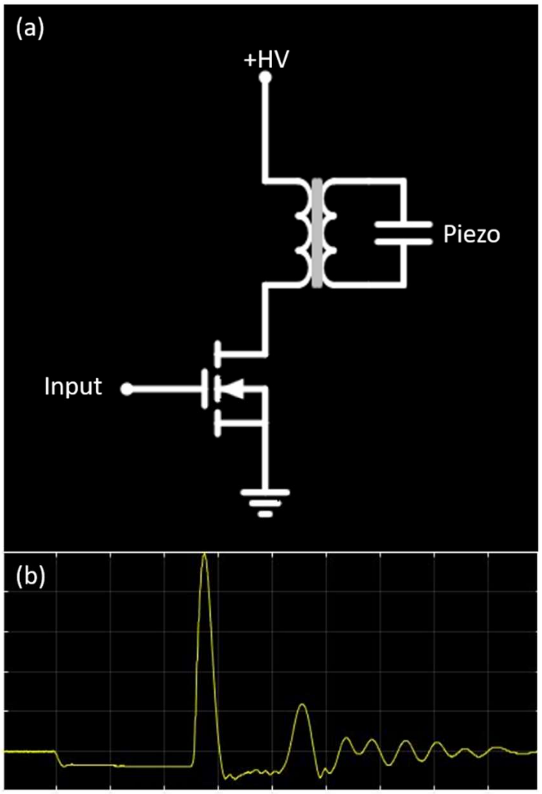

Figure 6.15. The (a) simplified circuit diagram of a single channel of the electronic drive system for the new transducer array and the (b) voltage waveform it produced. Transformers with a gain of ~3 were utilized to produce larger voltages across the piezoelectric transducer. The use of the transformer allowed larger voltages to be applied across the piezo than have been applied in the past.

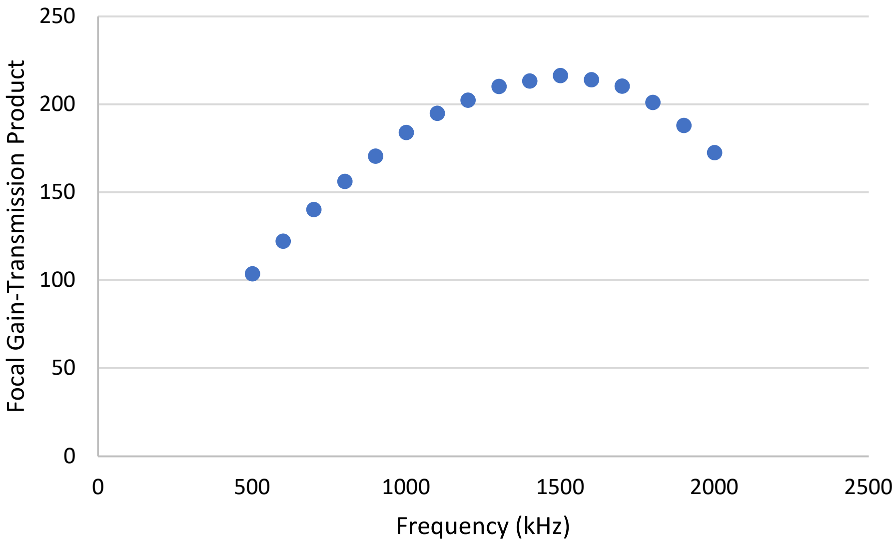

Figure 6.16. The focal gain multiplied by the trans-skull transmission across a range of frequencies. The focal gain was simulated for a 150 mm radius hemispherical shell (FOCUS, Michigan State University, East Lansing, MI). The transmission was obtained by fitting a polynomial to the trans-skull transmission vs. frequency data provided in Figure 6.26. From a perspective of maximizing the absolute pressure through the skull, 1.5 MHz is the optimal choice for the driving frequency.

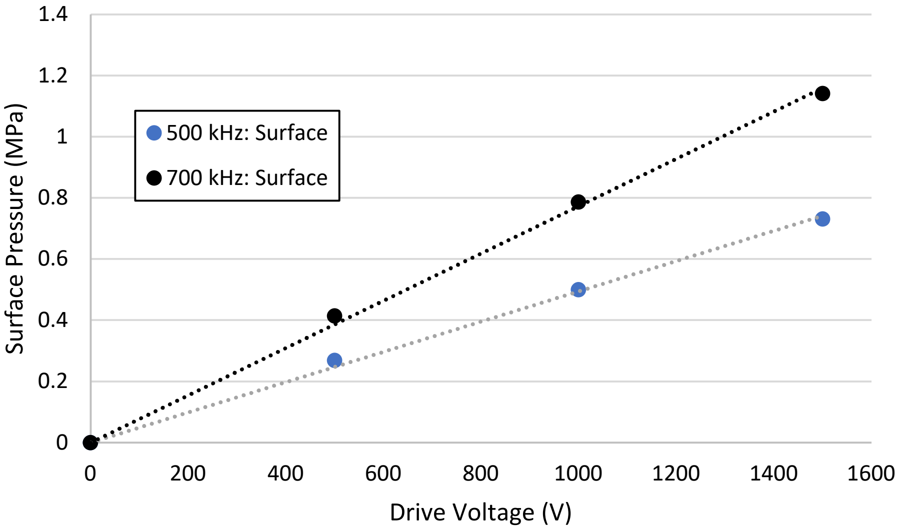

Figure 6.17. The surface pressure generated from a calibrated simulation of a 2 cm circular disk at 500 and 700 kHz (FOCUS, Michigan State University, East Lansing, MI). To calibrate the simulation, pressures were measured from 2 cm circular PZ36 elements (500 and 700 kHz) at 150 mm using a capsule hydrophone (HGL085, Onda Corporation, Sunnyvale, CA).

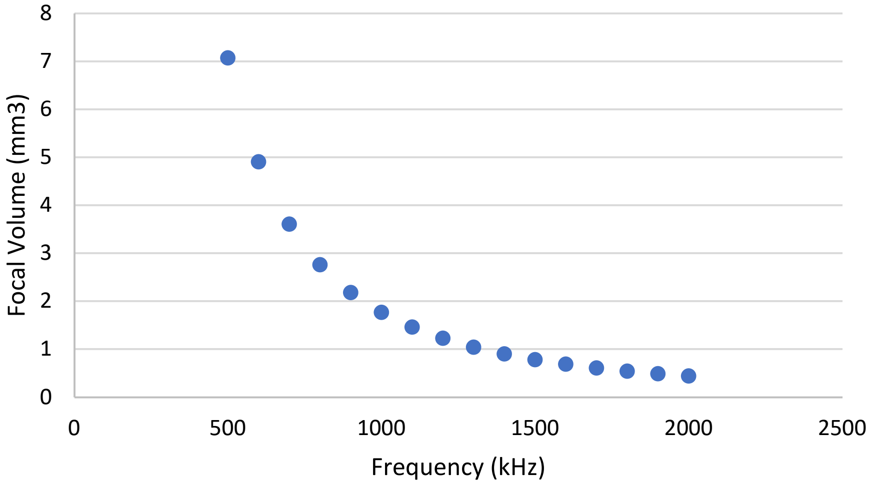

Figure 6.18. A plot of the focal volume vs frequency. The plot indicates a nearly 7-fold drop in focal volume between 500 kHz and 2 MHz. Focal volumes were calculated assuming 3-axis beam widths of λ/2.

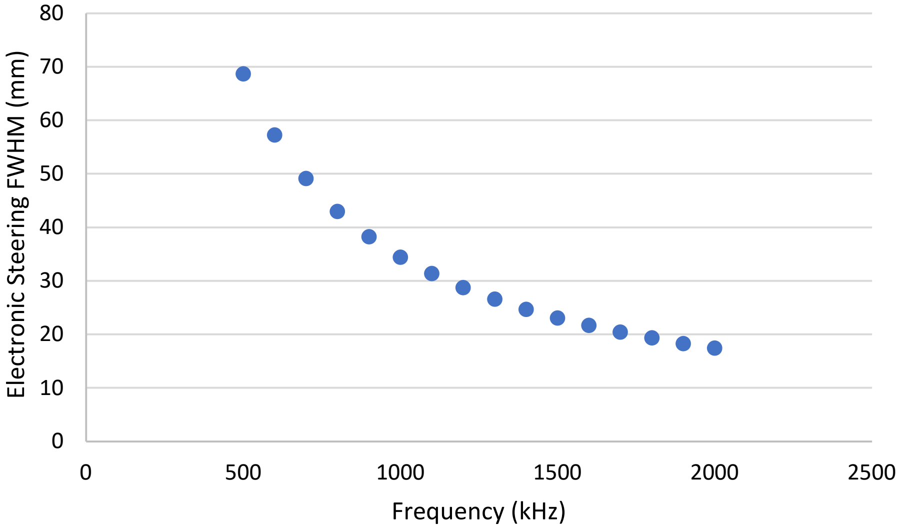

Figure 6.19. The full-width-half-max (FWHM) for the electronic focal steering profiles generated from a 968 element, 150 mm radius hemispherical transducer across different drive frequencies. There is a roughly 3.5-fold drop in the FWHM between 500 kHz and 2 MHz.

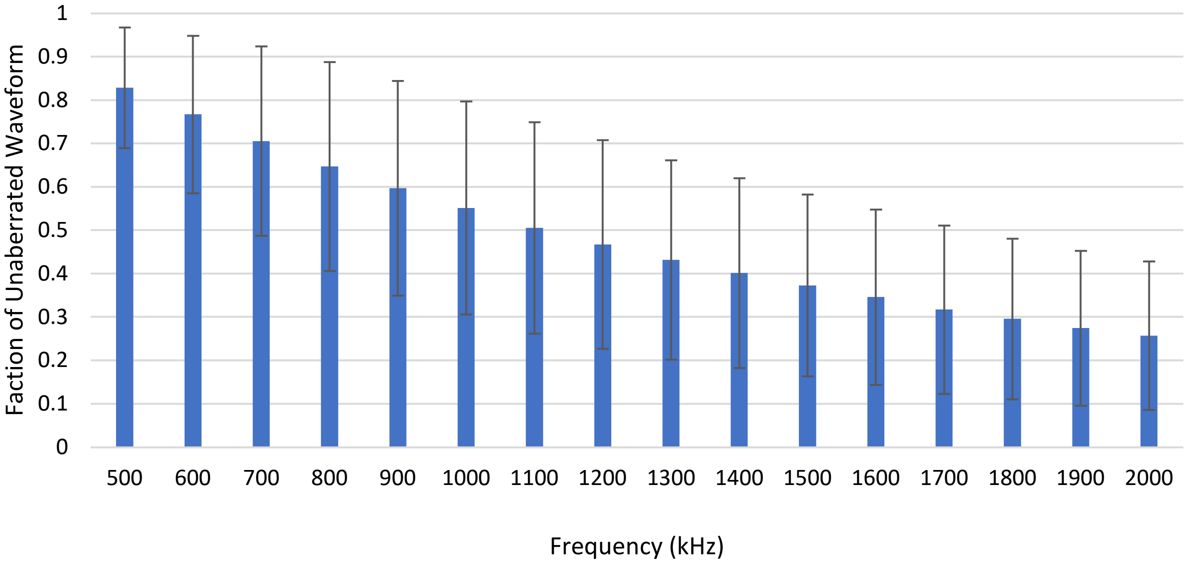

Figure 6.20. The ratio of the peak-negative pressure of a simulated aberrated waveform to the peak-negative pressure of a nonaberrated waveform was calculated to produce the fraction of the unaberrated waveform across different frequencies. A grid of spatially varying time values measured through sections of skullcaps (n = 7) was used to simulate the effects of aberration on histotripsy-like waveforms emitted through the skull. A Gaussian pulse was then generated in MATLAB to resemble a 1.5 cycle waveform at each frequency. To simulate the aberrated waveform for different frequencies, the un-aberrated waveform was shifted according the relative delays of the pixels within a 16×16 mm window. The shifted waveforms were then summed. The peak-negative amplitude of the shifted, summed waveforms was then divided by the peak-negative amplitude of un-shifted, summed waveforms. For more information on these methods refer to *Quantifying Spatiotemporal Variation through Excised Human Skulls* in the Materials and Methods section of this Chapter.

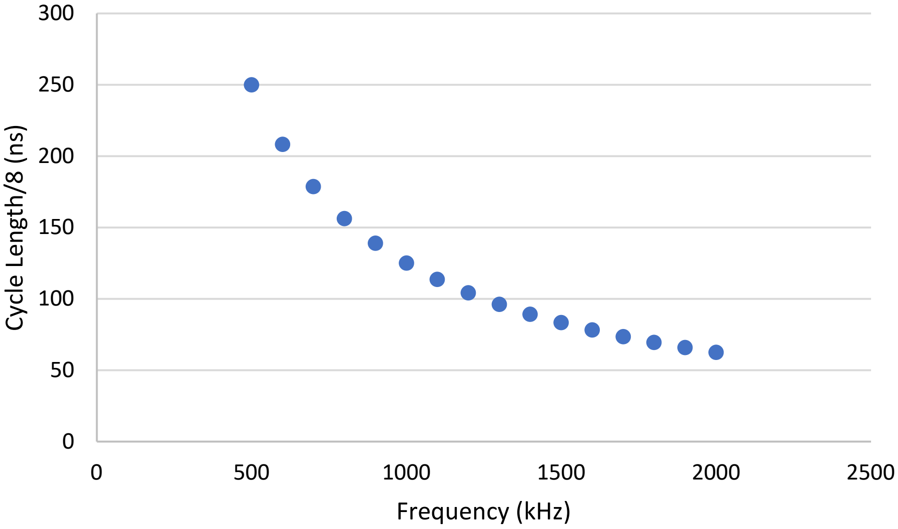

Figure 6.21. A plot of a fraction (1/8) of a cycle length at different frequencies. Assuming a constant fraction of a cycle worth of precision is needed for "good" aberration correction, a greater absolute temporal precision is needed at higher frequencies.

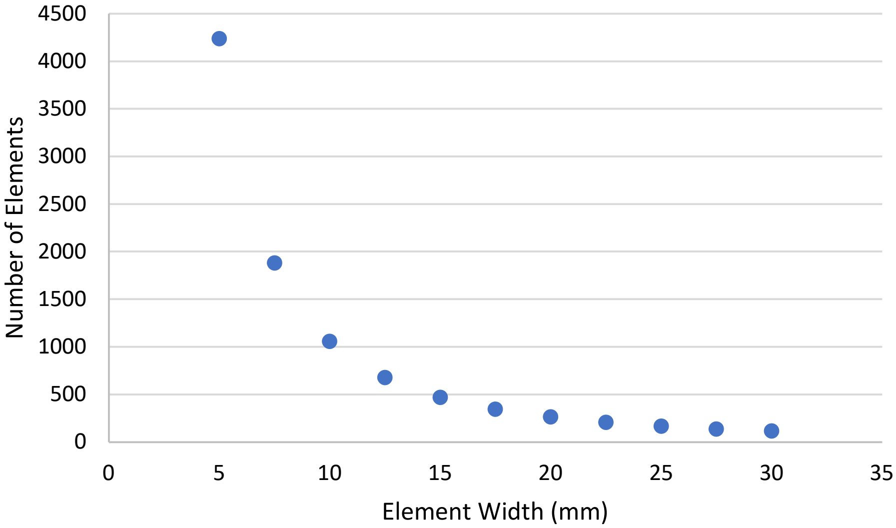

Figure 6.22. The number of square elements as a function element width for a 300 mm diameter hemisphere with a packing efficiency of 75%.

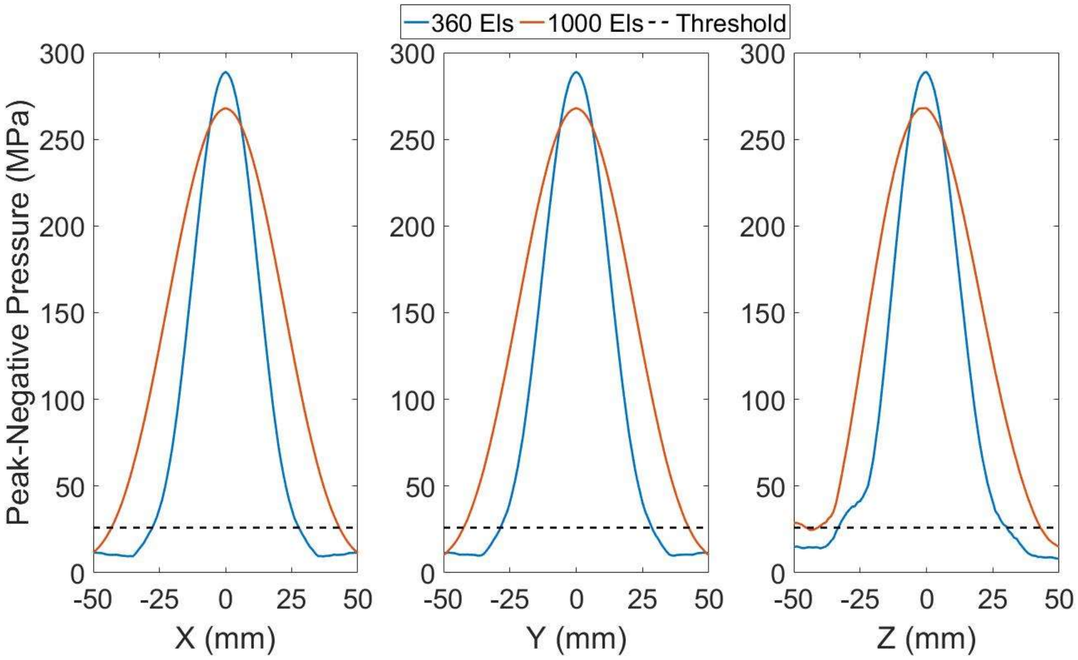

Figure 6.23. The peak-negative pressure output of a hemisphere array transducer with 360 17×17 mm and 1000 10×10 mm elements was simulated across a ± 50 mm electronic focal steering range. The simulation was calibrated to the output of a single 17×17 mm element driven at 3 kV through the skull (TC = transcranial). The dashed line indicates the histotripsy intrinsic threshold (26 MPa).

Table 6.5. The 3-axis steering range and above threshold volume through the skull for an array with 360 elements and 1000 elements.

		Steering Range			Volume
		X (mm)	Y (mm)	Z (mm)	(mL)
TC 360	-3 dB	29	29	29	-
17×17 mm Els	> 26 MPa	55	57	64	105
TC 1000	-3 dB	49	49	49	-
10×10 mm Els	> 26 MPa	86	85	84	321

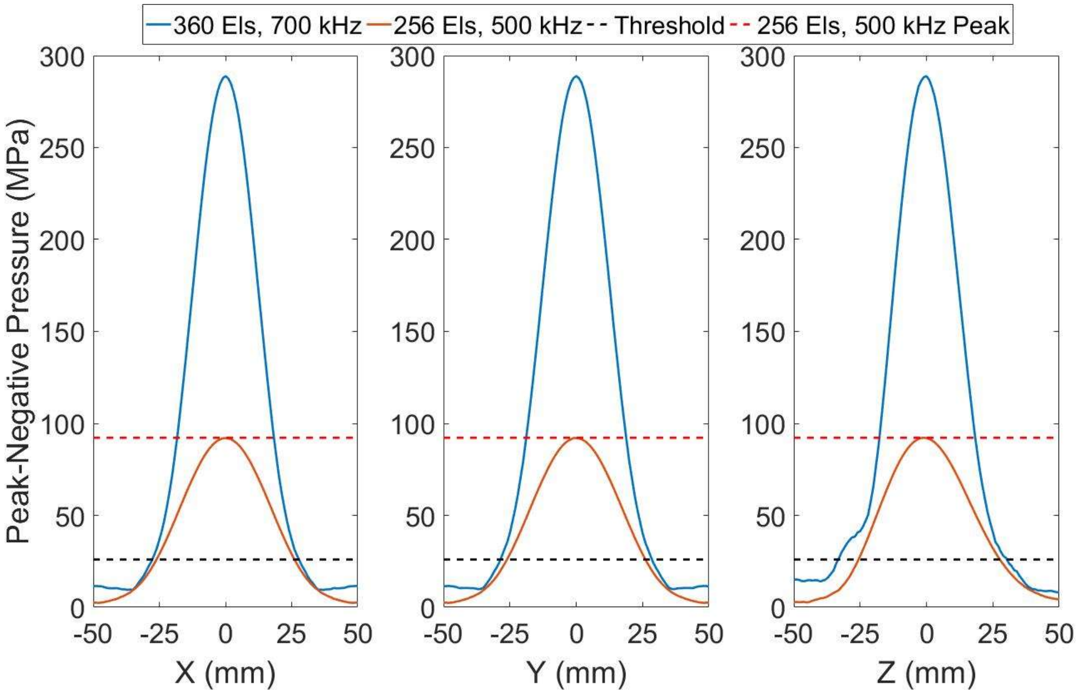

Figure 6.24. The peak-negative pressure output of a hemisphere array transducer with 360 17×17 mm 700 kHz elements and 256 20 mm diameter circular 500 kHz elements was simulated across a ± 50 mm electronic focal steering range. The simulation was calibrated to the output of a single element at each frequency driven at max driving conditions through the skull. The black dashed line indicates the histotripsy intrinsic threshold (26 MPa). The red dashed line indicates the peak output of the 256 element, 500 kHz array. The peak output of the 360 element, 700 kHz array was 3-fold greater than the peak output of the 256 element, 500 kHz array. At the peak output of the 256 element, 500 kHz array, the 360 element, 700 kHz array had a 36 mm steering range.

6.6.2 Impact of Incidence Angle on Trans-skull Transmission

Objective:

The effects of incidence angle on trans-skull transmission were evaluated experimentally and ray-tracing simulations were performed to assess the worst-case-scenario pressure loss that occurs when targeting different locations through the skull.

Methods:

Pressure Measurements through Excised Human Skulls: Experiments were performed to characterize the effect that the incidence angle of the acoustic wave from a single array element with the external surface of the skull had on pressure transmission through the skull. A capsule hydrophone (HGL200, Onda, Sunnyvale, CA) was placed 150 mm from a single element, 500 kHz ultrasound transducer that was fabricated in-house. A degassed, excised human skullcap (n = 2) was attached to a rotational stage (481A, Newport Corporation, Irvine, CA) and placed approximately halfway between the hydrophone and the ultrasound transducer. This distance was similar to the distanced between the skull and ultrasound transducer anticipated to be used in a therapy setting. A laser pointer was pointed through the axis of the rotation stage and used to line the external surface of the skullcap with the center of rotation of the stage. While driving the transducer with a ~1.5 cycle pulse, the skullcap was rotated through a range of angles in 5° steps and the pressure was captured at each angle. For each skullcap, this was performed at four regions of the skull: two central regions along the sagittal and coronal axis and an anterior and posterior region along the sagittal axis (Fig. 6.25).

Ray-tracing Simulations for Different Focal Locations within the Brain: Moving the focus of the histotripsy array transducer through different locations within the brain changes the angle at which the acoustic waves emitted by the individual elements of the array are incident on the external surface of the skull. To understand how the incidence angle changes as a function of the position of the geometric focus within the brain, ray-tracing simulations were performed. First, a point cloud of the external surface of a human skullcap was generated from a 3D CT scan of the skullcap. The skullcap point cloud was then positioned into the coordinate system of a point cloud defining the centers of the array elements. Discs of points with a 3 mm radius were sampled from the skullcap point cloud by tracing rays from the centers of array elements through the skullcap point cloud. Planes were fit to the sampled skull points using a 2D linear regression and the normal vector corresponding to each plane was obtained. The angles between the element rays and the skull surface normal from the section of points the rays intersected were then calculated. This process was repeated as the skullcap point cloud was translated through a range of different positions within the array element coordinate system.

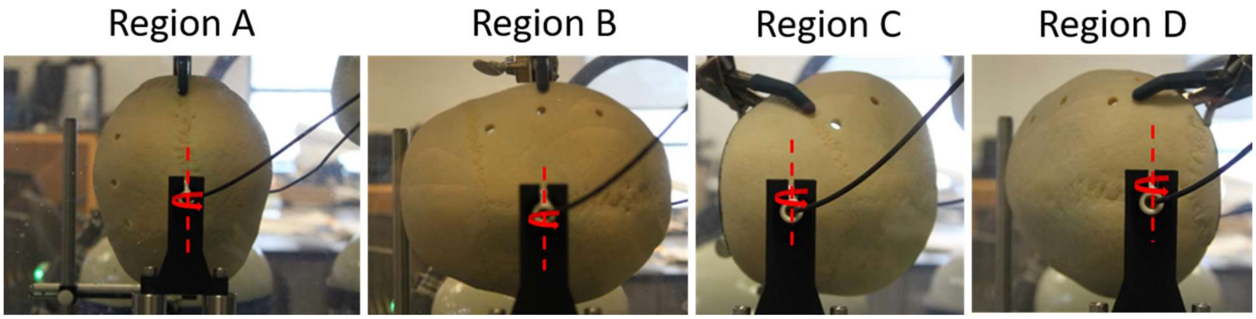

Figure 6.25. The anatomical regions on skullcaps and rotation orientations for incidence angle experiments.

Results:

Pressure Measurements through Excised Human Skulls: Experiments were performed to characterize the effect that the incidence angle of the acoustic wave from a single array element with the external surface of the skull had on pressure transmission through the skull. Figure 6.26 shows the average peak-negative pressure as a function of incidence angle, normalized to pressure measurements at normal incidence. The pressure curve showed a nonlinear, sinusoid like decrease in the pressure transmitted through the skull as a function of incidence angle. At an incidence angle of 25°, the pressure transmission was approximately half that at normal incidence. At an incidence angle of 45°, the pressure transmission was less than a tenth of that at normal incidence.

Ray-tracing Simulations for Different Focal Locations within the Brain: To understand how the incidence angles between waves emitted from individual elements and the skull surface change as a function of the position of the geometric focus within the brain, ray-tracing simulations were performed. Table 6.6 shows the average incidence angle across all elements of a hemispherical array with the focus placed at different locations within the internal skull cavity (brain). The average incidence angle was used to calculate the percent of pressure at normal incidence using the curve shown in Figure 6.26. With the focus at a central location within the brain, the average incidence angle was 19.8 ± 7.9°, corresponding to 65% of the pressure that could be achieved if waves emitted from all elements of the array were normal to the skull surface. With the transducer focus placed 40 mm superior to the central region, the average incidence was 42.9 ± 14.8°, corresponding to 7% of the pressure that could be achieved if waves emitted from all elements of the array were normal to the skull surface.

To create a comparison of the transcranial performance between the array design presented in this chapter and the 500 kHz array used in past transcranial histotripsy studies [3], the values in the third column of Table 6.6 were used to scale the simulated steering profiles shown in Figure 6.24 to consider effects of incidence angle. Table 6.7 shows the above threshold steering profiles and volumes (> 26 MPa) for the 360 element, 700 kHz array of 17×17 mm square elements and a 256 element, 500 kHz array of 20 mm diameter circular elements. The steering profiles and volumes are calculated across different focal locations within the brain that correspond to those presented in Table 6.6. Across most focal locations, the 360 element, 700 kHz array had a larger above threshold steering range than the 256, 500 kHz array, corresponding to a larger above threshold volume (up to an order of magnitude more in some cases). At the (0, 0, 40) mm position, the pressure drop was so great that neither array was above 26 MPa.

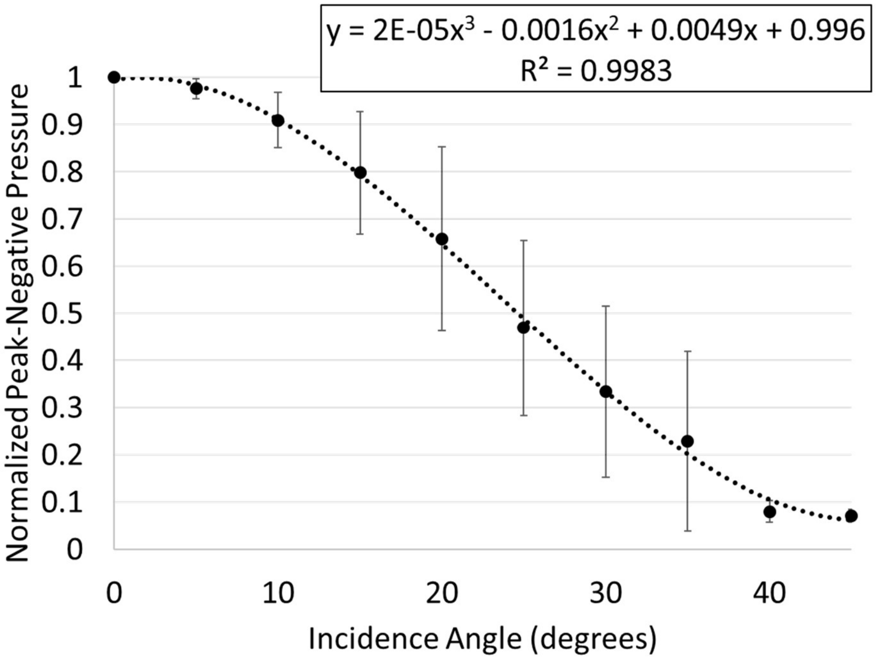

Figure 6.26. The average peak-negative pressure as a function of incidence angle, normalized to measurements at normal incidence.

Table 6.6. The average incidence angle across all elements of a hemispherical array at different focal locations within the brain. The average incidence angle was used to calculate the percent of pressure at normal incidence.

Focal Location Within Brain (X, Y, Z) mm	Average Incidence Angle	Percent of Pressure at Normal Incidence
(0, 0, 0)	19.8 ± 7.9°	65%
(0, 0, 20)	31.0 ± 10.7°	31%
(0, 0, 40)	42.9 ± 14.8°	7%
(0, 20, 0)	22.7 ± 9.4°	56%
(0, 40, 0)	30.0 ± 11.0°	33%
(20, 0, 0)	20.3 ± 8.8°	64%
(40, 0, 0)	27.0 ± 7.9°	43%
(20, 20, 20)	32.2 ± 12.0°	27%

Note: The (0, 0, 0) location corresponded to a central location within the brain (i.e., the midpoint between the lateral extremes and the posterior and anterior extremes and 10 mm from the cut plane of the skullcap toward the superior region of the skull). +X indicates translation of the focus toward the posterior region of the brain. +Y indicates translation of the focus toward the lateral region of the brain. +Z indicates translation of the focus toward the superior region of the brain.

Table 6.7. The 3-axis steering range and above threshold volume through the skull for the 360 element, 700 kHz and 256, 500 kHz array at different focal locations within the brain.

Focal Location	Array	Steering Range			Volume
		X (mm)	Y (mm)	Z (mm)	(mL)
(0, 0, 0)	360 Els, 700 kHz	49	50	51	65
	256 Els, 500 kHz	43	43	43	42
(0, 0, 20)	360 Els, 700 kHz	38	39	38	29
	256 Els, 500 kHz	15	15	15	2
(0, 0, 40)	360 Els, 700 kHz	0	0	0	0
	256 Els, 500 kHz	0	0	0	0
(0, 20, 0)	360 Els, 700 kHz	47	48	47	56
	256 Els, 500 kHz	39	39	40	31
(0, 0, 40)	360 Els, 700 kHz	39	40	38	31
	256 Els, 500 kHz	19	19	19	4
(20, 0, 0)	360 Els, 700 kHz	49	50	51	65
	256 Els, 500 kHz	42	42	43	40
(40, 0, 0)	360 Els, 700 kHz	43	44	42	42
	256 Els, 500 kHz	31	31	31	16
(20, 20, 20)	360 Els, 700 kHz	36	37	36	25
	256 Els, 500 kHz	0	0	0	0

Summary: The purpose of this set of experiments and analysis was to assess the worst-case-scenario pressure transmission loss that occurs when targeting different locations through the skull (i.e., pure translation, no rotation). Based on theoretical considerations and the results shown in Figure 6.26, the pressure transmission through the skull decreases as the incidence angle from normal incidence increases. According to the ray-tracing simulations, purely translating the array focus across different locations within the brain causes significant changes to the net (average) incidence angle between element rays and the skull surface. Based on the approximations made here, this can result in significant variation to the pressure transmitted through the skull.

Considering the (0,0,0) location as a baseline for treatment efficacy through the skull as in experiments described in [24], translation of the skull alone may cause a drop in pressure of up to 58% (i.e., in the anterior portion of the skull). Table 6.7 demonstrates the value of the new 360 element, 700 kHz array compared to a previous 256, 500 kHz array used in past transcranial studies [27]. Due to its significantly larger pressure overhead, the new 360 element array is able generate much larger volumes above threshold across a large range of focal locations within the brain, which is necessary for treating ICH. In some cases, the 360 element array had a significant volume (25 mL) above threshold while the field produced by the 256 element array remained below threshold. In some cases, the transmission loss due to incidence angle effects may be so great that pressure field generated by even the 360 element array may be insufficient to achieve above threshold volumes through the skull. In such cases, rotating the array about the geometric focus to some optimum Euler angle may significantly improve transmission through the skull.

6.6.3 Development of a Ray Tracing Optimization Model

Methods: A method for optimizing the orientation of a hemisphere array transducer with respect to the skull is proposed (Fig. 6.27). This is done using ray tracing methods. The concept takes the following form. Once the geometric focus of the histotripsy array is translated to the treatment location, the orientation of the array (Euler angles) with respect to the skull can be chosen to minimize the net incidence angle between the rays from the elements of the hemisphere array and the surface normal of the section of skull the ray intersects (Fig. 6.28). Minimizing the angle between these vectors corresponds to maximizing their inner product. Thus, the optimization model describing this problem is defined via the following equations.

$$Maximize \sum_{i}^{I=360} e_i^{Clot}(\gamma, \beta) \cdot n_i^{Clot}$$

s.t.

$$n_i^{Clot} = n_i^{Clot}[e_i^{Clot}(\gamma, \beta)]$$

$$\gamma_l \leq \gamma \leq \gamma_u$$

$$\beta_l \leq \beta \leq \beta_u$$

Where γ and β are the Euler angles that describe rotation around the x- and y-axis in the clot coordinate system, respectively, $e_i^{Clot}(\gamma, \beta)$ is the unit normal of the array elements which is a function of γ and β, n_i^{Clot} is the skull surface normal vector which is a function of $e_i^{Clot}(\gamma, \beta)$, γ_l β_l and γ_u, β_u are manually determined lower bounds and upper bounds to the Euler angles.

The calculation of n_i^{Clot} was performed using a computational method similar to the ray tracing calculations described in *Impact of Incidence Angle on Trans-skull Transmission*. First, a full head and neck CT scan from an anonymous person was obtained. The slice thickness for the scans was 0.625 mm and the lateral resolution was 0.395 mm. Point maps of the surfaces of all the bones within the skull were generated using edge detection methods. A point map of the array elements was virtually positioned to the clot coordinate system. In the idealized situation, the origin of the array coordinate system and clot coordinate system could be determined relative to that of a global coordinate system (e.g., treatment bed) using optical neuro-navigation or stereotactic methods. However, for the purposes of demonstrating this model, the clot coordinate system was treated as a global coordinate system. Once in the clot coordinate system, geometric methods were used to sample sections of bone surface points within a radius of 3 mm of the ray from each element array. Exclusion criteria were defined to ensure that only the external surface of the bone closest to the array element were chosen. This was done via a k-means clustering algorithm. Planes were fit to the sampled skull points using a two-dimensional (2D) linear regression. From these planes, the normal vector of the skull surface, n_i^{Clot}, was obtained.

To examine the initial value of the proposed optimization model, the geometric focus of the array was virtually positioned to a posterior region of the brain and the objective function was discretely solved through a range of manually defined angles.

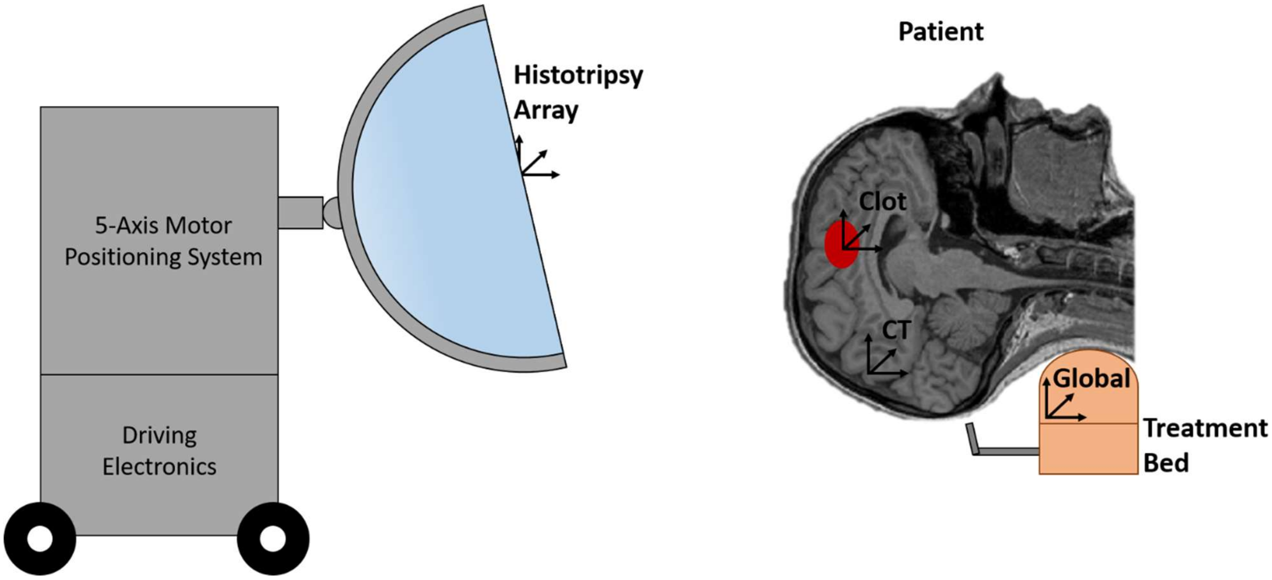

Figure 6.27. The treatment planning concept for histotripsy treatment of ICH.

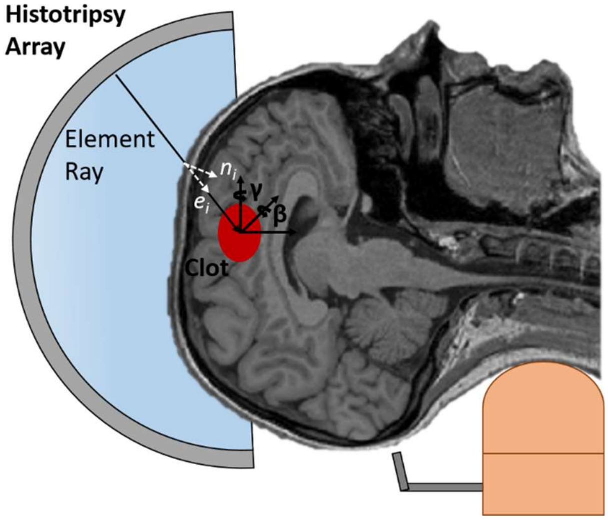

Figure 6.28. An image depicting the relationship between the element ray and the skull surface normal. Once the geometric focus of the array is placed at the center of the clot, the array orientation relative to the skull can be optimized by minimizing the angle between the element rays and skull surface normal.

Initial Results: Figure 6.29 shows the solution to the objective function at discrete angles with the geometric focus of the transducer placed at a posterior location within the brain. A maximum value for the objective function occurred with the array rotated 0° around the x-axis and 80° around the y-axis. This corresponded to the orientation shown in Figure 6.29c. The minimum to maximum increase in the objective function value was 6.7%. As this was not meaningful in terms of pressure recovery, the pressure vs. incidence angle curve in Figure 6.26 was used to relate the inner products between element rays and skull surface normal rays to pressure values. Figure 6.30 shows an estimate of the relative pressure change across the angle range examined in optimization model. The plot shows a 49.3% change between the minimum and maximum pressure estimates. Such an increase could bring the peak pressure either above the intrinsic threshold or provide significantly more pressure overhead for electronic focal steering.

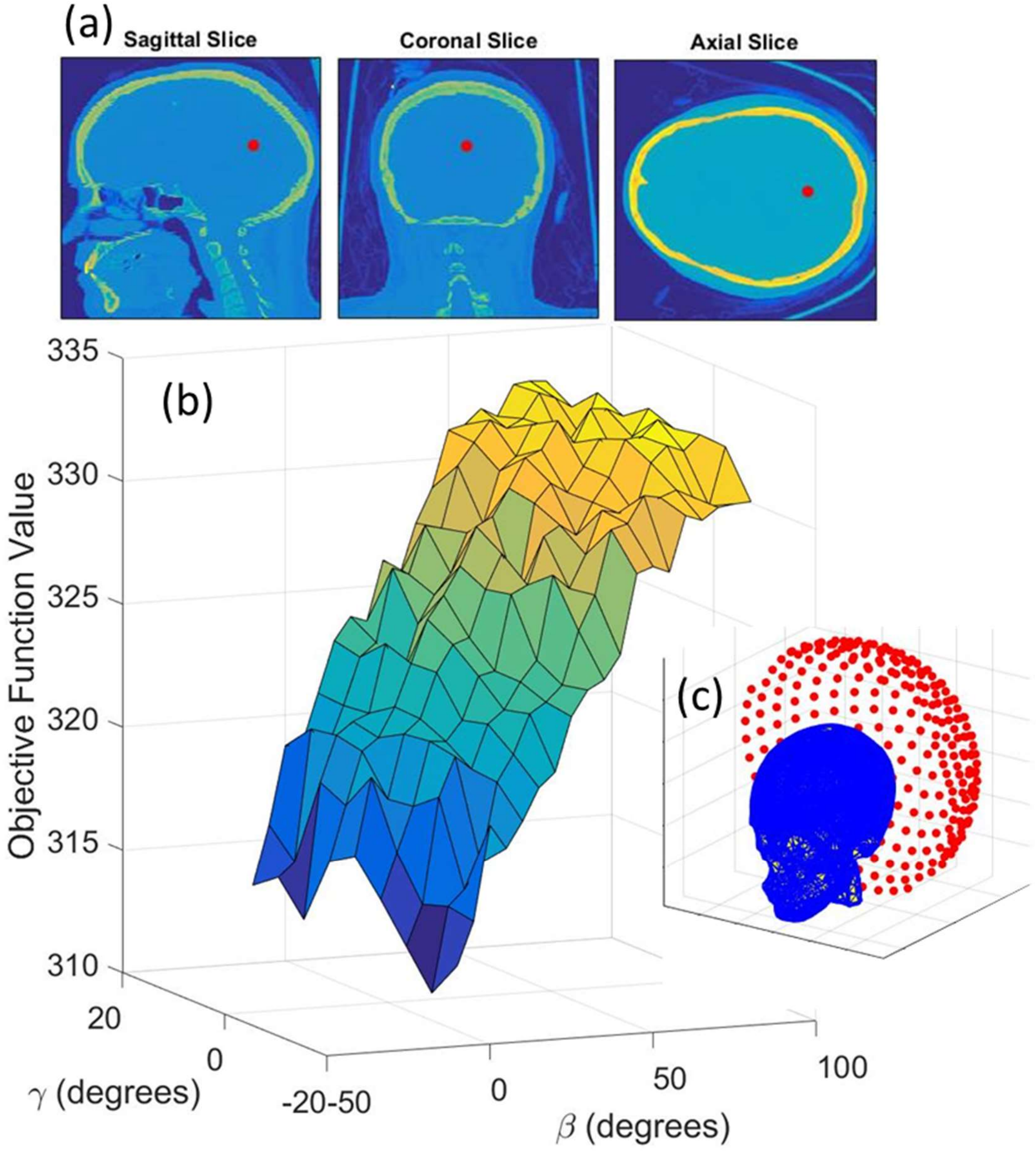

Figure 6.29. A summary of results for the ray tracing optimization model with the geometric focus of the hemisphere array placed in a posterior region within the brain. (a) Shows the location of the geometric focus of the array (red dot) within the brain via the CT scan. (b) Shows the objective function value plotted as a function of discrete values for γ and β. (c) Shows the array oriented in an optimum position based on the location of the geometric focus within the brain.

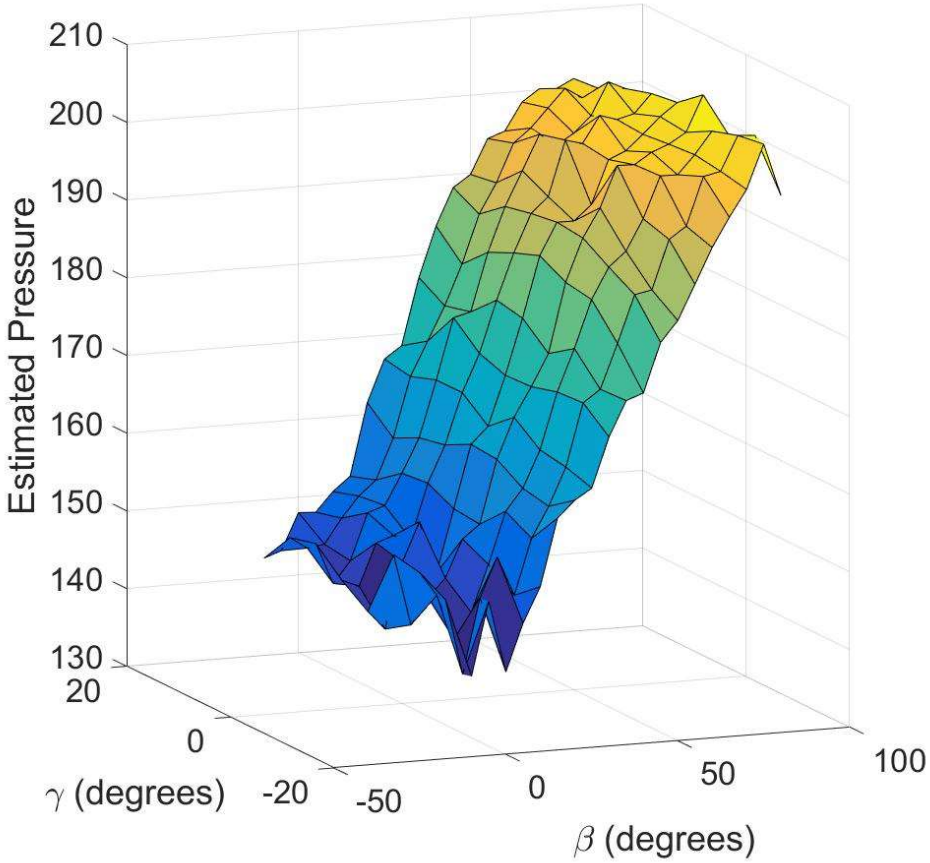

Figure 6.30. An estimate of the relative pressure change across the angle range examined in optimization model. Pressure estimates were made by calculating pressures using the inner product calculations and the polynomial fit to the experimentally obtained pressure vs. incidence angle data shown in Figure 6.26.

Future Work: The optimization model in its current state indicates some promising potential in orienting the hemispherical array transducer with respect to the skull to improve pressure transmission through the skull. Potential benefits of this method over full simulation methods include computational simplicity and reduced computation times. Further work for this model is necessary, most importantly, these results must be validated via simulations and experimental work. First, an adequate solver should be identified for the nonconvex nature of the objective function. Additionally, the implementation of optimization model solvers with graphical processing units (GPUs) are likely necessary to produce solutions to the model in clinically appropriate time frames (< 5 minutes). Many thanks to Professor Richard Hughes for his help developing and formalizing this model.

References

[1] M. Ramanan and a Shankar, “Minimally invasive surgery for primary supratentorial intracerebral haemorrhage,” *J. Clin. Neurosci.*, vol. 20, no. 12, pp. 1650–1658, 2013.

[2] M. D. C. Eames *et al.*, “Head phantoms for transcranial focused ultrasound,” *Med. Phys.*, vol. 42, no. 4, pp. 1518–1527, 2015.

[3] T. Gerhardson, J. R. Sukovich, A. S. Pandey, T. L. Hall, C. A. Cain, and Z. Xu, “Effect of Frequency and Focal Spacing on Transcranial Histotripsy Clot Liquefaction, Using Electronic Focal Steering,” *Ultrasound Med. Biol.*, vol. 43, no. 10, pp. 2302–2317, 2017.

[4] E. Vlaisavljevich *et al.*, “Effects of Ultrasound Frequency and Tissue Stiffness on the Histotripsy Intrinsic Threshold for Cavitation,” *Ultrasound Med. Biol.*, vol. 41, no. 6, pp. 1651–1667, 2015.

[5] T. Gerhardson, J. R. Sukovich, A. S. Pandey, T. L. Hall, C. A. Cain, and Z. Xu, “Catheter Hydrophone Aberration Correction for Transcranial Histotripsy Treatment of Intracerebral Hemorrhage: Proof-of-Concept,” *IEEE Trans. Ultrason. Ferroelectr. Freq. Control*, vol. 64, no. 11, 2017.

[6] J.-F. Aubry, M. Tanter, M. Pernot, J.-L. Thomas, and M. Fink, “Experimental demonstration of noninvasive transskull adaptive focusing based on prior computed tomography scans,” *J. Acoust. Soc. Am.*, vol. 113, no. 1, pp. 84–93, 2003.

[7] G. Maimbourg, A. Houdouin, T. Deffieux, M. Tanter, and J. F. Aubry, “3D-printed adaptive acoustic lens as a disruptive technology for transcranial ultrasound therapy using single-element transducers,” *Phys. Med. Biol.*, vol. 63, no. 2, 2018.

[8] Y. Hertzberg, A. Volovick, Y. Zur, Y. Medan, S. Vitek, and G. Navon, “Ultrasound focusing using magnetic resonance acoustic radiation force imaging: Application to ultrasound transcranial therapy,” *Med. Phys.*, vol. 37, no. 6, pp. 2934–2942, 2010.

[9] M. Pernot, G. Montaldo, M. Tanter, and M. Fink, “‘Ultrasonic stars’ for time-reversal focusing using induced cavitation bubbles,” *Appl. Phys. Lett.*, vol. 88, no. 3, pp. 1–3, 2006.

[10] M. Kim, J. Kim, and W. Cao, “Aspect ratio dependence of electromechanical coupling coefficient of piezoelectric resonators,” *Appl. Phys. Lett.*, vol. 87, no. 13, pp. 1–3, 2005.

[11] A. D. Maxwell *et al.*, “Cavitation clouds created by shock scattering from bubbles during histotripsy,” *J. Acoust. Soc. Am.*, 2011.

[12] K. W. Lin *et al.*, “Histotripsy beyond the intrinsic cavitation threshold using very short ultrasound pulses: Microtripsy,” *IEEE Trans. Ultrason. Ferroelectr. Freq. Control*, vol. 61, no. 2, pp. 251–265, 2014.

[13] Y. Kim, T. Hall, Z. Xu, and C. Cain, “Transcranial histotripsy therapy: A feasibility study,” *IEEE Trans. Ultrason. Ferroelectr. Freq. Control*, vol. 61, no. 4, pp. 582–593, 2014.

[14] J. P. Broderick, T. G. Brott, J. E. Duldner, T. Tomsick, and G. Huster, “Volume of intracerebral hemorrhage. A powerful and easy-to-use predictor of 30-day mortality,” *Stroke*, vol. 24, no. 7, pp. 987–993, 1993.

[15] M. Zuccarello *et al.*, “Early surgical treatment for supratentorial intracerebral hemorrhage: A randomized feasibility study,” *Stroke*, 1999.

[16] T. Brott *et al.*, “Early hemorrhage growth in patients with intracerebral hemorrhage,” *Stroke*, 1997.

[17] R. D. Zimmerman, J. A. Maldjian, N. C. Brun, B. Horvath, and B. E. Skolnick, “Radiologic estimation of hematoma volume in intracerebral hemorrhage trial by CT scan,” *Am. J. Neuroradiol.*, 2006.

[18] M. I. Aguilar and T. G. Brott, “Update in Intracerebral Hemorrhage,” *The Neurohospitalist*. 2011.

[19] J. R. Sukovich, Z. Xu, T. L. Hall, S. P. Allen, and C. A. Cain, “Treatment envelope of transcranial histotripsy applied without aberration correction,” in *The Journal of the Acoustical Society of America*, 2016.

[20] D. A. Orringer, A. Golby, and F. Jolesz, “Neuronavigation in the surgical management of brain tumors: Current and future trends,” *Expert Review of Medical Devices*. 2012.

[21] A. G. Chartrain *et al.*, “A review and comparison of three neuronavigation systems for minimally invasive intracerebral hemorrhage evacuation,” *J. Neurointerv. Surg.*, 2018.

[22] V. Rohde, I. Rohde, M. H. T. Reinges, L. Mayfrank, and J. M. Gilsbach, “Frameless stereotactically guided catheter placement and fibrinolytic therapy for spontaneous intracerebral hematomas: Technical aspects and initial clinical results,” *Minim. Invasive Neurosurg.*, 2000.

[23] H. Bjartmarz and S. Rehncrona, “Comparison of accuracy and precision between frame-based and frameless stereotactic navigation for deep brain stimulation electrode implantation,” *Stereotact. Funct. Neurosurg.*, 2007.

[24] T. Gerhardson, J. R. Sukovich, A. S. Pandey, T. L. Hall, C. A. Cain, and Z. Xu, “Effect of Frequency and Focal Spacing on Transcranial Histotripsy Clot Liquefaction, Using Electronic Focal Steering,” *Ultrasound Med. Biol.*, vol. 43, no. 10, 2017.

[25] J. J. Macoskey *et al.*, “Using the cavitation collapse time to indicate the extent of histotripsy-induced tissue fractionation,” *Phys. Med. Biol.*, vol. 63, no. 5, 2018.

[26] J. R. Sukovich, T. L. Hall, J. J. Macoskey, and Z. Xu, “Real-time transcranial histotripsy treatment monitoring and localization using acoustic cavitation emission feedback,” in *6th International Symposium on Focused Ultrasound*, 2018.

[27] E. Vlaisavljevich, T. Gerhardson, T. Hall, and Z. Xu, “Effects of f-number on the histotripsy intrinsic threshold and cavitation bubble cloud behavior,” *Phys. Med. Biol.*, vol. 62, no. 4, pp. 1269–1290, 2017.

CHAPTER 7 Histotripsy Mediated Immunomodulation in a Mouse GL261 Intracranial Glioma Model

A major component of the work in this chapter is part of a large multisite study currently being drafted for submission to the *Journal of Neurosurgery*.

7.1 Introduction

Glioblastoma (GBM) is the most common and most malignant primary brain tumor in adults [1]. Despite aggressive standard therapy including surgery, radiotherapy, and concomitant and adjuvant temozolomide the prognosis is poor with a median overall survival (OS) of less than 15 months [2]. GBM is a highly invasive and diffuse tumor with no clear margin between tumor and healthy brain tissue, making full surgical resection or ablation impossible. Furthermore, chemotherapy has a limited effect due to the blood brain barrier [3].

Histotripsy is a focused ultrasound (FUS) technology being developed for transcranial ablation applications. By using microsecond duration (duty cycle <0.1%), high amplitude acoustic pulses, histotripsy has the potential to provide a unique approach to rapid transcranial ablation. In contrast to other FUS techniques, that rely on the emission of long pulses (10% duty cycle) outside the skull to induce thermal necrosis of the targeted brain tissue, histotripsy can treat large (~40 mL) [4] and superficial regions [5] in short durations of time (20 mins) through human skulls while the skull heating remains within a clinically safe range [4].

The success of immunotherapies in treating cancers such as melanoma [6] has sparked interest in applying such therapies to GBM [7]. However, such immunotherapies have a limited affect as GBM is considered to be poorly immunogenic [8]. In an effort to enhance anti-tumor immunity in GBM, we hypothesize that histotripsy, due to its ability to induce non-thermal tumor ablation in a safe and targeted manner, could be used to increase tumor permeability and activity of the anti-tumor immune response. The goal of this initial study was to investigate the immune response of a mouse GL261 intracranial glioma model after histotripsy ablation of a fraction of an intracranial GBM.

7.2 Materials and Methods

7.2.1 Treatment Setup

The setup for histotripsy treatment of the mouse brain is shown in Figure 7.1. The mice were anesthetized with isoflurane gas and kept under anesthesia for the duration of the treatment via a small custom nose cone. The mouse was laid on its back on a stage above a water tank. The water in the tank was continuously degassed and kept warm (~37 °C). The mouse head was placed over a small hole in the stage that conformed to the sides of the mouse head but allowed it to dip into the water roughly 2 – 4 mm. A histotripsy transducer was attached to a 3-axis, motorized positioning system (Anaheim Automation, Anaheim, CA, USA) and positioned such that it was below the stage with the focus pointed toward the top of the tank. The histotripsy transducer was made in-house and consisted of a 1 MHz, 8 element transducer with aperture diameter of 58.6 mm and focal length of 32.5 mm. A phased array imaging probe was inserted coaxially within the transducer to allow tumor targeting and treatment monitoring. For mice inoculated with tumors, tumors were roughly targeted using the boundaries of the brain visible on a pretreatment MRI and the boundaries of the skull visible on the coaxially placed B-mode ultrasound probe.

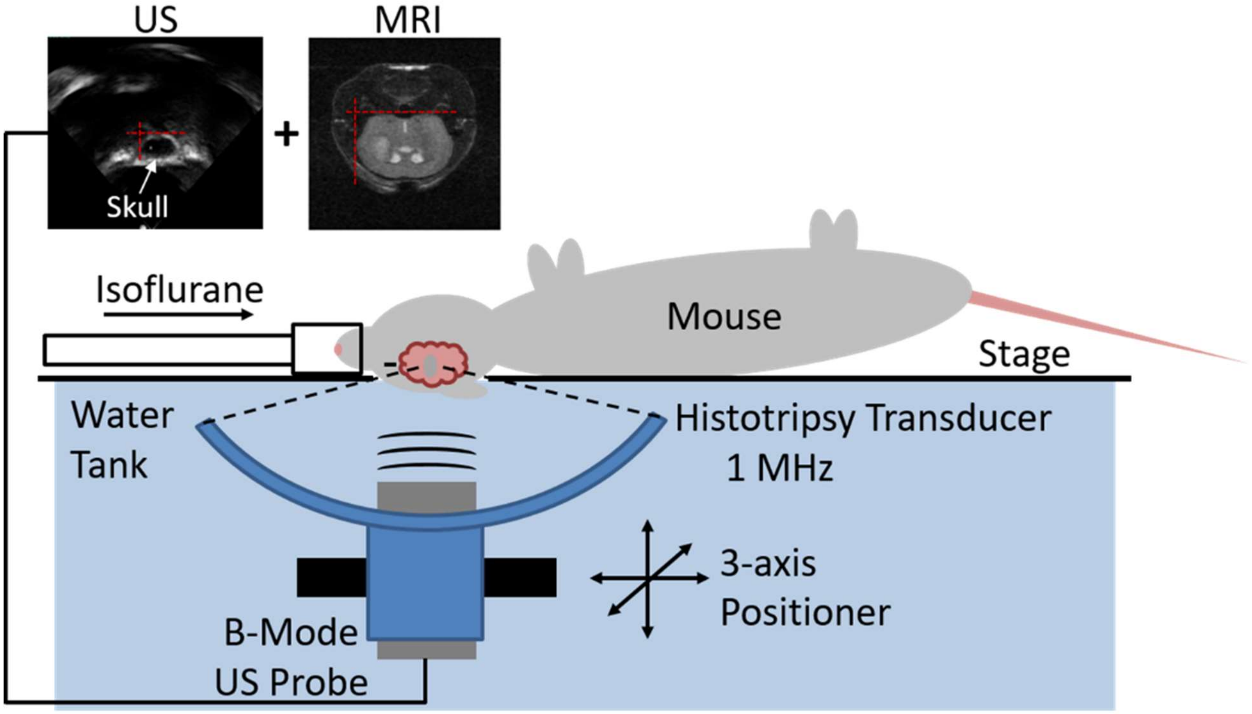

Figure 7.1. The experimental setup for applying transcranial histotripsy treatment to mouse brain. The histotripsy transducer was made in-house and consisted of a 1 MHz, 8 element transducer with aperture diameter of 58.6 mm and focal length of 32.5 mm.

7.2.2 Preliminary Histotripsy Dose and Survival Investigation – Normal Mice

To gain some understanding of what dose parameters to use for treating the tumor inoculated mice, some healthy, un-inoculated mice were treated with histotripsy. These mice were euthanized immediately following treatment. The brains were subsequently fixed in 10% phosphate buffered formalin for at least two weeks and sectioned for histology. For these mice, histotripsy pulses were applied at a pulse repetition frequency (PRF) of 1 Hz and an extrapolated peak-negative pressure of 40 MPa as measured in the free field. Histology was obtained for treatments with 10, 50 and 100 pulses applied to a single point.

In addition, to answer the question as to whether post-treatment mice would survive post-histotripsy-treatment for the length of time required for this study, two mice were survived for 8 days following histotripsy treatment. Histotripsy was applied at a PRF of 1 Hz and an extrapolated peak-negative pressure of 40 MPa. Based on the histology results of the previously described dose investigation (shown in Fig. 7.4), histotripsy treatment was applied by delivering 50 pulses to a single point. The brains of these mice were subsequently imaged via a T2-weighted fast spin-echo (FSE) sequence in a 7T MRI scanner (Varian, Inc., Palo Alto, CA, USA).

7.2.3 Study Timeline

The timeline for the tumor study is shown in Figure 7.2. A total of 27 mice were inoculated with tumor cells on Day 1 (detailed in section 7.2.4). Following inoculation and prior to histotripsy treatment mice were imaged using MR (7.0T or 9.4T horizontal bore, Agilent, Palo Alto, CA) and bioluminescence imaging (IVIS Spectrum, PerkinElmer, Waltham. MA) on days 7 and 12. A total of 15 of the inoculated mice were treated with histotripsy (treated group) on day 14, two weeks after inoculation, while 12 were left untreated as controls (control group). Both groups were further monitored via MRI and bioluminescence imaging on days 15, 18 and 20. For the treated group, successful tumor targeting was confirmed or denied according to the day 15 MRI. On day 21, both groups were euthanized and relevant organs were harvested for assessing the immune response (detailed in section 7.2.6).

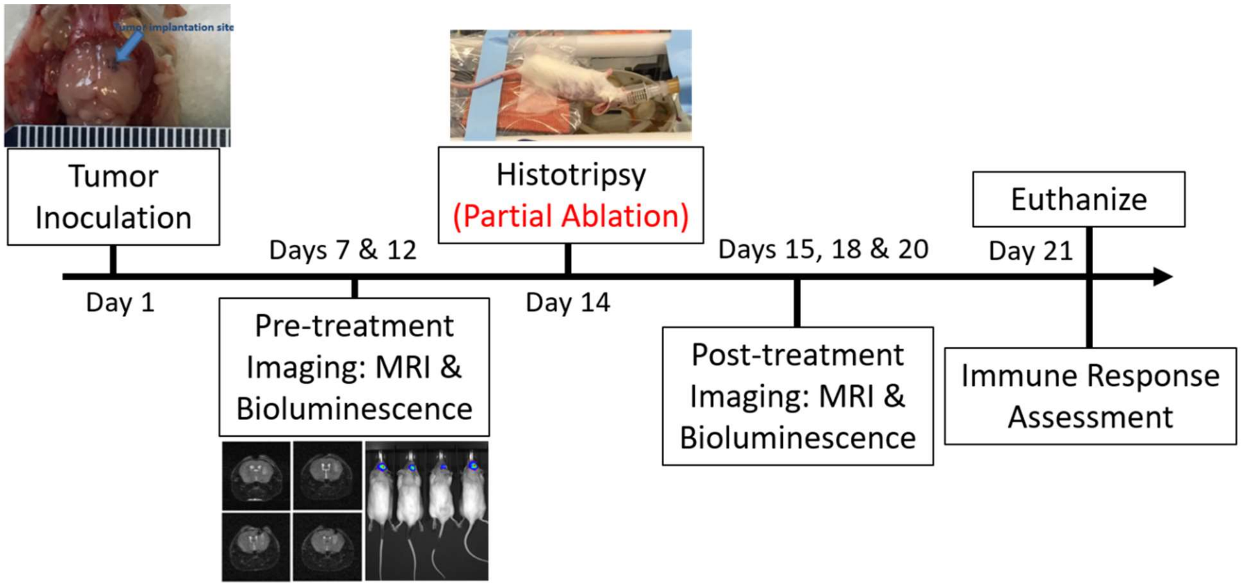

Figure 7.2. The overall timeline for the study. Of the 27 mice inoculated with tumor cells on Day 1, 15 were subject to histotripsy treatment while 12 were left untreated. All inoculated mice were subject to the same imaging and euthanasia time points.

7.2.4 Tumor Inoculation

A total of 27 female mice were inoculated with GBM according to a GL261-luc2 C57 BL/6 albino mouse model protocol similar to that described in [9]. Mice were anesthetized and placed on a stereotactic frame via a bite bar and ear bars. A spot 2.3 mm to the right and 0.1 mm back from the bregma was marked and a craniotomy was performed at the marked location using a micro-drill. A 33-gauge needle was used for injecting 1 µL of a cell sample concentration of 50×10^6 cells/mL. The needle was lowered 3.5 mm into the hole in the skull and then slowly lifted up 0.4 mm to make a “pocket” for the cells to be injected. Bone wax was used to fill the hole in the skull and the incision was closed using skin glue.

7.2.5 Tumor Monitoring

Tumor monitoring was performed via MRI and bioluminescence imaging on days 7, 12, 15, 18 and 20. MRI provided an estimate of the bulk tumor volume visible on MRI while bioluminescence provided a measure of tumor viability and tumor burden. The MRI protocol consisted of a T2-weighted FSE sequence acquired in axial and coronal slices with a slice thickness of 0.5 mm. Tumor volumes were calculated in MATLAB by hand sectioning tumor areas on individual MRI slices via the MATLAB function *imfreehand*, multiplying by the slice thickness and summing the sectioned areas across all slices. Bioluminescence was performed by injecting 150 μL of luciferase into the intraperitoneal cavity of the mice, placing them in a bioluminescence imaging system (IVIS Spectrum, PerkinElmer, Waltham. MA) and acquiring the luminescence overtime to ensure the peak luminescence for each mouse was captured. For each time point, the peak bioluminescence for each mouse was used to quantify the tumor burden.

7.2.6 Immune Response Assessment

A break-down of the immune response assessment is shown in Figure 7.3. Directly following euthanasia in both treatment and control mice, brain tumors, spleens and lymph nodes were harvested. A subset of all treated and control groups were processed for flow cytometry and histology, while interferon-γ production was also assessed in sections of the brain tumor from a subset of mice. The flow cytometry panel used to identify specific immune cells in the harvested and processed tissue samples is shown in Table 7.1.

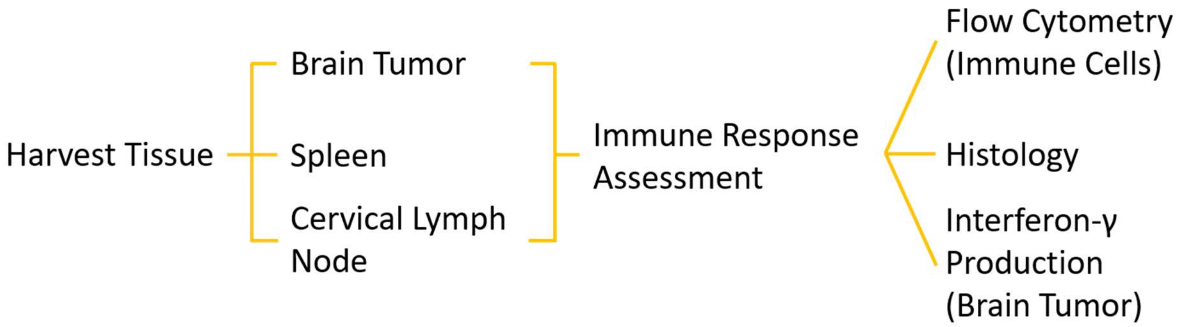

Figure 7.3. A break-down of the immune response assessment.

Table 7.1. The flow cytometry panel used to identify specific immune.

Cell Type	Gate 1	Gate 2	Gate 3	Gate 4
Natural Killer Cells	CD45	NK1.1	CD86	
MDSCs	CD45	CD11b	GR-1	
Dendritic Cells	CD45	CD11c	CD86	
T-Helper Cells	CD45	CD3	CD4hiCD8lo	
Cytotoxic T-Cells	CD45	CD3	CD4loCD8lo	
T-Regulatory Cells	CD45	CD3	CD4hiCD8lo	FoxP3
Exhausted T-Cells	CD45	CD3	PD-1	Tim3

7.3 Results

7.3.1 Preliminary Histotripsy Dose and Survival Investigation – Normal Mice

To gain some understanding of what dose parameters to use for treating the tumor inoculated mice and whether the mice would survive the necessary amount of time to perform the tumor study, some healthy, un-inoculated mice were treated with histotripsy. Figure 7.4 shows the H&E stained histology of a mouse brain treated with 10, 50 and 100 histotripsy pulses at a PRF of 1 Hz and an extrapolated peak-negative pressure of 40 MPa (as measured in the free field). Based on the histology sections, a dose of 50 pulses seemed appropriate as it appeared to produce a well-defined histotripsy lesion. Figure 7.5 shows the T2-weighted MRI of a mouse treated with histotripsy at various time points. A histotripsy lesion was generated within the mouse brain and the mouse survived until it was euthanized, 8 days after treatment.

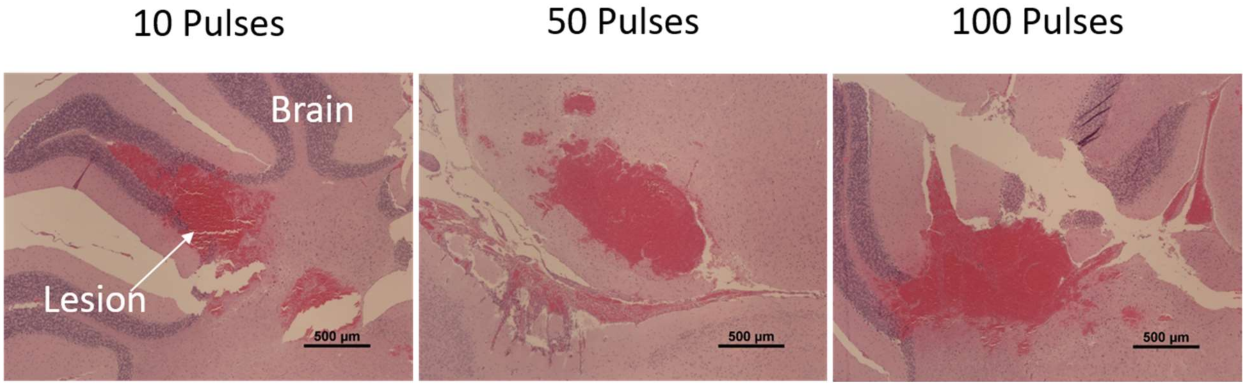

Figure 7.4. H&E histology sections of a mouse brain treated with 10, 50 and 100 histotripsy pulses.

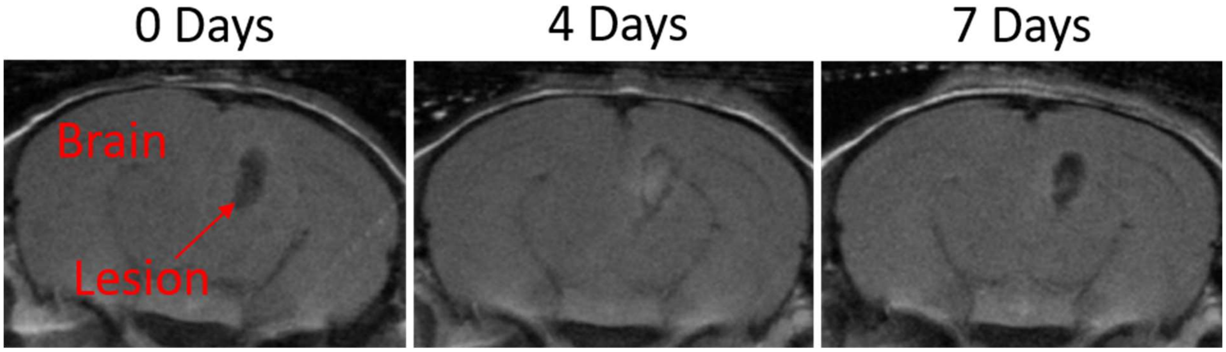

Figure 7.5. T2-weighted MRI of a healthy, un-inoculated mouse treated with histotripsy 0 days, 4 days and 7 days after histotripsy treatment.

7.3.2. Tumor Monitoring

Of the 15 mice treated with histotripsy, 14 survived treatments, all with lesions visible in post-treatment MRI. 12 of these mice were confirmed to have lesions in a portion of the bulk tumor volume as observed via MRI. Of the 12 control mice, 11 survived until the euthanasia date with 1 mouse dying 3 days prior to euthanasia. Mice treated with histotripsy were monitored before and after treatment via MRI and bioluminescence. Figure 7.6 shows an example of a treated mouse monitored before and after histotripsy treatment. The tumor viability was confirmed by day 7 via bioluminescence with the location of the bulk volume of the tumor visible on MRI. Histotripsy treatment was applied on day 14 and the lesions were visualized and confirmed or denied to hit the tumor in the day 15 post treatment MRI. Figure 7.7 and 7.8 show the average total flux and the average estimated tumor volume, respectively, for the treated and control group as a function of the number of days post inoculation. Based on these figures, no changes in the tumor burden were observed as a result of histotripsy treatment.

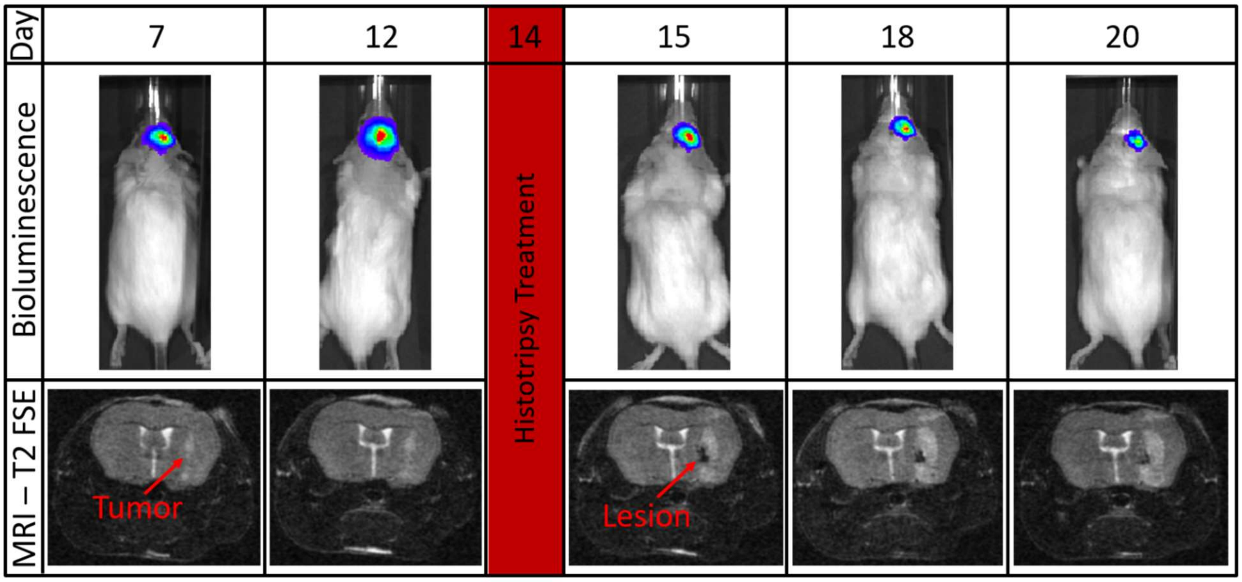

Figure 7.6. A visualization of the tumor monitoring performed on a mouse treated with histotripsy. Histotripsy treatment was applied on day 14 and the lesions were visualized and confirmed or denied to hit the tumor in the day 15 post treatment MRI.

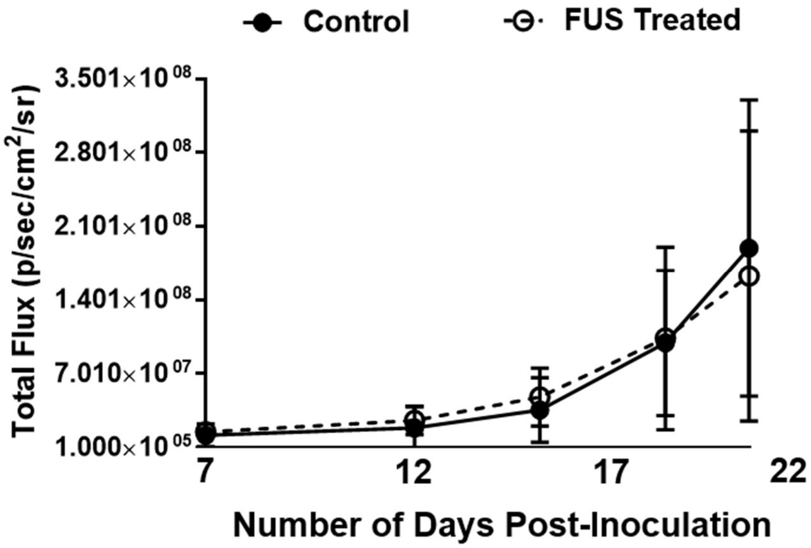

Figure 7.7. The average total flux for the treated and control group as a function of the number of days post inoculation.

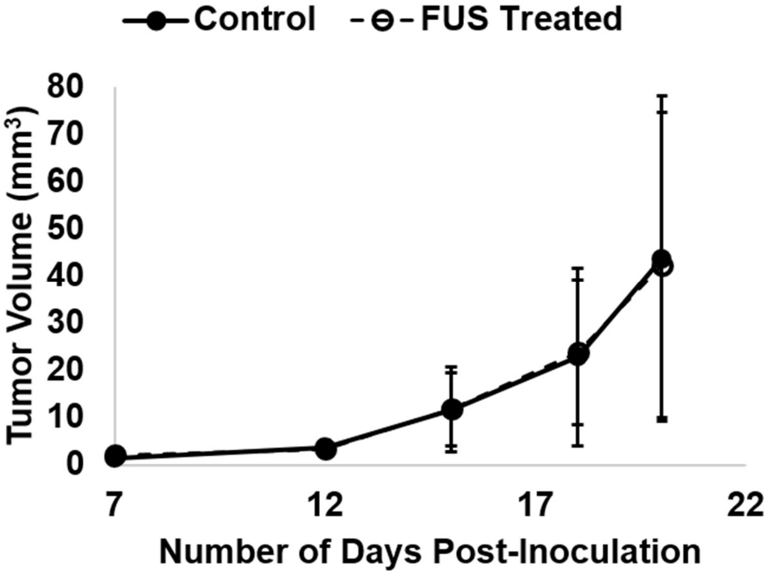

Figure 7.8. The average estimated tumor volume (based on T2-weighted MRI) as a function of the number of days post inoculation.

7.3.3 Immune Response Assessment

Following euthanasia, the immune response to histotripsy was assessed via flow cytometry. Figure 7.9 shows the percentage of lymphocytes that were classified as myeloid derived suppressor cells (MDSCs) in the brain tumor, spleen and superior and deep cervical lymph nodes. There was a two-fold reduction in the average percentage of MDSCs in the brain tumor of mice treated with histotripsy relative to the untreated controls (p-value < 0.05). Similar trends in the reduction of MDSCs were observed in the other organs examined but these reductions were not statistically significant (p-value > 0.05). No other statistically significant changes in the immune cell counts measured via flow cytometry were observed between the treated or control mice. The percentages of other immune cells (natural killer cells, dendritic cells, T-helper cells, cytotoxic T-cells, T-regulatory cells, exhausted T-cells) measured via flow cytometry are shown in Figures 7.12 – 7.16 in the Appendix of this chapter (section 7.6).

In addition to flow cytometry, the interferon gamma (IFN-γ) production in the brain tumors was assessed in treated and control mice (n = 3). Figure 7.10 shows the IFN-γ produced in one treated and control mouse in the absence and presence of Anti-CD3. In the absence of Anti-CD3 (Anti-CD3-), a similarly low concentration of IFN-γ was produced in the tumor of the treated and control mouse. In the presence of Anti-CD3 (Anti-CD3+), a low concentration of IFN-γ was produced in the tumor of the control mouse while a very large concentration of IFN-γ was produced in the tumor of the treated mouse. Similar increases in IFN-γ production were observed in two additional control and treatment mice, the IFN-γ measurements for these mice are shown the Appendix of this chapter (Fig. 7.17).

To examine the indirect effects of histotripsy ablation on the tumor cell phenotype, sections of brain tumors in control and treatment mice were sectioned for histology. Figure 7.10 shows a section of tumor from a control and treatment mouse stained with Giemsa stain (n = 2). The section of the tumor sampled from the treatment mouse was taken from a portion of the tumor not directly ablated with histotripsy. The sections were examined by a pathologist blinded from the study groups. The sections of control tumors were characterized as normal healthy tumor cells with a high mitotic index. In contrast, sections of tumors from treated mice showed shrunken tumor cells separated by edema with pyknotic nuclei. The treated sections lacked a sufficient number of healthy cells to assess the mitotic index.

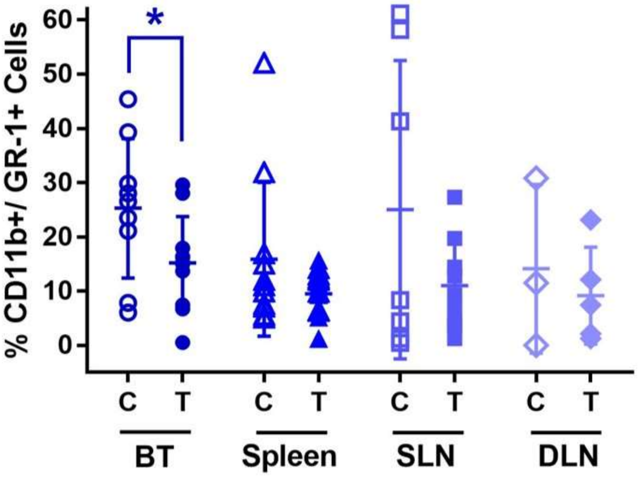

Figure 7.9. The percentage of total lymphocytes expressing CD11b and GR-1. This combination was used to identify myeloid derived suppressor cells (MDSCs). C = control group (n = 9), T = treated group (n = 9), BT = brain tumor, SLN = superficial cervical lymph node and DLN = deep cervical lymph node. *Indicates a p-value < 0.05.

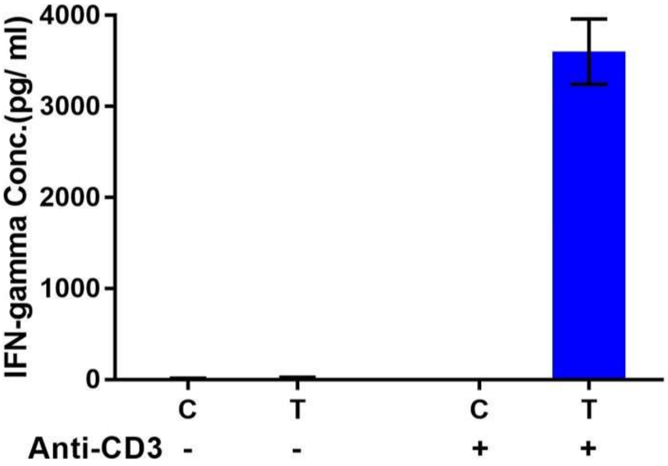

Figure 7.10. The interferon-gamma (IFN-γ) production in the brain tumor of a control and treated mouse in the absence and presence of Anti-CD3. The measurements were obtained from multiple sections of brain tumor from a single control and treatment mouse.

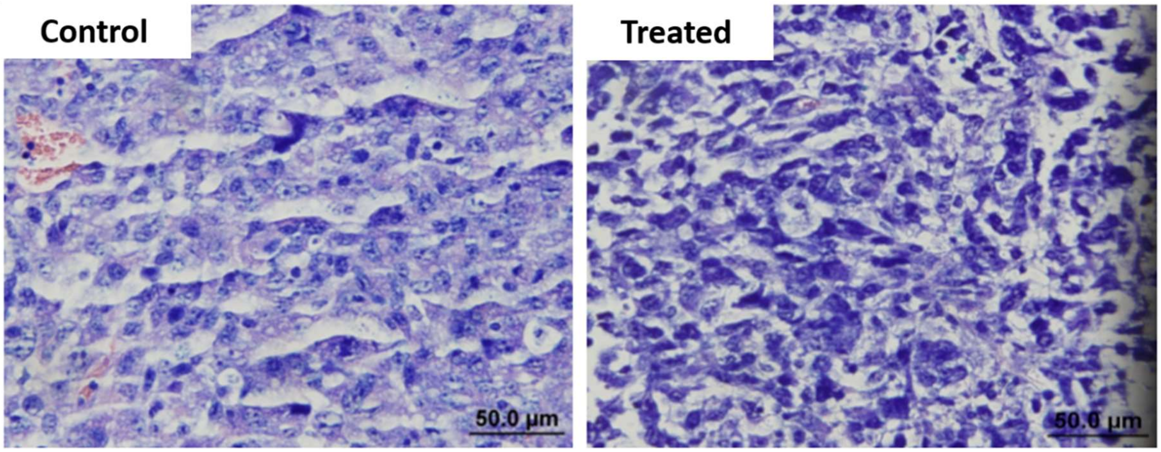

Figure 7.11. A section of tumor from a control and treatment mouse stained with Giemsa stain (n = 2). The section of the tumor sampled from the treatment mouse was taken from a portion of the tumor not directly ablated with histotripsy.

7.4 Discussion

This study presents the first analysis of the immunomodulatory effects of histotripsy in a GL261 intracranial glioma model. Despite the absence of changes in the tumor burden following histotripsy ablation, the changes observed in the immunomodulatory cell populations (MDSCs) and cytokines (IFN-γ) as well tumor histology provide initial insight to potential mechanisms that may be at work in increasing the immunogenicity and anti-tumor response resulting from partial ablation of the tumor with histotripsy.

The first significant observation is the reduction in the MDSCs in the brain tumor of mice treated with histotripsy relative to the untreated controls. There is a growing body of evidence that MDSCs are a strong contributor to the suppressed immune environment observed in cancer and other pathologies [10]–[12] and thus a contributing factor to the limited defense the body naturally has against the tumor. The number of these cells are typically increased in cancer patients and contribute to chronic inflammation in the tumor microenvironment [13]. Thus, the reduction of these cells observed following histotripsy treatment provides some insight into potential mechanisms that may be at work in mitigating the immunosuppressive environment following histotripsy treatment. The observed reduction in the MDSC population in the treated group may be related to the large production of IFN-γ observed in the brain tumors of the treated mice. This is supported by studies linking IFN-γ inhibition (typical in cancer patients) to increased MDSC levels [14]. With some evidence of the mechanistic relationship between MDSCs and IFN-γ, the synergistic effects observed via the reduced MDSC level and increased IFN-γ in tumors treated with histotripsy lend further evidence to potential immunomodulatory effects of histotripsy.

IFN-γ is an important regulatory cytokine for the activation of specific immunity [15]. Thus, the low levels generally observed in cancer patients are thought to contribute to the limited antitumor response against and the progression of cancer. However, the production of IFN-γ alone may be insufficient to initiate antitumor responses due to the expression checkpoint molecules (e.g., PD-1/PD-L1) by the tumor that can occur in the presence of IFN-γ [16]. This phenomenon might be playing out in the present study, where despite the large increase in IFN-γ, no effect on tumor burden is observed. This may suggest that a checkpoint is being expressed by the tumor and blocking the activation of specific immunity against the tumor. In this study, the presence or absence of IFN-γ blocking checkpoints was not examined and follow up studies are necessary to confirm such a hypothesis. If present, the checkpoint molecule can be blocked using "checkpoint inhibitors" (e.g., anti-PD-1/anti-PD-L1) that block the ability of the checkpoint to inhibit IFN-γ mediated immunity and ultimately regress and stabilize the tumor [17].

The argument for histotripsy immunomodulation may be further strengthened based on the near-apoptotic state of the tumors that were subject to histotripsy. The primary reason for this is that the apoptotic section of tumor was not directly ablated with histotripsy and thus the damage must have occurred by some indirect means caused by ablation via histotripsy. Thus, despite the specific mechanisms at work, it is clear that histotripsy therapy is producing some immunomodulatory effects that propagate to damaging the tumor cell phenotype.

7.5 Conclusion

In this initial study, we investigated the immune response of a mouse GL261 intracranial glioma model after treating a portion of the brain tumor with histotripsy. Flow cytometry analysis showed a decrease in highly immunosuppressive MDSCs in histotripsy treated tumors compared to untreated brain tumors. In addition, the IFN-γ production was found to be extremely low in the untreated control tumors (consistent with literature), whereas histotripsy treated tumors showed relatively large amounts of IFN-γ, suggesting that the decrease in MDSC resulted in a decreased immunosuppressive inratumoral environment. Analysis of tumor immunohistochemistry revealed that histotripsy treated tumors showed shrunken tumor cells with shrunken and pyknotic nuclei separated by edema which contrasted with the untreated brain tumors, which appeared relatively healthy. These initial results provide a compelling rationale for potential mechanisms that may be at work in increasing the immunogenicity of the tumors following histotripsy treatment. Future work include treating a greater proportion of the tumor[1], examining the presence of IFN-γ blocking checkpoints and the effects of histotripsy in combination with checkpoint inhibitors.

7.6 Appendix

7.6.1 Supplementary Methods

Cell line, source and maintenance

---

[1] One approach to treating a greater proportion of the tumor is to improve the targeting. A stereotactic MRI based method for improved tumor targeting has been developed. This method is briefly presented in the Appendix at the end of this chapter under *Stereotactic Targeting System.*

- Cell line: GL261-luc2 cells
- Source: Dr. Prafulla Gokhale @ Dana-Farber Cancer Institute
- Maintenance: Cultured in DMEM high glucose + 10% FBS + 100 µg/mL geneticin, 5% CO2, stored at -80C in liquid nitrogen until used

Mice (strain, vendor, age, sex)

- Strain: BL6 albino mice (Cat # 000058)
- Vendor: Jackson laboratory
- Age: 2 – 4 months
- Sex: Female

Tumor inoculations

- Number of cells: 100,000 via 2 µL
- Concentration: 50 million cells / mL
- Location: 0.5 mm caudally from the bregma and 1.5 mm laterally (right) from the bregma, 3.5 mm deep

Histology

Histology and immunohistochemistry were carried out at Research Histology & IHC Laboratory at University of Michigan Cancer Center. Brain tumor tissue samples for histological analysis were fixed overnight in 10% neutral buffered formalin (Sigma-Aldrich; catalog #HT501320), processed through graded alcohols, cleared in xylene, and embedded in paraffin. Formalin fixed and paraffin embedded tissues were sectioned at 8 µm and placed on charged slides.

Slides were H&E-stained and subjected to immunohistochemistry. To immunostain for CD4 and CD8, slides were deparaffinized in xylene and rehydrated through graded alcohols. Epitope retrieval was performed with10 mM Tris HCl, pH9 containing 10 mM EDTA. Anti-CD4 (Rabbit monoclonal Antibody, Clone EPR19514; Abcam #Ab183685; 1:1000) or anti CD8α (Rabbit monoclonal Antibody, clone D4W22, Cell Signaling #98941, 1:400) was applied and incubated for 60 min. at room temperature. Anti-rabbit Envision+ HRP Labeled Polymer (DakoCytomation) was applied for 30 min at room temperature and was used to detect the antibody. HRP staining was visualized with the DAB+ Kit (DakoCytomation).

Staining to assess comparative leukocyte infiltration in control vs histotripsy treated brain tumor samples was done using a May-Grunwald Giemsa (Catalog # D-250, Rowley Biochemical Inc, Danvers, MA). Four um thickness sections were cut using a rotary microtome and mounted on glass slides. Slides were stained by the May-Grunwald Giemsa method. Slides were examined by a board-certified veterinary pathologist (ILB) Ingrid L. Bergin (ULAM In Vivo Animal Core) using light microscopy (BX45 Olympus light microscope) at objective magnifications ranging from 2X-40X. The experimental treatment (group) was not known at the time of analysis.

Flow Cytometry

Tissue harvest: Mice were euthanized with CO_2 inhalation. The mouse skull was opened carefully and the brain tumor was harvested by scooping from the base avoiding any host tissue, which was facilitated by the specific shape and localization of the tumor. Spleen, and cervical lymph nodes (superficial and deep) were also harvested.

Processing into single cell suspensions: Single-cell suspensions of fresh brain tumor, spleen, superficial and deep cervical lymph nodes were prepared by mechanical crushing and passing through a 40-μm cell strainer, washed once with RPMI/10% FCS, and treated with RBC lysis buffer (BioLegend Cat. No. 420301) to eliminate RBC. Cells were washed two times in cell staining buffer (BioLegend Cat. No. 420201). To reduce nonspecific immunofluorescent staining, cells were blocked with Fc receptor (TruStain fcX™ (anti-mouse CD16/32, BioLegend Cat. No. 101319, clone 93).

Staining (antibodies, markers): A multicolor panel which facilitates simultaneous staining of 14 markers in a single sample was developed utilizing the expertise of BioLegend. The following panel was used for immunophenotyping of the brain tumor and lymphoid organs (Spleen, superficial and deep cervical lymph nodes). Single-cell suspensions were stained in cell staining buffer. For intracellular staining of Foxp3, cells were permeabilized (True-Nuclear™ Transcription Factor Buffer Set, Catalog No. 424401, Bioloegend) and stained with the PE-Cyanine5 anti-mouse Foxp3 staining set according to the manufacturer's recommendations.

Table 7.2. List of antibodies used.

Antibody	Clone	Company	Catalog No.	Dilution
Alexa Fluor® 700 anti-mouse CD45	30-F11	BioLegend	103127	1:100
PerCP/Cyanine5.5 anti-mouse CD3	17A2	BioLegend	100217	1:50
APC/Fire™ 750 anti-mouse CD4	RM4-5	BioLegend	100567	1:100
Brilliant Violet 510™ anti-mouse CD8a	53-6.7	BioLegend	100751	1:100
PE/Dazzle™ 594 anti-mouse/human CD11b	M1/70	BioLegend	101255	1:100
APC anti-mouse CD86	GL-1	BioLegend	105011	1:100
PE/Cy7 anti-mouse CD11c	N418	BioLegend	117317	1:100

Brilliant Violet 650™ anti-mouse NK-1.1	PK136	BioLegend	108735	1:50
FITC anti-mouse Ly-6G/Ly-6C (Gr-1)	RB6-8C5	BioLegend	108405	1:100
Brilliant Violet 421™ anti-mouse CD366 (Tim-3)	RMT3-23	BioLegend	119723	1:50
PE anti-mouse CD279 (PD-1)	RMP1-30	BioLegend	109103	1:100
PE-Cyanine5 anti-mouse FOXP3	FJK-16s	eBioscience™	15-5773-80	

IFNg Assay

A single cell suspension of $4x10^5$ brain tumor cells in complete culture media was added in duplicate or triplicates to each well of a 96 well assay plate coated, with anti-CD3 antibody (clone 145-2C11, Catalog #100302, Biolegend, San Diego, CA). Unstimulated cells were used in parallel as negative control. The culture plates were incubated at 37°C in 5% CO_2 and 100% humidity for 3 days. IFNg levels in the conditioned media were determined by sandwich capture ELISA (Duosets, R&D Systems, Minneapolis, MN) using the manufacturer's recommended protocol adapted to include an overnight sample incubation and were carried out by University of Michigan Cancer Center Immunology Core.

7.6.2 Miscellaneous Figures

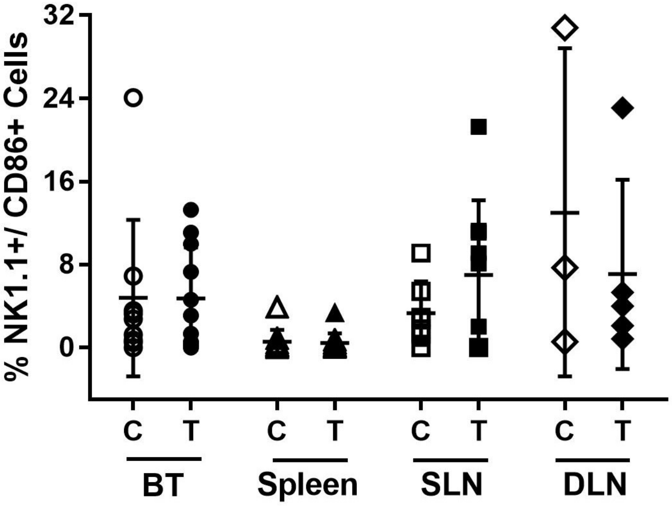

Figure 7.12. The percentage of total lymphocytes expressing NK1.1 and CD86. This combination was used to identify natural killer cells. C = control group (n = 9), T = treated group (n = 9), BT = brain tumor, SLN = superficial cervical lymph node and DLN = deep cervical lymph node.

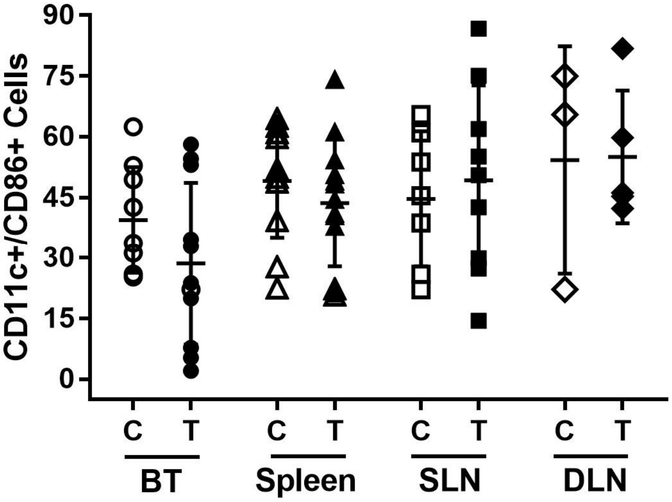

Figure 7.13. The percentage of total lymphocytes expressing CD11c and CD86. This combination was used to identify dendritic cells. C = control group (n = 9), T = treated group (n = 9), BT = brain tumor, SLN = superficial cervical lymph node and DLN = deep cervical lymph node.

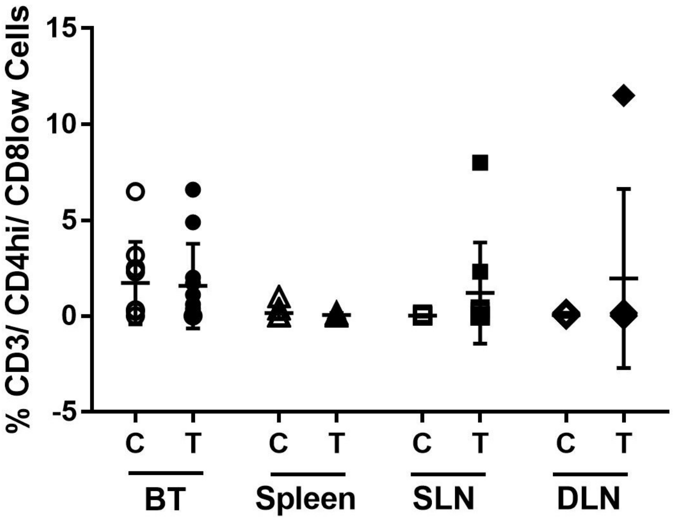

Figure 7.14. The percentage of total lymphocytes expressing CD3 and CD8low. This combination was used to identify T-helper cells. C = control group (n = 9), T = treated group (n = 9), BT = brain tumor, SLN = superficial cervical lymph node and DLN = deep cervical lymph node.

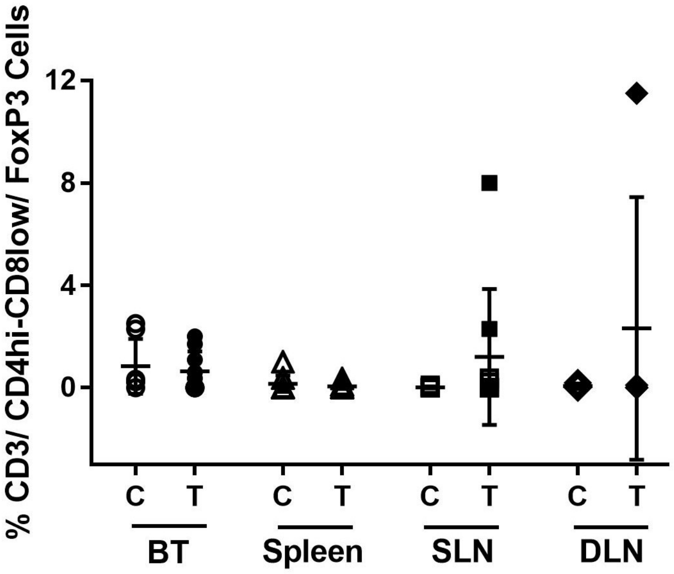

Figure 7.15. The percentage of total lymphocytes expressing CD3, CD4hi-CD8low and FoxP3. This combination was used to identify T-regulatory cells. C = control group (n = 9), T = treated group (n = 9), BT = brain tumor, SLN = superficial cervical lymph node and DLN = deep cervical lymph node.

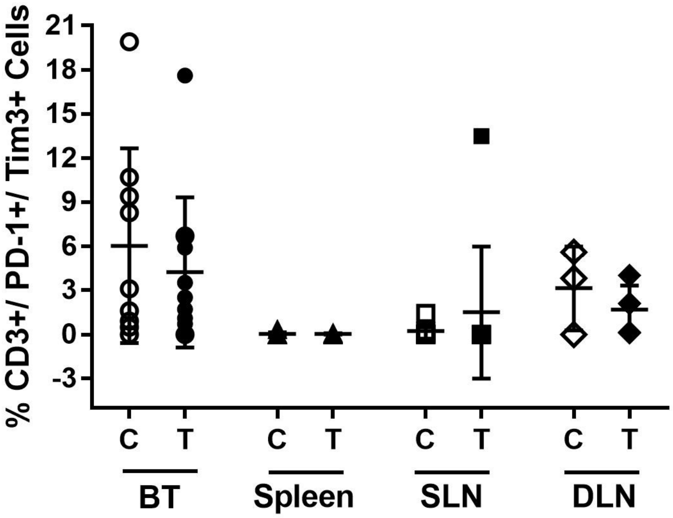

Figure 7.16. The percentage of total lymphocytes expressing CD3, PD-1 and Tim3. This combination was used to identify exhausted T-cells. C = control group (n = 9), T = treated group (n = 9), BT = brain tumor, SLN = superficial cervical lymph node and DLN = deep cervical lymph node.

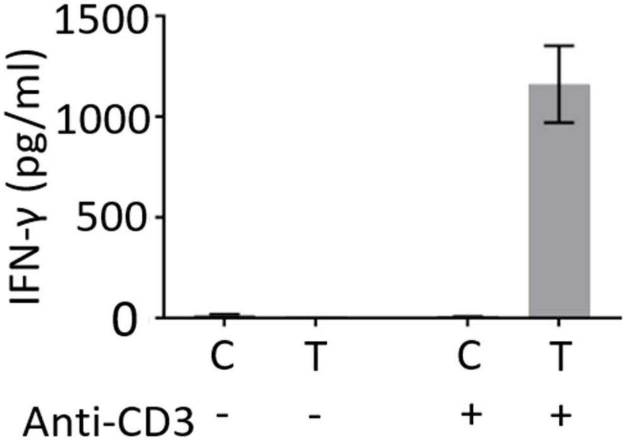

Figure 7.17. The interferon-gamma (IFN-γ) production in the brain tumor of a second control and treated mouse in the absence and presence of Anti-CD3. The measurements were obtained from multiple sections of brain tumor from a single control and treatment mouse.

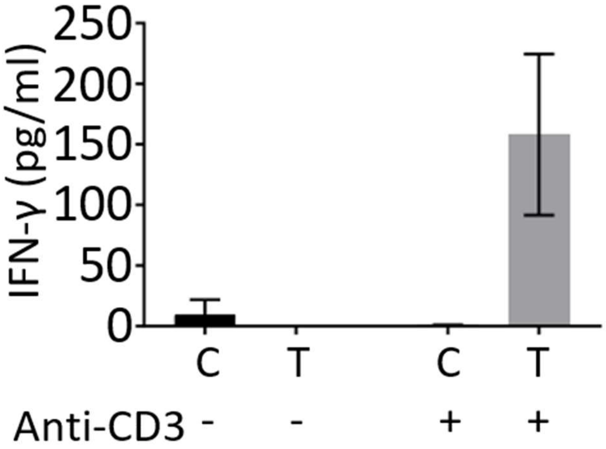

Figure 7.18. The interferon-gamma (IFN-γ) production in the brain tumor of a third control and treated mouse in the absence and presence of Anti-CD3. The measurements were obtained from multiple sections of brain tumor from a single control and treatment mouse.

7.6.2 Stereotactic Targeting System

System Schematic:

A stereotactic system was developed to improve the tumor targeting capabilities within the mouse brain. An MRI-compatible mouse tray was designed to hold the mouse head fixed with respect to two MRI visible fiducial markers (Fig. 7.19 left). The mouse tray interfaced with a gradient alignment frame that fit within a 60 mm O.D. RF-coil. The alignment frame is intended to align the mouse tray coordinate system with that of the small animal MRI system. After imaging the mouse brain in the tray, the mouse tray is transferred to a frame overlying the water tank of the treatment setup via alignment screws (Figure 7.19 right). A histotripsy transducer mates with this frame via alignment pins. Using a 3-axis motor positioning system and the tumors location with respect to the fiducials in the MR image, the geometric focus of the transducer is then able to be guided to the location of the tumor.

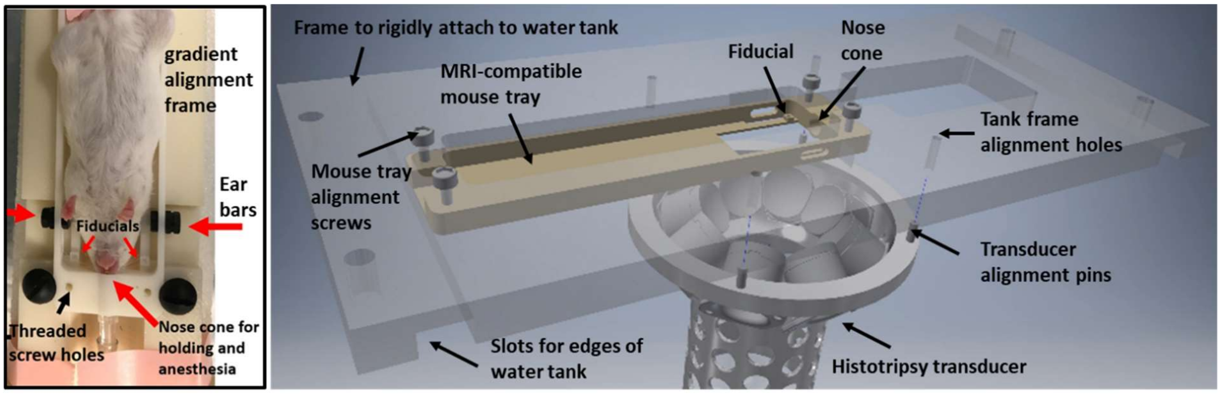

Figure 7.19.The MRI-compatible mouse tray (left) and the assembly of histotripsy treatment setup (right).

Initial Validation:

The accuracy of this method has been validated in mouse tumor phantoms and live mice inoculated with glioblastoma (credit: Sang Won Choi and Sarah Duclos). The method is capable of sub-millimeter accuracy in mice (Figure 7.20)

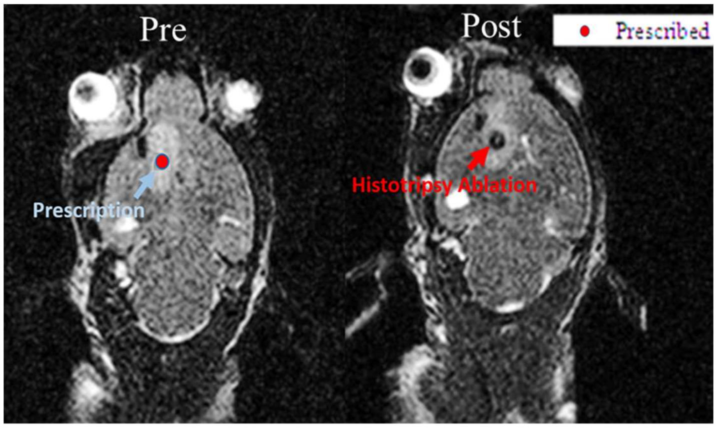

Figure 7.20. A MR image of a mouse brain inoculated with glioblastoma before (left) and after (right) histotripsy treatment. **Figure provided courtesy of Sang Won Choi.**

7.7 References

[1] A. Woehrer, L. Bauchet, and J. S. Barnholtz-Sloan, "Glioblastoma survival: Has it improved? Evidence from population-based studies," *Current Opinion in Neurology*, vol. 27, no. 6. pp. 666–674, 2014.

[2] D. R. Johnson and B. P. O'Neill, "Glioblastoma survival in the United States before and during the temozolomide era," *J. Neurooncol.*, vol. 107, no. 2, pp. 359–364, 2012.

[3] J. F. Deeken and W. Löscher, “The blood-brain barrier and cancer: Transporters, treatment, and trojan horses,” *Clinical Cancer Research*, vol. 13, no. 6. pp. 1663–1674, 2007.

[4] T. Gerhardson, J. R. Sukovich, A. S. Pandey, T. L. Hall, C. A. Cain, and Z. Xu, “Effect of Frequency and Focal Spacing on Transcranial Histotripsy Clot Liquefaction, Using Electronic Focal Steering,” *Ultrasound Med. Biol.*, vol. 43, no. 10, pp. 2302–2317, 2017.

[5] J. R. Sukovich, Z. Xu, T. L. Hall, S. P. Allen, and C. A. Cain, “Treatment envelope of transcranial histotripsy applied without aberration correction,” in *The Journal of the Acoustical Society of America*, 2016.

[6] C. G. Drake, E. J. Lipson, and J. R. Brahmer, “Breathing new life into immunotherapy: Review of melanoma, lung and kidney cancer,” *Nature Reviews Clinical Oncology*, vol. 11, no. 1. pp. 24–37, 2014.

[7] L. Ampie, E. C. Woolf, and C. Dardis, “Immunotherapeutic Advancements for Glioblastoma,” *Front. Oncol.*, vol. 5, 2015.

[8] B. Huang *et al.*, “Advances in immunotherapy for glioblastoma multiforme,” *Journal of Immunology Research*, vol. 2017. 2017.

[9] M. G. Abdelwahab, T. Sankar, M. C. Preul, and A. C. Scheck, “Intracranial Implantation with Subsequent 3D In Vivo Bioluminescent Imaging of Murine Gliomas,” *J. Vis. Exp.*, no. 57, 2011.

[10] A. Gieryng and B. Kaminska, “Myeloid-derived suppressor cells in gliomas,” *Wspolczesna Onkologia*, vol. 20, no. 5. pp. 345–351, 2016.

[11] J. E. Talmadge and D. I. Gabrilovich, “History of myeloid-derived suppressor cells,” *Nature Reviews Cancer*, vol. 13, no. 10. pp. 739–752, 2013.

[12] S. Nagaraj and D. I. Gabrilovich, “Myeloid-derived suppressor cells,” in *Advances in Experimental Medicine and Biology*, 2007, vol. 601, pp. 213–223.

[13] K. H. Parker, D. W. Beury, and S. Ostrand-Rosenberg, “Myeloid-Derived Suppressor Cells: Critical Cells Driving Immune Suppression in the Tumor Microenvironment,” *Adv. Cancer Res.*, vol. 128, pp. 95–139, 2015.

[14] B. L. Mundy-Bosse *et al.*, “Myeloid-derived suppressor cell inhibition of the IFN response in tumor-bearing mice,” *Cancer Res.*, vol. 71, no. 15, pp. 5101–5110, 2011.

[15] J. N. M. Ijzermans and R. L. Marquet, “Interferon-gamma: A Review,” *Immunobiology*, vol. 179, no. 4–5, pp. 456–473, 1989.

[16] M. Mandai, J. Hamanishi, K. Abiko, N. Matsumura, T. Baba, and I. Konishi, “Dual faces of ifnγ in cancer progression: A role of pd-l1 induction in the determination of proand antitumor immunity,” *Clinical Cancer Research*, vol. 22, no. 10. pp. 2329–2334, 2016.

[17] L. Chen and X. Han, “Anti-PD-1/PD-L1 therapy of human cancer: Past, present, and future,” *Journal of Clinical Investigation*, vol. 125, no. 9. pp. 3384–3391, 2015.

CHAPTER 8 Summary and Future Work

8.1 Summary

This dissertation is focused on the investigation and development of pulsed cavitational ultrasound therapy (histotripsy) as a noninvasive or minimally invasive transcranial ultrasound ablation therapy with primary emphasis on the treatment of intracerebral hemorrhage (ICH). The works starts with a demonstration of the feasibility of histotripsy clot liquefaction through excised human skullcaps. This is followed by an investigation into the initial safety of histotripsy clot liquefaction in a porcine ICH model. Technical innovations are then presented in the form of a catheter hydrophone aberration correction method and the development of a new pre-clinical array prototype for the treatment of ICH in human cadaver and porcine models. The dissertation ends with the first-pass investigation into histotripsy mediated immunomodulation within a mouse glioblastoma model. Although focused primarily on ICH, the insights and technical developments specific to transcranial treatment of ICH will likely translate to the treatment of other brain pathologies through the skull (e.g., brain tumors). The intention of this work is to provide an initial basis of scientific and engineering knowledge on histotripsy clot liquefaction to allow eventual clinical translation and adoption as a mainstay treatment option for ICH. The portion of this work investigating the immunomodulatory effects of histotripsy is intended to provide a basis of knowledge that can be further expanded on to understand and leverage any immunomodulatory effects of histotripsy that can be used as an adjunct to current immunotherapy methods.

1) Research: The initial feasibility and safety of histotripsy clot liquefaction was investigated *in vivo* and *in vitro.* The feasibility of liquefying clots with histotripsy through excised human skullcaps was demonstrated with results indicating an ability to liquefy up to ~35 mL of clot in about 20 minutes while skull heating remained within a clinically safe range [1]. The initial safety concerns of histotripsy clot liquefaction was then examined in a porcine ICH model indicating that histotripsy can safely liquefy clots without significant additional damage to the perihematomal region [2]. The liquefied content of the clot was easily evacuated, and the undrained clot had no effect on pig survival or neurological behavior. In addition to applications to ICH treatment, applications into other brain pathologies were investigated. A first-pass investigation into the immunomodulatory effects of histotripsy in a mouse glioblastoma model provided a compelling rationale for potential mechanisms that may be at work in increasing the immunogenicity of the tumors following histotripsy treatment [3]. Through this research activity the application of histotripsy to different brain pathologies has been explored. The results provide a promising basis for the further development and translation of histotripsy as a noninvasive or minimally invasive transcranial ablation therapy.

2) Development: To further develop histotripsy into a minimally invasive treatment for ICH, technical innovations were developed. The catheter hydrophone device utilized the need to drain the liquefied clot through a small hole in the skull as a means to administer a miniature hydrophone that allowed phase aberration to be corrected through the skull. In conjunction with this device, an aberration correction algorithm was developed to correct the aberrations introduced between histotripsy pulses from each array element. This method showed increases in focal pressures of up to 60% at the geometric focus and 27-62% across a range of electronic focal steering locations [4]. A strategy to allow the catheter hydrophone insertion through a burr hole in the skull was also developed. The insertion was done by designing and building a catheter holder that replaced one of the modular array elements in the histotripsy transducer and allowed the catheter hydrophone to be guided through the transducer and a burr hole in the skull to the transducer focus. Finally, a pre-clinical histotripsy array prototype for the treatment of ICH in human cadaver and porcine models was designed and built. A 360-element, 700 kHz hemispherical array with a 30 cm aperture was designed and integrated with an optical tracker surgical navigation system. Calibrated simulations of the transducer suggest a therapeutic range between 48 – 105 mL through the human skull with the ability to apply therapy pulses at pulse-repetition-frequencies up to 200 Hz. The navigation system allows real-time targeting and placement of the catheter hydrophone via a pre-operative CT or MRI. With these technical advancements, histotripsy treatment can be translated to perform further preclinical studies in human cadaver and porcine ICH models. The success of these preclinical studies will provide the basis for the eventual clinical translation and adoption of histotripsy treatment of ICH.

The remainder of this chapter details the key components of future work that will allow further translation of histotripsy treatment for ICH and investigation of histotripsy mediated immunomodulation to allow immune therapy of glioblastoma.

8.2 Future Work

Treatment of ICH Cadavers with Histotripsy

This work demonstrates the efficacy of histotripsy therapy primarily for moderate sized clots (~30 mL) in the central region of the brain [1]. Although this accounts for the majority of ICH cases [5]–[7], ICH can vary in volume and location within the brain [8], [9]. Thus, treating different volumes of ICH in different locations within the brain is necessary to understand the performance and potential limitations of the technology for ICH treatment. In terms of treatment efficacy, human cadavers provide an ideal anatomical model for validation of histotripsy ICH treatment. The pre-clinical setup described in Chapter 6 has been designed for use in human cadavers and is equipped with a neuro-navigation optical tracker (StealthStation S7 Surgical Navigation System, Medtronic, Dublin, Ireland). Such systems have been reported to have 1.5 – 3 mm accuracy [10] and should allow sufficient targeting accuracy for the treatment of large clots given that a similar sized rim of clot will be left intact (untreated) to prevent damage to the surrounding brain [2].

The primary goals of treating ICH cadavers is to show the feasibility and to understand the capacity to liquefy relevant volumes of clot (~20 – 40 mL) quickly (< 30 minutes) using a workflow similar to one that might be used in a clinic. First, the initial feasibility of clot liquefaction in different locations within the brain should be done using the setup described in Chapter 6. This will be done using 24 – 48 hour old cadavers with bovine blood clots implanted to different locations within the brain according to methods in [1]. After obtaining a pre-operative CT scan, the clots will be targeted via the neuro-navigation optical tracker. Treatment will be applied using parameters described in [1] as a starting point. Post-treatment MRI scans will be obtained to understand the targeting accuracy and treatment performance. MRI scans before and after draining the clot should be obtained to understand the capacity to drain clot liquefied with histotripsy using a simple drainage technique. In addition to MRI, whole brain histology should also be obtained to assess any off target damage that may have occurred from effects like prefocal cavitation [1]. Following the initial experiments on 24 – 48 hour old cadavers, a second set of experiments on patients that passed due to ICH should be performed at an early time point post-mortem (2 – 4 hours). This should be done using a system prototype more closely matching the clinical system concept described in Chapter 6. The system will be brought into the ICU or a similar environment and targeting of the transducer will be performed via the neuro-navigation system using a pre-operative CT scan. Such experiments will allow a true clinical level assessment of the workflow, efficacy and speed of the technology.

Long-term Survival Studies and Investigation of Rebleed

The initial safety concerns of histotripsy clot liquefaction *in-vivo* were addressed in a well-established porcine ICH model [2]. In this study, a primary concern that the lysed blood products generated by histotripsy treatment would cause severe neurological injury [11]–[16] was addressed. Additionally, the ability to avoid direct damage to the surrounding brain tissue was shown by leaving a small rim untreated at the periphery of the clot. Although this study provided a good baseline for the initial safety of histotripsy clot liquefaction *in-vivo* longer term survival studies (up to 3 months) are necessary to understand the long term safety of histotripsy treatment. For such studies, similar experimental methods as those presented in [2] should be used with MRI and neurological assessments performed throughout the duration of the survival period.

The effects of histotripsy on ICH rebleed should also be addressed. One important reason for this is that mild subarachnoid damage was reported in the initial safety study [2]. Although it was small in extent and confined to small regions at the periphery of the brain, the presence raises some safety concerns and further studies may be needed to understand its effects on rebleed. One issue with the current porcine ICH model is that the injection of blood into the brain does not model the mechanism by which ICH is generated (i.e., vessel rupture within the brain). To do this, an alternative bacterial collagenase porcine ICH model should be used [17]. As collagenase administered into the brain causes a local weakening of the vasculature leading to vessel rupture, the collagenase model will be implemented to induce an ICH that more closely models that occurring within patients (i.e., spontaneous rupture). As re-bleeds are likely associated with disruption of the initial rupture site triggering the ICH or weakened vasculature, the collagenase model should allow analyzing the risks of re-bleeding associated with histotripsy treatment. One thing to keep in mind with such experiments is that the collagenase-saline-heparin mixture works to induce vessel rupture directly at the location it is administered. Thus, it is possible that the collagenase model might not model the systemic weakened brain vasculature common in ICH patients. To account for this possibility, lower concentration doses of the collagenase-saline-heparin mixture can be applied to multiple regions to weaken or cause hemorrhage in adjacent parts of the vasculature. After refining this model and generating a clot within the brain, histotripsy treatment should be applied to the main bulk of the clot as in [2]. MRI and histology can then be used to assess the effects of bleeding associated with histotripsy treatment.

Improvement of Catheter Hydrophone Aberration Correction

The performance of catheter hydrophone aberration correction was sufficient to improve the focusing through the human skull across a range of electronic steering locations [4]. However, the pressure after correction was generally only within 82 – 85% of that achieved with a PVDF capsule hydrophone. Future performance improvements for the catheter hydrophone aberration correction strategy will lie in developing a catheter hydrophone that is less prone to directional phase variability. Piezoelectric hydrophones were chosen because of their high sensitivity and ability to measure signals with a high signal-to-noise ratio (SNR) through the skull. However, the limited geometry of the acoustic aperture as well as the fabrication procedures for these hydrophones likely led to the phase variability seen across measurements at the large range of incidence angles in this application. Thus, the geometry of these piezoelectric hydrophones may be a limiting factor for improved performance in future development of this technique. One potential avenue with promise is the use of fiber optic hydrophones (FOHPs) which may provide a more refined solution to the problems presented here. This is due to their small apertures, consistent directional response and minimal fabrication procedures, making them potentially less susceptible to some of the phase variation affects seen with piezoelectric hydrophones in this and previous studies [4]. Although these hydrophones have low sensitivity and SNR, adding thin layers to the aperture can significantly improve the sensitivity and may be an approach to pursue in future development of this technique [18]–[21].

In this dissertation, the catheter hydrophone was primarily suggested as a method for phase aberration correction through the skull. The correction of phase aberration allows improvements in focusing that translate to more effective or larger volume treatment through the skull using electronic focal steering. However, in addition to phase information of the measured field, the catheter hydrophone can also provide amplitude information. This information could be used to understand a given elements pressure contribution to the field through the skull. If the amplitude of an element is weekly contributing to the transcranial acoustic field, the loss through the skull can be attributed to significant reflection or absorption as the wave interacts with the skull. Such information would suggest greater absorption of the wave by the skull that may contribute to skull heating or interaction with air filled cavities such as the sinuses. Although the exact cause of the amplitude loss of a given element waveform may be undeterminable, such information could be used as a criterion for masking the output from elements that do not significantly contribute to the transcranial sound field.

Integration of Neuro-navigation with Acoustic Cavitation Emission Treatment Monitoring

One important item that this work does not address is the integration of a real-time treatment monitoring scheme that can be used in the clinical system concept to assess the degree clot liquefaction. In the past, B-mode ultrasound imaging has been used to allow real-time targeting and monitoring of the cavitation activity and treatment progress [22]. However, due to the low-pressure amplitude and high transmission loss through the skull, standard B-mode ultrasound does not allow real-time imaging through the intact human skull. Recent work suggests that the use of the acoustic emission from the cavitation activity generated by histotripsy can be used to monitor treatment progress in semi-real-time and real-time speed for soft-tissues [23]–[26]. Additional work has shown the potential for cavitation localization and treatment monitoring through the human skull [27], [28]. In a recently published study, treatment localization and mapping of the cavitation activity has been demonstrated through the skull in real-time using the acoustic cavitation emission [29].

The new pre-clinical system described in Chapter 6 is equipped with a custom send/receive electronic system that allows the individual transducers of the array to act as both acoustic emitters and receivers. The integration of the neuro-navigation system with the pre-clinical system is intended to allow the geometric focus of the transducer to be placed within the center of the clot based on a pre-operative or diagnostic CT scan. Current work is underway to integrate the receive arm of the electronic subsystem with the neuro-navigation system to allow the location of discrete cavitation events to be mapped onto the CT scan in real-time. This real-time mapping will allow the ability to ensure the cavitation activity remains within the clot. In addition to mapping, some of the treatment progression methods investigated in soft-tissue should be developed and incorporated into the system to allow the progression of the clot liquefaction to be monitored in real-time [25].

Combining Histotripsy Therapy with Check-point Inhibitors

One of the major findings from the histotripsy immunomodulation study in a mouse glioblastoma model (Chapter 7) was the large increase in IFN-γ within the brain tumor of mice treated with histotripsy relative to those left untreated. IFN-γ is an important regulatory cytokine for the activation of specific immunity [30]. Thus, the low levels generally observed in cancer patients are thought to contribute to the limited antitumor response against and the progression of cancer. However, the production of IFN-γ alone may be insufficient to initiate antitumor responses due to the expression checkpoint molecules (e.g., PD-1/PD-L1) by the tumor that can occur in the presence of IFN-γ [31]. This phenomenon might be playing out in the work presented here, where despite the large increase in IFN-γ, no effect on tumor burden is observed. This may suggest that a checkpoint is being expressed by the tumor and blocking the activation of specific immunity against the tumor. To address this issue, future studies should investigate the presence or absence of IFN-γ blocking checkpoints (e.g., PD-1/PD-L1). If present, additional studies using "checkpoint inhibitors" (e.g., anti-PD-1/anti-PD-L1) can be performed in attempt to block the ability of the checkpoint to inhibit IFN-γ mediated immunity and ultimately regress and stabilize the tumor [32].

References

[1] T. Gerhardson, J. R. Sukovich, A. S. Pandey, T. L. Hall, C. A. Cain, and Z. Xu, "Effect of Frequency and Focal Spacing on Transcranial Histotripsy Clot Liquefaction, Using Electronic Focal Steering," *Ultrasound Med. Biol.*, vol. 43, no. 10, pp. 2302–2317, 2017.

[2] T. Gerhardson *et al.*, "Histotripsy Clot Liquefaction in a Porcine Intracerebral Hemorrhage Model," *Neurosurgery*, 2019.

[3] T. Gerhardson *et al.*, "Histotripsy mediated immunomodulation in a mouse GL261 intracranial glioma model," in *International Sympossium on Therapeutic Ultrasound*, 2018.

[4] T. Gerhardson, J. R. Sukovich, A. S. Pandey, T. L. Hall, C. A. Cain, and Z. Xu, "Catheter Hydrophone Aberration Correction for Transcranial Histotripsy Treatment of Intracerebral Hemorrhage: Proof-of-Concept," *IEEE Trans. Ultrason. Ferroelectr. Freq. Control*, vol. 64, no. 11, 2017.

[5] J. P. Broderick, T. G. Brott, J. E. Duldner, T. Tomsick, and G. Huster, "Volume of intracerebral hemorrhage. A powerful and easy-to-use predictor of 30-day mortality," *Stroke*, vol. 24, no. 7, pp. 987–993, 1993.

[6] M. Zuccarello *et al.*, "Early surgical treatment for supratentorial intracerebral hemorrhage: A randomized feasibility study," *Stroke*, 1999.

[7] T. Brott *et al.*, “Early hemorrhage growth in patients with intracerebral hemorrhage,” *Stroke*, 1997.

[8] R. D. Zimmerman, J. A. Maldjian, N. C. Brun, B. Horvath, and B. E. Skolnick, “Radiologic estimation of hematoma volume in intracerebral hemorrhage trial by CT scan,” *Am. J. Neuroradiol.*, 2006.

[9] M. I. Aguilar and T. G. Brott, “Update in Intracerebral Hemorrhage,” *The Neurohospitalist*. 2011.

[10] D. Paraskevopoulos, A. Unterberg, R. Metzner, J. Dreyhaupt, G. Eggers, and C. R. Wirtz, “Comparative study of application accuracy of two frameless neuronavigation systems: Experimental error assessment quantifying registration methods and clinically influencing factors,” *Neurosurg. Rev.*, vol. 34, no. 2, pp. 217–228, 2011.

[11] G. Xi, R. F. Keep, and J. T. Hoff, “Mechanisms of brain injury after intracerebral haemorrhage.,” *Lancet. Neurol.*, vol. 5, no. 1, pp. 53–63, 2006.

[12] G. Xi, Y. Hua, R. R. Bhasin, S. R. Ennis, R. F. Keep, and J. T. Hoff, “Mechanisms of edema formation after intracerebral hemorrhage: effects of extravasated red blood cells on blood flow and blood-brain barrier integrity.,” *Stroke.*, vol. 32, no. 12, pp. 2932–8, 2001.

[13] G. Xi, R. F. Keep, and J. T. Hoff, “Erythrocytes and delayed brain edema formation following intracerebral hemorrhage in rats.,” *J. Neurosurg.*, vol. 89, no. 6, pp. 991–996, 1998.

[14] J. Wu, Y. Hua, R. F. Keep, T. Schallert, J. T. Hoff, and G. Xi, “Oxidative brain injury from extravasated erythrocytes after intracerebral hemorrhage,” *Brain Res.*, vol. 953, no. 1–2, pp. 45–52, 2002.

[15] P. G. Matz, P. R. Weinstein, and F. R. Sharp, “Heme oxygenase-1 and heat shock protein 70 induction in glia and neurons throughout rat brain after experimental intracerebral hemorrhage,” *Neurosurgery*, vol. 40, no. 1, pp. 152–162, 1997.

[16] K. R. Wagner, G. Xi, Y. Hua, G. M. de Courten-Myers, and J. P. Broderick, “Blood components and acute white matter edema development following intracerebral hemorrhage: are hemolysates edemogenic?,” in *Stroke*, 2000, p. 345.

[17] S. Mun-Bryce, A. C. Wilkerson, N. Papuashvili, and Y. C. Okada, “Recurring episodes of spreading depression are spontaneously elicited by an intracerebral hemorrhage in the swine,” *Brain Res.*, vol. 888, no. 2, pp. 248–255, 2001.

[18] C. Koch, “Coated fiber-optic hydrophone for ultrasonic measurement,” *Ultrasonics*, vol. 34, no. 6, pp. 687–689, 1996.

[19] V. Wilkens and C. Koch, “Fiber-optic multilayer hydrophone for ultrasonic measurement,” *Ultrasonics*, vol. 37, no. 1, pp. 45–49, 1999.

[20] P. C. Beard and T. N. Mills, "Extrinsic optical-fiber ultrasound sensor using a thin polymer film as a low-finesse Fabry–Perot interferometer," *Appl. Opt.*, vol. 35, no. 4, p. 663, 1996.

[21] P. Morris, A. Hurrell, A. Shaw, E. Zhang, and P. Beard, "A Fabry–Pérot fiber-optic ultrasonic hydrophone for the simultaneous measurement of temperature and acoustic pressure," *J. Acoust. Soc. Am.*, vol. 125, no. 6, pp. 3611–3622, 2009.

[22] T. L. Hall, J. B. Fowlkes, and C. A. Cain, "A real-time measure of cavitation induced tissue disruption by ultrasound imaging backscatter reduction," *IEEE Trans. Ultrason. Ferroelectr. Freq. Control*, vol. 54, no. 3, pp. 569–575, 2007.

[23] X. Zhang *et al.*, "Real-time feedback of histotripsy thrombolysis using bubble-induced color doppler," *Ultrasound Med. Biol.*, vol. 41, no. 5, pp. 1386–1401, 2015.

[24] R. M. Miller, X. Zhang, A. D. Maxwell, C. A. Cain, and Z. Xu, "Bubble-Induced Color Doppler Feedback for Histotripsy Tissue Fractionation," *IEEE Trans. Ultrason. Ferroelectr. Freq. Control*, vol. 63, no. 3, pp. 408–419, 2016.

[25] J. J. Macoskey *et al.*, "Using the cavitation collapse time to indicate the extent of histotripsy-induced tissue fractionation," *Phys. Med. Biol.*, vol. 63, no. 5, 2018.

[26] J. J. Macoskey *et al.*, "Bubble-Induced Color Doppler Feedback Correlates with Histotripsy-Induced Destruction of Structural Components in Liver Tissue," *Ultrasound Med. Biol.*, vol. 44, no. 3, pp. 602–612, 2018.

[27] J. R. Sukovich, Z. Xu, T. L. Hall, J. J. Macoskey, and C. A. Cain, "Transcranial histotripsy acoustic-backscatter localization and aberration correction for volume treatments," *J. Acoust. Soc. Am.*, vol. 141, no. 5, pp. 3490–3490, 2017.

[28] J. R. Sukovich, Z. Xu, T. L. Hall, J. J. Macoskey, and C. A. Cain, "Histotripsy pulse-reflection for 3D image forming and bubble cloud localization in transcranial applications," *J. Acoust. Soc. Am.*, vol. 140, no. 4, pp. 3083–3084, 2016.

[29] J. R. Sukovich, J. J. Macoskey, J. Lundt, T. Gerhardson, T. L. Hall, and Z. Xu, "Real-time transcranial histotripsy treatment localization and mapping using acoustic cavitation emission feedback," *IEEE Trans Ultrason Ferroelectr Freq Control*, 2020.

[30] J. N. M. Ijzermans and R. L. Marquet, "Interferon-gamma: A Review," *Immunobiology*, vol. 179, no. 4–5, pp. 456–473, 1989.

[31] M. Mandai, J. Hamanishi, K. Abiko, N. Matsumura, T. Baba, and I. Konishi, "Dual faces of ifnγ in cancer progression: A role of pd-l1 induction in the determination of proand antitumor immunity," *Clinical Cancer Research*, vol. 22, no. 10. pp. 2329–2334, 2016.

[32] L. Chen and X. Han, "Anti-PD-1/PD-L1 therapy of human cancer: Past, present, and future," *Journal of Clinical Investigation*, vol. 125, no. 9. pp. 3384–3391, 2015.